

# Magazine of Civil Engineering

111(3), 2022

ISSN  
2712-8172



**Magazine of Civil Engineering**

ISSN 2712-8172

Online peer-reviewed open-access scientific journal in the field of Civil and Construction Engineering

**Founder and Publisher:** Peter the Great St. Petersburg Polytechnic University

This journal is registered by the Federal Service for Supervision of Communications, Information Technology, and Mass Media (ROSKOMNADZOR) in 2020. Certificate EI No. FS77-77906 issued February 19, 2020.

**Periodicity:** 8 issues per year

Publication in the journal is open and free for all authors and readers.

**Indexing:** Scopus, Web of Science (ESCI, RSCI), DOAJ, Compendex, EBSCO, Google Academia, Index Copernicus, ProQuest, Ulrich's Serials Analysis System, CNKI

**Corresponding address:** 29 Polytechnicheskaya st., Saint-Petersburg, 195251, Russia

**Chief science editor:** associate member of RAS, Sc.D. in Engineering, Vitaly V. Sergeev

**Deputy chief science editor:**

Sc.D. in Engineering, Galina L. Kozinets

**Executive editor:** Ekaterina A. Linnik

**Translator, editor:** Darya Yu. Alekseeva

**DT publishing specialist:**

Anastasiya A. Kononova

**Contacts:**

E-mail: [mce@spbstu.ru](mailto:mce@spbstu.ru)

Web: <http://www.engstroy.spbstu.ru>

**Editorial board:**

T. Awwad, PhD, professor, Damascus University, Syrian Arab Republic

M.I. Balzannikov, D.Sc., professor, Samara State University of Economics, Russia

A.I. Belostotsky, D.Sc., professor, StaDyO Research & Engineering Centre, Russia

A.I. Borovkov, PhD, professor, Peter the Great St. Petersburg Polytechnic University, Russia

A. Borodinecs, Dr.Sc.Ing., professor, Riga Technical University, Latvia

M. Veljkovic, PhD, professor, Delft University of Technology, The Netherlands

R.D. Garg, PhD, professor, Indian Institute of Technology Roorkee (IIT Roorkee), India

M. Garifullin, PhD, postdoctoral researcher, Tampere University, Finland

T. Gries, Dr.-Ing., professor, RWTH Aachen University, Germany

T.A. Datsyuk, D.Sc., professor, Saint-Petersburg State University of Architecture and Civil Engineering, Russia

V.V. Elistratov, D.Sc., professor, Peter the Great St. Petersburg Polytechnic University, Russia

T. Kärki, Dr.-Ing., professor, Lappeenranta University of Technology, Russia

G.L. Kozinets, D.Sc., professor, Peter the Great St. Petersburg Polytechnic University, Russia

D.V. Kozlov, D.Sc., professor, National Research Moscow State Civil Engineering University, Russia

S.V. Korniyenko, D.Sc., professor, Volgograd State Technical University, Russia

Yu.G. Lazarev, D.Sc., professor, Peter the Great St. Petersburg Polytechnic University, Russia

M.M. Muhammadiev, D.Sc., professor, Tashkent State Technical University, Republic of Uzbekistan

H. Pasternak, Dr.-Ing.habil., professor, Brandenburgische Technische Universität, Germany

F. Rögener, Dr.-Ing., professor, Technology Arts Science TH Köln, Germany

V.V. Sergeev, D.Sc., professor, Peter the Great St. Petersburg Polytechnic University, Russia

T.Z. Sultanov, D.Sc., professor, Tashkent Institute of Irrigation and Agricultural Mechanization Engineers, Republic of Uzbekistan

M.G. Tyagunov, D.Sc., professor, National Research University "Moscow Power Engineering Institute", Russia

M.P. Fedorov, D.Sc., professor, Peter the Great St. Petersburg Polytechnic University, Russia

D. Heck, Dr.-Ing., professor, Graz University of Technology, Austria

A.G. Shashkin, D.Sc., "PI Georekonstruktsiya", LLC, Russia

V.B. Shtilman, D.Sc., JSC "B.E. Vedeneev VNIIG", Russia

---

Date of issue: 16.05.2022

© Peter the Great St. Petersburg Polytechnic University. All rights reserved.

© Coverpicture – Ilya Smagin



**Contents**

|   |       |
|---|-------|
| Stupishin, L.Yu., Moshkevich, M.L. Limit states design theory based on critical energy levels criterion in force method form  | 11101 |
| Arshadi, H., Kheyroddin, A., Asadollahi Nezhad, A. High-strength steel effects on the behavior of special shear walls   | 11102 |
| Wu, T., Zhou, X.M., He, X.N., Xu, Y., Zhang, L.G. Detection and prediction of weak points of a frozen wall based on grey theory   | 11103 |
| Abdulhadi, A.H., Mussa, M.H., Kadhim, Y. The clay rocks properties for the production of the ceramic bricks   | 11104 |
| Wehbi, N., Masri, A., Baalbaki, O. Flexural behavior of partially composite concrete-encased steel tubular beams  | 11105 |
| Barham, W.S., Obaidat, Y.t., Alkhatatbeh, H.A. Behavior of heat damaged reinforced recycled aggregate concrete beams repaired with NSM-CFRP strips                                    | 11106 |
| Butko, D.A., Volodina, M.S. Regularities of rapid filter backwash water clarification in reagent-free mode  | 11107 |
| Zhao, Q.Q., Fu, Q., Zhang, H.T., Wang, J.W. Performance improvement model of cement pavement in seasonal-frost regions  | 11108 |
| Baev, O.A., Kosichenko, Yu.M., Silchenko, V.F. Effect of subsoil moisture on filtration through a screen defect   | 11109 |
| Stepanov, S.V., Strelkov, A.K., Panfilova, O.N. Removal of heavy metals from wastewater with natural and modified sorbents  | 11110 |
| Gaile, L., Pakrastins, L., Ratnika, L. Structural health monitoring by merging dynamic response data  | 11111 |
| Bolshev, A., Frolov, S.A., Shonina, E.V. Mooring system optimization for marine floating hydrotechnical structures  | 11112 |
| Kuz'min, M.P., Larionov, L.M., Kuz'mina, M.Yu., Kuz'mina, A.S., Ran, J.Q., Burdonov, A.E., Zenkov, E.V. Production of portland cement using fluorine gypsum – hydrofluoric acid waste | 11113 |
| Kirsanov, M.N., Safronov, V.S. Analytical estimation of the first natural frequency and analysis of a planar regular truss oscillation spectrum                                       | 11114 |
| Slavcheva, G.S., Britvina, E.A. 3D-printable artificial marble  | 11115 |



Research article

UDC 624.046

DOI: 10.34910/MCE.111.1

## Limit states design theory based on critical energy levels criterion in force method form

L.Yu. Stupishin<sup>a</sup> , M.L. Moshkevich<sup>b</sup> 

<sup>a</sup> National Research Moscow State Civil Engineering University, Moscow, Russia

<sup>b</sup> Southwest State University, Kursk, Russia

 [lusgsh@yandex.ru](mailto:lusgsh@yandex.ru)

**Keywords:** structural analysis, limit states design, force method, critical levels of energy, pin-jointed structures

**Abstract.** The article deals with the development of the theory of limit states of structures. There are various approaches to the formulation of limiting states of structures. They are related to issues of strength, structural stability (ULS) or safe operational requirements (SLS). All known theories are oriented to a certain hypothesis of the limiting state and exist separately from each other. Therefore, there is an opinion that there is no systematic view of the limit state theory. The article suggests a general approach to creating the theory of limit states based on the criterion of critical levels of internal energy proposed by one of the authors. The problem of determination of the structure limit state is formulated as finding critical energy levels by varying system stresses. The change of energy level is accompanied by removal of linkages in the structure. Self-stressing states of the system make it possible to find out the most loaded elements. Mathematical model of general approach is the eigenvalue problem. It is formulated in the force method form and the resolving equations are derived. The physical meaning of the obtained relations and the links between the variables are explained. The proposed technique allows making a forecast that shows the element and the load from which destruction of the system will begin and trace the progressive failure of structural elements. Depending on the hypothesis of the ultimate limit state of the structure or serviceability limit state, we can analyze the behavior of the structure under load and predict violation of the conditions LSD. The problem solving method of finding the limit states is shown in the example of the pin-jointed structure.

### 1. Introduction

Issues that related to the structures bearing capacity loss are still relevant from the moment the doctrine of the strength deformable systems arose. The conceptual framework of the limit state design (LSD) of the structure is the main in the construction field.

The limit state method came into designers practice of building codes in the Soviet Union in 1955 (N.S. Streletsky and others) and became the main throughout the world [1, 2].

In the regulatory documents two main groups are identified: ultimate limit state (ULS) that associated with the appearance of the greatest stresses or critical forces in the structure, and serviceability limit state (SLS) associated with safe operational requirements. The first includes hypotheses of design criteria: strength, stability, etc., related to the behavior of materials and structures, based on the continuum models of the deformable body [3–11].

Stupishin, L.Yu., Moshkevich, M.L. Limit states design theory based on critical energy levels criterion in force method form. Magazine of Civil Engineering. 2022. 111(3). Article No. 11101. DOI: 10.34910/MCE.111.1

© Stupishin, L.Yu., Moshkevich, M.L., 2022. Published by Peter the Great St. Petersburg Polytechnic University.



This article is licensed under a CC BY-NC 4.0



The hypotheses of the second group do not take into account the causes of structural failure associated with the defects of the material of construction and the structure listed above. The SLS in the practice of designing building structures means a state that does not meet the operational requirements for building structures. Therefore, the designer takes into account the requirements of safe operation, that do not directly lead to bearing capacity loss, but make the operation processes dangerous or complicate normal operation [12–14].

There are researches connecting the physicochemical processes occurring in the material with its strength characteristics [15]. Particularly intensive studies of bearing capacity loss occasion are conducted for materials at the nano-scale [16–18] that allow a deeper understanding of the processes occurring in deformable bodies.

For combining existing theories of limit states into one it seemed the most productive to use probabilistic approaches. Research in this direction is ongoing, but work is not quite finished [19–21].

The optimal design of structures is another way to combine criteria of different nature into one statement of the problem [22–25]. However, too many hypotheses of the limiting state make it difficult to formulate the objective function, and its large number does not allow obtaining a solution to the optimization problem.

The above approaches try to combine many hypotheses that cannot be limited. The attempt to combine existing LSD theories in a single mathematical model causes great difficulties. Therefore, there is an opinion that “there is still no theory of LSD as an exposition of a certain systematic view of the subject” [26].

This paper is devoted to the formulation of a general theory and criterion of the LSD for the deformable structures. The created methodology for structural analysis of deformable systems is illustrated with a simple example.

## 2. Methods

### 2.1. Backgrounds of the method

One of the goals of structural mechanics is to determine the maximum displacements and stresses of structure element. For this structure element must be written down the corresponding condition of LSD. At the same time, the formulation of LSD criteria for the structure elements remains outside the structural mechanics boundaries. In this regard, the question about the ultimate goal of structural mechanics as a scientific discipline, which, obviously, consists in determining the parameters of LSD for structure, remains open. Accordingly, there must be a phenomenological criterion that allows, from a single point of view, to find a structural element in LSD, or to determine the LSD criterion of a complex physical model of a building (structure). In turn, indication of the parameters of the LSD of the structure will provide the basis for the further application of hypotheses about the causes of destruction or the appearance of defects in the material of the structure.

In structural mechanics, there are criteria for the LSD based on the phenomenological approach of structural loss of stability, or the occurrence of resonance, which can be figuratively formulated as “at some point, everything went not as it used to be”. Such a general approach it can be possible to construct a mathematical model of physical phenomena related to the concept of LSD on the basis of eigenvalue problem.

LSD hypothesis can be formulated as a statement that the structure response different than before the moment of the limiting state. The next fact is that in formulating limit state of structures, as a rule, it is not the deformation process is the main, but the structure parameters at the time of a critical condition. Finally, it should be recognized that the design takes only such deformed forms that depend on the conditions of support, mechanical and geometric characteristics and the physical law of deformation. The type of load and the law of its distribution over the structure have little effect on its shape in the ultimate state.

It is possible to determine the limiting states of the structure in the sequence:

1. determination of the element with the highest stresses and strains based on the criterion of critical levels of the internal potential energy of the system [25];
2. to compare this state of possible types of loading and the corresponding level.

That is, to make a map of the external loads for the system under LSD condition. Then you can select the hypothesis for the possible types of loss of structural bearing capacity.

## 2.2. The loss of the bearing capacity as the removal of linkages

The fact that the failure of the system to bear the load is associated with the loss of geometric stability, forces us to turn to the structure instability analysis (kinematic analysis of structures). There are only three objects of kinematic analysis: a rigid body, constraints (linkages, in rare cases, deformable), and a hinge, which allows us to conclude that the appearance of geometric instability depends on the removal of linkages.

In this case, the removal of linkages leads to a decrease of the degree of static indeterminability and, ultimately, to a geometrically instable system. That is means the loss of bearing capacity by the entire structure. The Fig. 1 shows a rod with a remote longitudinal linkage, illustrating the developed theory using the example of a system of pin trusses.

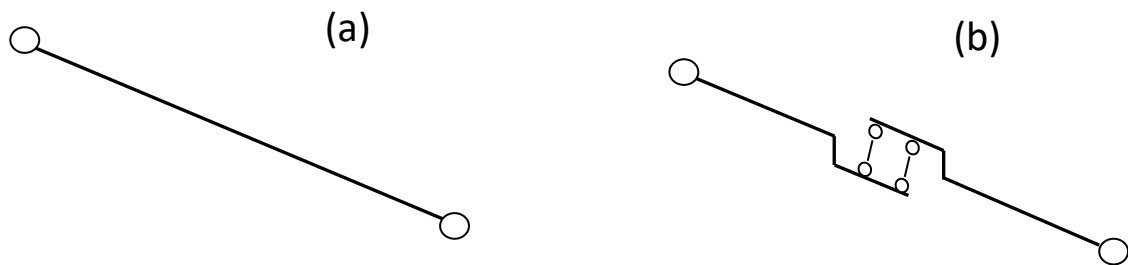


**Figure 1. (a) Bar element, (b) element with longitudinal bond removed.**

Thus, in order to formalize the concept of structural failure to satisfy operational requirements from the point of view of structural mechanics, we can accept it as equivalent to removing the system connection [27].

The reason for removing the connection is determined by the requirements for structural elements. This may be a loss of bearing capacity during tension (or compression) of the bar due to the appearance of yield strains. This can be loss of stability or brittle fracture due to the appearance and development of cracks, etc. Theoretically, any criterion corresponding to the concept of LSD can be used.

## 2.3. Self-stressing state of the structure

The concept of the self-stressed structure was introduced almost a century ago, but is used by various authors to explain the physical phenomena that occur in a solid deformable body, depending on the problem being solved. So A.R. Rzhancyn [28] stated that the state of self-stress can occur only in statically indeterminate systems at zero loads. In this case, the cause of such stresses is the discontinuity of elements or the effect of temperature, i.e. external influences. A.V. Perel'muter and V.I. Slivker [29] talk about the state of self-stress in the main system of the force method, which is also a statically determinate system. Dzh. Robinson, G.V. Haggemajer, R. Kontini [30] said about the equivalent concept of a self-balanced system is introduced and the concept of amplitudes of self-balanced forces is used.

The criterion of critical energy levels requires an understanding of the state of self-stress as an objectively existing state of the entire deformable structure as a whole at any stage of its loading. This state is determined by the geometry of the structure, the geometric and mechanical characteristics of its elements and the conditions of support. The distribution of forces in the static indeterminate system is determined by the system of equations written in the form of the force method, displacement method, etc. The solution of the problem will be the principal values of the deflections of the entire system and eigenvectors present internal forces distributions in the system. The principal stiffness values and the corresponding displacement distributions are determined similarly.

A state of self-stress without a load on the system is detected by varying displacements or forces in the bars, while the magnitude of the variations is not specified, since the energy levels are a discrete set of critical values. The state of self-stress, in the sense of the distribution of internal forces in the bars or their deformations, exists both in the absence of loading and at any non-destructive level of loading. It can be argued that the state of self-stress in the system does not change during loading process until any linkage will remove. Failure will occur in the most rigid (flexible member) element of the system, that is, the element with the maximum (minimum, depending on the statement of the problem) eigenvalue.

We obtain a new design scheme without one connection, to which the above reasoning applies. The new system has a different level of internal potential energy of deformation, as well as a system of self-balanced internal forces (stresses), which may differ from the previous one.

The most important property of self-balanced efforts or movements is that they are described by an orthonormal system of functions.

## 2.4. Critical strain levels in form the force method

The criterion of critical energy levels can be used as the basis for formulating the limiting state, which allows one to describe the limiting states of the system.

Generalized internal effort  $\Phi_i^{\text{in}}$  in  $i$ -th displacement connection  $m$  times of a statically indeterminable system arising from a generalized external force  $\Phi^{\text{ex}}$ , can be represented as the sum of internal efforts

$$\Phi_i^{\text{in}} = \Phi_{i\Phi^{\text{ex}}} + \sum_{k=1}^m \Phi_k^{\text{in}} \Phi_{ki}^{\text{in}}. \quad (1)$$

Here is  $\Phi_{i\Phi^{\text{ex}}}$  the effort in the  $i$ -th element of the main system, devoid of all unknown redundant constraints arising from the applied external load  $\Phi^{\text{ex}}$ ,

$\Phi_k^{\text{in}}$  is the internal efforts in the redundant structure links ( $k = 1, 2, \dots, m$ );

$\Phi_{ki}^{\text{in}}$  is the unit efforts in  $i$ -th element of the simple system from the effort  $\Phi_k^{\text{in}} = 1$ , exerted on  $k$ -th element.

Note that the presented expression for efforts does not depend on the choice of the method for static indeterminacy solving. Moreover, the initial statically indeterminate structure can be taken as the primary system. The principle of deriving equations in the form of the force method and the displacement method, as you know, is the same.

We will apply the methodology of the force method in the following considerations, which will not change the results for the case of using other methods for revealing static indeterminacy.

Define generalized deflections  $\delta_k$  in the direction redundant unknowns. We write down the possible work of the redundant unknowns  $\Phi_{kk}^{\text{in}}$  and the internal efforts caused by them  $\Phi_{ik}^{\text{in}}$  in the  $n$  elements of the simple system at the corresponding generalized displacements  $\xi_i$

$$\Phi_{kk}^{\text{in}} \delta_k - \sum_{i=1}^n \Phi_{ik}^{\text{in}} \xi_i = 0, \quad k = 1, 2, \dots, n. \quad (2)$$

Here, the summation is carried out over all elements of the system  $n$ .

Putting force in  $k$ -th element equal to one, i.e.  $\Phi_{kk}^{\text{in}} = 1$ , getting for  $k$ -th state equation of displacements in this rod

$$\delta_k = \sum_{i=1}^n \Phi_{ik}^{\text{in}} \xi_i, \quad k = 1, 2, \dots, n. \quad (3)$$

Considering that the variation of the self-stress system will always occur near the equilibrium state, we introduce the stiffness coefficient of the system element  $K_i$ . In our case denoted  $K_i = E_i A_i$ , where elastic module of rods is  $E_i$ , area of its cross section is  $A_i$ . Then we can determine the generalized displacements through the generalized efforts in the form:

$$\delta_{k\Phi^{\text{ex}}} = \sum_{i=1}^n \frac{\Phi_{ik}^{\text{in}} \Phi_{i\Phi^{\text{ex}}}^{\text{in}}}{K_i}; \quad (4)$$

for deflections dependent on external load, and

$$\delta_{kl} = \sum_{i=1}^n \frac{\Phi_{ik}^{\text{in}} \Phi_{il}^{\text{in}}}{K_i}, \quad (5)$$





$$[L] = \begin{bmatrix} \delta_{11} & \delta_{12} & \dots & \delta_{1n} \\ \delta_{21} & \delta_{22} & \dots & \delta_{2n} \\ \dots & \dots & \dots & \dots \\ \delta_{n1} & \delta_{n2} & \dots & \delta_{nn} \end{bmatrix}, \quad [\lambda_0] = \begin{bmatrix} \lambda_{01}^G & 0 & \dots & 0 \\ 0 & \lambda_{02}^G & \dots & 0 \\ \dots & \dots & \dots & \dots \\ 0 & 0 & \dots & \lambda_{0n}^G \end{bmatrix}.$$

Eigenvalues  $\lambda_{0i}^G$  is the main values of deflections in the structure bars, and the eigenvectors  $\{\delta\Phi_k^{\text{in}}\}$  is amplitude values of the distribution of self-stress. For small variations, the relation for the eigenvalues of the flexibility and stiffness matrices is valid

$$[\lambda_{0i}^K] = [\lambda_{0i}^L]^{-1}.$$

Here are  $\lambda_{0i}^K$  is the eigenvalues of the system stiffness matrix.

The physical meaning of the derived equations (12), (13) is the state of self-stress in a multiply connected system at critical energy levels. Solving the eigenvalue problem gives the main node displacements of the core system and the corresponding vectors of the amplitude values of the structure nodal reactions.

### 3. Results and Discussion

#### 3.1. Example of calculating a redundant construction

Let us take as an example the three-bar pin-jointed system shown in Fig. 2. The cross-sectional areas of the structural members  $A_i, i=1,2,3$  and the elastic modulus  $E_i, i=1,2,3$  are designated for members 0-1, 1-2, and 1-3, respectively. It is required to indicate the possible limiting states of the structure, as well as the values of ultimate loads.

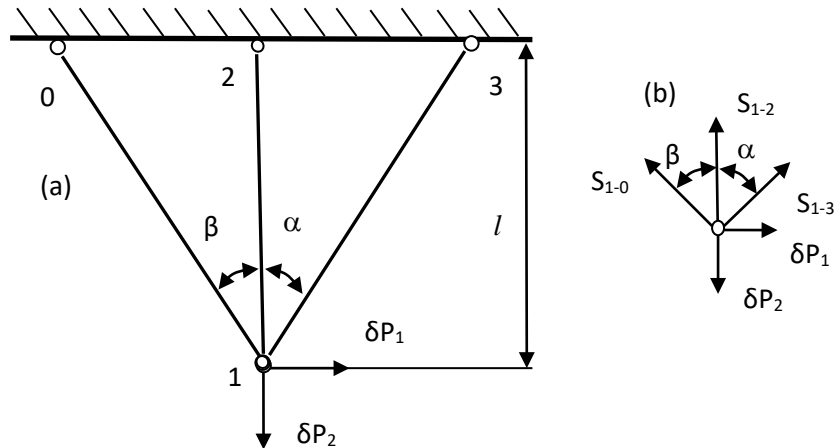


**Figure 2. Three-bar system: (a) design scheme, (b) node 1.**

To simplify the calculations, we will carry out the calculation in the matrix form of the force method in accordance with (13). Equilibrium equations in Node 1

$$\begin{aligned} -S_{0-1} \sin \beta + S_{1-3} \sin \alpha + \delta P_1 &= 0, \\ -S_{0-1} \cos \beta - S_{1-2} - S_{1-3} \cos \alpha + \delta P_2 &= 0, \end{aligned} \quad (14)$$

allow you to compose a static matrix of the three-rod system

$$[A] = \begin{bmatrix} -\sin \beta & 0 & \sin \alpha \\ -\cos \beta & -1 & -\cos \alpha \end{bmatrix}. \quad (15)$$

The matrix of internal deflections of the three-bar system, taking into account the notation  $\eta_1 = EA/E_1A_1$ ,  $\eta_2 = EA/E_2A_2$ ,  $\eta_3 = EA/E_1A_1$ , has the form

$$[B] = 1/EA \begin{vmatrix} \eta_1/\cos\beta & 0 & 0 \\ 0 & \eta_2 & 0 \\ 0 & 0 & \eta_3/\cos\alpha \end{vmatrix}. \quad (16)$$

Expressions for calculating next matrixes, the eigenvalues and eigenvectors will not be written out due to the large volume.

The flexibility matrix of the three-rod system is written as

$$[L] = ([A]^T [B]^{-1} [A])^{-1}. \quad (17)$$

The internal forces in the structure rods are defined as

$$[N] = [B]^{-1} [A]^T [L] \{P\}. \quad (18)$$

The strain caused by internal forces is

$$[\varepsilon] = [A][L][A]^T \{N\}. \quad (19)$$

The deflections of node 1 in the direction of the initial degrees of freedom

$$[u] = [L]\{P\}. \quad (20)$$

**Example 1.** Let the stiffness values of the rods be the same ( $\eta_1 = \eta_2 = \eta_3 = 1$ ), and the rods are tilted at the same angles ( $\alpha = \beta = \pi/4$ ).

Stage 1.

The system is considered at the first critical level (when all connections are in place). Due to the complete symmetry of the system, the flexibility matrix is diagonal.

$$[L] = \frac{1}{EA} \begin{vmatrix} 1.4143 & 0 \\ 0 & 0.5858 \end{vmatrix}. \quad (21)$$

We consider the unit impacts in the node directed along the degrees of freedom of node 1 shown in Figure 1.

$$[\Psi] = \begin{vmatrix} 1 & 0 \\ 0 & 1 \end{vmatrix}. \quad (22)$$

We consider the load to be unit and directed along the degrees of freedom of node 1 shown in Fig. 1.

If we take only  $\delta P_2$  force to load the system, will have the same internal forces, which A.R. Rzhanicyn yield in "Theory of plasticity"

$$\bar{S}_{1-2} = 0.5858, \bar{S}_{1-0} = \bar{S}_{1-3} = 0.2929. \quad (23)$$

Internal forces from two directed unit external forces are

$$\bar{S}_{1-0} = 1, \bar{S}_{1-2} = -0.5858, \bar{S}_{1-3} = 0.2929. \quad (24)$$

At the first stage, the ultimit limit state occurs in the extended rod 0-1.

Stage 2



Further investigation is conducted for the three-bar system without linkage 0-1. Fig. 3 shows a new design scheme of the system, which continues to be loaded in the directions of the degrees of freedom  $\delta P_1, \delta P_2$ . Loads continue to increase.

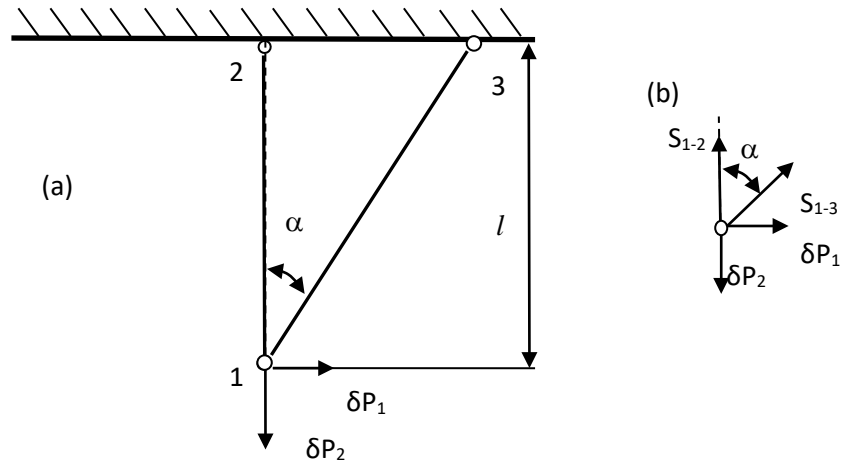


**Figure 3. (a) Three-bar system without one bar, (b) node 1 (a).**

Equilibrium equations in Node 1

$$\begin{aligned} S_{1-3} \sin \alpha + \delta P_1 &= 0, \\ -S_{1-2} - S_{1-3} \cos \alpha + \delta P_2 &= 0. \end{aligned} \quad (24)$$

allow you to compose a static matrix of the two-rod system

$$[A] = \begin{bmatrix} 0 & \sin \alpha \\ -1 & -\cos \alpha \end{bmatrix}. \quad (25)$$

Easy to see that  $\text{Det}[A] \neq 0$ , and therefore, the system is stable.

The matrix of the external deflections of the two-rod system is written as

$$[L] = \begin{bmatrix} 3.829 & 1 \\ 1 & 1 \end{bmatrix}. \quad (26)$$

Eigenvalues of the flexibility matrix is  $\lambda_1 = 4.146$ ,  $\lambda_2 = 0.682$ .

The eigenvectors of the external deflection matrix

$$[\Phi] = \begin{bmatrix} 0.9530 & -0.3029 \\ 0.3029 & 0.9530 \end{bmatrix}. \quad (27)$$

Longitudinal forces in the system

$$S_{1-2}^{\text{cr}} = 5.207, S_{1-3}^{\text{cr}} = -5.588. \quad (28)$$

The ultimate state from compressive strength will occur in inclined rod, the inclined one should be checked for stability.

The full ultimate load taking into account the both stage of deformation will be

$$P_{\text{total}}^{\text{cr}} = 6.588 P^{\text{cr}}. \quad (29)$$

The critical force acting on the structure is taken in accordance with the concept of the type of loss of bearing capacity by the rod.

If we assume that the bars lose strength in the plastic stage of deformation  $\sigma_{\max} = \sigma_t$ , and the load acting in the direction of degrees of freedom  $P_2 = 1, P_1 = 0$ , we get a complete match with the result given A.R. Rzhanicyn.

$$P_{\text{total}}^{\text{cr}} = 2.414P^{\text{cr}}. \quad (30)$$

where  $P^{\text{cr}} = A\sigma_t$ .

**Example 2.** Let the stiffness values of the rods be the same ( $\eta_1 = \eta_2 = \eta_3 = 1$ ), and the rods are tilted at the same angles ( $\alpha = \pi/4, \beta = \pi/3$ ).

Stage 1.

The system is considered at the first critical level (when all connections are in place).

Due to the system nonsymmetrical, the flexibility matrix is

$$[L] = \frac{1}{EA} \begin{bmatrix} 1.397 & 0.1295 \\ 0.1295 & 0.6883 \end{bmatrix}. \quad (31)$$

Eigenvalues of the flexibility matrix is

$$[\lambda] = \frac{1}{EA} \begin{bmatrix} 1.4199 & 0 \\ 0 & 0.6654 \end{bmatrix}. \quad (32)$$

Vector-matrix of the eigenvectors is

$$[\Phi] = \begin{bmatrix} 0.9847 & -0.1743 \\ 0.1743 & 0.9847 \end{bmatrix}. \quad (33)$$

For the main vector with the maximum eigenvalue, we obtain the longitudinal self-stress forces

$$\bar{S}_{1-0} = 0.9475, \bar{S}_{1-2} = 0.3514, \bar{S}_{1-3} = -0.8169.$$

The greatest tensile force arises in the left bond, inclined at an angle of 60 degrees to the vertical.

The full maximum load at the first stage for removing one connection will be

$$P_1^{\text{cr}} = 0.9475P^{\text{cr}}. \quad (34)$$

Stage 2.

Further investigation is conducted for the three bar system without linkage 0-1. Fig. 3 shows a new design scheme of the system, which continues to be loaded in the directions of the degrees of freedom  $\delta P_1, \delta P_2$ . Loads continue to increase.

Since the solution for such a scheme was already carried out in the previous problem, we write out the value of the critical force that turns the system into an unstable one

$$\bar{S}_{1-3}^{\text{cr}} = -5.5882P^{\text{cr}}. \quad (35)$$

The total limit load in two stages will be

$$P_{\text{total}}^{\text{cr}} = 6.5357P^{\text{cr}}. \quad (36)$$

## 4. Conclusion

1. The limiting states of the structure correspond to the extreme values of stresses arising in the deformable body or the corresponding deformations.

2. Critical strain energy levels of a deformable body are detected by changing self-stress state. Due to this fact, it is possible to identify for the designed structure under what conditions the ultimate state and values of ultimate loads come.

3. It is possible to predict from which element and at what load the destruction of the building will begin and trace the sequence of exclusion of structural elements from work on the load.

4. Depending on the hypothesis of the ultimate limit state of the structure or serviceability limit state, one can analyze the behavior of the structure under load and predict violation of the conditions of the LSD at the one mathematical model.

5. The proposed technique opens up new possibilities for the analysis and synthesis of structures:

- 1) analysis of the sequence of rods output from work on the load;
- 2) selection of the structural element from which its progressive destruction will begin;
- 3) reinforcement of structural elements in order to regulate the forces in the structure;
- 4) design of smart structures.

## References

1. BS EN-1990:2002. Eurocode – Basis of structural design.
2. ICC IBC-2009. International Building code.
3. Satti, H., Krawczyk, R. Issues of Integrating Building Codes in CAD. 1<sup>st</sup> ASCAAD International Conference, e-Design in Architecture. 2004. Pp. 89–107.
4. Torgeir, M. Development of accidental collapse limit state criteria for offshore structures. *Structural Safety*. 2009. 31. Pp.124–135. DOI: 10.1016/j.strusafe.2008.06.004
5. Djebbar, N., Chikh, N. Limit period based on approximate analytical methods estimating inelastic displacement demands of buildings. *Journal of civil engineering and management*. 2007. XIII. 4. Pp. 283–289.
6. Liew, J., Punniyakotty, N., Shanmugam, N. Limit – state Analysis and Design of Cable-tensioned Structures. *International Journal of Space Structures*. 2001. 16. 2. Pp. 95–110. DOI: 10.1260/0266351011495205
7. Mr'oz, K.M., Mr'oz, Z. Crack growth modes in inhomogeneous materials: analysis of bi- and multi-material interfaces. In *Proceedings of the International Symposium on "Crack Paths*. 2011. Pp. 17–25.
8. Krishnan, A., Xu, L.R. Systematic evaluation of bonding strengths and fracture toughnesses of adhesive joints. *The Journal of Adhesion*. 2011. 87. 1. Pp. 53–71.
9. Verma, S.S., Amritphale, S. Das Improvement of strength and radiation protection properties of biodegradable jute fiber reinforced material. *Strength of Materials*. 2017. 49. 5. Pp. 689–698.
10. Teixeira, A.P., Ivanov, L.D., Guedes Soares, C. Assessment of characteristic values of the ultimate strength of corroded steel plates with initial imperfections. *Engineering Structures*. 2013. 56. Pp. 517–527. DOI: 10.1016/j.engstruct.2013.05.002
11. Hong-Shuang Li, An-Long Zhao Kong Fah Tee. Structural reliability analysis of multiple limit state functions using multi-input multi-output support vector machine. *Advances in Mechanical Engineering*. 2016. 8(10). Pp. 1–11. DOI: 10.1177/1687814016671447
12. Ching, J., Beck, J.L. Real-time reliability estimation for serviceability limit states in structures with uncertain dynamic excitation and incomplete output data. *Probabilistic Engineering Mechanics*. 2007. 22. Pp. 50–62. DOI: 10.1016/j.probenmech.2006.05.006
13. Pisano, A.A., Fuschi, P., De Domenico, D. Peak loads and failure modes of steel-reinforced concrete beams: predictions by limit analysis. *Engineering Structures*. 2013. 56. Pp. 477–488.
14. Sanzharovsky, R., Manchenko, M., Hadzhiev, M., Musabaev, T., Ter-Emmanuilyan, N., Varenik, K. System of insufficiency of the modern theory of long-term resistance of reinforced concrete and designers' warnings. *Structural mechanics of engineering constructions and buildings*. 2019. 15 (1). Pp. 3–24. DOI: 10.22363/1815-5235-2019-15-1-3-24
15. Makhutov, H.A., Gadenin, M.M., Reznikov, D.O. Analysis of stress-strain and limit states in extremely loaded zones of machines and constructions. *Chebyshevskiy sbor-nik*. 2017. 18. 3. Pp. 394–416. DOI: 10.22405/2226-8383-2017-18-3-390-412
16. Mitasov, V.M., Adishchev, V.V., Statsenko, N.V. The concept of limit states of structures and their check on Russian standards and eurocodes. *Izvestiya vuzov. Stroitel'stvo*. 2017. 8. Pp. 15–23.
17. Yang, Y., Gao, F., Cai, C., Chen, P. A novel polyaxial strength criterion for rock materials under general stress condition. *International Journal of Applied Mechanics*. 2018. Pp. 1–24. DOI: 10.1142/S1758825118500825
18. Perelmuter, A.V., Kabantsev, O.V. About the problem of analysis resistance bearing systems in failure of a structural element. *International Journal for Computational Civil and Structural Engineering*. 2018. 14(3). Pp. 103–113.
19. Zenkov, E.V., Tsvik, L.B. Update of the equations of the limit state of the structural materials with the realization of their deformation. *Systems. Methods. Technologies*. 2017. 2 (34). Pp. 28–34. DOI: 10.18324/2077-5415-2017-2-28-34
20. Poluektov, M., Freidin, A., Figiel, Ł. Modelling stress-affected chemical reactions in non-linear viscoelastic solids with application to lithiation reaction in spherical Si particles. *International Journal of Engineering Science*. 2018. 128. Pp. 44–62. DOI: 10.1016/j.ijengsci.2018.03.007
21. Ovidko, I.A., Sheynerman, A.G. Elastic fields of nanoscopic inclusions in nanocomposites. *Materials Physics and Mechanics*. 2010. 10. Pp. 1–29.
22. Bochkarev, A.O., Grekov, M.A. Lokalnaya poterya ustoychivosti plastiny s krugovym nanootverstiyem pri odnoosnom rastyazhenii [Local loss of stability of a plate with a circular nanohole under uniaxial extension]. *Doklady akademii nauk*. 2014. 457. 3. Pp. 282–285. DOI: 10.7868/S0869565214210099 (rus)



23. Rajapakse, N. Nanobeam mechanics: theory and experimental comparison. International Conference on Sustainable Built Environments (ICSBE-2010). 2010. Pp. XX–XXI.
24. Attia, M., Mahmoud, F. Analysis of nanoindentation of functionally graded layered bodies with surface elasticity. International Journal of Mechanical Sciences. 2015. 94–95. Pp. 36–48. DOI: 10.1016/j.ijmecsci.2015.02.016
25. Schifferle, F., Bandi, T., Neels, A., Dommann, A. Where is the limit? Yield strength improvement in silicon microstructures by surface treatments. Phys. Status Solidi. 2016. A 213. 1. Pp. 102–107. DOI: 10.1002/pssa.201532444
26. Bian, X., Zheng, J., Xu, Z. Incorporating Serviceability Limit State Requirements into Reliability-based Analysis and Design of Piles. Korean Society of Civil Engineers Journal of Civil Engineering. 2015 19(4). Pp. 904–910.
27. Perel'muter, A.V. Izbrannye problemy nadezhnosti i bezopasnosti stroitel'nykh konstrukcij [Selected problems of reliability and safety of building structures] Promyshlennoe i grazhdanskoe stroitel'stvo. 2018. 9. Pp. 44–48. (rus)
28. Stupishin, L.U. Limit state of building structures and critical energy levels. Promyshlennoe i grazhdanskoe stroitel'stvo. 2018. 9. Pp. 44–48.
29. Rzhancyn, A.R. Raschet sooruzhenij s uchetom plasticheskikh svoystv materialov [Calculation of structures taking into account the plastic properties of materials]. Moscow, Gostrojizdat Publ. 1954. Pp. 283. (rus)
30. Perel'muter, A.V., Slivker, V.I. Raschetnye modeli sooruzhenij i vozmozhnost' ih analiza [Design models of structures and the possibility of their analysis]. Moscow, DMK Press Publ., 2007. 600 p. (rus)
31. Robinson, Dzh., Haggenmajer, G.V., Kontini, R. Static analysis of structures using force method and displacement as a problem of eigenvalues. Raschet uprugih konstrukcij s ispol'zovaniem EVM [Calculation of elastic structures using computers]. Leningrad, Sudostroenie Publ., 1974. Vol. 2. Pp. 91–102. (rus)
32. Stupishin, L.U. Variational criteria for critical levels of internal energy of a deformable solids. Applied Mechanics and Materials. 2014. 574–579. Pp. 1584–1587. DOI: 10.4028/www.scientific.net/AMM.578-579.1584
33. Stupishin, L.U. Evaluation of load bearing capacity of structures with defects. Promyshlennoe i grazhdanskoe stroitel'stvo. 2017. 10. Pp. 39–44.

#### **Information about authors:**

**Leonid Stupishin,**

*PhD in Technical Sciences,*

ORCID: <https://orcid.org/0000-0002-1794-867X>

E-mail: [lusgsh@yandex.ru](mailto:lusgsh@yandex.ru)

**Mariya Moshkevich,**

*PhD in Economics,*

ORCID: <https://orcid.org/0000-0001-8749-2252>

E-mail: [mmoshkevich@yandex.ru](mailto:mmoshkevich@yandex.ru)

*Received 25.03.2020. Approved after reviewing 20.07.2021. Accepted 21.07.2021.*



Research article

UDC 624.04

DOI: 10.34910/MCE.111.2

## High-strength steel effects on the behavior of special shear walls

H. Arshadi\* , A. Kheyroddin , A. Asadollahi Nezhad

Semnan University, Semnan, Iran

 [hamed.arshadi@semnan.ac.ir](mailto:hamed.arshadi@semnan.ac.ir)

**Keywords:** high-strength steel (HSS), reinforced-concrete (RC) structures, shear wall, finite element analysis (FEA), nonlinear behavior

**Abstract.** In this research, the effects of applying high-strength steel (HSS) bars as horizontal and vertical bars of the web, and as the flexural and shear bars of the boundary elements on the behavior (load-displacement and maximum moment) of shear walls, were analytically investigated in 45 specimens by finite element analysis (FEA). In addition, the influence of concrete strength along with using HSS bars in the shear walls was studied. The results showed that HSS application as flexural bars of boundary elements improved the performance of shear walls more than other cases of bar locations. However, their shear reinforcement application did not affect their performance significantly. Moreover, HSS usage as the horizontal and vertical bars of the web of the shear walls improved the performance of the specimens. Finally, using higher-strength steel was more effective on the shear performance of shear walls than their moment performance.

### 1. Introduction

Reinforced-concrete (RC) material is the most popular construction material, because of its financial benefits. The failure mode of RC members is complex with respect to the brittle failure mode of concrete and the ductile failure mode of steel. One of the important issues related to the RC structures is the lateral-resisting systems to endure lateral loads such as wind and earthquake loads. The lateral-resisting systems are generally classified into three categories: shear walls, moment frames, and dual systems [1]. Shear walls are rather the most efficient systems in earthquake-resistant structures. They have several benefits in comparison to the moment frames. They are used either with or without boundary elements. They provide high strength and stiffness, which leads to a decrease in the lateral displacements of the RC structures. Thus, they also limit the P- $\Delta$  effects which can be a significant benefit in the tall buildings. However, shear walls can cause uplift forces in the bottom of structures which is a disadvantage. They can be used along with steel or RC moment frames. In this case, they have an interaction with the moment frames and cause negative shear forces at the top of the structures. For this reason, the thickness of the shear walls should gradually be decreased in the higher stories of the structures. Dual systems have two defensive fronts, unlike only the moment frames or shear walls. This issue is a great advantage.

These days, steel bars with an  $f_y$  of greater than 500 MPa are considered as HSS bars. The motivation of using HSS bars is their various economic and executive benefits such as decreasing steel consumption, expenses related to their shipment and placement, improving the concrete quality by decreasing the setback of steel congestion in the RC members, and reducing construction time [2].

Arshadi, H., Kheyroddin, A., Asadollahi Nezhad, A. High-strength steel effects on the behavior of special shear walls. Magazine of Civil Engineering. 2022. 111(3). Article No. 11102. DOI: 10.34910/MCE.111.2

© Arshadi, H., Kheyroddin, A., Asadollahi Nezhad, A., 2022. Published by Peter the Great St. Petersburg Polytechnic University.



This article is licensed under a CC BY-NC 4.0

However, there are serious obstacles against using HSS bars, such as crack widening under service loads due to increasing stress level of steel bars, brittle failure (where concrete crushing happens before steel yielding), decreasing the stiffness of RC members, and decreasing ductility of RC structures [3]. Thus, HSS use is limited in the seismic areas by building codes, especially in the structural RC members such as shear walls. Some of these limitations are due to a lack of sufficient information and analytical data about HSS influences on the behavior of shear walls. In the 1971 edition of ACI 318, the yield strength of HSS bars was limited to 560 MPa [4]. Also, ACI 318-08 allowed steel bars with a yield strength not exceeding 560 MPa [5]. In Japan, bars with an  $f_y$  of 700 MPa are permitted to be applied in the structural elements [6].

The seismic performance of RC structures with HSS bars has been investigated by researchers, lately. Zhou *et al.* (2013) tested a series of RC beams with HSS to investigate the crack widths and displacement of them [7]. The most important technical source about HSS application in structures is a report collected by the NEHRP consultant joint venture [5]. This report reviewed all the published researches about HSS bars all over the world until the time of its production. Kolozvary and Wallace (2016) analytically studied nonlinear modeling of RC shear walls [8]. They utilized numerical models that combined coupled P-M-V behavior in a five-story RC wall-frame building. Kolozvari *et al.* (2018) researched new modeling approaches for simulating nonlinear flexural and coupled shear-flexural behavior of shear walls [9]. Arshadi *et al.* (2019) performed a series of experiments on the special moment frames and beam-column connections (BCCs) subjected to seismic loading [3, 10]. They studied several criteria such as energy absorption, ductility, cracking, etc. They demonstrated that applying HSS bars led to decreases in energy dissipation and ductility of these specimens. Arshadi *et al.* (2020) also experimentally studied several damage indices of RC frames and BCCs with HSS bars [11]. They reported that using HSS bars generally expedited the damage distribution and failure of the specimens.

As discussed in the paragraphs above, despite the various benefits of HSS bars, their application is restricted due to the mentioned challenges, especially in the special shear walls and moment frames [12]. This phenomenon can be due to a lack of experimental and analytical data about the seismic behavior of shear walls with HSS bars. Unfortunately, most of the studies have been focused on using HSS bars in beams or columns and not in the shear walls. Then, the NEHRP report strongly advised studying the HSS effects on the behavior of shear walls [5]. Thus, the effects of HSS bars with the yield strengths of 560 and 700 MPa as horizontal and vertical bars of the web, and also as the flexural and shear bars of the boundary elements on the behavior of shear walls were analytically investigated by finite element analysis (FEA) in this research. The effects of compressive strength of concrete (with the compressive strengths of 30, 45, and 60 MPa) along with the application of HSS bars were studied in the shear walls, too. The results showed that HSS application as flexural bars of boundary elements improved the performance of shear walls. However, their application as the shear bars of them did not affect their performance, conspicuously. Moreover, HSS application as the horizontal and vertical bars of the web of the specimens improved their performance. Also, using higher-strength concrete was less effective than using higher-strength steel on the maximum base shear and the ultimate moment of the specimens. The results showed that applying higher-strength steel was more effective on the shear performance of shear walls than their moment performance.

## 2. Methods

### 2.1. Concrete Damage Plasticity (CDP)

There are three different models to simulate the concrete behavior in the FEA software such as smeared crack concrete (SCC) model, brittle cracking (BC) model, and concrete damage plasticity (CDP) model [13]. Every model is suitable for special types of structures and loading situations. However, the most comprehensive model is the CDP model which is a continuous one with damage based on plasticity for concrete. According to the basic presumption of CDP, the major failure mechanisms of RC structures are described by tensile cracking in tension and compressive crushing [14]. In this section, the basic presumptions of CDP modeling are asserted. Equation 1 is used to reach strain decomposition rate, which is assumed for the rate-independent model [14]:

$$\dot{\varepsilon} = \dot{\varepsilon}^{el} + \dot{\varepsilon}^{pl}, \quad (1)$$

$\dot{\varepsilon}$  is the total strain rate,  $\dot{\varepsilon}^{el}$  is the elastic portion of strain, and  $\dot{\varepsilon}^{pl}$  is the plastic portion of it. With respect to scalar damaged elasticity, the stress-strain relationship is defined as Equation 2:

$$\sigma = (1-d)D_0^{el} : (\varepsilon - \varepsilon^{pl}) = D^{el} : (\varepsilon - \varepsilon^{pl}), \quad (2)$$



$D_0^{el}$  is undamaged elastic stiffness of material;  $D^{el} = (1-d)D_0^{el}$  is degraded elastic stiffness, and  $d$  is scalar stiffness depreciation variable (regarded as zero for undamaged material and as one for the completely damaged one). With regard to the scalar-damage notion, the stiffness depreciation is regarded as isotropic and characterized by  $d$  (a single depreciation parameter). Succedent the continuum-damage mechanics, the effective stress is calculated by Equation 3. Moreover, Equation 4 is utilized to compute the Cauchy stress (related to the effective stress by the scalar depreciation formulation):

$$\bar{\sigma}^{def} = D_0^{el} : (\varepsilon - \varepsilon^{pl}), \quad (3)$$

$$\sigma = (1-d)\bar{\sigma}, \quad (4)$$

$\bar{\varepsilon}_t^{pl}$  and  $\bar{\varepsilon}_c^{pl}$  are hardening variables and assigned to regard damage situations in tension and compression.  $\bar{\varepsilon}_t^{pl}$  is equivalent plastic tensile strain and  $\bar{\varepsilon}_c^{pl}$  is the equivalent plastic compressive strain. Cracking distribution initiates by an increase in the values of hardening parameters. Lubliner *et al.* suggested a model to define the yield surface function which was revised by Lee and Fenves (Fig. 1)[15]. The yield surface function can be computed by Equation 5:

$$F = \frac{1}{1-\alpha} \left( \bar{q} - 3\alpha\bar{p} + \beta \left( \tilde{\varepsilon}^{pl} \right) \left( \bar{\sigma}_{\max} - \gamma \left( \bar{\sigma}_{\max} \right) \right) \right) - \bar{\sigma}_c \left( \tilde{\varepsilon}_c^{pl} \right) \leq 0, \quad (5)$$

$\bar{q}$  is the equivalent Von-Mises stress,  $\bar{p}$  is effective hydrostatic pressure,  $\langle x \rangle = \frac{1}{2}(x + |x|)$  is the Macauley bracket function;  $\bar{\sigma}_{\max}$  is the algebraically maximum eigenvalue of tensor  $\bar{\sigma}_c$ ;  $\alpha$ ,  $\beta$  and  $\gamma$  are dimensionless constants of materials, calculated by Equations 6, 7, and 8:

$$\alpha = \frac{\left( \sigma_{b0} / \sigma_{c0} \right) - 1}{2 \left( \sigma_{b0} / \sigma_{c0} \right) - 1}; \quad 0 \leq \alpha \leq 0.5, \quad (6)$$

$\left( \sigma_{b0} / \sigma_{c0} \right)$  is the ratio of biaxial compressive stress to uniaxial compressive yield one which influences the yield surface in a plane-stress situation.  $\left( \sigma_{b0} / \sigma_{c0} \right)$  values for concrete are in the range from 1.10 to 1.16. Then, the  $\alpha$  values will be between 0.08 and 0.12.

$$\beta \left( \tilde{\varepsilon}^{pl} \right) = \frac{\bar{\sigma}_c \left( \tilde{\varepsilon}_c^{pl} \right)}{\bar{\sigma}_t \left( \tilde{\varepsilon}_t^{pl} \right)} (1-\alpha) - (1+\alpha), \quad (7)$$

$\bar{\sigma}_c \left( \tilde{\varepsilon}_c^{pl} \right)$  and  $\bar{\sigma}_t \left( \tilde{\varepsilon}_t^{pl} \right)$  are the effective cohesion stress in compression and tension, respectively.

$$\gamma = \frac{3(1-k_c)}{2k_c - 1}, \quad (8)$$

The  $\gamma$  coefficient is used only for the triaxial compressive stress state.  $k_c$  is the ratio of the hydrostatic effective stress in tensile meridian to that of the compressive meridian when the maximum principal stress is negative. As shown in Fig. 1, this parameter is the coefficient that ascertains the shape of the deviatoric cross-section. According to experimental results, the CDP damage proposes to regard the default value  $k_c = \frac{2}{3}$ .

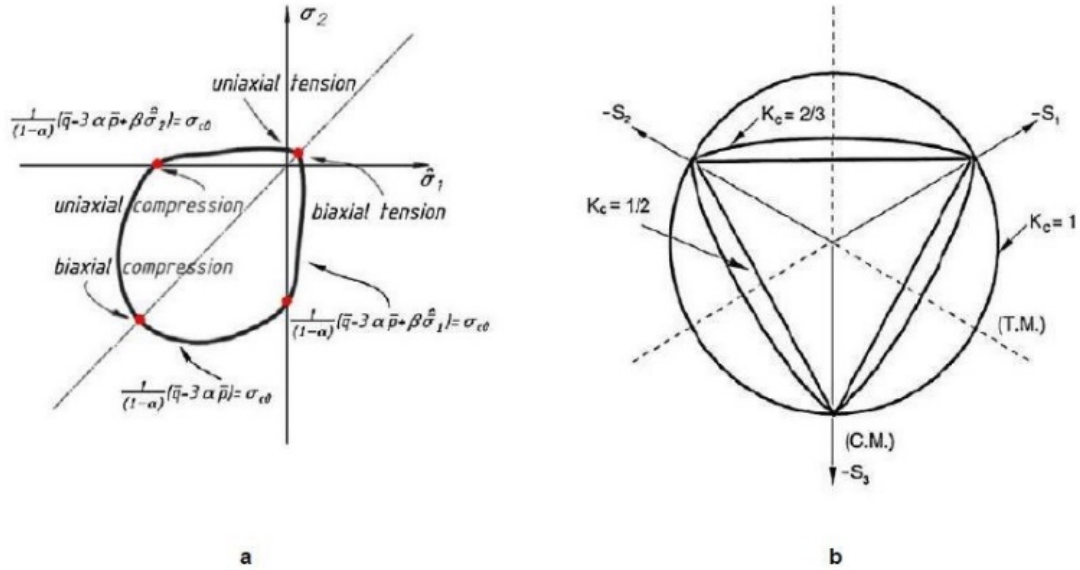


**Figure 1. Concrete damage plasticity (CDP) model:**  
**a) yield surface in plane stress, and b) yield surface in the deviatoric plane [15].**

The flow rule is utilized to make a relation between the yield surface stress and the stress-strain relationship. The CDP model utilizes Drucker-Prager hyperbolic function as a non-associated flow potential function using Equation 9 [15]:

$$G = \sqrt{(\zeta \sigma_{t0} \tan \psi)^2 + \bar{q}^2} - \bar{p} \tan \psi, \quad (9)$$

$\zeta$  is the potential flow eccentricity that sets the hyperbola shape in plastic potential flow function.  $\zeta$  is a low positive value that is described as the ratio of concrete tensile strength to its compressive strength,  $\sigma_{t0}$  is uniaxial tensile stress,  $\psi$  is dilatation angle. This parameter characterizes concrete performance when it is subjected to a triaxial compound stress state.

## 2.2. Finite Element Analysis

In this research, a 2-noded truss element (T3D2) with three freedom degrees in each node was used to model bars. 8-noded brick element (C3D8R) with reduced integration and three freedom degrees in each node was used to model concrete. The embedded method with a perfect bond between concrete and steel was assigned to simulate the concrete-reinforcement reaction.

### 2.2.1 Concrete

As shown in Fig. 2, the stress-strain behavior of concrete was simulated by the Equations 10.a, 10.b, and 10.c:

$$\sigma_{c,1} = E_c \varepsilon_c, \quad \varepsilon_c \leq \frac{0.4 f'_c}{E_c}; \quad (10a)$$

$$\sigma_{c,2} = \frac{\eta_c \frac{\varepsilon_c}{\varepsilon_0} - \left( \frac{\varepsilon_c}{\varepsilon_0} \right)^2}{1 + (\eta_c - 2) \frac{\varepsilon_c}{\varepsilon_0}} f'_c, \quad \frac{0.4 f'_c}{E_c} \leq \varepsilon_c \leq 0.0035; \quad (10b)$$

$$\sigma_{c,3} = \left( \frac{2 + \lambda_c f'_c \varepsilon_0}{2 f'_c} - \lambda_c \varepsilon_0 + \frac{\lambda_c \varepsilon_c^2}{2 \varepsilon_0} \right)^{-1}, \quad 0.0035 \leq \varepsilon_c \leq 0.03. \quad (10c)$$

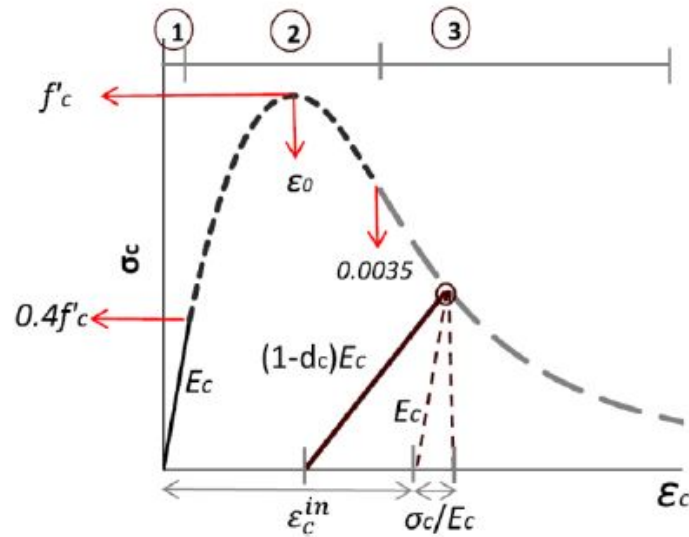


**Figure 2. Uniaxial compressive stress-strain diagram for concrete [16].**

Equation 10a demonstrates the linear-elastic branch, where  $\varepsilon_c$  is a variable changes from zero to  $0.4f'_c/E_c$ , and  $E_c$  is the initial modulus of elasticity. The linear branch ends at the stress level  $0.4f'_c$ . Equation 9b defines the second branch up to the strain level of 0.0035 in the descending branch. The corresponding strain level at the peak stress is defined as  $\varepsilon_0 = 2f'_c/E_c$ ;  $\eta_c$  is material constant. The stress and strain compatibility at the strain level of  $\varepsilon_c = 0.4f'_c/E_c$ , Equations (10a) and (10b) gives the value of  $\eta_c$ . Equation 10c indicates the third and descending branch;  $\lambda_c$  is crushing energy constant as a material property. Utilizing the stress and strain compatibility at the strain level of  $\varepsilon_c = 0.0035$ , for Equation 10b and 10c enables the value of  $k_c$  to be determined. The ultimate strain ( $\varepsilon_u$ ) of concrete was set to a large value of 0.035 to avoid any numerical setbacks. Table 1 indicates CDP parameters, used in the FEA software.

**Table 1. CDP parameters [17].**

| Parameter | $\left(\sigma_{b0}/\sigma_{c0}\right)$ | $k_c$ | $\psi$ | $\zeta$ | $\mu(s)$ |
|-----------|--|-------|--------|---------|----------|
| Value     | 1.16                                   | 0.667 | 40°    | 0.1     | 0.00001  |

In this research, the linear uniaxial stress-strain behavior was used for concrete material. Concrete has a linear elastic behavior before reaching the peak tensile strength (in the first branch of modeling). Cracking and its propagation in concrete under tension happen in the second branch. The linear, bilinear, or nonlinear model used to model the softening procedure of concrete, is illustrated in Fig. 3. As regards to the computer configuration used to analyze the specimens, a computer system with a Core i7 CPU (central processing unit) with a capacity of 2.81 GHz (Gigahertz), an installed memory (RAM) 12 GB (Gigabyte), a hard disk drive with a capacity of 1000 GB, and a solid-state drive with a capacity of 128 GB was used.

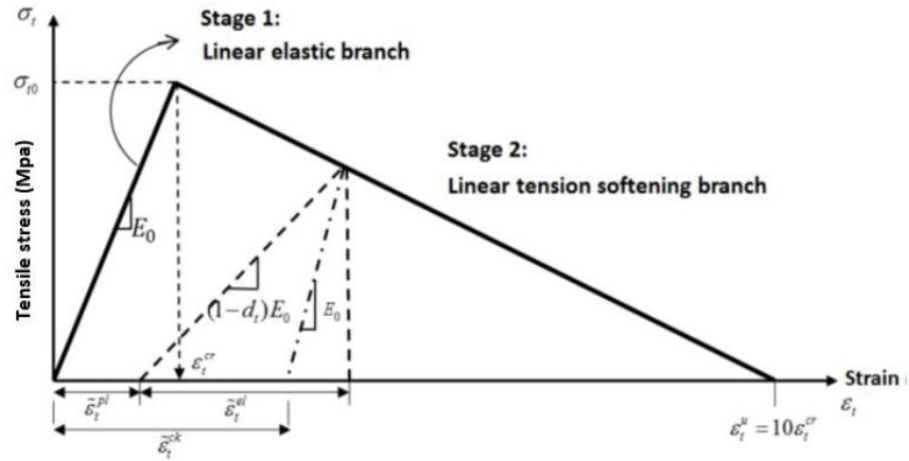


**Figure 3. Uniaxial tensile stress-strain behavior of concrete with softening branch [18].**

Equation 11 is used to evaluate the tensile strength of concrete:

$$f'_t = 0.33\sqrt{f'_c}. \quad (11)$$

### 2.2.2 Steel Reinforcement Modelling

The uniaxial tensile stress-strain behavior of bars was considered to be elastic with regard to conventional Young's modulus and Poisson's ratio. Also, the plastic behavior of steel was modeled. Bilinear behavior was used to define the properties of the plastic phase. Fig. 4 illustrates the typical stress-strain behavior of steel.

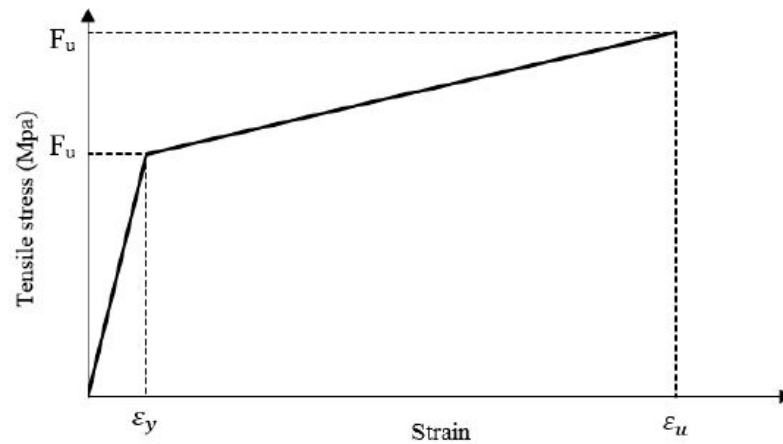


**Figure 4. Uniaxial stress-strain behavior of steel [15].**

### 2.2.3. Model Verification

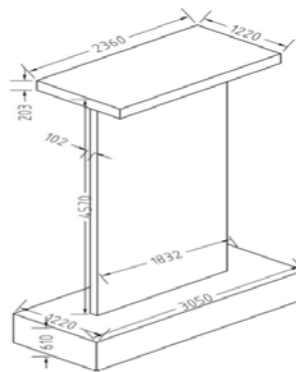
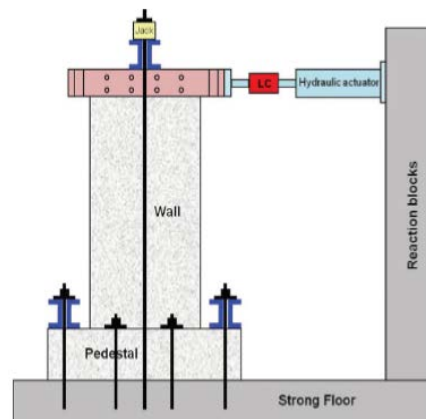
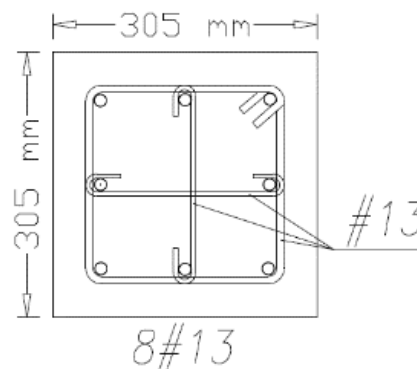
The reliability of the analytical modeling to perform non-linear analysis on the numerical shear walls was investigated by verification of one shear wall based on the experimental studies of Oesterle *et al.* in 1979 [19]. The specifications of this specimen are shown in Tables 1 and 2. Fig. 5 and 6 also show the geometry of this specimen and the experimental setup. The geometry and steel bar layout of its boundary elements are demonstrated in Fig. 7. This specimen was analyzed under a unidirectional incremental lateral force. Applying the lateral load continued until failure of vertical moment bars of the boundary elements was observed. Moreover, this is the reference specimen and other specimens were designed based on it. In order to model a shear wall in the FEA software (ABAQUS), it had to be divided into seven different parts such as the shear wall, foundation, slab, longitudinal bar of the boundary elements, transverse bars of the boundary elements, vertical and the horizontal bars of the web. These parts were modeled separately and then assembled. The freedom degrees of both the top and bottom ends of the wall were fixed as shown in Fig. 8.

**Table 2. Specifications of the material used in the reference specimen [19].**

| Model name         | Shape                  | % (Reinforcement) |          |          |          | $f_y$ (MPa) | $f'_c$ (MPa) | Axial load (kN) |
|--------------------|------------------------|-------------------|----------|----------|----------|-------------|--------------|-----------------|
|                    |                        | $\rho_s$          | $\rho_n$ | $\rho_h$ | $\rho_f$ |             |              |                 |
| Reference specimen | With boundary elements | 1.28              | 0.29     | 0.31     | 1.11     | 450         | 45           | 0               |

**Table 3. Steel bars layout in the reference specimen [19].**

| Bar location                           | Bar layout  | Considerations |
|--|-------------|----------------|
| Flexural bars of the boundary elements | 8 #13       | ---            |
| Horizontal bars of the web             | #8 @330 mm  | In two meshes  |
| Vertical bars of the web               | #8 @350 mm  | In two meshes  |
| Confinement bars                       | 3#13 @60 mm | ---            |

**Figure 5. The geometry of the shear wall [19].****Figure 6. Experimental setup [19].****Figure 7. Specifications of the boundary elements.**

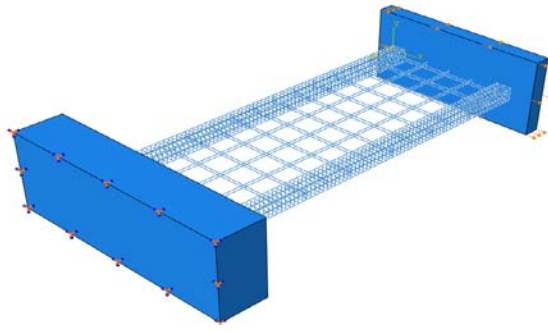


**Figure 8. Modeling of steel bars and boundary condition.**

Table 4 indicates the mechanical and analytical parameters used in the FEA software to model the reference specimen. The compressive strength of concrete in the reference specimen was 45 MPa, which its stress-strain diagram in tension and compression is shown in Fig. 9. In some of the specimens, concrete with compressive strengths of 30 or 60 MPa was used, which Fig. 10 and 11 show their stress-strain behavior.

**Table 4. Mechanical and analytical parameters to model the 45 MPa concrete.**

| Name               | $f'_c$<br>(MPa) | $n$  | $E_c$<br>(MPa) | $\varepsilon_0$ | $\varepsilon_{cu}$ | $K$ for<br>$\frac{\varepsilon_c}{\varepsilon_{c0}} > 1$ | $f'_t$<br>(MPa) | $\varepsilon_{cr}$ |
|--------------------|-----------------|------|----------------|-----------------|--------------------|---|-----------------|--------------------|
| Reference specimen | 45              | 3.45 | 29,040         | 0.0022          | 0.008              | 1.396   | 3.7             | 1.28E-4            |

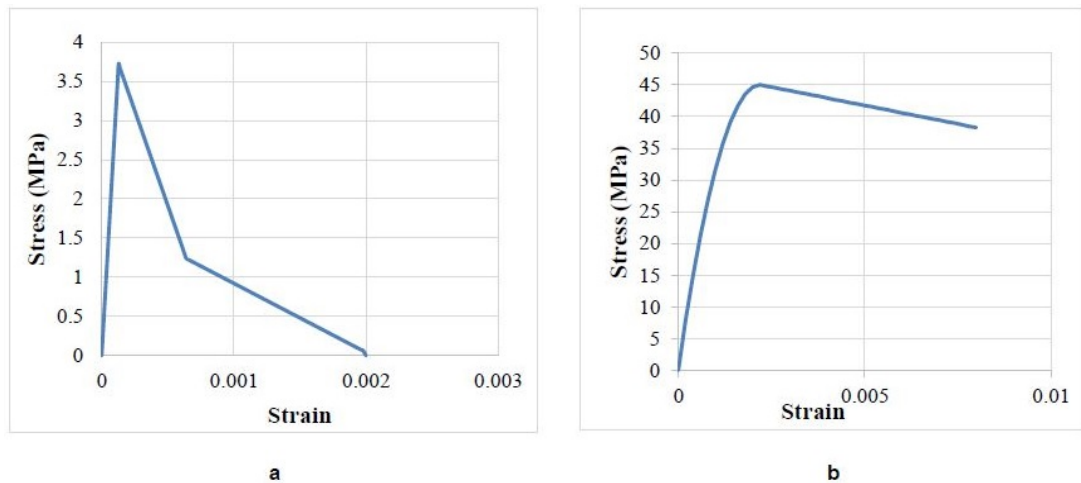


**Figure 9. Stress-strain diagram of 45 MPa concrete: a) tension and b) compression.**

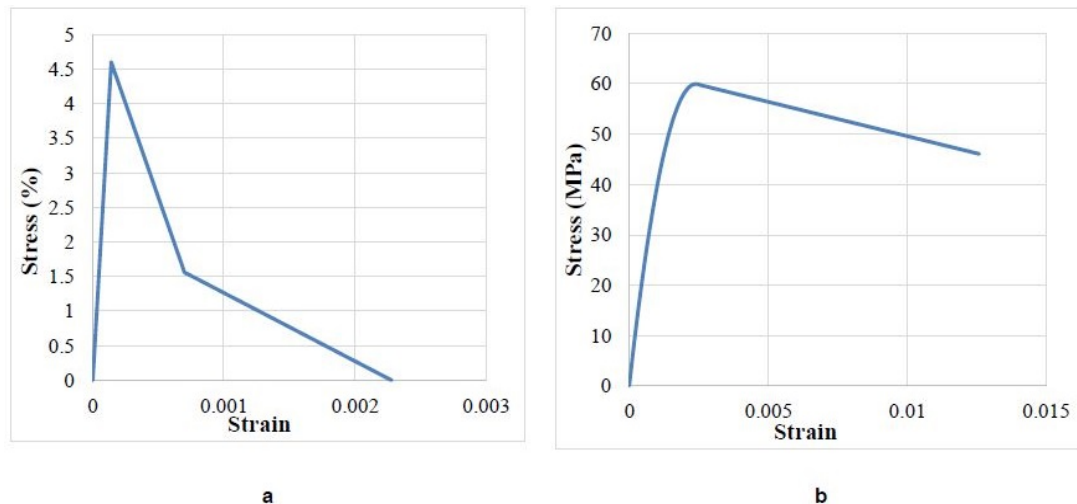


**Figure 10. Stress-strain diagram of 30 MPa concrete: a) tension and b) compression.**

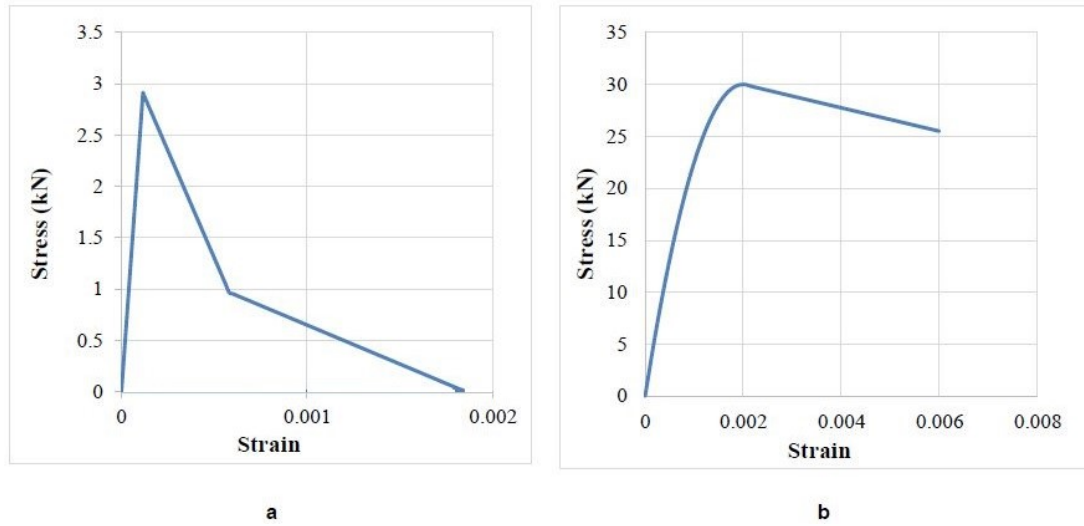


**Figure 11. Stress-strain diagram of 60 MPa concrete: a) tension and b) compression.**

### 2.3. Mesh Configuration

Shear walls have plain stress behavior because of their small thickness in comparison to the other dimensions. There are three types of meshes such as fine, intermediate, and coarse ones. The more sensitive the structural parts, the finer the meshes. However, the results of the FEA software usually depend on the mesh sizes. This issue is a serious setback and its reason is modeling the cracks especially in the (SCC) modeling where the cracks propagate in the elements. There is effective mesh size in the non-linear FEA. This means that by using finer meshes, the more accurate results necessarily are not reached. This phenomenon is known as “mesh dependency”. Kheyroddin and Shayanfar (1997) proposed the below formulation for the effective mesh size in concrete (Equation 12) [20]:

$$\varepsilon_{tu} = 0.004e^{-0.008h}, \quad (12)$$

$h = \sqrt{A}$  and  $A$  is the area of the meshes, then  $h$  is their dimension. Then, with regard to the fact that  $\varepsilon_{tu} = 0.002$ , the size of meshes in this study got 87 mm. Fig. 12 indicates the mesh configuration of specimens.

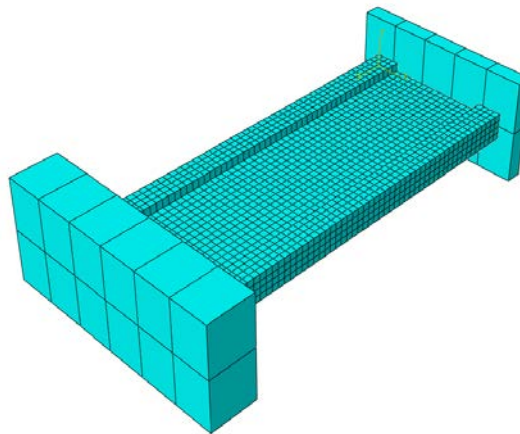


**Figure 12. The meshing of the specimens.**

### 2.4. Detail of Specimens

In this study, 45 shear walls were analyzed. With regard to the reference specimen, the first series of specimens were modeled by using concrete with the compressive strength of 45 MPa and steel bars with the yield strengths of 560 and 700 MPa as the vertical and horizontal bars of the web of specimens, and also as the flexural and shear bars of the boundary elements. Then, the other series of specimens were modeled by using concrete with the compressive strengths of 30 and 60 MPa along with the HSS bars.

The tantamount amounts of steel bars in the specimens were calculated by Equations 13 and 14 (based on the specifications of the bars in the reference specimen):



For the longitudinal bars:

$$N_1 A_{s1} f_{y1} = N_2 A_{s2} f_{y2}. \quad (13)$$

For the stirrups:

$$N_1 A_{sv1} f_{y1} (d_1/S_1) = N_2 A_{sv2} f_{y2} (d_2/S_2), \quad (14)$$

$N$  is the number of bars,  $f_y$  is the yield strength of bars,  $A_s$  and  $A_{sv}$  are areas of longitudinal and transverse bars,  $d$  is effective depth of sections and  $S$  is the distance of stirrups. It must be noted that it is sufficient to put the number, yield strength, areas of bars of the base specimen in one side of the above equations, and the yield strength and areas of bars on the other side of the equation to find the equivalent number of the bars in the case of using the other types of bars. Indices 1 and 2 refer to the basic specimen and the specimen that was intended to find its equivalent number of the bars.

Table 6 shows the characteristics of the specimens. The specimens are named with respect to a rule, where the letter (C) stands for the concrete and the following number for its compressive strength in MPa. The letter (R) stands for reinforcement and the following number for one-tenth of yield strength of it in MPa. The final words stand for the location of HSS bars, for example, the word (all) stands for the case that HSS bars are used in all the bars, the word (bel) for the case of HSS bars as the flexural bars of the boundary elements, the word (s) for the case of using HSS bars as stirrups, the word (bels) for the flexural and shear bars of the boundary elements, the word (hw) for the case of using HSS bars as the horizontal bars of the web of the specimens, the word (vw) for the case of using HSS bars as the vertical bars of the web, and the word (hvw) for both the vertical and horizontal bars of the web.

**Table 5. Specifications of the specimens.**

| Specimen   | $f_y$ (MPa) | $f'_c$ (MPa) |
|------------|-------------|--------------|
| C45R56all  | 560         | 45           |
| C45R56bel  | 560         | 45           |
| C45R56bels | 560         | 45           |
| C45R56s    | 560         | 45           |
| C45R56hw   | 560         | 45           |
| C45R56vw   | 560         | 45           |
| C45R56hvw  | 560         | 45           |
| C45R70all  | 700         | 45           |
| C45R70bel  | 700         | 45           |
| C45R70bels | 700         | 45           |
| C45R70s    | 700         | 45           |
| C45R70hw   | 700         | 45           |
| C45R70vw   | 700         | 45           |
| C45R70hvw  | 700         | 45           |
| C30R56all  | 560         | 30           |
| C30R56bel  | 560         | 30           |
| C30R56bels | 560         | 30           |
| C30R56s    | 560         | 30           |
| C30R56hw   | 560         | 30           |
| C30R56vw   | 560         | 30           |
| C30R56hvw  | 560         | 30           |
| C30R70all  | 700         | 30           |
| C30R70bel  | 700         | 30           |
| C30R70bels | 700         | 30           |
| C30R70s    | 700         | 30           |
| C30R70hw   | 700         | 30           |
| C30R70vw   | 700         | 30           |
| C30R70hvw  | 700         | 30           |
| C60R56all  | 560         | 60           |
| C60R56bel  | 560         | 60           |

| Specimen   | $f_y$ (MPa) | $f'_c$ (MPa) |
|------------|-------------|--------------|
| C60R56bels | 560         | 60           |
| C60R56s    | 560         | 60           |
| C60R56hw   | 560         | 60           |
| C60R56vw   | 560         | 60           |
| C60R56hvw  | 560         | 60           |
| C60R70all  | 700         | 60           |
| C60R70bel  | 700         | 60           |
| C60R70bels | 700         | 60           |
| C60R70s    | 700         | 60           |
| C60R70hw   | 700         | 60           |
| C60R70vw   | 700         | 60           |
| C60R70hvw  | 700         | 60           |
| C45R42     | 420         | 45           |
| C60R42     | 420         | 60           |
| C30R42     | 420         | 30           |

### 3. Results and Discussion

#### 3.1. Load-Displacement Diagrams

One of the important results of the FEA is the diagram of load (shear force) – displacement. There are paramount parameters that can be deducted from this diagram such as the loading capacity, ductility, and energy absorption. Fig. 13 indicates the comparison of the load-displacement diagram of the specimens which have the concrete with compressive strength of 45 MPa and HSS bars with a yield strength of 700 MPa. The results showed that using 700 MPa bars as the different bar types of specimens led to an increase in their loading capacity. The WC45R70all specimen which had 700 MPa steel as all of its bars, had the greatest loading capacity in comparison to the other specimens. This loading-capacity increase was nearly 57 % in comparison to the reference specimen.

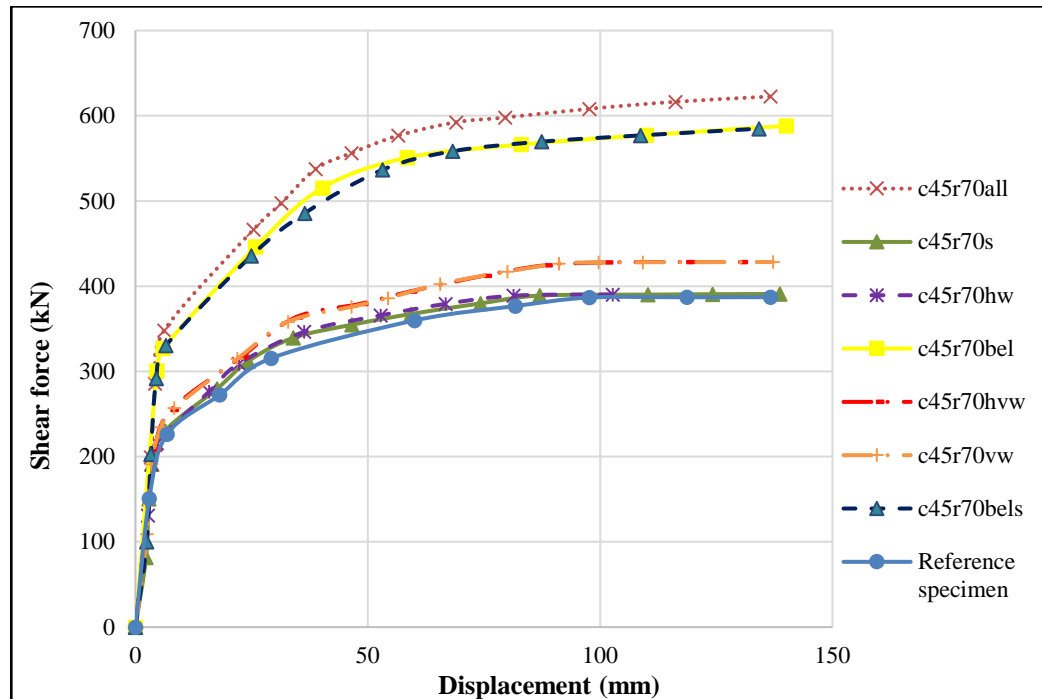


Figure 13. Load-displacement diagram of the specimens with 700 MPa HSS bars.

Fig. 14 demonstrates the effect of using different types of concrete along with HSS bars on the load-displacement diagram. The results showed that using different types of concrete did not have a considerable effect on the behavior of specimens. These results were in accordance with the experimental observations of Arshadi et al. in their experiments on the HSS effects on the load-displacement diagrams of RC members [2, 11].

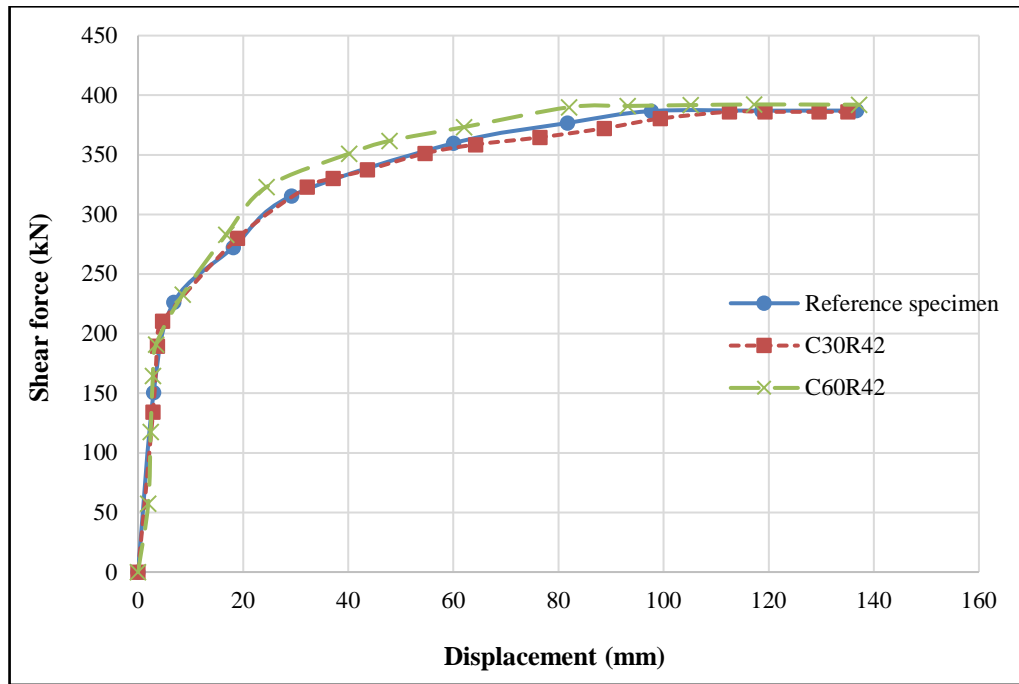
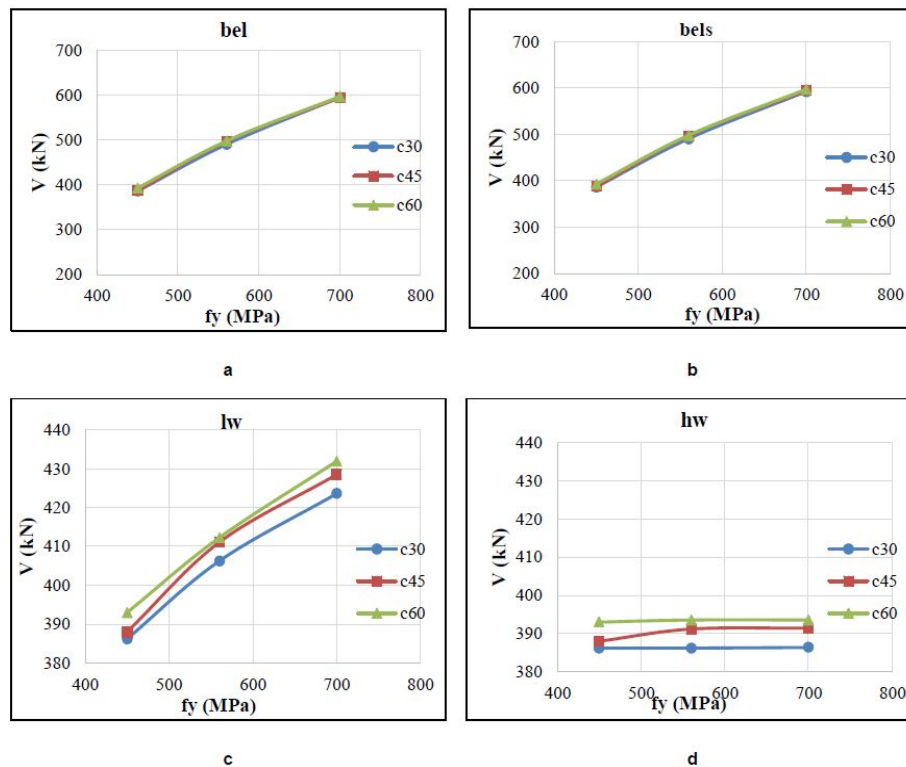
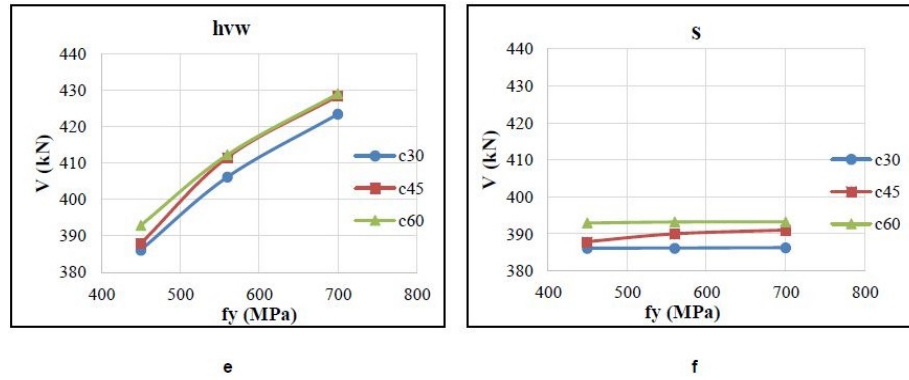


Figure. 14. Load-displacement diagram of the specimens with different concrete types.

### 3.2. Base Shear

Fig. 15 indicates the effect of using HSS bars and different types of concrete along with each other. Generally, it was observed that using higher-strength concrete along with HSS bars led to increasing the maximum base shear of the specimens. However, the differences between the maximum base shear of specimens with different concrete types were not considerable. These differences were rather negligible in the cases of using HSS bars as the flexural and shear bars of the boundary elements (bels) and as the flexural bars of the boundary elements (bel). On the other hand, the effects of applying HSS bars in different cases were considerable. It was also observed that the higher the steel strength, the greater the maximum base shear. It must be mentioned that in the cases of using HSS bars as the horizontal bars of the web of the specimens (hw) and as the stirrups, the diagrams approximately became horizontal. This means that the effects of using higher-strength bars in these cases were not considerable. These results and patterns were similar to those of Kolozvary and Wallace (2016) and Arshadi *et al.* (2019) [8, 10].





**Figure 15. Effects of HSS bars and different concrete types on the maximum base shear in different cases of: a) bel, b) bels, c) lw, d) hw, e) hvw, and f) s.**

Fig. 16 and 17 indicate the comparison of maximum base shears in different cases of using HSS bars in the specimens. In order to prevent more complications and make the figures simpler, numbers from 1 to 6 are assigned to the different cases of using HSS bars, as shown in Table 6. The results showed that the C60R70all and C45R70all had the greatest maximum base shears among the specimens. Moreover, the C30R56s, C30R56hw, C30R56s, and C30R56hw had the least maximum base shears among the specimens. The results also showed that using lower-strength bars (such as bars with the  $f_y$  of 300 and 560 MPa) had fewer effects on the maximum base shear than using 700 MPa steel.

**Table 6. Numbering different cases of the reinforcement layout.**

| Notation | Number |
|----------|--------|
| s        | 1      |
| hw       | 2      |
| vw       | 3      |
| hvw      | 4      |
| bel      | 5      |
| bels     | 6      |
| all      | 7      |

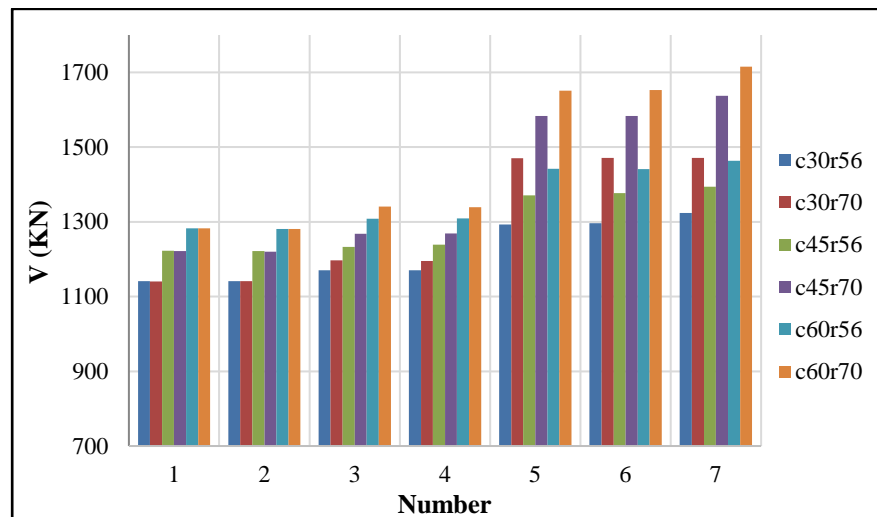


**Figure 16. Comparison of the maximum base shears.**

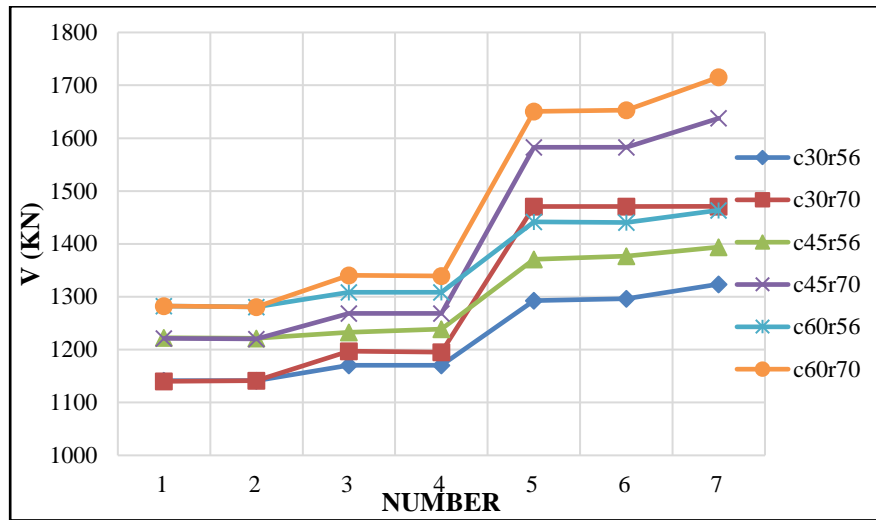
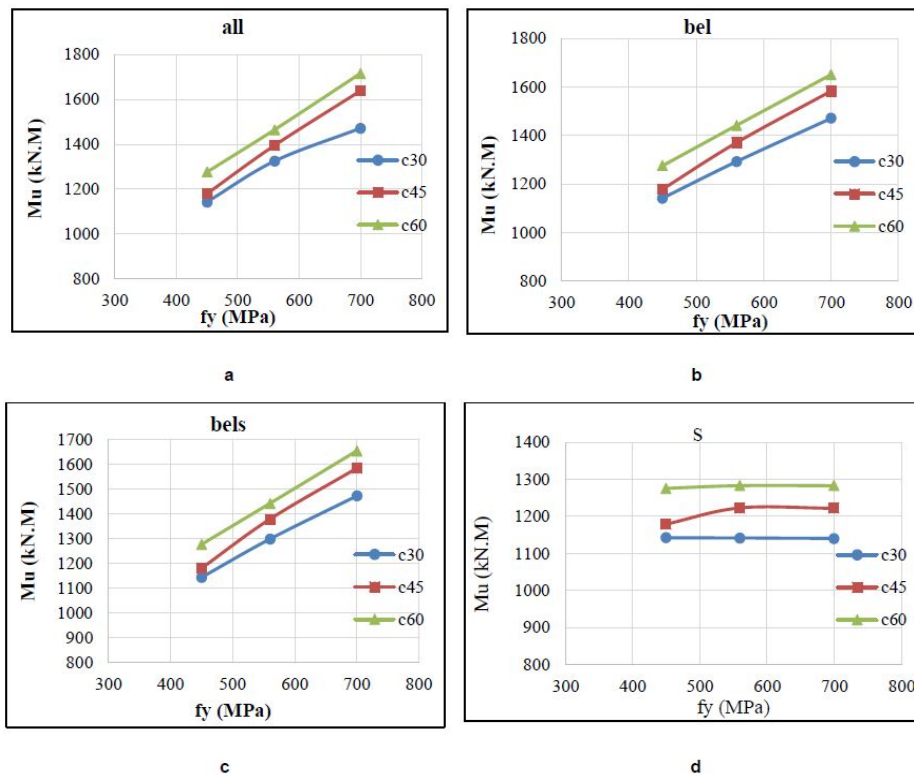


**Figure 17. Comparative diagrams of the maximum base shears.**

The results generally demonstrated that HSS usage as flexural bars of boundary elements improved the performance of specimens in terms of the maximum base shear more than the other cases of the bar locations. However, their application as shear reinforcement of the boundary elements did not affect their performance, significantly. Besides, HSS application as the horizontal and vertical bars improved the performance of specimens. It must be mentioned that using HSC and HSS bars also improved the behavior of specimens and C60R70 had the best behavior among the specimens.

### 3.3. Ultimate Moment

Fig. 18 indicates the effect of using HSS bars and different types of concrete along with each other in different locations of HSS bars on the ultimate moment of the specimens. The results demonstrated that applying higher-strength concrete along with HSS bars ended up increasing the ultimate moment of the specimens. Unlike the maximum base shear force, the differences between the ultimate moments of the specimens with different concrete types were not negligible. Besides, the influences of using HSS bars in discrepant cases were conspicuous. Like the maximum base shear, the higher the strength of the steel, the greater the ultimate moment. The diagrams got approximately horizontal by applying HSS bars as the horizontal and vertical bars of the web of the specimens (hvw), as the horizontal bars of the web of the specimens (hw), as the vertical bars of the web of the specimens, and as the stirrups. This means that the effects of using higher-steel bars in these cases were not considerable.



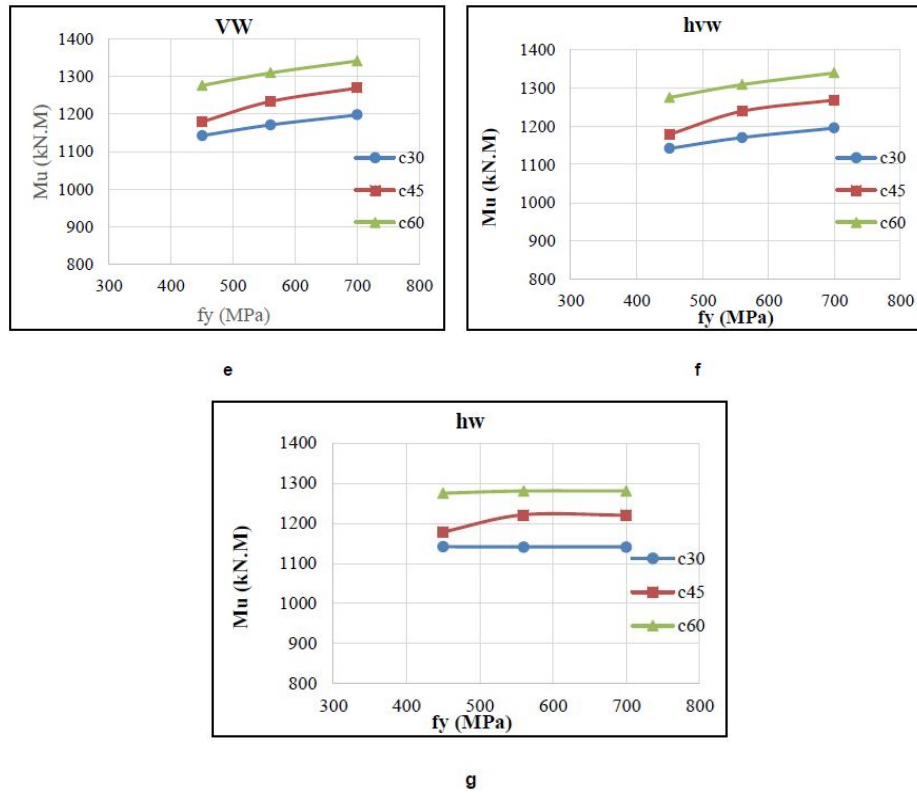


**Figure 18. Effects of HSS bars and concrete types on the ultimate moments in different cases of: a) all, b) bel, c) bels, d) s, e) vw, f) hvw, and g) hw.**

Fig. 19 and 20 demonstrate the analogy between the ultimate moment values in different cases of applying HSS bars in the specimens. As for the ultimate moment a rather similar process was observed, too. The results indicated that the C60R70all and C45R70all specimens had the greatest ultimate moment among the specimens. The C30R56s, C30R56hw, C30R56s, and C30R56hw specimens had the least ultimate moment among the specimens. Besides, using lower-grade steel bars (such as steel bars with the  $f_y$  of 300 and 560 MPa) had fewer influences on the ultimate moment than using 700 MPa steel. At last, the results demonstrated that using higher-strength steel was more effective on the shear base values of the specimens than their ultimate moment values. These results were in accordance with those of previous studies such as the studies of Kolozvary *et al.* (2018) and Tanyeri *et al.* (2014) [9, 19].

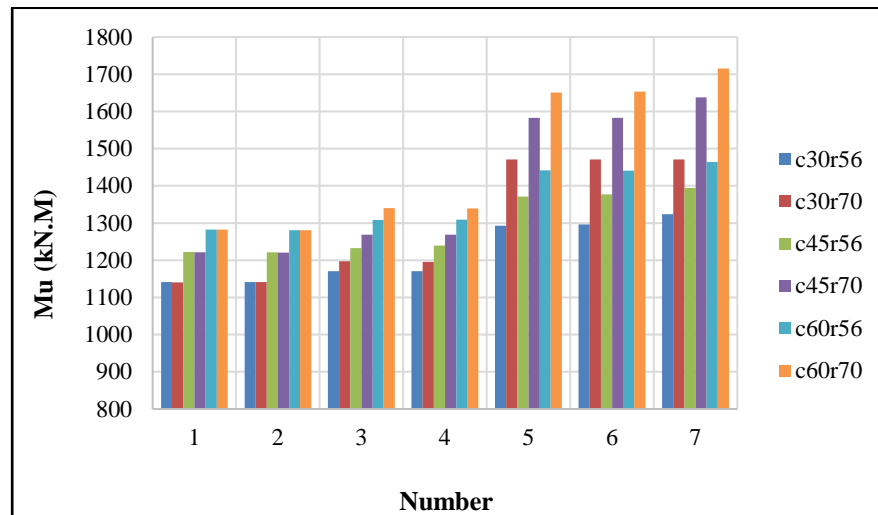


**Figure 19. Comparison of the ultimate moments of the specimens.**

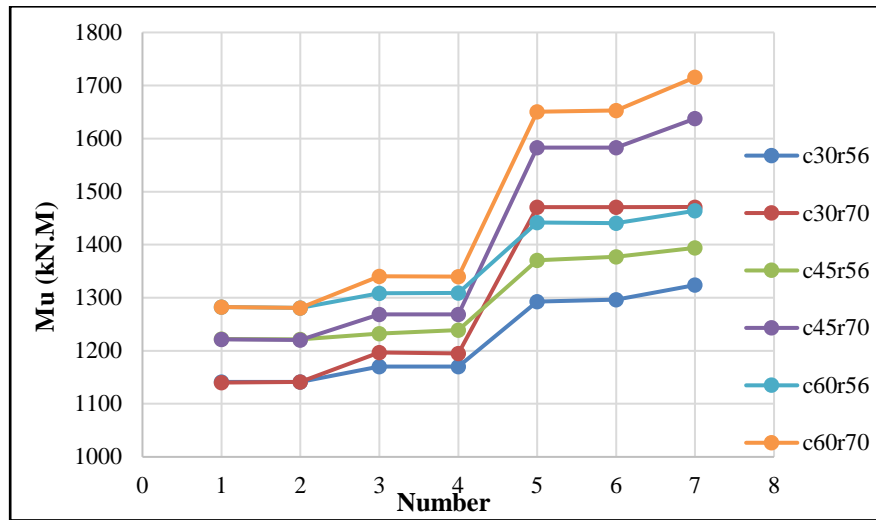


**Figure 20. Comparative diagrams of the ultimate moments of the specimens.**

As for the ultimate moment, a similar method to the maximum base shear is observed, too. The results generally indicated that HSS usage as flexural bars of boundary elements improved the performance of shear walls (in terms of the ultimate moment) more than the other cases of bar locations. However, their application as the shear bars of the boundary elements did not affect their performance, considerably. Besides, HSS application as the horizontal and vertical bars improved the performance of specimens. Also, using higher-strength concrete was less effective than using higher-strength steel on the maximum base shear and the ultimate moment of the specimens. Finally, the application of both HSC and HSS bars together improved the behavior of specimens. The C60R70 had the best behavior among the specimens.

Table 7 indicates the maximum base shear and ultimate moment variation percentages of the specimens in comparison to those of the reference specimen. As for the maximum base shear, the C30R70all specimen had the greatest maximum base shear variation percentage (69 %) and the C30R42 had the least percentage (−0.5 %) among the specimens. Moreover, as for the ultimate moment, the C60R70all had the greatest ultimate moment variation percentage (45 %) and the C30R42 had the least percentage (−3.1 %).

**Table 7. Variation percentages of the maximum base shear and the ultimate moment of the specimens.**

| Specimen   | $\Delta M_U$ (%) | $\Delta V$ (%) |
|------------|------------------|----------------|
| C45R56all  | 18               | 33             |
| C45R56bel  | 16               | 28             |
| C45R56bels | 17               | 28             |
| C45R56s    | 4                | 1.4            |
| C45R56hw   | 4                | 1.4            |
| C45R56vw   | 6                | 5.9            |
| C45R56hvw  | 6                | 6              |
| C45R70all  | 39               | 63             |
| C45R70bel  | 34               | 53             |
| C45R70bels | 34               | 53             |
| C45R70s    | 4                | 1.4            |
| C45R70hw   | 4                | 1.4            |
| C45R70vw   | 8                | 6.4            |
| C45R70hvw  | 9                | 10.4           |
| C30R56all  | 13               | 32             |
| C30R56bel  | 9.7              | 26             |
| C30R56bels | 10               | 26             |
| C30R56s    | −3               | −0.46          |
| C30R56hw   | −3               | −0.46          |
| C30R56vw   | −1               | 4.7            |
| C30R56hvw  | −1               | 4.7            |



| Specimen   | $\Delta M_U$ (%) | $\Delta V$ (%) |
|------------|------------------|----------------|
| C30R70all  | 26               | 69             |
| C30R70bel  | 25               | 53             |
| C30R70bels | 26               | 53             |
| C30R70s    | -3               | -0.4           |
| C30R70hw   | -3               | -0.4           |
| C30R70vw   | -1               | 6.4            |
| C30R70hvw  | -1               | 6.4            |
| C60R56all  | 24               | 46             |
| C60R56bel  | 22               | 28             |
| C60R56bels | 23               | 28             |
| C60R56s    | 9                | 1              |
| C60R56hw   | 9                | 1.4            |
| C60R56vw   | 11               | 6.2            |
| C60R56hvw  | 11               | 6.3            |
| C60R70all  | 45               | 63             |
| C60R70bel  | 40               | 53             |
| C60R70bels | 41               | 54             |
| C60R70s    | 9                | 1.43           |
| C60R70hw   | 9                | 1.4            |
| C60R70vw   | 14               | 6.4            |
| C60R70hvw  | 14               | 6.5            |
| C45R42     | 0                | 0              |
| C60R42     | 8                | 1.3            |
| C30R42     | -3.1             | -0.5           |

#### 4. Conclusion

Scientific developments facilitated producing HSS bars with suitable engineering characteristics such as appropriate ductility along with high strength. Despite several economical and executive profits of HSS bars, their application is limited in special shear walls and moment frames, because of possible repercussions related to their possible effects on decrease in ductility, energy absorption, and so forth. A lack of experimental and analytical data about the seismic behavior of shear walls with HSS bars can be the source of this problem. In this research, the influences of using HSS bars with the yield strengths of 560 and 700 MPa as horizontal and vertical bars of the web, and as the flexural and shear bars of the boundary elements on the behavior of shear walls, were analytically investigated by FEA. The effects of concrete strength (with the compressive strengths of 30, 45, and 60 MPa) in the case of using HSS bars in the shear walls were investigated, too. The results indicated that HSS application as flexural bars of boundary elements improved the performance of the specimens significantly. However, their application as the shear bars of the boundary elements did not considerably affect their performance. Moreover, HSS application as the horizontal and vertical bars of the web of specimens improved their performance. It was also observed that using higher-strength concrete was less effective than using higher-strength steel on the maximum base shear and the ultimate moment of the specimens. Finally, the results showed that using higher-strength steel was more effective in the shear performance of specimens than their ultimate moment.

#### References

1. Arshadi, H., Kheyroddin, A. Shear lag phenomenon in the tubular systems with outriggers and belt trusses. *Magazine of Civil Engineering*. 2019. 86(2). Pp. 105–118. DOI: 10.18720/MCE.86.10
2. Siddika, A., Mamun, M.A., Al, Alyousef, R., Amran, Y.H.M. Strengthening of reinforced concrete beams by using fiber-reinforced polymer composites: A review. 25. Elsevier Ltd, 2019.
3. Arshadi, H., Kheyroddin, A., Naderpour, H. An investigation into the behavior of special moment frames with high-strength reinforcement subjected to cyclic loading. *Journal of Building Engineering*. 2019. DOI: 10.1016/j.jobe.2019.100905
4. Kelly, D.J., Lepage, A., Mar, D., Restrepo, J.I., Sanders, J.C., Taylor, A.W. Use of high-strength reinforcement for earthquake-resistant concrete structures. NCEE 2014 – 10<sup>th</sup> U.S. National Conference on Earthquake Engineering: Frontiers of Earthquake Engineering. 2014. DOI: 10.4231/D3Z31NP6Z
5. Aoyama, H. Design of modern highrise reinforced concrete structures 2001.
6. Zhou, J., Chen, S., Chen, Y. Calculation methods of the crack width and deformation for concrete beams with high-strength steel bars. *Frontiers of Structural and Civil Engineering*. 2013. DOI: 10.1007/s11709-013-0211-0
7. Kolozvari, K., Wallace, J.W. Practical Nonlinear Modeling of Reinforced Concrete Structural Walls. *Journal of Structural Engineering (United States)*. 2016. DOI: 10.1061/(ASCE)ST.1943-541X.0001492

8. Kheyroddin, A., Arshadi, H., Binaipur, F. An Overview of the Effects of High-Strength Reinforcement (HSR) on the Intermediate Moment-Resisting Frames. 2017. 1(2). Pp. 177–187. DOI: 10.22060/ceej.2017.12406.5207
9. Kolozvari, K., Orakcal, K., Wallace, J.W. New openses models for simulating nonlinear flexural and coupled shear-flexural behavior of RC walls and columns. Computers and Structures. 2018. DOI: 10.1016/j.compstruc.2017.10.010
10. Arshadi, H., Kheyroddin, A., Naderpour, H. High-strength reinforcement effects on the seismic behaviour of beam–column joints. Proceedings of the Institution of Civil Engineers – Structures and Buildings. 2019. DOI: 10.1680/jstbu.18.00225.
11. Alaei, P., Li, B. High-strength concrete exterior beam-column joints with high-yield strength steel reinforcements. Engineering Structures. 2017. 145. Pp. 305–321. DOI: 10.1016/j.engstruct.2017.05.024
12. Sadraie, H., Khaloo, A., Soltani, H. Dynamic performance of concrete slabs reinforced with steel and GFRP bars under impact loading. Engineering Structures. 2019. 191(December 2018). Pp. 62–81. DOI: 10.1016/j.engstruct.2019.04.038.
13. Feng, D.C., Ren, X.D., Li, J. Cyclic behavior modeling of reinforced concrete shear walls based on softened damage-plasticity model. Engineering Structures. 2018. 166(November). Pp. 363–375. DOI: 10.1016/j.engstruct.2018.03.085
14. Hafezolzghorani, M., Hejazi, F., Vaghei, R., Jaafar, M.S. Bin, Karimzade, K. Simplified damage plasticity model for concrete. Structural Engineering International: Journal of the International Association for Bridge and Structural Engineering (IABSE). 2017. 27(1). Pp. 68–78. DOI: 10.2749/101686616X1081
15. Liao, F.Y., Han, L.H., Tao, Z. Performance of reinforced concrete shear walls with steel reinforced concrete boundary columns. Engineering Structures. 2012. DOI: 10.1016/j.engstruct.2012.05.037
16. Khani, J., Bozorg, M., Zahrai, S.M. Investigating Seismic Behavior of Reinforced Concrete Columns with SFRP Using Finite Element Method. American Journal of Engineering and Applied Sciences. 2018. 11(2). Pp. 996–1004. DOI: 10.3844/ajeassp.2018.996.1004
17. Mo, Y.L., Zhong, J., Hsu, T.T.C. Seismic simulation of RC wall-type structures. Engineering Structures. 2008. DOI: 10.1016/j.engstruct.2008.04.033
18. Tanyeri, A.C., Moehle, J.P., Nagae, T. Seismic performance and modeling of post-tensioned, precast concrete shear walls. NCEE 2014 – 10<sup>th</sup> U.S. National Conference on Earthquake Engineering: Frontiers of Earthquake Engineering. 2014. DOI: 10.4231/D34M91B3B
19. Colotti, V. Shear behavior of RC structural walls. Journal of Structural Engineering (United States). 1993. DOI: 10.1061/(ASCE)0733-9445(1993)119:3(728)
20. Colotti, V. Shear behavior of RC structural walls. Journal of Structural Engineering (United States). 1993. DOI: 10.1061/(ASCE)0733-9445(1993)119:3(728)

#### **Information about authors:**

**Hamed Arshadi, PhD,**

ORCID: <https://orcid.org/0000-0002-3305-1782>

E-mail: [hamed.arshadi@semnan.ac.ir](mailto:hamed.arshadi@semnan.ac.ir)

**Ali Kheyroddin, PhD,**

ORCID: <https://orcid.org/0000-0001-7802-2013>

E-mail: [kheyroddin@semnan.ac.ir](mailto:kheyroddin@semnan.ac.ir)

**Amir Asadollahi Nezhad,**

E-mail: [hamed.arshadi@yahoo.com](mailto:hamed.arshadi@yahoo.com)

*Received 05.07.2020. Approved after reviewing 12.07.2021. Accepted 13.07.2021.*



Research article

UDC 624


DOI: 10.34910/MCE.111.3

## Detection and prediction of weak points of a frozen wall based on grey theory

T. Wu<sup>a</sup> , X.M. Zhou<sup>a</sup> , X.N. He<sup>a</sup>, Y. Xu<sup>a</sup>, L.G. Zhang<sup>b</sup>

<sup>a</sup> University of Science and Technology Beijing, Beijing, China

<sup>b</sup> China Coal Handan Special Drilling Well Co., Handan City, Hebei Province, China

 w616000360@126.com

**Keywords:** frozen soils, longitudinal temperature monitoring, whole field monitoring theory, grey system theory, prediction

**Abstract.** The purpose of this article is to use theoretical analysis to determine the cause of an artificial frozen wall not closing. Due to the influence of the energy difference received by each freezing apparatus, groundwater flow, freezing hole spacing and other factors, their heat transfer with the surrounding soil layer has limited efficiency. Theoretical calculations and engineering examples are compared to verify the validity of the theoretical model. According to the longitudinal temperature measurement of the temperature measuring hole and the freezing apparatus, the whole field monitoring theory based on grey correlation method is proposed. Through the calculation of the hole-to-hole correlation degree to evaluate and predict the working effect of each freezing apparatus, it is determined that the freezing pipes No. 7~9 and No. 18~22 are the weak parts of the freezing wall. Therefore, the grey correlation analysis was compared and analyzed in the case of the "window" accident of the frozen wall of the shaft, which verified the practicability of the theory.

### 1. Introduction

Artificial ground freezing method (AGF) is a special construction method for solving the underground construction of soft water-bearing strata such as quicksand, silt, etc. By placing freezing pipes at intervals in the stratum and circulating low-temperature brine through them, the stratum becomes hard frozen soil [1, 2]. The artificial stratum freezing method has been developed for more than 130 years, and it has been vigorously promoted by various countries in coal mines, subways and foundation pit projects. The technology is also becoming more and more mature, but the groundwater flow often leads to the accident of the frozen wall not closing, causing project delays and economic losses. For the freezing construction under high water content and complex environmental conditions, the change of temperature field determines the thickness and average temperature change of the frozen wall. Therefore, the ways of determining the tightness and strength of the frozen wall are the focus of scholars from various countries. Therefore, the calculation of the freezing temperature field is related to the success or failure of the entire freezing project. The main research methods of the temperature field include analytical methods, numerical simulation methods, field data measurement, and in-situ test methods.

Professor Trupak first proposed the calculation method for the temperature field of the frozen wall [3]. He began to study the temperature field of a single-tube frozen cylinder, and derived the analytical solution formula of the temperature field in the frozen soil wall under the condition of a single-row linear

Wu, T., Zhou, X.M., He, X.N., Xu, Y., Zhang, L.G. Detection and prediction of weak points of a frozen wall based on grey theory. Magazine of Civil Engineering. 2022. 111(3). Article No. 11103. DOI: 10.34910/MCE.111.3

© Wu, T., Zhou, X.M., He, X.N., Xu, Y., Zhang, L.G., 2022. Published by Peter the Great St. Petersburg Polytechnic University.



This work is licensed under a CC BY-NC 4.0

arrangement of frozen tubes according to the geometric relationship between the frozen tube and the frozen soil column. Bakholdin uses the concept of ideal freezing tubes to interfere with each other to derive the theoretical formula of the temperature field distribution after the frozen wall of a single row of tubes under a linear arrangement [4]. Hu Xiangdong applied conformal transformation to transform the annular single-circle freezing model into a special linear arrangement model to complete the analytical solution of the unfrozen temperature field in the single-circle tube freezing circle [5]. In the literature [6–8], the calculation formula of the frozen wall thickness of the double-row tube and the 3-row tube and the analytical solution of the temperature field have been deduced successively, and the calculation results are relatively consistent with the measured data.

Literature [9] used the monitoring data of the construction site of the connected aisle freezing method to analyze the disturbance of each construction process on the freezing temperature field, grasped the influence law of each construction process on the connected aisle freezing temperature field, and provided a safety reference for similar projects in the future. Literature [10] based on the tunnel freezing project, studied the weakening effect of freezing waterproof curtain caused by construction thermal disturbance through model tests.

With the popularization of numerical software, the numerical simulation of the frozen wall temperature field has been valued by scholars [11–15].

However, freezing engineering usually sets up several temperature measuring holes to monitor the state of the frozen wall [16]. When calculating specific engineering examples, the temperature measurement data is substituted into the theoretical analytical formula or numerical software to obtain the thickness of the frozen wall, so the data of the temperature measuring holes can only represent the temperature characteristics at a specific location, and can not provide timely feedback on the overall state of the frozen wall.

The purpose of this article is to establish the research object of each freezing apparatus, and collect the longitudinal temperature data of freezing apparatus, and obtain the longitudinal temperature distribution in the freezing tube through comprehensive data analysis, in order to qualitatively judge and predict the overall state of the frozen wall. To achieve the above goals, the following problems need to be solved:

1. Establish a set of scientific mathematical analysis methods to form a complete basic theory.
2. In the engineering example, establish a model to determine the development status of the frozen wall, find the weak point of the frozen wall, and verify the theory.

## 2. Materials and Methods

### 2.1. Monitoring method and theoretical basis of frozen wall condition

The traditional method to study the temperature field of frozen wall is based on the single-hole freezing steady-state theory of Professor Trupak of the former Soviet Union [3, 17]. The temperature field model of frozen wall is established as shown in Fig. 1, and the temperature distribution function formula of frozen soil area is deduced as follows:

$$T_f(x, y) = T_p \ln \frac{\sqrt{E^2 + L^2}}{2\sqrt{x^2 + y^2}} \bigg/ \ln \frac{\sqrt{E^2 + L^2}}{d_p} \left( -\frac{L}{2} \leq x \leq \frac{L}{2}, -\frac{\sqrt{E^2 + L^2}}{2} \leq y \leq \frac{\sqrt{E^2 + L^2}}{2} \right), \quad (1)$$

where  $T_f$  is the temperature field function in the frozen soil area;  $T_p$  is the temperature of the freezing pipe wall;  $E$  is the thickness of the frozen soil wall;  $L$  is the hole spacing;  $d_p$  is the diameter of the freezing pipe.

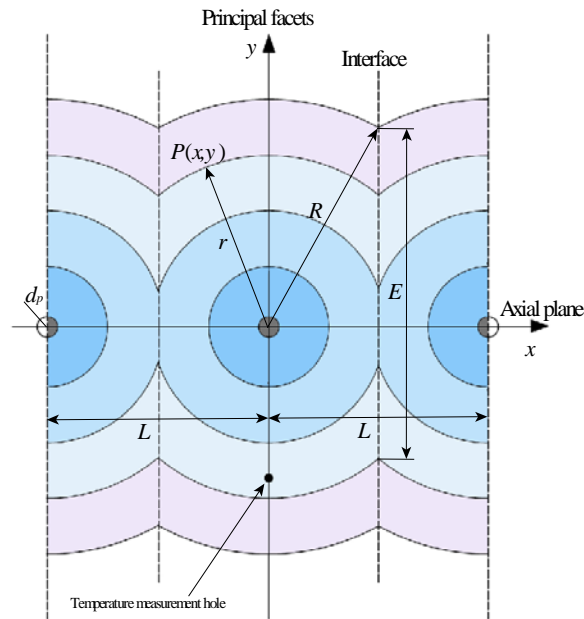


**Figure 1. The frozen wall temperature field model.**

A temperature measuring hole is provided near the freezing hole, and the frozen thickness of the frozen wall is calculated by the formula (1) through the detected temperature data in the temperature measuring hole, which is the traditional temperature field monitoring method. In practical engineering, the development of frozen wall is affected by many factors such as the energy regulation of each freezing apparatus, the flow of groundwater, the spacing of frozen holes, the heat conductivity of the stratum and so on. The interior of the stratum belongs to the concealed space, so it is difficult to fully grasp the development process of the frozen wall of the stratum.

In the engineering construction, a technical method of longitudinal temperature measurement in the freezing apparatus has been gradually developed to diagnose and deal with engineering accidents, as shown in Fig. 2. Literature [18] studied the relationship between the temperature change in the center of the freezing pipe and the thickness of the frozen wall after the freezing apparatus was temporarily shut down, and proposed a new method to use the longitudinal temperature measurement of the freezing apparatus to solve the internal situation of the frozen wall.

$$v = \left. \frac{dT}{dt} \right|_{r=0} = a \left( \frac{\alpha}{R} - \frac{\beta}{R^2} \right), \quad (2)$$

where  $v$  is the temperature rise rate;  $R$  is the radius of the frozen soil;  $a$  is the coefficient of thermal conductivity of the frozen soil;  $\alpha$  and  $\beta$  are the correlation coefficients of the initial temperature field of the frozen wall before freezing.

Because there are a lot of random factors in the project, it is still difficult to apply formula (2) directly, but its significance lies in revealing the substantial value of the longitudinal temperature measurement data of the freezing apparatus, which is to make full use of the temperature measurement holes, hydrological holes and freezing apparatus to implement the whole field monitoring of the frozen wall temperature field thereby increasing the output of system information. The methods and requirements for the construction of freezing holes, temperature measuring holes and hydrological holes are basically the same, and the main difference lies in the different installation structures. The freezing apparatus is installed in the freezing hole, which is composed of a freezing pipe, a liquid supply pipe, and the head of the freezing apparatus, as shown in Fig. 3(a). The water pipe is arranged in the hydrological hole, which is composed of impervious steel pipe and permeable pipe. The permeable pipe is made of steel pipe with evenly distributed holes, as shown in Fig. 3(b). In the temperature measuring hole, the steel pipe with closed lower end is placed, and the inside of the pipe is generally in air state. Several temperature sensors are installed in the temperature measurement hole, as shown in Fig. 3(c). Then a large amount of information output of the system needs scientific information processing technology in order to extract more valuable parts for engineering construction services.

The main idea of the whole field monitoring theory is as follow. Firstly, we should vigorously develop new temperature measurement technology and increase the number of temperature measurement points to improve the amount of information in the temperature data of the shaft. Secondly, the longitudinal

temperature in the freezing apparatus is the main body, combining with the longitudinal temperature in the hydrological hole and the temperature measurement data of the temperature measuring hole to form a new temperature measurement engineering system. Finally, a data analysis system for predicting, forecasting and controlling the temperature field of the frozen wall is established to gradually transform the development of the frozen wall from a hidden state to a transparent state, thereby improving the safety of the quality of the frozen wall engineering and the technical level of freezing shaft construction.

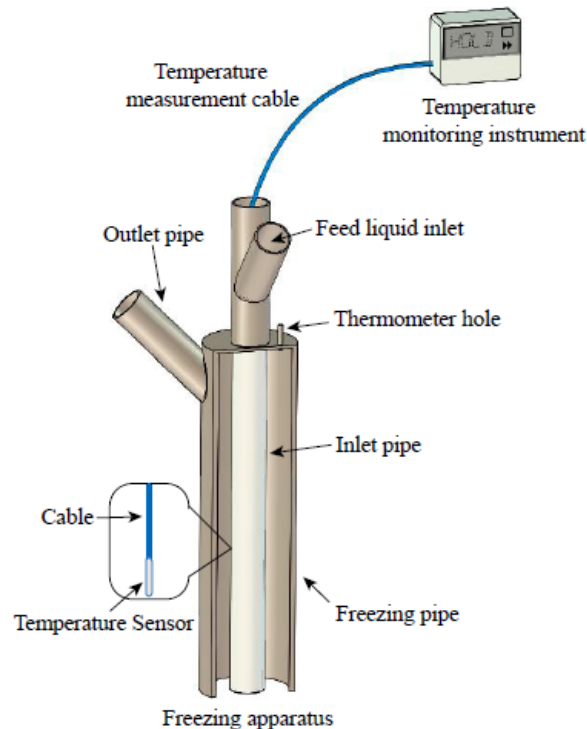


**Figure 2. The principle of longitudinal temperature measurement in the freezing apparatus.**

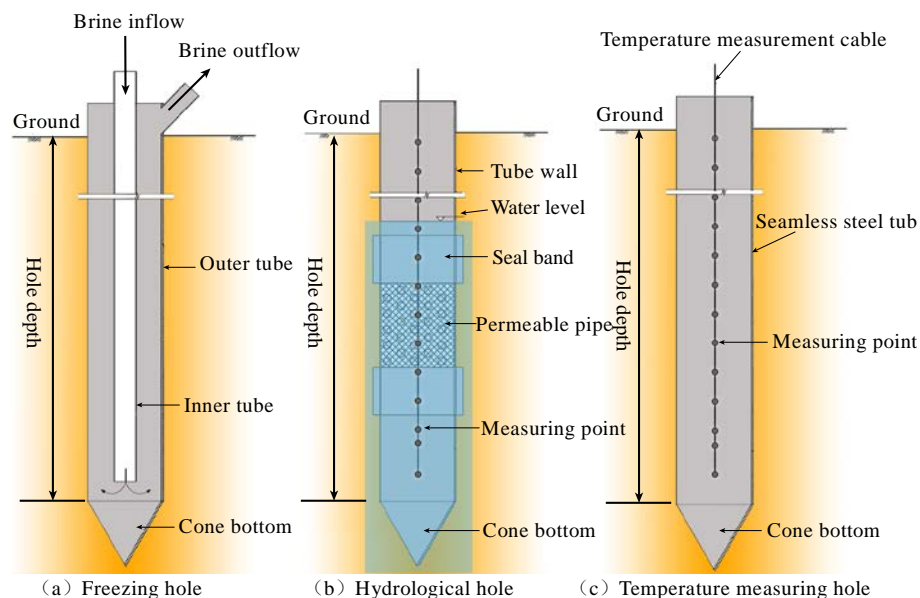


**Figure 3. Different installation structures of freezing holes.**

## 2.2. Principle of grey correlation analysis of longitudinal temperature measurement data

According to modern control theory, engineering system is a "black box". Ways to increase the amount of information in the system is an important technical direction of engineering monitoring. Grey theory [19–20] presents the output of the system state as a sequence, so the temperature data output along the depth direction is a data sequence. Here, the longitudinal temperature measurement data of the temperature measuring hole and the freezing apparatus are organized into the following sequence:

$$\begin{aligned}
T_1(h) &= \{t_1(1), t_1(2), t_1(3), \dots, t_1(M)\}, \\
T_2(h) &= \{t_2(1), t_2(2), t_2(3), \dots, t_2(M)\}, \\
&\vdots \\
T_i(h) &= \{t_i(1), t_i(2), t_i(3), \dots, t_i(M)\}, \\
&\vdots \\
T_N(h) &= \{t_N(1), t_N(2), t_N(3), \dots, t_N(M)\},
\end{aligned}$$

where  $h$  is the depth or serial number of the longitudinal measuring point,  $h = 1, 2, \dots, M$ ;  $i$  is the hole number of the frozen hole,  $i = 1, 2, \dots, N$ .

The definition of relevance in the grey theory borrows the concept of geometric similarity, assuming that these sequences are plotted on a two-dimensional rectangular coordinate system with time as the horizontal coordinate, as shown in Fig. 4. If the sequence  $T_1(h)$  curve and the sequence  $T_2(h)$  curve are relatively parallel or similar, it is said that the correlation between  $T_2(h)$  and  $T_1(h)$  is large, which is recorded as  $\gamma_{12}$ . If the similarity between curves  $T_3(h)$  and  $T_1(h)$  is small, and the similarity between curves  $T_4(h)$  and  $T_1(h)$  is the worst, then  $\gamma_{12} > \gamma_{13} > \gamma_{14}$ . Here,  $T_1(h)$  is called the parent factor sequence, and  $T_2(h)$ ,  $T_3(h)$  and  $T_4(h)$  are called sub factor sequences.

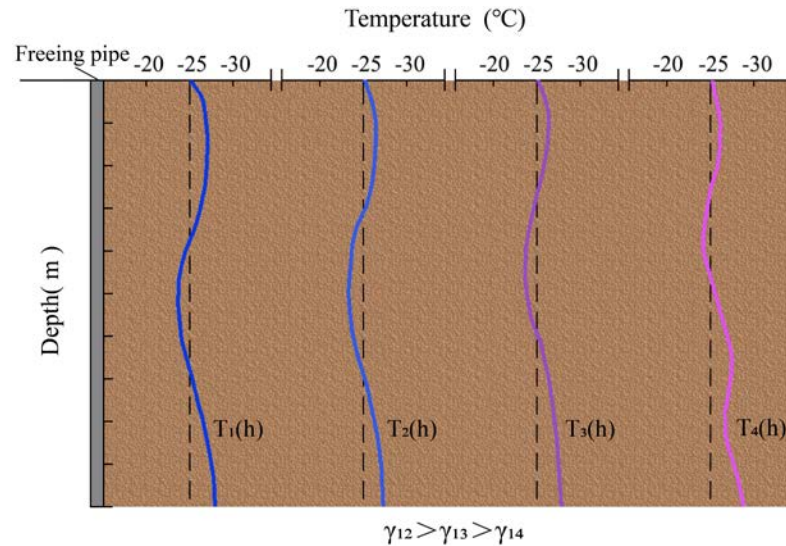


**Figure 4. The geometric meaning of grey correlative degree.**

In order to evaluate the overall condition of the frozen wall, it can be analyzed by the correlation of the temperature measurement data of each freezing apparatus. For example, in an ideal situation, the flow distribution of each freezing apparatus is uniform, and the conditions of the stratum are also the same. The temperature measurement curve between them should be exactly the same, the correlation degree should be very good. According to the temperature measurement data in the temperature field, the relevant concepts and definitions of the slope correlation degree are introduced.

Correlation coefficient  $\xi(t)$ : Let the sequence be  $X(t)$  and  $Y(t)$ ,  $X, Y \in R$ ,  $t \in T$ , then

$$\xi(t) = \frac{1}{1 + \left| \frac{1}{\sigma_x} \frac{\Delta x(t)}{\Delta t} - \frac{1}{\sigma_y} \frac{\Delta y(t)}{\Delta t} \right|}, \quad (3)$$

where  $\Delta x(t) = x(t+1) - x(t)$ ;  $\Delta y(t) = y(t+1) - y(t)$ ;  $\Delta t = (t+1) - t = 1$ .



$$\sigma_{xi} = \sqrt{\frac{1}{N} \sum_{i=1}^N (x_{ik} - \bar{x}_i)^2}; \sigma_{yi} = \sqrt{\frac{1}{N} \sum_{i=1}^N (y_{ik} - \bar{y}_i)^2},$$

where  $\sigma_{xi}$  and  $\sigma_{yi}$  are the standard deviations of the  $X(t)$  and  $Y(t)$  sequences, respectively.

The nature of  $\xi(t)$ :  $0 \leq \xi(t) \leq 1$ , the closer the slope of  $X(t)$  and  $Y(t)$  at time  $t$ , the greater the  $\xi(t)$ , and the correlation coefficient is 1;  $\xi(t)$  is related to the geometric shape, but not the starting position.

Definition of correlation degree:

$$\gamma_{xy} = \frac{1}{N-1} \sum_{t=1}^{N-1} \xi(t), (t = \{1, 2, 3, \dots, N-1\}). \quad (4)$$

The main characteristics of slope correlation: (1) The original data does not need to select reference points and standardization, which is convenient for computer processing, and the restrictions on detection conditions are also small; (2) The calculation is not affected when the original data contains zero or negative values, so the adaptability of engineering data application is good; (3) The resolution of the correlation degree is high.

Each freezing apparatus can be regarded as either a parent factor or a sub factor, thus forming a correlation matrix; it is a symmetric matrix with a main diagonal element of 1, i.e.

$$\begin{array}{c} \text{Number} \end{array} \quad \begin{array}{ccccc} 1 & 2 & \cdots & n-1 & n \end{array}$$

$$\begin{array}{c} 1 \\ 2 \\ \vdots \\ n-1 \\ n \end{array} \quad \begin{bmatrix} 1 & \gamma_{1,2} & \cdots & \gamma_{1,n-1} & \gamma_{1,n} \\ \gamma_{2,1} & 1 & \cdots & \gamma_{2,n-1} & \gamma_{2,n} \\ \vdots & \vdots & \ddots & \vdots & \vdots \\ \gamma_{n-1,1} & \gamma_{n-1,2} & \cdots & 1 & \gamma_{n-1,n} \\ \gamma_{n,1} & \gamma_{n,2} & \cdots & \gamma_{n,n-1} & 1 \end{bmatrix}. \quad (5)$$

For the above matrix, you can use the analysis of variance to study the overall situation of the frozen wall. (1) The element  $\gamma_{i,j}$  in the matrix represents the degree of correlation between holes  $i$  and  $j$ . Obviously,  $\gamma_{i,i} = 1$ , the closer  $\gamma_{i,j}$  is to 1, the closer is the working condition between  $i$  and  $j$  holes.  $\gamma_{i,j} < \gamma_{i,k}$ , indicating that the freezing condition of hole  $k$  is closer to that of hole  $i$  than that of hole  $j$ ; (2)

The average correlation of hole  $i$ ,  $\bar{\gamma}_i = \frac{1}{n} \sum_{j=1}^n \gamma_{i,j}$ , which reflects the comprehensive degree of the

correlation between hole  $i$  and other holes, and reflects the state of hole  $i$  in the whole; (3) The overall

average correlation degree of the freezing apparatus  $\bar{\gamma} = \frac{1}{n} \sum_{i=1}^n \left( \frac{1}{n} \sum_{j=1}^n \gamma_{i,j} \right)$ , which reflects the average

effect of each freezing apparatus in the whole frozen wall. The closer  $\bar{\gamma}$  is to 1, the more similar are the working conditions such as the distribution of cold energy and stratum conditions; (4) Parameters  $\gamma_{i,j}$ ,  $\bar{\gamma}_i$ ,  $\bar{\gamma}$  are all functions of time (or depth), that is, when analyzed in different depth segments, the above parameters will change, which can directly reflect the changes of objective conditions, such as groundwater flow, lithology and other conditions.

### 2.3. Example calculation

The net diameter of Xipang shaft of Dongpang Mine in China is 4.5 m, the thickness of the topsoil layer is 136 m, the aquifer is mainly composed of a pebble formation with a vertical depth of 22 m, a sand layer and a pebble formation of 111~135.65 m, and the freezing depth is 175 m. The ring diameter of the freezing apparatus is 9.556 m, the hole spacing is 1.247 m, and there are 24 freezing holes. During the active freezing period, the brine temperature is  $-26 \sim -28$  °C. BRR specific heat calorimeter and QTM-PD2

thermal conductivity measuring instrument in Fig. 5 are used to test the heat flux and thermal conductivity of soil layer respectively. The thermal physical properties of soil are shown in Table 1. When the active freezing time reaches the design period, and the temperature of the temperature measuring holes has reached the design temperature, an experimental excavation is performed on the shaft. When the fine sand layer of  $-41.7$  m was excavated, water leaked in the shaft. After preliminary judgment, it was determined that the frozen wall of the shaft was not closed. In order to find the reason, the longitudinal temperature measurement of all freezing apparatuses of the shaft was carried out. Part of the data is shown in Table 2. Firstly, it was found that the longitudinal temperature of the C1 temperature measuring hole, No. 18, No. 19, No. 20, No. 21 and No. 22 freezing holes had an obvious inflection point at 50 m~60 m, and the temperature was  $2\sim 3$  °C higher than other layers. Therefore, it was found the frozen wall did not close due to the abnormality of these freezing holes. However, it is necessary to specifically determine the location of the "window" of the frozen wall and take remedial measures.

Then, we used the grey correlation theory to conduct a whole field monitoring analysis and find the corresponding "window" position. We established the holes Nos. 20 and 21 had the largest longitudinal temperature fluctuation as the parent factor, and analyzed the longitudinal temperature measurement data of the freezing apparatus with a depth of 65m or more in the topsoil aquifer, using the slope correlation method. The freezing holes with a high degree of correlation with holes 20 and 21 may be weak holes in the frozen wall. After analyzing all the longitudinal temperature measurement data, it was finally confirmed that there was groundwater flow phenomenon at the vertical depth of about 57m on the frozen wall, and there were water-conducting channels between the holes No. 18~22 and the holes No. 7~9.

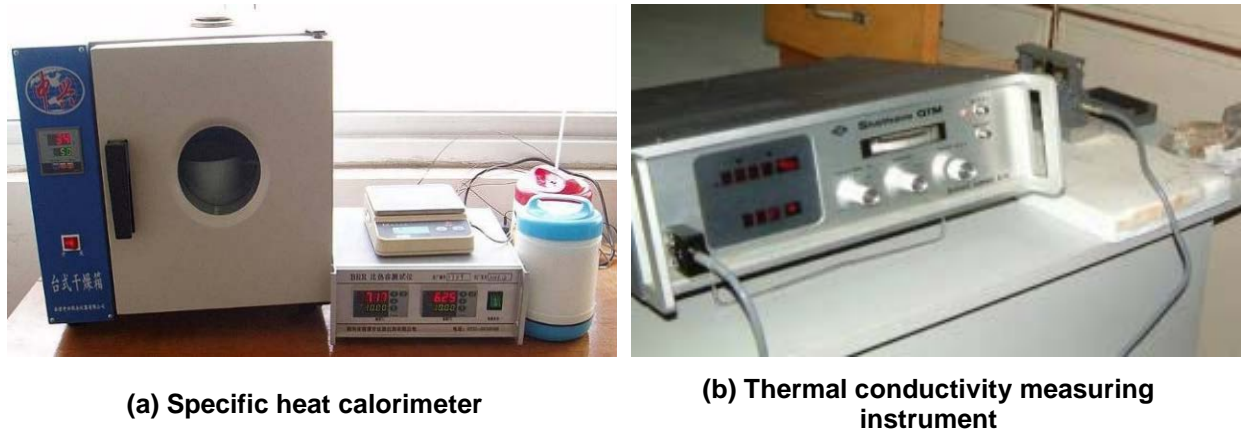


**Figure 5. Measurement of soil thermophysical properties.**

**Table 1. Soil properties.**

| Soil property | Depth (m)   | Moisture content (%) | Density (g/cm <sup>3</sup> ) | Dry density (g/cm <sup>3</sup> ) | Specific heat (J·g <sup>-1</sup> ·K <sup>-1</sup> ) | Thermal conductivity (kCal/m·h·°C) |
|---------------|-------------|----------------------|------------------------------|----------------------------------|---|------------------------------------|
| Sandy clay    | 43.68~80.87 | 14.68                | 2.095                        | 1.831                            | 1.504   | 1.872                              |
| Clayey sand   | 25.30~72.20 | 24.76                | 1.898                        | 1.521                            | 1.485   | 1.787                              |

**Table 2. Lengthwise temperature survey along freeze pipe of main shaft in Dongpang mine, China.**

| Hole number | Depth |       |       |       |       |       |       |       |
|-------------|-------|-------|-------|-------|-------|-------|-------|-------|
|             | 25 m  | 35 m  | 40 m  | 45 m  | 50 m  | 55 m  | 60 m  | 65 m  |
| 1           | -19.8 | -20.0 | -20.1 | -20.2 | -20.5 | -20.3 | -20.4 | -20.2 |
| 3           | -21.6 | -21.9 | -21.8 | -21.9 | -22.1 | -22.0 | -22   | -22.6 |
| 5           | -22.1 | -22.4 | -22.5 | -22.4 | -22.3 | -22.1 | -22.1 | -22.4 |
| 7           | -21.5 | -21.8 | -22.1 | -22.2 | -22.2 | -22.0 | -22.1 | -22.2 |
| 8           | -21.5 | -21.5 | -21.6 | -21.6 | -21.4 | -21.0 | -21.3 | -21.2 |
| 9           | -21.8 | -21.8 | -21.8 | -22.0 | -21.8 | -20.5 | -21.7 | -21.9 |
| 12          | -21.4 | -21.2 | -21.1 | -21.4 | -21.4 | -21.3 | -21.3 | -21.5 |
| 14          | -19.7 | -19.6 | -19.7 | -20.2 | -20.3 | -20.2 | -20.2 | -20.3 |
| 16          | -20.1 | -19.8 | -19.9 | -20.4 | -20.4 | -20.0 | -20.2 | -20.1 |

| Hole number | Depth |       |       |       |       |       |       |       |
|-------------|-------|-------|-------|-------|-------|-------|-------|-------|
|             | 25 m  | 35 m  | 40 m  | 45 m  | 50 m  | 55 m  | 60 m  | 65 m  |
| 18          | -20.0 | -20.0 | -20.0 | -20.1 | -20.0 | -20.0 | -20.4 | -20.6 |
| 19          | -19.8 | -20.2 | -20.1 | -19.7 | -19.4 | -18.1 | -19.3 | -19.8 |
| 20          | -20.3 | -20.9 | -21.1 | -21.1 | -19.9 | -19.0 | -21.0 | -21.3 |
| 21          | -21.0 | -21.2 | -21.3 | -21.2 | -20.6 | -19.3 | -20.8 | -21.1 |
| 22          | -20.4 | -20.4 | -20.3 | -20.3 | -19.6 | -19.1 | -19.8 | -20.3 |
| 23          | -21.8 | -21.8 | -21.9 | -21.9 | -22.0 | -21.9 | -21.9 | -22.1 |

### 3. Results and Discussions

#### 3.1. Results

By using the slope correlation method to analyze the above longitudinal temperature measurement data, the results are shown in Fig. 6. It can be seen that the correlation between No. 7~9 and No. 18~22 is particularly high, indicating that the groundwater flow forms a channel along No. 18~22 and No. 7~9, so the correlation analysis between freezing holes can determine the location of the frozen wall weakness caused by abnormal freezing pipes.

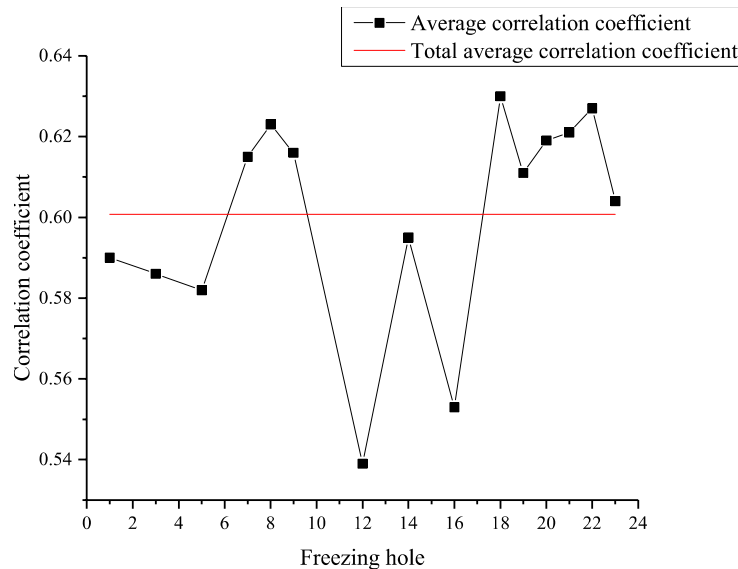


**Figure 6. Correlation analysis of longitudinal temperature measurement data of freezing apparatus.**

The on-site investigation and analysis showed that due to the accident stratum being a highly permeable gravel layer affected by spring irrigation pumping, the groundwater flow scoured the frozen wall from the northwest to the southeast taking away a large amount of cold energy and making it difficult to close the frozen wall. The water flow enters the shaft with the freezing holes No. 18, No. 19, No. 20, No. 21 and No. 22 as a main channel, one flow enters the shaft along the S2 hydrological hole, and the other flow flows from No. 7, No. 8 and No. 9 freezing holes taking away the cooling energy. This further confirms the accuracy of the grey correlation theory in accident analysis, as shown in Fig. 7. In order to speed up the progress of the freezing project, the brine temperature was lowered from  $-28^{\circ}\text{C}$  to  $-33^{\circ}\text{C}$ . Pipeline pumps were added to the eight freezing holes of No. 18~22 and No. 7~9 of the annular groove of the shaft to increase the brine flow rate of the freezing hole. The C1 and C2 temperature measuring holes are changed into freezing holes to increase the cooling capacity. By taking the above measures, the healing of the frozen wall was ensured, and the accident was dealt with pertinently. During the excavation process, the location of the "window" of the frozen wall was verified. Holes 18~22 and 7~9 have traces of repair of the frozen wall window at a vertical depth of about 57 m, and there is ice formation in the gravel gap (size 50 mm  $\times$  80 mm), as shown in Fig. 8, which is completely consistent with the correlation analysis.

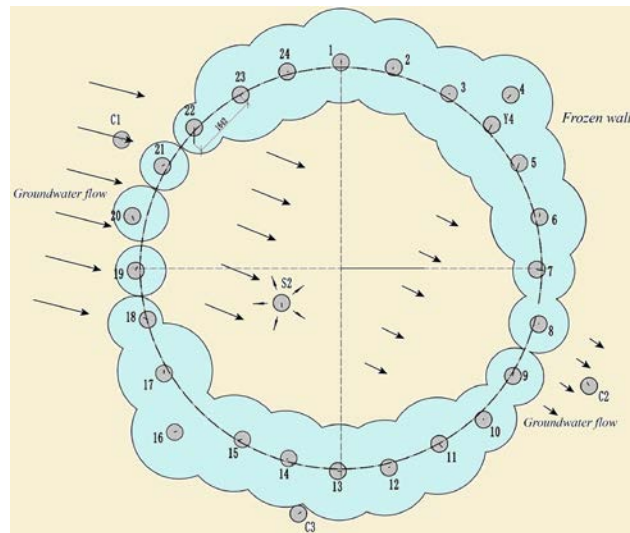


Figure 7. Schematic diagram of the 57 m frozen wall outlet of the shaft.



Figure 8. Freezing point on the west side of shaft at 57.3 m.

### 3.2. Discussions

In the process of studying the temperature field of the frozen wall, the researchers calculated the thickness, strength and closing time of the frozen wall using theoretical analysis methods and finite element numerical methods through the temperature measurement hole data. In this case, the calculation result obtained by the theoretical analysis method reflects the state of the local range of the frozen wall, and the solution is also approximate [3, 5, 21]. The modeling process of the finite element numerical calculation method is ideal, requiring the model to be homogeneous and continuous, and the obtained simulation calculation results have certain errors from the actual measurement [22, 23]. In addition, in the face of complex geological conditions and hydrological environments, the development of complex freezing temperature field under some special working conditions is no longer applicable to the above method.

Literature [24] applied the area correlation analysis method to analyze the longitudinal temperature measurement data of the frozen shaft of Jian Chang Ying Mine in China, and determined the weak position of the frozen wall. However, this method cannot be calculated when there are zero values in the original series.

In this study, the longitudinal temperature measurement data of freezing tube is used to comprehensively analyze the development of frozen wall, which overcomes the shortage of only relying on the local temperature measurement hole to understand the situation of frozen wall in the traditional technology; the slope correlation method also effectively solves the defect that zero value cannot be calculated in the data, and realizes the prediction and evaluation of the all-round development of frozen wall.

## 4. Conclusion

From the above results:

1. The longitudinal temperature measurement of the temperature measuring hole and the freezing apparatus is a technical means to understand the local and overall freezing conditions of the shaft. The proposal of whole field monitoring is the supplement and development of the longitudinal temperature measurement technology in theory.
2. The use of slope correlation analysis is a practical method of longitudinal temperature measurement data processing, and an application of grey theory in artificial ground freezing engineering.
3. The correlation analysis of the longitudinal temperature measurement data between freezing apparatuses reflects the relatively good or bad freezing effect of the freezing apparatus, and is the basis for conclusion on the weak position of the frozen wall.
4. The normal operation of each freezing apparatus is a necessary guarantee for the smooth freezing of the shaft. It is affected by many subjective and objective factors such as the cold supply of the freeze pipe, the flow of groundwater, and the thermal conductivity of the formation. It combines the longitudinal temperature detection data of the freezing pipe with the temperature measurement hole detection data to achieve the goal of comprehensively monitoring the formation effect of the frozen wall.

## References

1. Ito, Y., Yoshida, S. Transition of ground improvement technologies in Japan V: Artificial ground freezing method and its application. *Journal of the Society of Materials Science, Japan*. 2016. 65(12). Pp. 883–889. DOI: 10.2472/jsms.65.883
2. Hu, X. Dong, Yu, J. Zhu, Ren, H., Wang, Y., Wang, J. Tai. Analytical solution to steady-state temperature field for straight-row-piped freezing based on superposition of thermal potential. *Applied Thermal Engineering*. 2017. 111. Pp. 223–231. DOI: 10.1016/j.applthermaleng.2016.09.058
3. Trupak, N.G. *Zamorazhivaniye Gornykh Porod Pri Prokhodke Stvolov*. Ugletekhizdat. Moskva, 1954.
4. Bakholdin, B.V. *Vybor optimalnogo rezhima zamorazhivaniya gruntov v stroitelnykh tselyakh*. Gosstroyizdat. Moskva, 1963.
5. Hu, X.D., Zhang, L.Y. Analytical solution to steady-state temperature field of single-circle-pipe freezing. 34(3) 2013.
6. Xiao, Z., Hu, X., Zhang, Q. Characters of temperature field in frozen soil wall with multirow freeze-tubes and limited depth freezing. *Chinese Journal of Rock Mechanics and Engineering*. 2007. 26 (SUPPL. 1). Pp. 2694–2700. DOI: 10.3321/j.issn:10-00-6915.2007.z1.015
7. Hu, X.D., Ren, H. A trapezoidal-parabolic arch superimposed equivalent temperature field model and its average temperature formula for triple-row-pipe freezing. *Journal of the China Coal Society*. 2014. 39(1). Pp. 78–83. DOI: 10.13225/j.cnki.jccs.2013.0166
8. Shao, Z. Li, Hu, X. Dong, Han, Y. Guang, Fang, T. Generalized analytical solution to steady-state temperature field of double-circle-piped freezing. *Cold Regions Science and Technology*. 2020. 175. Pp. 103076. DOI: 10.1016/j.coldregions.2020.103076
9. Changzhong, Z., Xiangdong, H., Jianz, Z., Fan, Q. Influence of construction process by freezing method on the temperature field of the frozen soil curtain for cross passage in shield tunnels. *The 9<sup>th</sup> China Academic Congress of Rock Mechanics and Engineering*. 2006. Pp. 556–562.
10. Li, Z., Wang, W., Hu, X. Research on influence of construction thermal disturbance on the freezing-sealing pipe roof. *China Civil Engineering Journal*. 2015. 48. Pp. 374–379.
11. Zhao, D.J., Liu, Y.M., Sun, Y.H., Zhao, Y., Bai, F.T. Experiments and simulations of underground artificial freezing with the use of natural cold resources in cold regions. *Building and Environment*. 2015. 87. Pp. 224–233. DOI: 10.1016/j.buildenv.2015.01.032
12. Li, Z., Chen, J., Sugimoto, M., Ge, H. Numerical simulation model of artificial ground freezing for tunneling under seepage flow conditions. *Tunnelling and Underground Space Technology*. 2019. 92 (October 2018). Pp. 103035. DOI: 10.1016/j.tust.2019.103035
13. Pimentel, E., Papakonstantinou, S., Anagnostou, G. Numerical interpretation of temperature distributions from three ground freezing applications in urban tunnelling. *Tunnelling and Underground Space Technology*. 2012. 28(1). Pp. 57–69. DOI: 10.1016/j.tust.2011.09.005
14. Vitel, M., Rouabhi, A., Tijani, M., Guérin, F. Modeling heat transfer between a freeze pipe and the surrounding ground during artificial ground freezing activities. *Computers and Geotechnics*. 2015. 63. Pp. 99–111. DOI: 10.1016/j.compgeo.2014.08.004
15. Zhou, X.M., Xiao, L.G. Numerical research on the temperature and seepage fields of artificial seepage ground freezing. *Journal of the China Coal Society*. 2007. 32(1). Pp. 24–28. DOI: 10.13225/j.cnki.jccs.2007.01.005
16. Chinese National Standard MT/T 1124-2011 Coal mine technical specification for vertical shaft sinking by freezing method.
17. Hu, X., Bai, N., Yu, F. Analysis of Trupak and Bakholdin formulas for temperature field of single-row-pipe frozen soil wall. *Journal of Tongji University*. 2008. 36(7). Pp. 906–910. DOI: 10.3321/j.issn:0253-374X.2008.07.008
18. Zhou, X.M., Zhang, X.Z. Research on the thickness estimation of freezing wall according to temperature measurement along freeze tube. *Meitan Xuebao/Journal of the China Coal Society*. 2003. 28(2). Pp. 162. DOI: 10.3321/j.issn:0253-9993.2003.02.012
19. Liu, S., Forrest, J., Yang, Y. A brief introduction to grey systems theory. *Grey Systems: Theory and Application*. 2012. 2(2). Pp. 89–104. DOI: 10.1108/20439371211260081
20. Liu, S., Lin, Y. Introduction to grey systems theory. *Understanding Complex Systems*. 2010. 68. Pp. 1–399. DOI: 10.1007/978-3-642-16158-2\_1
21. Hu, X.D., He, T.X. Equivalent-trapezoid method of average temperature calculation for multi-row-pipe straight frozen soil wall. 34(11) 2009. DOI: 10.13225/j.cnki.jccs.2009.11.010

22. Liu, J., Liu, Q., Zhou, D., Zhu, X. Influence of Groundwater Transverse Horizontal Flow Velocity on the Formation of Artificial Horizontal Freezing Wall. Journal of Basic Science and Engineering. 2017. 25(2). Pp. 258–265. DOI: 10.16058/j.issn.1005-0930.2017.02.005
23. Hu, J., Zeng, H., Wang, X. Numerical Analysis of Temperature Field of Cup-shaped Frozen Soil Wall Reinforcement at Shield Shaft. 2013. 342. Pp. 1467–1471. DOI: 10.4028/www.scientific.net/AMM.341-342.1467
24. Wang, J. Theoretical Forecast of Gray Control System and Temperature Data in Frozen Construction. Selected Papers of China Mining Construction Academic Conference (Second Volume). 2003. Pp. 515–521. URL: [http://www.wanfang-data.com.cn/details/detail.do?\\_type=conference&id=4700562](http://www.wanfang-data.com.cn/details/detail.do?_type=conference&id=4700562).

**Information about authors:**

**Tao Wu,**

ORCID: <https://orcid.org/0000-0003-0736-8046>

E-mail: [w616000360@126.com](mailto:w616000360@126.com)

**Xiaomin Zhou, PhD**

ORCID: <https://orcid.org/0000-0001-8765-862X>

E-mail: [b20170024@xs.ustb.edu.cn](mailto:b20170024@xs.ustb.edu.cn)

**Xiaonan He,**

E-mail: [651600363@qq.com](mailto:651600363@qq.com)

**Yan Xu,**

E-mail: [475546253@qq.com](mailto:475546253@qq.com)

**Ligang Zhang,**

E-mail: [116124556@qq.com](mailto:116124556@qq.com)

*Received 09.06.2020. Approved after reviewing 28.04.2021. Accepted 20.06.2021.*





Research article

UDC 691.4

DOI: 10.34910/MCE.111.4

## The clay rocks properties for the production of the ceramic bricks

A.M. Abdulhadi, M.H. Mussa , Y. Kadhim

Department of Civil Engineering, College of Engineering, University of Warith Al-Anbiyaa, Karbala, Iraq

 [dr.mhmussa@uowa.edu.iq](mailto:dr.mhmussa@uowa.edu.iq)

**Keywords:** clay rocks, properties, electrochemical interactions, technology, ceramic brick

**Abstract.** This paper aimed to study the properties of clay rocks in terms of chemical, mineralogical, and granulometric compositions during the pre- and post-firing processes as compared to regulatory documents. Moreover, the electrochemical interactions between the clay rocks elements have been evaluated due to the electrophoresis of its core. The results revealed that the properties of the investigated clay rocks agreed well with the requirements of regulatory documents and it is suitable to produce the ceramic bricks by plastic and dry methods. However, the calculated energy charges of clay oxides prove that the chemical composition of clay rocks will provide an unstable and irritable brick system due to the negative charges being 1.6 times greater than the positive charges. To modify the composition, it is suggested to insert feedstock or additives containing 2.3 times more positive charge selected on the basis of the structure of s-, p- and d-electrons. Further studies are recommended to take into account the thermodynamic characteristics of the feedstock to monitor the firing process, reduce energy costs and improve the quality of bricks.

### 1. Introduction

Most of the countries spend almost half of the annual income on construction. For centuries, the industry of producing artificial ceramic occupied an important place in Material science and production; its quality was determined by an ancient technology – clay science [1, 2]. According to the principle “what you sow, you reap” the quality of quarry clay rock determines the quality of the final ceramic product, particularly bricks. Clay soils are unique in terms of the inhomogeneity of their properties. Note that, when their solid ingredients are converted into a viscous fluid, in certain circumstances, they change their compositions and properties [3, 4]. Clay rocks can be rock-like, dry or wet, depending on the region, soil strata conditions and groundwater levels. They have different moisture, as well as different particle size distribution, they are lean, medium or high ductility, different formability, furthermore they have different attitude to temperature interactions (drying, firing).

The chemical compositions of clay rocks vary widely:  $\text{SiO}_2$  – 45–80 %,  $\text{CaO}$  – 0.5–25 %, that is 1.7–50 times [5, 6]. Atoms and molecules are in free and bound states, the ratio between them is different in energies. They are energetically charged either positively or negatively. However, when raw materials and technology are selected, the electrical core of atoms and their energetics are not taken into consideration [7–9]. Excessive amounts of salt in the original materials cause fading and destruction in the surface layer of products [10, 11]. The granulometric composition of clay rocks is closely related to the mineralogical composition; furthermore, it is very diverse [12–14]. For example, grains of less than 5  $\mu\text{m}$  are attributed to clay rock, their amount is in the range of 8–60 %, while grains of 50–350  $\mu\text{m}$  are attributed

Abdulhadi, A.H., Mussa, M.H., Kadhim, Y. The clay rocks properties for the production of the ceramic bricks. Magazine of Civil Engineering. 2022. 111(3). Article No. 11104. DOI: 10.34910/MCE.111.4

© Abdulhadi, A.H., Mussa, M.H., Kadhim, Y., 2022. Published by Peter the Great St. Petersburg Polytechnic University.



This article is licensed under a CC BY-NC 4.0



to sand, their amount is in the range of 1–22 %, i.e., their fluctuations are 7.5–22 times. Such a specific inhomogeneity and the variety of composition, structure and properties greatly change used technology and efficiency as well as affect the quality of the product [15].

Clay rocks used to produce bricks should exhibit good formability with no thermic cracks or deformations during the processes of drying or firing, and provide the required physical and mechanical properties as well as durability of the bricks. Therefore, in a newly developed quarry, clay rocks should not only be subjected to a thorough study of their primer properties but they should be periodically monitored and compared with the requirements of regulatory documents throughout the whole process. The regulatory documents, in the age of nanotechnology, must take into account all the properties of atoms, including the electrochemistry ones. In this research, the properties of clay rocks have been studied and compared with the requirements of regulatory documents to evaluate their compatibility to produce ceramic brick:

- State Standards of Ukraine DSTU BV 2.7-60-97. Clay raw materials for the production of ceramic building materials. Classification [16].
- Government Standard of Russia GOST 21-2116.1-81. Clay raw materials: Methods for determining plasticity [17].
- Industry standard of Russia OST 21-78-88. Clay raw materials for the production of ceramic bricks and stones. Technical requirements. Test method p:59 [18].

This research aimed to study the quality indicators of clay rocks: pre-firing, during firing and post-firing as compared with the above regulatory documents. Moreover, attention was drawn to the electrochemistry properties of clay rocks due to the lack information about these properties, whereas the mismatching between the energy charges of clay rock oxides could have a noticeable effect on the values of the maximum temperature and duration of firing.

## 2. *Materials and Methods*

In this study, clay rocks of a quarry under development have been adopted with the aim of producing ceramic bricks. Methods of studying the technological parameters of clay rock (in the quarry) and clay raw materials (in the factory) are stipulated in regulatory documents and implemented in the processes of our laboratory research. Depending on the samples, pre-calcining properties were studied and the clay rock composition was characterized: macroscopic description, chemical and mineralogical composition as well as the particle size distribution. Characteristics of clay raw materials by moisture and cohesion of clay were determined in the quarry: molding, moisture, ductility and cohesion. The drying properties of clay puddle were determined: shrinkage and sensitivity of drying. Methods of studying the properties of clay rocks are described in regulatory documents and in the process of our laboratory research. The methodological analysis of this research was carried out in the technological sequence of brick production: clay rocks characteristics, particle size distribution of clay raw materials, clay moisture and cohesion, drying and firing properties of clay.

### 2.1. *Clay Rocks Properties*

#### 2.1.1. *Sampling*

For mineralogical and physical-mechanical tests, representatives of the customer and the contractor took an average clay sample. We chose it from a developed quarry located 2 km north of the village of Hulyaivka and 8 km southeast of an urban-type settlement in Beryozovsky District, Odessa region. The quarry depth was 6 m at the sampling site, and three samples were selected at different positions. The first sample was chosen at a depth of 1 m from the lower layer of overburden, while the second sample was selected at depth 5 m and the last sample was chosen at the middle depth between the above mentioned samples. The weight of the sample was 50 kg and the clay rock of the selected three samples was scattered with a thin layer on an area of 1 m<sup>2</sup>. The clay was thoroughly mixed and divided by two diagonals into four triangles and the large blocks were smashed with a wooden mallet, and this process was repeated four times, after which it was used for laboratory research.

#### 2.1.2 *Macroscopic Description*

A macroscopic description was carried out with a microscope MPB-2 to study clay rocks, which made it possible to determine that the fraction of less than 0.001 mm consists of particles with clearly expressed morphological features.

#### 2.1.3 *Chemical Composition*

The chemical composition (%) of clays of the study area according to State Project Development & Research Institute "CHORNOMORNDIPROEKT" is shown in Table 1.

**Table 1. Chemical composition of clays rocks.**

| Oxides                               | Value       |
|--------------------------------------|-------------|
| SiO <sub>2</sub>                     | 57.4 – 62.7 |
| CaO                                  | 3.3 – 4.7   |
| MgO                                  | 2.4 – 2.8   |
| Al <sub>2</sub> O <sub>3</sub>       | 14 – 15.4   |
| Fe <sub>2</sub> O <sub>3</sub> + FeO | 5.4 – 6.3   |
| TiO <sub>2</sub>                     | 0.6 – 0.8   |
| K <sub>2</sub> O + Na <sub>2</sub> O | 3.3 – 3.7   |
| SO <sub>3</sub>                      | 0.04 – 0.07 |
| MnO                                  | 0.08 – 0.14 |

### 2.1.4 Moisture Content

Quarry moisture content of averaged clay rocks is determined by the amount of moisture lost during drying as shown in Table 2.

**Table 2. Quarry moisture of clay.**

| Sample number | Sample weight, g | Weight of dry sample, g | Moisture of clay, % |
|---------------|------------------|-------------------------|---------------------|
| 1             | 1000             | 910                     | 10.4                |
| 2             | 1120             | 980                     | 14.3                |
| 3             | 1150             | 1020                    | 12.7                |
| Average       | 1135             | 970                     | 12.5                |

### 2.1.5 Granular Distribution of Clay Raw Materials

The content of finely divided fractions, i.e. clay, dust and sand particles were determined according to the recommendations of "State Standards of Ukraine DSTU and State Standard GOST" as shown in Table 3.

**Table 3. Quantity determination of clay dust and sand fractions.**

| Quarry<br>height tier | The content of clay particle size (mm) |                    |      |           |              |          |
|-----------------------|--|--------------------|------|-----------|--------------|----------|
|                       | Size of less than 0.005                |                    |      |           | 0.05 – 0.005 | 0.05 – 1 |
|                       | V cm <sup>3</sup>                      | V1 cm <sup>3</sup> | K    | Clayey %  | Dusty %      | Sandy %  |
| Upper                 | 10                                     | 12.0               | 0.29 | 6.6       | 20.4         | 73.0     |
|                       |  | 13.1               | 0.31 | 7.0       | 25.4         | 68.0     |
|                       |  | 12.4               | 0.24 | 5.4       | 22.6         | 70.5     |
| Medium                | 10                                     | 11.7               | 0.17 | 3.9       | 33.1         | 63.0     |
|                       |  | 14.0               | 0.40 | 9.1       | 26.0         | 65.0     |
|                       |  | 13.1               | 0.31 | 7.0       | 40.0         | 58.0     |
| Lower                 | 10                                     | 11.5               | 0.15 | 3.4       | 19.6         | 77.0     |
|                       |  | 11.3               | 0.13 | 3.0       | 21.0         | 76.0     |
|                       |  | 11.2               | 0.12 | 2.7       | 20.3         | 79.0     |
| The average sample    |  |                    |      | 3.0 – 6.7 | 20 – 33      | 64 – 77  |

After the volume of clay in a beaker with water seized to increase, the volume of clay suspension  $V_1$  was determined. In addition, the rate of increment  $K$  was calculated, per cm<sup>3</sup> of the initial volume  $V_o$  by the formula:

$$K = (V_1 - V_o) / V_o. \quad (1)$$

The percentage of clay fractions was determined by the formula:

$$G = 22.7 * K. \quad (2)$$

After elutriation of the contents in the beaker, the amount of sand fractions deposited on the bottom was determined. The content of coarse inclusions was determined by screening on sieves according to "Industry standard OST" as shown in Table 4.

**Table 4. The content of coarse inclusions.**

| Sieve size (mm) | Private residues on sieves |             |           |             | Total sieve residues % |
|-----------------|----------------------------|-------------|-----------|-------------|------------------------|
|                 | Weight, g                  | Quantity, % | Weight, g | Quantity, % |                        |
| 5               | 0                          | 0           | 70        | 4           | 0 – 4                  |
| 2               | 65                         | 3           | 82        | 5           | 3 – 9                  |
| 1               | 97                         | 5           | 137       | 7           | 8 – 16                 |
| 0.5             | 141                        | 7           | 1095      | 55          | 15 – 71                |

### 2.1.6 Clay Moisture and Cohesion

The molding of the clay determines the amount of water needed to give the clay raw material a normal working consistency, as clay paste showing plastic and molding properties without deformation retains its shape and does not stick to hands and metal when rolling. To control the normal molding moisture of the clay paste, "Vika" device was used, which was designed to determine the normal density and setting time of the cement paste with a needle. Normal molding moisture was determined by the difference in masses between wet and dry clay; it was evaluated in percentage as shown in Table 5.

**Table 5. Required molding moisture for the clay samples.**

| Sample number | Weight of moist sample, g | Weight of dry sample, g | Moisture, % |          |
|---------------|---------------------------|-------------------------|-------------|----------|
|               |                           |                         | Absolute    | Relative |
| 1             | 20.0                      | 17.1                    | 14.5        | 16.9     |
| 2             | 22.4                      | 19.6                    | 12.5        | 14.2     |
| 3             | 23.6                      | 20.0                    | 13.8        | 17.8     |
| Average       | 22                        | 18.9                    | 13.6        | 16.3     |

### 2.1.7 The Plasticity of Clay Raw Materials

The ability to change shape under pressure, i.e. the deformation without the formation of cracks or breaks, and to keep this shape after unloading. These clay properties are characterized and evaluated by the plasticity index as shown in Table 6, i.e. the difference between the clay moisture in the case of plasticity limit and the clay moisture in the case of rolling limit.

**Table 6. The plasticity of clay rocks.**

|    |      | Weight, g                 |                         | Limit, % |         | Plasticity number |
|----|------|---------------------------|-------------------------|----------|---------|-------------------|
|    |      | Container with moist clay | Container with dry clay | Fluidity | Rolling |                   |
| 50 | 10   | 37.63                     | 32.34                   | 20       | 8.10    | 12                |
| 50 | 10   | 48.50                     | 44.30                   | 20       | 4.22    | 16                |
| 50 | 15   | 30.57                     | 24.70                   | 30       | 16.30   | 14                |
| 50 | 11,5 | 25.15                     | 22.87                   | 23       | 14.60   | 8                 |

### 2.1.8 The Cohesion of Clay Raw Materials

The compressive, tensile and bending strength of samples molded in a plastic way for the pastes with normal moisture that were dried at a temperature of 105–110 °C. The research results are shown in Table 7.

**Table 7. Cohesion of clay raw material.**

| Sample |                 | Loading, kgf | Rcom.<br>kgf/ cm <sup>2</sup> | Loading, kgf    | Rcom.<br>kgf/cm <sup>2</sup> | Loading, kgf               | Rcom.<br>kgf/ cm <sup>2</sup> |
|--------|-----------------|--------------|-------------------------------|-----------------|------------------------------|----------------------------|-------------------------------|
| No     | cm <sup>2</sup> |              |                               |                 |                              |                            |                               |
| 1      | 7.07            | 720          | 102                           | 79              | 17                           | Samples<br>137×50×10<br>mm | 18.2                          |
| 2      | 7.07            | 700          | 99                            | 88              | 19                           |                            | 19.1                          |
| 3      | 7.07            | 840          | 119                           | 84              | 18                           |                            | 18.9                          |
| 4      | 7.07            | 900          | 127                           | Samples "Eight" |                              |                            |                               |

Clay rock with a moisture content of 7–9 %, i.e. powder, was loaded into a mold cylinder with a diameter of 50 mm and pressed at a pressure of 200 kgf/cm<sup>2</sup>. The molded sample was removed and immediately tested in the press. We found that the compressive strength of the freshly formed press powder was 23–28 kgf/cm<sup>2</sup>.

## 2.2. Clay Drying Properties

### 2.2.1 Air Shrinkage

The mechanism of this phenomenon is an approach taken by the solid particles when the thickness of the water layer decreases between them and shrinkage of the products lasts until the moisture evaporates and the solid particles appeared. To determine that, a clay paste of normal density was prepared, tile samples were formed in the size of 100×100×10 mm and then dried to constant weight as shown in Table 8.

**Table 8. Air shrinkage of clay raw material.**

| No. | Non-pressed samples |                |             | Pressed with 200 kg/cm <sup>2</sup> |                |             |
|-----|---------------------|----------------|-------------|-------------------------------------|----------------|-------------|
|     | $L_{moist}$ , mm    | $L_{dry}$ , mm | Shrinkage % | $L_{moist}$ , mm                    | $L_{dry}$ , mm | Shrinkage % |
| 1   | 100                 | 93.8           | 6.6         | 16.4                                | 16.1           | 1,8         |
| 2   | 100                 | 93.2           | 7.2         | 16                                  | 15,6           | 2,5         |
| 3   | 100                 | 91.6           | 9.1         | 32.8                                | 31,9           | 2,8         |

### 2.2.2 Drying Sensitivity of Clay

We determined it via the Chizhsky method [19] by forming three tile samples 100×100×10 mm. We found their weight and sent them for drying. It was revealed that the moisture of the samples at which the shrinkage stops is critical moisture. According to the theory of drying, critical moisture is understood as moisture at which the constant drying speed stops and the falling drying speed begins. The clay sensitivity coefficient for drying was determined by the formula:

$$K_s = \frac{V_1}{V_o \frac{m_o - m_1}{V_o - V_1}}, \quad (3)$$

where,  $m_o$  and  $V_o$  are the mass and volume of the freshly formed sample;  $m_1$  and  $V_1$  are the mass and volume of the sample in an air-dry state. Tests were carried out on cylindrical molds with a diameter of 13 mm and a height of 39 mm: the samples were placed in them after being cut out by a clipper from a clay paste with normal moisture. Then the prepared samples were weighed and measured by length and diameter after a day and then periodically every 3-4 hours. Then we weighed the samples at the moment of reaching constant weight to determine the clay sensitivity coefficient for drying using the parameters presented in Table 9.

**Table 9. The clay sensitivity coefficient for drying.**

| No.     | The weight of sample, g |      | The length of the sample, mm |      | The diameter of the sample, mm |      | Ks   |
|---------|-------------------------|------|------------------------------|------|--------------------------------|------|------|
|         | Moist                   | Dry  | Moist                        | Dry  | Moist                          | Dry  |      |
| 1       | 10.9                    | 9.69 | 41.1                         | 39.6 | 12.4                           | 12.0 | 0.96 |
| 2       | 10.93                   | 9.72 | 43.8                         | 39.1 | 12.5                           | 12.1 | 0.89 |
| 3       | 10.86                   | 9.69 | 39.1                         | 38.3 | 12.3                           | 11.9 | 0.97 |
| Average | 10.9                    | 9.7  | 41                           | 39   | 12.4                           | 12.4 | 0.95 |

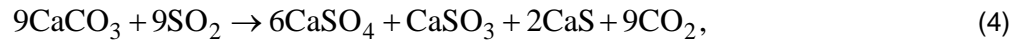
These results are confirmed by the method of Z.A. Nosova [20] who used different sample sizes: 50×50×8 mm and 50×50×15 mm. The results are shown in Table 10.

**Table 10. Determination of the clay sensitivity coefficient for drying.**

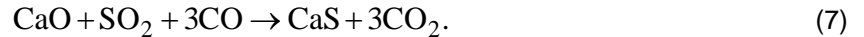
| No.     | Moist. sample |           |                         | Dried sample |           |                         | $K_s$ | Sample size, mm |
|---------|---------------|-----------|-------------------------|--------------|-----------|-------------------------|-------|-----------------|
|         | $L_o$ , cm    | $M_o$ , g | $V_o$ , cm <sup>3</sup> | $L_I$ , cm   | $M_I$ , g | $V_I$ , cm <sup>3</sup> |       |                 |
| 1       | –             | 51.47     | 24.93                   | –            | 43.30     | 22.45                   | 0.51  | 50×50×15        |
| 2       | –             | 46.94     | 22.93                   | –            | 39.76     | 20.86                   | 0.57  |                 |
| 3       | 5             | 58.61     | 28.52                   | 4.70         | 49.42     | 25.38                   | 0.51  | 50×50×8         |
| 4       | 5             | 50.37     | 25.7                    | 4.67         | 42.80     | 25.06                   |       |                 |
| Average |               | 54.49     | 27.11                   |              | 46.11     | 24.07                   | 0.51  |                 |

### 2.3. Clay Firing Properties

The thermal properties of clay rocks which included refractory materials and fire shrinkage were studied according to the requirements of State Standard of Russia GOST 21216.11-93 [21]. During the fire, the raw clay materials are burned to form the calcium sulfate ( $\text{CaSO}_4$ ) in complex reactions as shown in equations below [22, 23]:



Equation 6 can be changed if insufficient oxygen is provided as follows:



Pyrometric cone samples (sometimes called pyroscope) made from a clay paste with normal molding moisture were prepared. The refractoriness was estimated via the firing temperature at which the pyroscope started softening. The fire shrinkage was determined at 900–1250 °C for 67×30×15 mm tile samples according to the formula:

$$U = 100 * (l_o - l_1) / l_o, \quad (8)$$

where  $l_o$  and  $l_1$  represent the length of the sample before and after firing in mm as shown in Table 11. The same formula was used to calculate the air shrinkage at 105–110 °C where  $l_o$  and  $l_1$  represent the length of the sample before and after drying.

**Table 11. Determination of fire shrinkage.**

| No.                       | The distance between the sample marks, mm |      |       | Air shrinkage, % | Fire shrinkage, % |
|---------------------------|---|------|-------|------------------|-------------------|
|                           | Freshly molded                            | Dry  | Fired |                  |                   |
| Firing temperature 1000°C |   |      |       |                  |                   |
| 1                         | 18.5                                      | 18.2 | 18.2  | 1.6              | 0.0               |
| 2                         | 19.3                                      | 19.2 | 18.9  | 0.5              | 1.6               |
| 3                         | 18.8                                      | 18.7 | 18.6  | 0.5              | 0.5               |
| Firing temperature 1200°C |   |      |       |                  |                   |
| 1                         | 29.1                                      | 28.9 | 28.7  | 0.7              | 0.7               |
| 2                         | 27.4                                      | 27   | 26.5  | 1.4              | 1.9               |
| 3                         | 32.8                                      | 31.9 | 31.9  | 2.7              | 0.0               |
| 4                         | 31  | 30.2 | 30.1  | 2.8              | 0.3               |

We determined the degree of sintering which represented the value of the water absorption of burnt pottery. We used using tile samples with dimension of 60×30×10 mm prepared from paste with normal moisture, then dried at 105–110 °C and fired in an oven at three to four temperatures, taking into account that the temperature of each subsequent firing was 50 °C higher than the previous one. The results are shown in Table 12.

**Table 12. Determination of the clay sintering temperature.**

| No. | Temperature, °C | The weight of sample, g |                 | Water absorption, % |         | Average density, g/cm <sup>3</sup> |
|-----|-----------------|-------------------------|-----------------|---------------------|---------|------------------------------------|
|     |                 | Fired                   | Water saturated | Individual          | Average |                                    |
| 1   | 1140            | 44.13                   | 49.12           | 11.13               | 11      | 1.95                               |
| 2   |                 | 43.85                   | 48.62           | 10.9                |         | 1.89                               |
| 3   |                 | 41.52                   | 46              | 10.8                |         | 1.96                               |
| 4   | 1220            | 43.18                   | 41.1            | 4.8                 | 4.4     | 1.97                               |
| 5   |                 | 44.23                   | 42.24           | 4.5                 |         | 1.99                               |
| 6   |                 | 45.1                    | 43.34           | 3.9                 |         | 1.95                               |

Bloating, i.e. an increase of the volume of samples during high-temperature firing, was evaluated by the average density of the samples before and after firing.

**Table 13. Determination of clay bloating coefficient.**

| No. | Sample volume, cm <sup>3</sup> |              | K bl. | Weight, g     |              | Volume, cm <sup>3</sup> |              | Loss on ignition % | K bl. |
|-----|--------------------------------|--------------|-------|---------------|--------------|-------------------------|--------------|--------------------|-------|
|     | Before firing                  | After firing |       | Before firing | After firing | Before firing           | After firing |                    |       |
| 1   | 22.25                          | 22.4         | 1.01  | 4.73          | 4.54         | 2.05                    | 1.96         | 4.4                | 1.01  |
| 2   | 25.10                          | 26.26        | 1.05  | 4.75          | 4.3          | 2.01                    | 1.95         | 4.1                | 0.99  |
| 3   | 24.00                          | 25.32        | 1.06  | 4.24          | 4.0          | 2.0                     | 1.89         | 3.6                | 1.02  |

Cylinder samples with a diameter of 13, 30 and 50 mm were used to evaluate the ability of burnt ceramic materials to resist the destructive action of internal stresses arising under the influence of external forces. The average density and porosity were also determined on 67×3×15 mm samples. The amount of water absorption was also obtained for each sample which should be no less than 8 %. The result of the post-fired physic-mechanical properties of the fired samples was also obtained.

**Table 14. Physical and mechanical properties of fired ceramics.**

| Sample Area, cm <sup>2</sup> | Load of press, kg | Rcom, kgf/cm <sup>2</sup> | Average density, g/cm <sup>3</sup> | Porosity, % |            |        | Water absorption % | LOI % |
|------------------------------|-------------------|---------------------------|------------------------------------|-------------|------------|--------|--------------------|-------|
|                              |                   |                           |                                    | True        | Accessible | Sealed |                    |       |
| 1.33                         | 200               | 150                       | 1.89                               |             |            |        |                    |       |
|                              | 260               | 195                       | 1.89                               |             |            |        |                    |       |
|                              | 300               | 225                       | 1.95                               |             |            |        |                    |       |
| 7.07                         | 920               | 130                       | 1.89                               | 28          | 11.3       | 6.6    | 11.3               | 4.4   |
|                              | 950               | 134                       | 1.95                               | 26          | 19.6       | 5.4    | 10.8               | 3.9   |
|                              | 1000              | 141                       | 1.96                               | 25          | 11.4       | 13.6   | 10.9               | 3.6   |
| 19.625                       | 4400              | 224                       | 1.95                               |             |            |        |                    |       |
|                              | 3945              | 201                       | 1.9                                |             |            |        |                    |       |
|                              | 3830              | 195                       | 1.89                               |             |            |        |                    |       |

### 3. Results and Discussions

#### 3.1. Macroscopic Results

The color of clay in the dry case is light yellow and in the wet case is dark yellow and its texture is formed as lumpy, dense, messy and disoriented. The clay grains are located without any noticeable orientation and they have different sizes: from dusty to several centimeters. The viscosity of clay is weak in the wet case so that the clay rocks and clay pieces are easily crumbled when pressed on with fingers; in the dry case, they are firmly dense and adhering grains. In addition, we think that it is worth noting the presence of impurities and inclusions observed under the microscope:

- Light gray granular porous inclusions of both fine-dispersed and coarse-dispersed carbonates;
- Rounded, colorless grains of quartz, in the vast majority up to 0.05 mm in size;
- Dark-colored grains of pyrite up to 0.1 mm in size.

#### 3.2. Compared with Ukraine DSTU BV Standard

The properties of the investigated clay rocks were compared with State Standards of Ukraine DSTU BV 2.7-60-97. The results proved that these rocks are suitable for production of ceramic bricks by plastic and dry methods.

In the dry places in the quarry on the sharp corners of the large dry pieces, white efflorescence was visible signaling presence of salts [24]. The amount of silica in the clay rocks is inversely proportional to the strength of the resulting ceramic, as the amount of silica determines the amount of sand fractures present in the clay rocks, which cause an increase in the porosity that negatively affect the strength of the resulting ceramic. The high content of alumina requires a high firing temperature, and a low content reduces the strength of the products and lengthens the preparation time of the paste. Iron oxides reduce the temperature range of clay sintering, give color to the products from light cream to cherry-red. Calcium and magnesium oxides make firing difficult, lowering the melting point, increase porosity, and reduce the strength of the

ceramics [25]. The alkaline components,  $K_2O$  and  $Na_2O$ , lower the melting point, condense and increase the strength of the ceramics.

The swelling index (3–6.7) is very weak which means that the water holding capacity is low, and according to the standard documents, this allows us to classify the studied clays as “kaolinite-hydromicaceous” that is the average content of clay particles is 3.0–6.7 %, i.e. less than 15 %. In addition, with regard to the dust, the percentage is 20–33 %, i.e. almost up to 30 %; therefore, the studied clay rocks belong to the “coarse” group. In addition, with regard to the content of sand fractions:  $100 \% - (6.6 + 20.4) = 73 \%$ , the research data on the granulometric composition of clay rocks indicate that clay rocks belong to the “dusty sandy loam” group [26].

The number of the coarse inclusions larger than 0.5 mm is 0.15–0.71 %, which is less than 1 % according to the standard requirements, therefore the clays under study were assigned to the group “with low content of inclusions” and “with small inclusions” as shown in Table 4 above. The type of predominant inclusions when examined under an MPB-2 microscope and exposed to 1% HCl solution, showed presence (more than 50 %) of calcite, dolomite and similar substances. In addition, according to our data, the carbonate inclusions were 0.15–0.53 % corresponding to the group of clay rocks “with carbonate inclusions”. Molding moisture means the amount of water needed to make the clay paste, that exhibits its forming and plastic properties, keeping its shape without deformation and does not stick to the arms and metal of the equipment when rolling in order to give the ceramic mass a normal working consistency [27]. To control the normal molding moisture of the clay paste, a “Vika device” TMM-2450A was used as given in Table 5.

In this research, the sensitivity coefficient of the tested clay rocks  $K_s$  is in the range 0.82–0.97 as shown in Table 9, which is less than the value recommended by the standard documents. Thus, these clays belong to the “insensitive to drying” group as well as the tested samples in Table 10 because the obtained coefficient of clay sensitivity to drying  $K_s$  was within “0.51–0.57” [28]. The sensitivity coefficient of clay to drying becomes higher if the dust content is greater. With regard to plasticity, when the plasticity index fluctuates within 8–16, this means that the clay rocks belong to the “moderately plastic” group [29, 30].

### 3.3. Electrochemical Interactions

From the studied pre-firing properties of clay rocks, it is worth paying attention to their chemical composition. The properties of clay rocks are determined by the degree of particles dispersion and their energy [31]. Hence, the degree of particles dispersion and the energy consumption of clay oxides was calculated according to Putz et al.[32] as shown in Table 15.

**Table 15. The electric charge of clay oxides.**

| Oxides           |            | The value of atomic charges in each oxide, eV |              | The value of the effective charges of oxides, $\pm q$ , eV |
|------------------|------------|---|--------------|--|
| Type             | Amount, %  | Positive, +q                                  | Negative, -q |  |
| $SO_3$           | $\leq 1$   | 5.2   | 12.9         | -7.7   |
| $Al_2O_3$        | 7 – 23     | 6.8   | 12.9         | -6.1   |
| $SiO_2$          | 53 – 81    | 4   | 8.6          | -4.6   |
| $Fe_2O_3$        | 1,5 – 4    | 8.6   | 12.9         | -4.3   |
| MgO              | 0.5 – 2    | 2.8   | 4.3          | -1.5   |
| CaO              | 0.7 – 14   | 2.8   | 4.3          | -1.5   |
| $Na_2O$          | $\leq 4.5$ | 4.4   | 4.3          | +0.1   |
| $K_2O$           |            | 4.4   | 4.3          | +0.1   |
| FeO              | 1 – 4      | 4.3   | 4.3          | 0  |
| Total charge, eV |            | +43.5   | -68.8        |  |

The majority of oxides are characterized by the presence of excessive negative charges. Therefore, it should be equalizing for each other due to the greater quantity of similar charges, which may lead to greater repulsion. Up to 4.5 % of positively charged alkaline oxides  $Na_2O$  and  $K_2O$  will be neutralized by reacting with negatively charged and electrically neutral 4 % FeO, which can react with charges of any sign and create a solid. However, the problem is only that there are over 1.6 times more negatively charged oxides compared with similar positive charges. Moreover, the synthesis of positively charged atoms with negatively charged atoms gives the electronic structure of “the brick” as a future constructive product. The building materials with equal amounts of different positive and negative signs are always electronically stable, which gives them durability. Therefore, the result with respect to the studied clay rock as a raw



material for the production of bricks, which contains about 40 % of the excess electrical charge of negative atoms:

- First: instead of synthesis, these atoms will push each other off.
- Second: the brick system will be unstable and could reduce the durability because it may react with positively charged atoms during the operation.

Therefore, to obtain high-quality brick in these studies, at this stage, there is a need for refinement of clay rock to eliminate this problem. There are recommendations to pay attention to the energetic aspect of the firing process and the energy of the atomic composition of bricks. It is necessary to take into account the natural essence of clay rock as it consists of atoms, and the natural essence of atoms is the electrical composition and electronic structure: a positively charged nucleus and negatively charged electrons. The moving force is the charge of electric atoms as indivisible particles since the adhesive force of these atoms with others creates new materials with an electromagnetic field (chemical bond) as electrochemistry provides unlimited possibilities in creating new materials [33, 34]. It also can be said that the atoms are primordial by nature but the molecules and minerals of clay rocks and additives sometimes are not accurate because there are certain interventions by a researcher and a human.

It is known that a positive nuclear charge determines all the properties of an atom as they depend mainly on the number of negatively charged electrons and on the number of their orbitals around the nucleus. In this case, the chemical properties of atoms are strongly determined by the number of electrons in the outer electron layer and on the distance between the nucleus and the outer layer (orbital quantum number of the electron). In the outer electron layers, the farther the electron's orbital from the nucleus, the weaker its association with the nucleus.

With regard to the science of building materials, we can distinguish electrons of s-, p- and d- molecular orbitals. Since the electrons are in essence the material itself, so the respective materials are also called: s- p- and d- substances. The greatest bonding force of the nucleus is with s-substance while the smallest is with d-substance [35, 36]. These forces do not only affect the properties of the produced brick but also determine the firing mode. Thus, it is known that with increasing temperature the interatomic chemical bonds become longer and lose their bond strength. However, as the d-bonds are basically also weak in nature, they will break at a low firing temperature and transfer to the liquid phase faster, which is economically advantageous. The properties of clay soils are determined by electric forces (charges), whereas the main substances of clay rock are: s-elements (H, K, Na, Mg, Ca, Be), p-elements (Cl, N, B, O, F, Al, Si, C, P, S) and d-elements (Fe, Cr, Cu). It is only possible to obtain a building material with desired properties, if the energy properties of the feedstock are taken into account [37]. The calculations shown in Table 16 are for the quantitative content of s-, p- and d-substances in the studied clay sample.

**Table 16. The degree of charge by the removal electronic orbit from the atomic nucleus.**

| Oxides                         |           | The number and type of orbital substances of oxide atoms |             |             |
|--------------------------------|-----------|--|-------------|-------------|
| Type                           | Amount, % | S-substance  | P-substance | D-substance |
| SO <sub>3</sub>                | 1         | -  | 4           | -           |
| Al <sub>2</sub> O <sub>3</sub> | 15        | -  | 5           | -           |
| SiO <sub>2</sub>               | 67        | -  | 3           | -           |
| Fe <sub>2</sub> O <sub>3</sub> | 5         | -  | 3           | 2           |
| MgO                            | 1         | 1  | 1           | -           |
| CaO                            | 7         | 1  | 1           | -           |
| Na <sub>2</sub> O              | 4         | 2  | 1           | -           |
| K <sub>2</sub> O               | 4         | 2  | 1           | -           |
| FeO                            | 3         | -  | 1           | 1           |
|                                |           | 6  | 20          | 3           |
| Total types of substances %    |           | 21   | 69          | 10          |

According to the above results, there is an extremely low 10 % d-substance; therefore, further studies should be conducted to illustrate the effect of this reduction on the maximum temperature and duration of firing during production process of ceramics bricks [38, 39].

## 4. Conclusion

1. Assessment of the properties of clay rocks by their chemical composition meets the requirements of regulatory documents. They are suitable for the production of ceramic bricks by plastic and dry methods.

2. The results of electrochemical interactions indicated that the chemical composition of the studied clay rocks contained 1.6 times more negatively charged atoms as compared to positively charged ones. To modify the composition, it is suggested to insert feedstock or additives containing 2.3 times more positively charged atoms with the selection based on the structure of s-, p- and d-electrons to achieve more stable and durable brick structure.

In the future, it is necessary to study the thermodynamic characteristics of clay rocks consisting of electrically charged atoms, and the possibility of refinement of the feedstock in order to reduce the maximum temperature and duration of firing.

## References

1. Aghayev, T., Küçükuysal, C. Ceramic properties of Uşak clay in comparison with Ukrainian clay. *Clay Minerals*. 2018. 53(4). Pp. 549–562.
2. Mussa, M.H., Abdulhadi, A.M., Abbood, I.S., Mutalib, A.A., Yaseen, Z.M. Late age dynamic strength of high-volume fly ash concrete with nano-silica and polypropylene fibres. *Crystals*. 2020. 10(4). Pp. 243.
3. Sutakova, E., Mestnikov, A. Basics of recreation of ancient ceramics production technology in MATEC Web of Conferences. 2018. Pp. 02001.
4. Mussa, M.H., Mutalib, A.A., Hamid, R., Naidu, S.R., Radzi, N.A.M., Abedini, M. Assessment of damage to an underground box tunnel by a surface explosion. *Tunnelling and Underground Space Technology*. 2017. 66. Pp. 64–76.
5. Christidis, G., Dunham, A. Compositional variations in smectites: Part I. Alteration of intermediate volcanic rocks. A case study from Milos Island, Greece. *Clay Minerals*. 1993. 28(2). Pp. 255–273.
6. Kulovaná, T., Vejmelková, E., Pokorný, J., Siddique, J.A., Keppert, M., Rovnaníková, P., Ondráček, M., Keršner, Z., Černý, R. Engineering properties of composite materials containing waste ceramic dust from advanced hollow brick production as a partial replacement of Portland cement. *Journal of Building Physics*. 2016. 40(1). Pp. 17–34.
7. Kucherenko, A., Ahmed, A.-H. About mineral genetic engineering elements in lime slaking process. *Journal of Technical University of Moldova and Moldavian Engineering Association*. 2015. 21(2). Pp. 64–66.
8. Mussa, M.H., Mutalib, A.A., Hamid, R., Raman, S.N. Blast damage assessment of symmetrical box-shaped underground tunnel according to peak particle velocity (PPV) and single degree of freedom (SDOF) criteria. *Symmetry*. 2018. 10(5). Pp. 158.
9. Mutalib, A.A., Mussa, M.H., Hao, H. Effect of CFRP strengthening properties with anchoring systems on PI diagrams of RC panels under blast loads. *Construction and Building Materials*. 2019. 200. Pp. 648–663.
10. Stryzewska, T., Kaňka, S. The effects of salt crystallization in ceramic bricks in terms of line deformations. *Procedia Engineering*. 2017. 193. Pp. 120–127.
11. Kouonang, S.T., Wouatong, A., Nemaleu, J.D., Yerima, K., Njopwouo, D. Assessment of Ceramic Properties of Fired Clayey Brick Materials from Bamessing in North-West Cameroon (Central Africa). *InterCeram-International Ceramic Review*. 2016. 65(3). Pp. 87–95.
12. Brewer, R. Fabric and mineral analysis of soils. *Soil Science*. 1965. 100(1). Pp. 73.
13. Mutalib, A.A., Mussa, M.H., Taib, M.A. Behaviour of prestressed box beam strengthened with CFRP under effect of strand snapping. *GRADEVINAR*. 2020. 72(2). Pp. 103–113.
14. Saadun, A., Mutalib, A.A., Hamid, R., Mussa, M.H. Behaviour of polypropylene fiber reinforced concrete under dynamic impact load. *Journal of Engineering Science and Technology*. 2016. 11(5). Pp. 684–693.
15. Ion, R.M., Fierăscu, R.C., Teodorescu, S., Fierăscu, I., Bunghez, I.R., Țurcanu-Caruțu, D., Ion, M.L. Ceramic Materials Based on Clay Minerals in Cultural Heritage Study. *Clays, Clay Minerals and Ceramic Materials Based on Clay Minerals*. 2016. Pp. 159–184.
16. State Standards of Ukraine DSTU B V.2-7-60-97. Clay raw materials for the production of ceramic building materials. 1997.
17. Government Standard of Russia GOST 21-2116.1-81. Clay raw materials: Methods for determining plasticity. 1981.
18. Industry standard of Russia OST 21-78-88. Clay raw materials for the production of ceramic bricks and stones. Technical requirements. Test method p. 59 1988.
19. Eralievna, K.J., Myrzakhankyzy, S.M. Investigation of the properties of clay of Kulantobinsky (almaty region) and Soyuznoe (Aktyubinsk region) deposits in their fitness for the production of wall ceramics. *Nauka i obrazovaniye segodnya*. 2017(5 (16)).
20. Nosova, Z. Sensitivity of clays to drying. BT1, MPSM, RSFSR. 1946.
21. Government Standard of Russia GOST 21216.11-93. Clay raw material. Method for determining the refractoriness of low-melting clays. 1993.
22. Akinshipe, O., Kornelius, G. Chemical and thermodynamic processes in clay brick firing technologies and associated atmospheric emissions metrics-a review. *Journal of Pollution Effects & Control*. 2017. 5(2).
23. Abdulhadi, A.H.A.M. Effects water solution of active agents on the modified lime binding. *Journal of Engineering Science and Technology*. 2020. 15(2). Pp. 1046–1055.
24. Aguilar-Penagos, A., Gómez-Soberón, J.M., Rojas-Valencia, M.N. Physicochemical, mineralogical and microscopic evaluation of sustainable bricks manufactured with construction wastes. *Applied Sciences*. 2017. 7(10). Pp. 1012.
25. Nascimento, J.J.d.S., Belo, F., de Lima, A.G.B. Experimental drying of ceramics bricks including shrinkage in Defect and Diffusion Forum. 2015. Pp. 106–111.
26. Kusiorowski, R. MgO-ZrO<sub>2</sub> refractory ceramics based on recycled magnesia-carbon bricks. *Construction and Building Materials*. 2020. 231. Pp. 117084.
27. Muliawan, J., Astutiningsih, S. Preparation and characterization of phosphate-sludge kaolin mixture for ceramics bricks. *International Journal of Technology*. 2018. 9(2). Pp. 317–324.
28. Tkachev, A., Kozyarskii, A.Y., Tkacheva, O. Optimization of brick mixture formula based on drying properties. *Glass and Ceramics*. 1999. 56(7-8). Pp. 266–267.

29. Saboya, Jr.F., Xavier, G., Alexandre, J. The use of the powder marble by-product to enhance the properties of brick ceramic. *Construction and Building Materials*. 2007. 21(10). Pp. 1950–1960.
30. Mussa, M.H., Mutalib, A.A., Hao, H. Numerical formulation of PI diagrams for blast damage prediction and safety assessment of RC panels. *Structural Engineering and Mechanics*. 2020. 75(5). Pp. 607–620.
31. Belarbi, A., Zadjiaoui, A., Bekkouche, A. Dispersive clay: influence of physical and chemical properties on dispersion degree. *EJGE*. 2013. 18. Pp. 1727–1738.
32. Putz, M.V., Cimpoesu, F., Ferbinteanu, M. *Structural Chemistry: Principles, Methods, and Case Studies*. 2018: Springer.
33. Morales, J., Goguitchaichvili, A., Aguilar-Reyes, B., Pineda-Duran, M., Camps, P., Carvallo, C., Calvo-Rathert, M. Are ceramics and bricks reliable absolute geomagnetic intensity carriers? *Physics of the Earth and Planetary Interiors*. 2011. 187(3-4). Pp. 310–321.
34. Mussa, M.H., Mutalib, A.A., Hamid, R., Raman, S.N. Advanced dynamic response analysis of under-ground tunnel affected by blast ground distance in The 5<sup>th</sup> International Technical Conference (ITC). Malaysia, 2020. Pp. 37–45.
35. Tong, C. *Fundamentals of Materials and Their Characterization Methodologies for Energy Systems*, in *Introduction to Materials for Advanced Energy Systems*. 2019, Springer. Pp. 87–170.
36. Mussa, M.H., Mutalib, A.A. Effect of geometric parameters ( $\beta$  and  $\tau$ ) on behaviour of cold formed stainless steel tubular X-joints. *International Journal of Steel Structures*. 2018. 18(3). Pp. 821–830.
37. Benlalla, A., Elmoussaouiti, M., Dahhou, M., Assafi, M. Utilization of water treatment plant sludge in structural ceramics bricks. *Applied Clay Science*. 2015. 118. Pp. 171–177.
38. Mutalib, A.A., Mussa, M.H., Abdulghafoor, A.M. Finite element analysis of composite plate girders with a corrugated web. *Journal of Engineering Science and Technology*. 2018. 13(9). Pp. 2978–2994.
39. Mutalib, A.A., Mussa, M.H., Abusal, K.M. Numerical evaluation of concrete filled stainless steel tube for short columns subjected to axial compression load. *Jurnal Teknologi*. 2018. 80(2).

**Information about authors:**

**Ahmed Abdulhadi, PhD**

ORCID: <https://orcid.org/0000-0002-1794-867X>

E-mail: [ahmedmouse@uowa.edu.iq](mailto:ahmedmouse@uowa.edu.iq)

**Mohamed Mussa, PhD,**

ORCID: <https://orcid.org/0000-0003-4745-7916>

E-mail: [dr.mhmussa@uowa.edu.iq](mailto:dr.mhmussa@uowa.edu.iq)

**Yasir Kadhim,**

E-mail: [yasirneamah@gmail.com](mailto:yasirneamah@gmail.com)

*Received 27.07.2020. Approved after reviewing 11.05.2021. Accepted 14.05.2021.*



Research article

UDC 69.04

DOI: 10.34910/MCE.111.5

## Flexural behavior of partially composite concrete-encased steel tubular beams

N. Wehbi ✉, A. Masri, O. Baalbaki

Beirut Arab University, Beirut, Lebanon

✉ [n.wehbi@bau.edu.lb](mailto:n.wehbi@bau.edu.lb)

**Keywords:** flexural behavior, composite beams, concrete-encased steel tubular beams, polypropylene fiber, joists

**Abstract.** Composite steel-concrete construction has been widely implemented in high-rise buildings and bridges having long spans due to its favorable characteristics inherited from both materials acting as one unit. The main objective of this research is to propose a new beam system having a high strength-weight ratio, and to replace the shear studs used in composite beams by steel mesh wraps around the steel tube without any flexural or shear reinforcements. This new structural beam can be part of a lightweight-precast floor system with fast and easy ducting through its hollow tubular part. Four simply supported T-shaped beams of 3 m length are investigated experimentally to study and compare their flexural behavior. All beams are tested under two points quasi-static point loading. A comparison was initially performed between a control T-shaped reinforced concrete (RC) beam and a fully encased steel tube in a T-shaped RC beam of the same section dimensions as the control beam and without any mesh wrapping. The effect of full and partial wrapping of the steel tube was also investigated in the other two beams where 100 % and 60 % of the encased steel tube length were wrapped by a 3 mm steel mesh. Discussions and interpretation of the load-deflection behaviors and the failure modes are presented in this paper. The obtained results showed that the composite beam with unwrapped encased steel tubular section provided an advantage over the control RC beam in terms of load/weight ratio and ductility by 28.5 % and 22.4 % respectively. Besides, the use of steel mesh wraps in different length percentages revealed a much better partial composite action between the steel tube and the surrounding concrete. The attained strength ranged between 18.2 % and 33 %, whereas the ductility was enhanced by 63.8 % and up to 66.7 %.

### 1. Introduction

Composite construction is known in the context of civil engineering structures as the use of steel and concrete to build a single unit that exhibits better characteristics than having members made from either steel or concrete alone. Nowadays, composite construction is widely used to achieve a higher level of performance and more ductility as compared to the case of having two materials functioning separately, especially in the cases of long spans and high rise buildings [1–3]. Although a perspective approach was previously utilized in the form of codes that introduced certain limitations for the design and construction of composite structures, the guidelines provided by codes are applicable for standard shapes of composite sections. This paved the way for various researches in the domain of composite construction to investigate the composite behavior of new sections over the past years.

For instant, the American Institute for Steel Construction (AISC) [4] specifications covered two types of composite sections. The first type is related to composite beams fully encased in concrete in which the composite action depends on the natural bond between steel and concrete. The other type is related to

Wehbi, N., Masri, A., Baalbaki, O. Flexural behavior of partially composite concrete-encased steel tubular beams. Magazine of Civil Engineering. 2022. 111(3). Article No. 11105. DOI: 10.34910/MCE.111.5

© Wehbi, N., Masri, A., Baalbaki, O., 2022. Published by Peter the Great St. Petersburg Polytechnic University.



This article is licensed under a CC BY-NC 4.0

composite sections in which the steel section is attached to concrete slab by mean of shear studs. However, there has been always a need for further research on composite members due to the limited guidelines provided by codes and specifications regarding new parameters or sections of interest.

Yong Liu [5] investigated the use of new type of shear connectors, alternative to the widely used studs, made from steel angles welded either to the top flanges or the web of a U-shaped steel girder infilled with concrete. All of the tested specimens were made from same span length, girder dimension, slab thickness, and steel angles. It was concluded that the installation of angles at the flange level provides full composite behavior with better ductile manner and shear transfer capacity. Also, Weng et al [6] handled the splitting shear failure in encased beams. It was concluded that the ratio of the steel flange width to that of concrete width should be less than 0.67 to avoid splitting shear failure- otherwise, shear connectors should be used.

Besides, recent studies have focused on studying static and dynamic behavior of new types of composite beams. Recently, the use of concrete filled steel tubular (CFST) beams has become increasingly studied and implemented in high rise buildings and bridges [7–11].

Furthermore, the usage of concrete encased steel tubes (CEST) is significantly increased in the building industry and especially for the case of high rise buildings accounting for advantages of ductility and high tensile strength afforded by steel, as well as, stiffness and fire resistance of concrete. One of the recent studies on CEST is done by Mohammad M. El Basha [12] to explore its flexural behavior experimentally and analytically. The main purpose of this study was to prove the possibility of having a 20 % reduction in the depth of the CEST composite section, compared to conventional reinforced concrete (RC) beam, without influencing the overall stiffness and flexural capacity. So, nine beams of 6-meter span lengths with the same reinforcement and number of shear connectors, were studied under the influence of different tube dimensions and lengths. It was found that the CEST sections had 40 % to 70 % improvement in ultimate flexural strength (directly proportional to tube depth), enhanced ductility, and increased elastic deformations compared to RC beams with the same depth and a 20 % higher depth.

In addition, Nasser H. Tuma [13] presented the flexural behavior of simply supported composite beams made from ultra-high performance reinforced concrete encasing steel tubular section. The studied parameters were related to the usage of shear connectors, location of steel tubular section, and longitudinal reinforcement ratio. It was concluded that the flexural capacity of composite beams, with hollow tubular section and shear studs, increased significantly compared to solid RC beams and non-composite beams (without shear studs). Also, the load capacity of composite beams having tubular section located in tension zone has slightly increased (only 4 %) compared to that located at the middle of the section.

Besides, a research domain in CEST beams that gained huge interest is related to the shear behavior and splitting strength of the composite section including the effect of shear reinforcement [14–18]. One research was carried by Neelima [19] who concluded that the absence of shear reinforcement in CEST beams results in markedly increase in the crack width with concrete crushing failure in diagonal tension.

Moreover, to ensure crack control, enhanced tensile strength, concrete toughness, and improved deformation when dealing with steel-concrete composite members, fibers must be used. One of the most widely used fibers is polypropylene fiber (PP fiber) due to being non-magnetic, free of rust, alkali resistant, and widely available with cheap price compared to other fiber types. Hence several studies were launched to investigate the effect of PP fiber on concrete workability [20], durability [21], and mechanical properties [22]. Many studies [23–25] have agreed that the recommended amount of PP fiber must be less than 1 % for best improvement in flexural strength at normal and elevated temperature.

In fact, all studies related to composite members aim to find methods to enhance the efficiency of different composite section shapes by studying several parameters. For example, [26] and [27] studied the effect of compressive strength on the flexural capacity of concrete filled steel tubular beams. Both concluded that the increase in concrete compressive strength has limited influence on the ultimate capacity of composite beams. On the other hand, [28] proved that concrete filling in hollow steel tubular beams of large scale is considered an effective method to enhance ductility and flexural performance of composite beams. Also, [29] handled a traditional method to ensure the composite action using shear studs and thus recommending that the significant enhancement in flexural capacity is maintained by positioning studs vertically on flanges.

In conclusion, the domain of composite structures has been always a source of interest to many researchers due to its complex behavior and interaction between different materials. However, the flexural behavior of composite beams made from CEST beams in the absence of any type of reinforcement and shear connectors, to satisfy the purpose of light weight- easy precast system, was not investigated yet. Therefore, the main objective of this research is to investigate the efficiency of 2 mm steel mesh wrapping around the steel tube in different locations to ensure satisfying composite action and ultimate load capacity

of the specimens of interest. Also, polypropylene fiber is used in the concrete mix to provide better ductility according to recommended percentage from literature ( $< 2\%$  of cement).

## 2. Methods

### 2.1. Test Specimens and Plan

The flexural capacity of three simply supported composite beams and RC control beam of 3 m length was studied under two-point bending.

The composite specimens were made up from steel tubular section denoted by ST235 JRH and having dimensions of 160x80x4 mm totally encased in concrete in the absence of any flexural and shear reinforcement as well as shear connectors. The difference among the three specimens depends on the degree of steel-concrete interaction provided by different percentages of beam length being wrapped by 3 mm steel mesh. These percentages vary from 0 % for the case of no mesh wrapping (Fig. 1(a)) till 60 % partial wrapping and 100 % full wrapping (Fig.1 (b)). However, all specimens have the same section dimensions and deck reinforcement.

In order to prove the advantage of the studied composite beams in terms of ductility and load carrying capacity, a comparison of composite beam deprived from steel mesh (ST1) was made with traditional RC beam. The later beam has a cross section dimensions similar to ST1 beam with exactly same reinforced concrete deck reinforcements as shown in Fig. 1(c). Also, the flexural and shear reinforcement were chosen to provide close load capacity to that of ST1 beam based on analytical calculations and numerical simulation. The aim of this specimen is to show the significance of the new composite section compared to widely used reinforced concrete section in terms of strength /weight ratio.

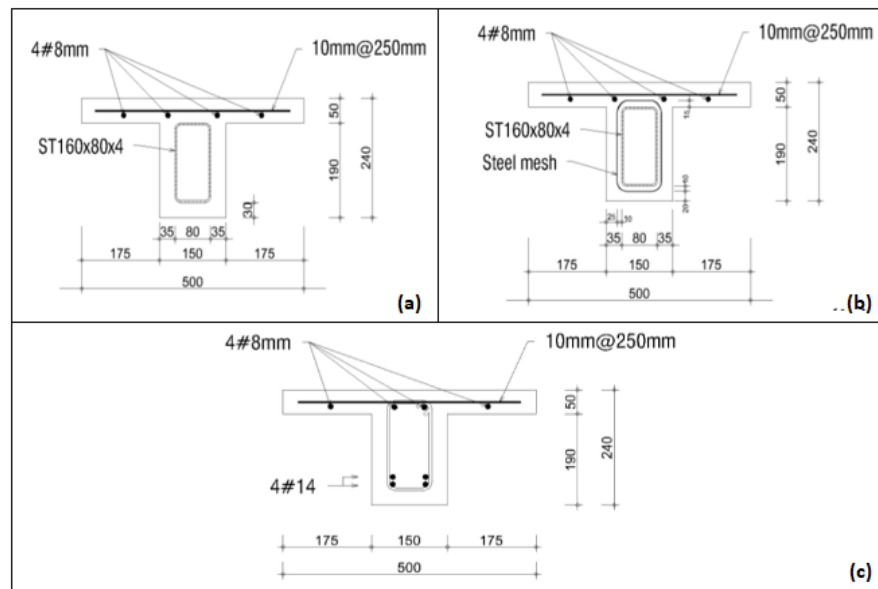


**Figure 1. Cross sections of composite beams and control RC beam (dimensions in mm).**

Table 1 summarizes the test plan followed in the experimental program to display the percentage of mesh wrapping in each specimen.

In addition, Fig. 2 displays the location of steel mesh wrapping along the beam length for different ST beams. As its shown, for the 60 % case of ST3 composite beam, the steel mesh was divided 45 % at the mid span and 15 % on each edge to study the influence of steel mesh at locations of high loading on the ductility and failure mode. However, for ST2 beam, full mesh wrapping was used along the entire steel tube length.

**Table 1. Test Plan.**

| Test Group   | Specimen | Length(mm) | Steel Section (mm) | Mesh (% of beam Length) | Deck Type |
|--------------|----------|------------|--------------------|-------------------------|-----------|
| Control Beam | RC       | 3000       | NA*                | NA                      | RC        |
|              | ST1      | 3000       | ST. 160x80x4       | 0%                      | RC        |
| ST Beams     | ST2      | 3000       | ST. 160x80x4       | 100%                    | RC        |
|              | ST3      | 3000       | ST. 160x80x4       | 60%                     | RC        |

\*NA stands for not applicable case.

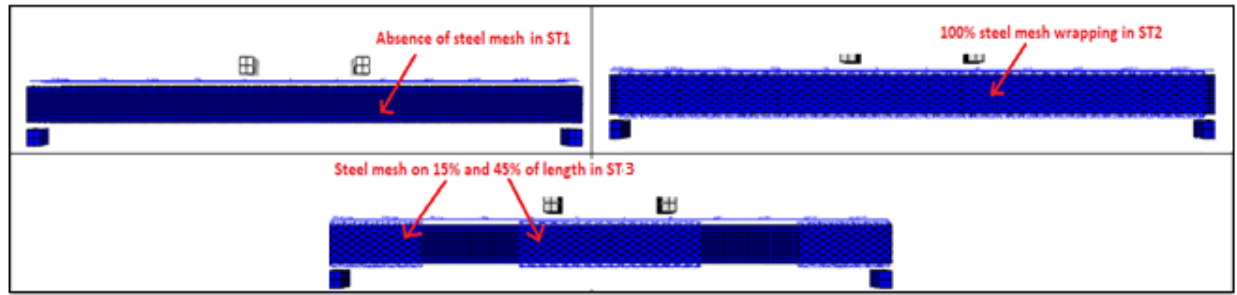


Figure 2. Steel mesh wrapping of different percentages in ST beams.

## 2.2. Material Properties

### 2.2.1. Structural Steel Tube

In this research, a steel bar of type S235JR was subjected to Coupon Tensile test at Beirut Arab University Construction Material Lab at a speed of 0.05 in-per minute till failure as shown in Fig. 3. The steel bar has the same grade of that of the steel tube used in this research. Fig. 4 (a) and (b) displays the fractured specimen at failure and stress-strain curve for the tested bar as obtained from the coupon test records. It can be noticed that the tested steel material shows good ductility based on its ability of resisting plastic deformations long before reaching its ultimate capacity. Also, the cup-cone failure ensures the ductility of the mild steel tested specimen. The obtained results of interest are summarized in Table 2.



Figure 3. Experimental setup for coupon tensile strength testing.

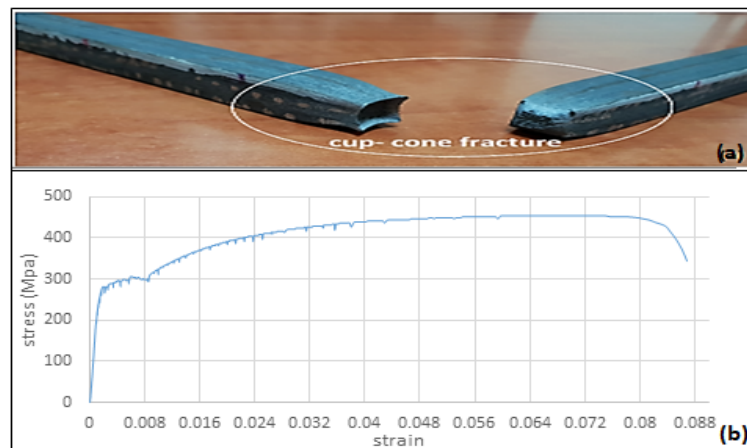


Figure 4. Coupon tensile test results: (a) fractured specimen; (b) stress-strain curve.

Table 2. Summarized results of coupon tensile test.

| Steel<br>S235JR<br>specimen | $F_y$ (Mpa) | $F_u$ (Mpa) | $E_s$ (Mpa) | Dimensions (cm) | $\Delta u$ (cm) | $\frac{\Delta u}{\Delta y}$ |
|-----------------------------|-------------|-------------|-------------|-----------------|-----------------|-----------------------------|
|                             | 280         | 453         | 198748      | 2x2x50.4        | 6.5             | 3.25                        |

where,  $F_y$ ,  $F_u$ ,  $E_s$ ,  $\Delta u$ , and  $\Delta y$  stand for yielding steel strength, ultimate steel strength, steel modulus of elasticity, ultimate deflection, and deflection at yielding strength respectively.



### 2.2.2. Concrete

Tables 3 and 4 summarize the aggregate properties and concrete mix proportions used in the experimental program. Cylinders of 15×30 dimensions were then taken according to ASTM C39 standards [30], cured for 28 days, and crushed at the day of testing. The average compressive strength was 24.2 Mpa.

**Table 3. Aggregates properties.**

| Aggregate Type   | Absorption(%) | Moisture (%) | Specific Gravity (g/cm <sup>3</sup> ) |
|------------------|---------------|--------------|---------------------------------------|
| Aggregate 9.5 mm | 1.79          | 0.76         | 2.47                                  |
| Natural Sand     | 1.6           | 2            | 2.68                                  |

**Table 4. Concrete mix proportions for W/C = 0.5.**

| Material                                | Corrected batch weight |
|---|------------------------|
| Cement (Kg/m <sup>3</sup> )             | 350                    |
| Water (l/m <sup>3</sup> )               | 180.8                  |
| 9.5 mm aggregate                        | 908                    |
| Natural sand (Kg/m <sup>3</sup> )       | 887                    |
| Sikament admixture (Kg/m <sup>3</sup> ) | 5.25                   |
| Fiber (Kg/m <sup>3</sup> )              | 2.1                    |

### 2.2.3. Steel Mesh

SSEM-04 expanded steel mesh of 3 mm thickness, shown in Fig. 5, was used in replacement of flexural rebar and shear studs to check its ability in providing good interaction with the surrounding concrete in the new composite system. In this research, the 3 mm mesh is cut in to pieces of 60 cm width each and wrapped around the steel tube with a clear cover of 1.5 cm at the top of steel flange.



**Figure 5. Steel mesh wrapping around the steel tube.**

### 2.3. Test Setup

The flexural behavior of composite beams was studied under two-point bending testing machine of Fig. 6 (a). The beam specimens were placed on two supports that were adjusted at 10 cm from the faces of the 3 m length beams. The specimens were positioned such as the web is centered over the supports while the loading pads are in contact with the reinforced concrete deck and being spaced 60 cm from each other as shown in Fig. 6(b).

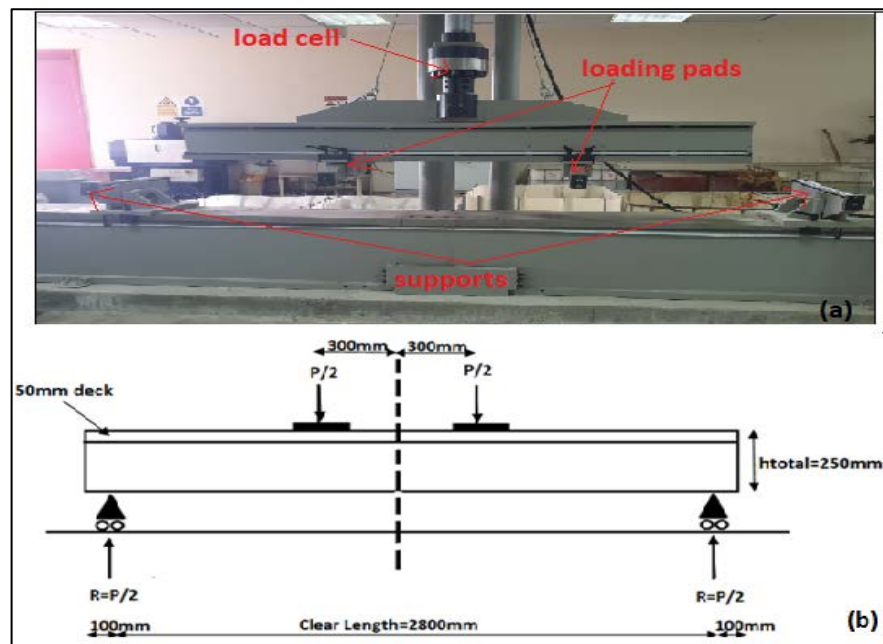


**Figure 6. Test setup: (a) testing machine; (b) test schematic representation.**

During the entire test, the deflection at the mid-span of the beam was recorded automatically at specific time increments using an external linear variable differential transducer (LVDT) connected to external data acquisition system as shown in Fig. 7. The rate of load increase was kept constant of 0.1 KN/sec and provided in a tabulated form by the data acquisition system connected to the testing machine as in Fig. 8.



**Figure 7. LVDT Installation.**



**Figure 8. Data acquisition system.**

### 3. Results and Discussion

#### 3.1. Advantage of Studied Composite Beams

Fig. 9 shows the advantage of using composite section made from tubular structural steel with the absence of any flexural or shear reinforcement over conventional reinforced concrete beams (control beam) of same dimensions based on experimental results. For instant, at early loading stages below 10 KN, both beams experience similar stiffness. Then by increasing the load and beginning of tensile concrete cracks formation and degradation of stiffness, the composite beam showed better stiffness and capacities till reaching the ultimate capacity. In fact, the usage of ST1 beam had provided 12.7 % enhancement in the ultimate strength and 22.4 % increase in the beam ductility. For instant, the ductility was defined as the difference between the deflection records at ultimate capacities of ST1 and control beams.

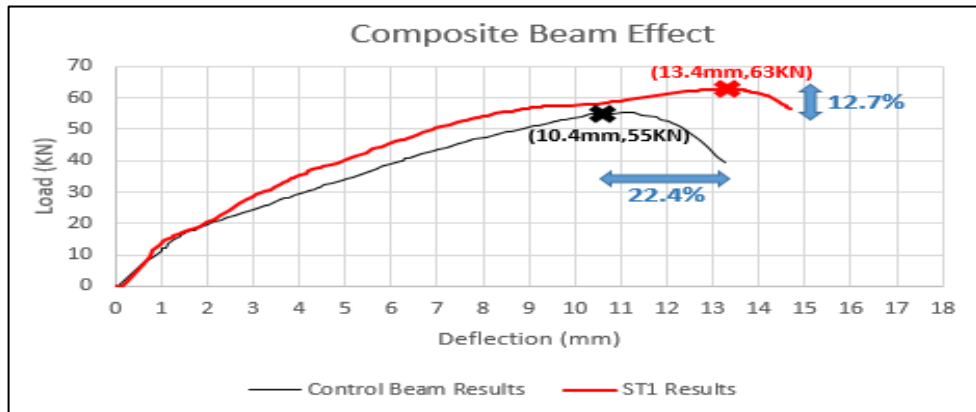


Figure 9. Comparison of load-deflection curves of control beam and ST1 composite beam.

In addition, by comparing the *load-weight* ratio of these two beams we found the ratio of RC beam is:  $\frac{55\text{KN}}{519.5\text{Kg}} = 0.1058$  and for SP1 beam :  $\frac{63\text{KN}}{424\text{Kg}} = 0.148$ . Based on these values, it was obtained that the usage of ST1 beam has modified the capacity to weight ratio by 28.5 % as well as providing easy passage of ducts, so our aim of checking the practical implementation of this section as part of long span precast floor system having high strength-weight ratio is achieved.

The obtained results gave a motivation to study the effect of using steel mesh of relatively low weight on enhancing the flexural behavior more.

#### 3.2. Effect of Steel Mesh on Strength and Ductility

As it can be noticed from Fig. 10, the usage of steel mesh wrapping around the structural steel section prior to casting plays an important role in enhancing the ultimate capacity of the composite beam as well as the corresponding ductility. For instant, at low loading values, all the composite beams that are made from steel tubular section or hollow pipe section, have same stiffness. However, by increasing the applied load, degradation in material stiffness was obvious from the reduction in slopes till reaching ultimate capacity at different deflection records.

Comparing the ultimate capacity of composite beams with steel wrapping versus ST1 beam (0 % mesh), we can see that the ultimate loading capacity has increased by increasing the length of mesh wrapped around the structural steel. This increase was significant in beam ST2 (32.98 %) and noticeable in ST3 beam (18.18 %).

Besides, the ductility has improved significantly by the usage of wrapped steel mesh. It increased by 63.78 %, and 66.71 % due to increasing the percentage of mesh used to 60 % and 100 % respectively.

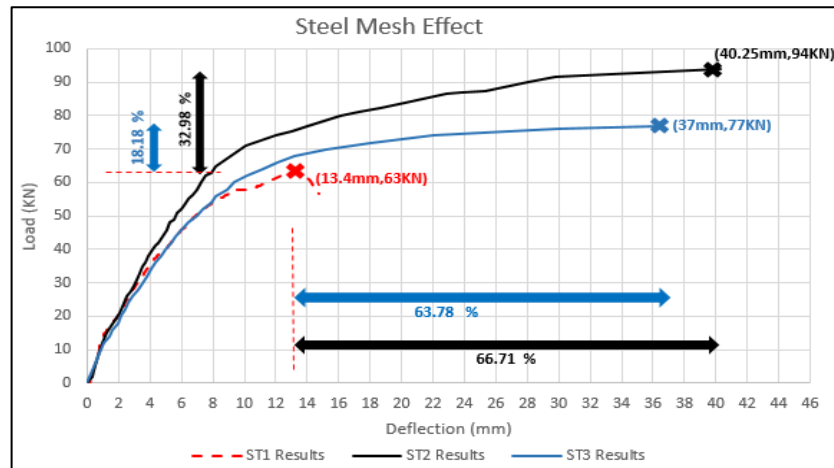


**Figure 10. Comparison of load-deflection curves of ST1, ST2, and ST3 composite beams.**

These results also display the advantage of steel mesh as one piece on the entire beam length by providing better bond, reducing relative deformation between beam parts, and thus enhancing the capacity and ductility. Also, composite beam ST3 of 60 % wrapping can be considered as optimized specimen since it has acceptable enhancement in ultimate capacity compared to ST1 case and very close ductility improvement to the case of full mesh wrapping in ST2 beam. In this comparison, the ductility was also defined as the difference between the deflection records at ultimate capacities of different mesh-wrapped composite beams relative to ST1 beam.

### 3.3. Effect of Steel Mesh on Failure Mode

Comparing the failure modes of composite beams made from steel tubular sections in Fig. 11, we can check the importance of steel mesh on the flexural behavior and ductility of the studied beams. In fact, the absence of steel mesh in Fig. 11 (a) has led to wide horizontal crack propagation till concrete spalling at the edges of the beam with some flexural cracks at mid-span as the applied load reached the ultimate capacity. On the other hand, Fig.11 (c) proves that the usage of steel mesh at the location of mid span and edges (ST4 beam) provided better ductility on the entire length of the beam due to generation of many fine flexural cracks at meshed zones and prevented spalling at the edges due to the presence of steel mesh. So, the failure in ST3 beam was due to widening of two tensile cracks in the unmeshed zone and their propagation below the deck. In addition, Fig. 11 (b) satisfies the advantage of steel mesh by providing best ductile behavior of cracks being distributed on the entire beam length and no spalling of concrete with a small slippage at the edges of the beam of 0.5 cm. Hence, the presence of wrapped steel mesh provided favorable ductile failure mode.

Based on the drawn analysis, the influence of steel mesh wrapped at the edges of the steel tube only or at the mid span needs further investigation to better understand the influence of steel mesh on each location separately.

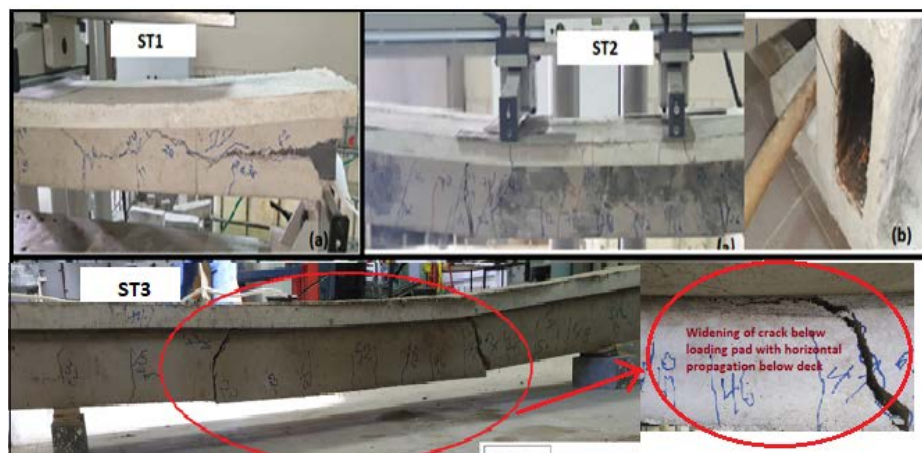


**Figure 11. Comparison of failure modes of ST1, ST2, and ST3 composite beams.**

### 3.4. Comparison to other Research

Since the experimental setup is applicable to a limited range of section dimensions and being working with relatively new section regarding the absence of any shear and longitudinal reinforcement with the

implementation of steel mesh wrapping to ensure steel-concrete interaction, there is no similar previous research to compare results to. However, steel mesh wrapping can be considered as an alternative efficient method to enhance the strength and ductility of composite beams as compared to previous parameters mentioned in the state of art.

#### 4. Conclusion

The flexural behavior of an innovative composite joist, made from steel tubular section totally encased in concrete in the absence of flexural reinforcement and shear connector, was experimentally studied using a two-point bending test. The following conclusions can be drawn:

1. The studied composite beam made from steel tubular section without mesh wrapping showed advantage over conventional RC beam of same dimensions in terms of enhanced strength/weight ratio and ductility by 28.5 % and 22.4 % respectively.
2. The studied composite beams can be used as part of light weight-high strength precast floor system as a replacement of higher weight reinforced concrete system of a close capacity.
3. As the percentage of beam length being covered with mesh increases, the ultimate capacity and ductility increases up to maximum values of 66.7 % and 32.98 %, respectively, for the case of full mesh wrapping versus no mesh in ST beams.
4. The fully wrapped composite beams experienced the best ductility and load capacity due to maintaining almost full bond between the steel tube and the surrounding concrete by using the steel mesh on full length. Thus preventing large relative slippage between all components and attaining excellent bonding.
5. The presence of steel mesh at the beam edges is critical for preventing the formation of horizontal cracks near the edges and concrete splitting.
6. Although full mesh wrapping in ST specimens provided best ductility and capacity results, yet the 60 % mesh wrapping can be considered as optimized section for designers by having a small difference in capacity and ductility compared to full mesh wrapped sections (15 % maximum difference).
7. The proposed composite beam can be used as part of precast floor system having advantage of high strength-weight ratio. It can be easily prefabricated and rapidly erected with the privilege of being economic by replacing the usually used shear studs with the light steel mesh.

#### References

1. Uy, B., Bradford, M.A., Liang, Q., Pi, Y. Ductility of profiled composite beams. Part I: experimental study. *Journal of Structural Engineering*. 1995. 121(5). Pp. 876–882.
2. Hajjar, F. Composite steel and concrete structural systems for seismic engineering. *Journal of Constructional Steel Research*. 2002. 58(5). Pp. 703–723.
3. Johnson, R. *Composite Structures of Steel and Concrete: Beams, Slabs, Columns, and Frames for Buildings*. Blackwell Pub, 2004.
4. AISC. *Specifications for Structural Steel Buildings*. American Institute of Steel Construction. Chicago, IL, 2010.
5. Liu, Y., Guo, L., Qu, B., Zhang, S. Experimental investigation on the flexural behavior of steel-concrete composite beams with u-shaped steel girders and angle connectors. *Engineering Structures* 2017. 31. Pp. 492–502.
6. Weng, C.C., Yen, S.I., Jiang, M.H. Experimental study on shear splitting failure of full –scale composite concrete encased steel beams. *Journal of Structural Engineering*. 2002. 128(9). Pp.1186–1194.
7. Fan, H., Li, Q.S., Tuan, A.Y., Xu, L. Seismic analysis of the world's tallest building. *Journal of Constructional Steel Research*. 2008. 65(5). Pp. 1206–1215. DOI: 10.1016/j.jcsr.2008.10.005
8. Fujikura, S., Bruneau, M. Dynamic analysis of multi hazard -resistant bridge piers having concrete-filled steel tube under blast loading. *Journal of Bridge Engineering*. 2012. 17(2). Pp. 249–258. DOI: 10.1061/(ASCE)BE.1943-5592.0000270
9. Mossahebi, N., Yakel, A., Azizinamini, A. Experimental investigation of a bridge girder made of steel tube filled with concrete. *Journal of Constructional Steel Research*. 2005. 61(3). Pp. 371–386.
10. Liew, R., Xiong, M., Xiong, D. Design of high strength concrete filled steel tube columns for tall buildings. *Building Structure*. 2015. 45(11). Pp. 37–42.
11. Han, L. *Concrete Filled Steel Tube Structure—Theory and Practice*. Science Press. China, 2007.
12. El Basha, M., Hassan, T., Mohammad, M., Elnawawy, O. Efficiency of hollow reinforced concrete encased steel tube composite beams. *International Journal of Civil Engineering and Technology (IJCIET)*. 2018. 9(3). Pp. 720–735.
13. Tuma, N., Aziz, M. Flexural strength estimation for composite UHPC- tubular steel beam. *Journal of Engineering Science and Technology*. 2020. 15(3). Pp. 1520–1541.
14. Weng, C.C., Yen, S.I., Jiang, M.H. Experimental study on shear splitting failure of full-scale composite concrete encased steel beams. *Journal of structural Engineering*. 2002.128(9). DOI: 10.1061/(ASCE)0733-9445(2002)128:9(1186)
15. Nakamura, S., Narita, N. Bending and shear strengths of partially encased composite I-girders. *Journal of constructional steel research –ELSEVIER*. 2003. 59(12). Pp. 1435–1453.



16. Nie, J., Xiao, Y., Chen, L. Experimental studies on shear strength of steel–concrete composite beams. *Journal of structural Engineering*. 2004.130(8). DOI: 10.1061/(ASCE)0733-9445(2004)130:8(1206)
17. Mahmoud, M., Elafandy, T., Okail, H., Abdelrahman, A. Interfacial shear behavior of composite flanged concrete beams. *HBRC Journal*. 2013.10(2). Pp. 206–214.
18. Chisari, C., Amadio, C. An experimental, numerical and analytical study of hybrid RC-encased steel joist beams subjected to shear. *Engineering Structures –ELSEVIER*. 2014. 61. Pp. 84–98.
19. Neelima, K., Shingade, V.S. Experimental study on performance of composite beams with and without shear reinforcement. *International Journal of Engineering Research and Development*. 2016. 12 (7). Pp. 10–16.
20. Madhavi, T., Raju, S., Mathur, D. Polypropylene fiber reinforced concrete – a review. *International Journal of Emerging Technology and Advanced Engineering*. 2014. 4(4).
21. Zhang, P., Li, Q. Effect of polypropylene fiber on durability of concrete composite containing fly ash and silica fume. *Composites: part B*. 2013. 45. Pp. 1587–1594.
22. Mohamed R.A.S. (2006). Effect of poly polypropylene fibers on the mechanical properties of normal concrete. *Journal of Engineering Sciences, Assiut University*.2006. 34(4). Pp. 1049–1059.
23. Mohod, M. Performance of polypropylene fiber reinforced concrete. *IOSR Journal of Mechanical and Civil Engineering (IOSR-JMCE)*. 2015. 12(1). Pp. 28–36.
24. Shihada, S. Effect of polypropylene fibers on concrete fire resistance. *Journal of Civil Engineering and Management*. 2011. 17(2). Pp. 259–264.
25. Behnood, A., Ghandehari, M. Comparison of compressive and splitting tensile strength of high strength concrete with and without polypropylene fibers heated to high temperatures. *Fire Safety Journal*. 2009. 44(8). Pp. 1015–1022.
26. Ghannam, S. Flexural strength of concrete-filled steel tubular beam with partial replacement of coarse aggregate by granite. *International Journal of Civil Engineering and Technology (IJCIET)*. 2016. 7(5). Pp. 161–168, Article ID: IJCIET\_07\_05\_018.
27. AIObaidi, S., Salim, T., Hemzah, S. Flexural behavior of concrete filled steel tube composite with different concrete compressive strength. *International Journal of Civil Engineering and Technology*. 2018. 9(7). Pp. 824–832.
28. Flor, J., Fakoury, R., Caldas, R. Experimental study on the flexural behavior of large-scale rectangular concrete-filled steel tubular beams. *Revista IBRACON de Estruturas e Materiais*. 2017. 10(4). Pp. 895–905. DOI: 10.1590/s1983-4195201700040-0007
29. Nardin, S., De Cresce El Debs, A. Study of partially encased composite beams with innovative position of stud bolts. *Journal of Constructional Steel Research*. 2009. 65(2). Pp. 342–350. DOI: 10.1016/j.jcsr.2008.03.021
30. ASTM C39. Manual of Aggregate and Concrete Testing. American Society for Testing and Materials. West Conshohocken. Pennsylvania, 2000.

#### **Information about authors:**

**Nour Wehbi,**

E-mail: [n.wehbi@bau.edu.lb](mailto:n.wehbi@bau.edu.lb)

**Adnan Masri,**

E-mail: [amasri@bau.edu.lb](mailto:amasri@bau.edu.lb)

**Oussama Baalbaki,**

E-mail: [obaalbaki@bau.edu.lb](mailto:obaalbaki@bau.edu.lb)

*Received 11.09.2020. Approved after reviewing 04.06.2021. Accepted 06.06.2021.*



Research article

UDC 69.04

DOI: 10.34910/MCE.111.6

## Behavior of heat damaged reinforced recycled aggregate concrete beams repaired with NSM-CFRP strips

W.S. Barham , Y.T. Obaidat , H.A. Alkhatatbeh 

Jordan University of Science and Technology, Irbid, Jordan

 [wsbarham@just.edu.jo](mailto:wsbarham@just.edu.jo)

**Keywords:** reinforced concrete, fiber reinforced plastics, recycling, heating, flexural strength, near-surface mounted strips, heat damage, experimental

**Abstract.** The behavior of heat damaged Recycled Aggregate Concrete (RAC) beams repaired with NSM-CFRP strips is the subject of this experimental study. The effect of heat damage on the RAC beams and the post-heating residual strength of beams were studied and compared with natural beams. Different volumetric percentages (0 %, 25 % and 50 %) of coarse Recycled Concrete Aggregates (RCA) were used in three concrete mixes (N, R25 and R50), producing a total of 16 reinforced beams having the same cross-section (100 mm×150 mm×1150 mm). Specimens were exposed to two levels of heat, 25 °C at ambient air and 400 °C for a three-hour period. The post-heating residual strength of RAC beams was studied and compared with natural ones. The flexural test conducted indicated a reduction in the load carrying capacities and stiffness due to mechanical deterioration in concrete properties and bond strength. The reduction in stiffness increased as RCA content increased due to a large amount of weak decomposed cement mortar in the RAC. The NSM-CFRP strips technique was used with epoxy adhesive for strengthening/recovering the flexural capacities of intact/ heat-damaged RAC beams. Four groups of simply supported beams were tested in a four-point bending test; the enhancement/reduction in strength and the mechanical properties were recorded. Results indicated that strengthened beams showed comparable behavior with those made with conventional concrete at room temperature. On the other hand, the behavior of repaired beams after being exposed to 400 °C showed different failure modes depending on the RCA percentage and the repairing configurations. RAC with higher RCA replacement ratio has a lower bond strength and therefore, a larger slippage was reported. The weak bond between the epoxy adhesive and the surrounding concrete caused the reduction in stiffness. Finally, using NSM CFRP with two strips at the sides (one strip at each side) for strengthening and repairing of intact/heat-damaged RAC beams resulted in slight improvement of the load carrying capacities. It reduced the induced strain in the CFRP strips to about 40 % of its value when a single concentrated strip at the bottom is used, and minimizing the slippage due to lower stresses and strains in the CFRP strips.

### 1. Introduction

Concrete recycling has become an alternative solution to use concrete debris rather than routinely trucking it to landfills for disposal [1]. Recently, the structural applications of recycled aggregate concrete have become a field of interest for engineers and scientists. Therefore, the strengthening and repairing of recycled concrete structures became a necessity. These structures may need to be enhanced or rehabilitated because they are in a weakened state, not only due to deterioration, but also due to errors

Barham, W.S., Obaidat, Y.t., Alkhatatbeh, H.A. Behavior of heat damaged reinforced recycled aggregate concrete beams repaired with NSM-CFRP strips. Magazine of Civil Engineering. 2022. 111(3). Article No. 11106. DOI: 10.34910/MCE.111.6

© Barham, W.S., Obaidat, Y.T., Alkhatatbeh, H.A., 2022. Published by Peter the Great St. Petersburg Polytechnic University.



This article is licensed under a CC BY-NC 4.0



that could be committed in the design and execution processes. Therefore, repairing or strengthening of the existing structures may be needed whenever the structural members are damaged. Experimental studies conducted on the field of concrete materials recycling concluded the possibility to transform the concrete waste into good quality recycled concrete aggregate to be used in the concrete industry. The recycled concrete aggregates possess lower specific gravity, bulk density, and resistance against mechanical action including impact load and crushing value, but higher water absorption capacity and porosity when compared with the natural ones. This is due to the presence of low-density cement paste adhered to the old aggregate [2–5]. These properties are strongly affected by the strength of the parent concrete [6]. Moreover, any gradation could be achieved with recycled aggregate by monitoring the crushing process. However, the crushing may produce some residual dust on the coarse aggregate surfaces, and hence washing it becomes essential.

Many studies were conducted to evaluate damage in the recycled aggregate concrete in terms of its mechanical properties and stress-strain relationships. Although most of the studies showed properties of concrete degrade as the level of exposure temperature rises, the post-heating and post-fire mechanical behavior of recycled aggregate concrete was satisfactory and comparable with the natural concrete [6–10]. Moreover, the elastic modulus of recycled aggregate concrete degraded with an increase in recycled aggregate content at any level of heat exposure [7–9, 12], whereas the peak strain increased [10]. Also, recycled aggregate concrete shows adequate thermal compatibility, since no spalling or fragmentation of the specimen was noticed when heated [7, 9, 13]. Finally, it is worth to point out that recycled aggregate concrete with higher replacement ratio and lower w/c ratio behaves better than the natural concrete upon heating due to thermal compatibility of the old and new cement mortars, therefore, the effect of the high temperatures in this zone is less important [12]. The principal results of successive bending tests conducted over years showed flexural strength of recycled and natural aggregate concrete beams are considered the same for the service and ultimate loading [14–17]. However, the cracking moment is significantly affected by the recycled concrete aggregate content as well as the maximum cracks propagation and deflection under serviceable load [14, 18]. On the other hand, the increase in recycled aggregate content leads to an increase in the ultimate flexural deflections and a decrease in the initial stiffness [19].

Fiber-reinforced polymer composites (FRP) is one of the discoveries that received a positive acceptance from civil engineers for strengthening and repairing of structures [20–23]. One of the essential techniques that has been used is carbon fiber reinforced polymer (CFRP) in a polymeric matrix fabricated into different forms, such as plates, strips, or flexible sheets. CFRP can be bonded to the outer face of the RC element using high strength epoxy or cement mortar, known as externally bonded, or installed into grooves cut into the RC element in the predetermined direction, known as Near Surface Mounted (NSM) technique. The last becomes particularly attractive for flexural and shear strengthening for different structural elements [24, 25]. Research conducted indicated that Externally Bonded Reinforcement (EBR) has lower efficiency than NSM technique due to debonding of FRP material. In addition, FRP material, in the case of the EB technique, is vulnerable against physical damage, fire facing, thermal changes, and ultraviolet radiation [26–29]. All the experiments implemented with NSM FRP technique have proved its effectiveness in enhancing flexural capacity of structural members. Beams strengthened with NSM technique showed a rise in flexural capacity at different percentages with respect to control beam depending on the type of failure [30, 31]. The failure mode of RC with NSM CFRP is dependent on different parameters. Two types of rupture are possible for NSM systems. These are pull-out and peeling off [32]. Debonding is another common failure mode, which occurs in different ways: bond failure at the CFRP-adhesive interface, adhesive-concrete interface, splitting of adhesive cover, concrete cover separation, and secondary debonding failure mechanisms [33]. Usually, debonding failure occurring at the CFRP–adhesive or the adhesive–concrete interfaces control the failure of beams strengthened with EBR CFRP strips, whereas the failure of beams strengthened with NSM CFRP strips is controlled by debonding of CFRP strips and cover separation by peeling off the CFRP strips together with the concrete cover [27].

The bond behavior and its characteristics represent a key issue in evaluating the structural performance of the strengthening/repairing systems. Many factors could affect the bond and the local bond-slip behavior of these strengthening/repairing systems, including mechanical properties of constituent materials, surface state of the FRP reinforcement, and finally, the geometry of grooves. The lack of bond between FRP and concrete beams will cause serious problems and lead to different modes of failure. In the NSM FRP method, certain types of failure have been observed during the experiments, including flexure and debonding failure. The former is caused by the yielding of steel bars accompanying concrete crushing or FRP rupture [34, 35]. In addition to the above-stated factors, the test set-up used has a significant effect on both the bond-slip relationship and the debonding load [36–38]. This research aims to explore the effect of using RAC in the flexural behavior of unheated and heat-damaged beams, to investigate the effect of using CFRP NSM strips in the flexural capacity of the RAC beams, and finally, to examine its effect on increasing/recovering the capacity and failure modes of heat-damaged beams.

## 2. Methods

### 2.1. Material properties

#### 2.1.1 Constituent materials of the concrete

All concrete mixtures were produced using type I ordinary Portland cement (CEM I 42.5). Two types of coarse aggregate with maximum aggregate size of 19 mm, were used: natural crushed limestone and Recycled Concrete Aggregate (RCA). In addition, a blend of fine crushed limestone and natural silica sand (75 % fine crushed limestone and 25 % silica sand) was used. Tap water was used in mixing and curing of concrete. Properties of materials used in concrete were tested according to ASTM specifications [39–42] and summarized in Table 1. Coarse RCA used in this research was produced by manual crushing of waste concrete cylinders used in previous studies with parent strength concrete at 50 MPa.

**Table 1. Shortlist of physical and mechanical properties of materials used in concrete.**

|                           | ASG  | BSG (SSD) | BSG (OD) | Absorption % | M.C % | Dry Rodded Unit Weight (Kg/m <sup>3</sup> ) | Abrasion Resistance % | F.M  |
|---------------------------|------|-----------|----------|--------------|-------|---|-----------------------|------|
| Cement                    | 3.15 | –         | –        | –            | –     | 3150  | –                     |      |
| Natural Coarse Aggregate  | 2.67 | 2.56      | 2.53     | 2.63         | 0.14  | 1502.55                                     | 25                    | 6.86 |
| Recycled Coarse Aggregate | 2.63 | 2.36      | 2.21     | 7.24         | 2.43  | 1290.52                                     | 35                    | 7.05 |
| Natural Fine Aggregate    | 2.68 | 2.58      | 2.52     | 2.4          | 0.5   | 1922.53                                     | –                     | 3.12 |
| Silica sand               | 2.67 | 2.64      | 2.61     | 0.5          | 0.65  | 2010.3                                      | –                     | 1.41 |

BSG: Bulk Specific Gravity; ASG: Apparent Specific Gravity M.C: Moisture content; F.M. Fineness Modulus.

#### 2.1.2 Reinforcing steel

Grade 60 (yield stress = 420 MPa) deformed steel bars, 10 mm in diameter, were used for the longitudinal reinforcement, and Grade 40 (yield stress = 280 MPa) 8 mm diameter undeformed steel bars were used for transverse reinforcement (Stirrups). Steel bars used for reinforcing were tested at room temperature about 25 °C and after exposure to an elevated temperature of 400 °C for three hours; the pre and post-heating mechanical properties were determined according to ASTM A370 [43]. Table 2 shows the mechanical properties of the bars tested. Results indicated a reduction in mechanical strength of both types of steel bars upon heating, including yielding and ultimate stresses.

**Table 2. Post heating mechanical properties of the reinforced steel.**

| Temperature | Nominal Bar Diameter (mm) | Yield Stress $f_y$ (MPa) | Ultimate Stress $f_u$ (MPa) |
|-------------|---------------------------|--------------------------|-----------------------------|
| 23 °C       | 10.2                      | 440                      | 625                         |
|             | 8.1                       | 340                      | 431                         |
| 400 °C      | 10.2                      | 426                      | 613                         |
|             | 8.1                       | 295                      | 404                         |

#### 2.1.3 Carbon Fiber Reinforced Polymer and Epoxy Resin.

Unidirectional high-strength NSM-CFRP strips, manufactured by SIKA, were used in the strengthening and repairing of different specimens using epoxy resin adhesive (Sikadur -30LP). Epoxy resin was used as bonding adhesive to fill the grooves and glue the strips to the concrete surface. This adhesive was prepared from two parts: 4.5 kg of white resin (part A) and black hardener (part B) with mixing proportion Resin (A): Hardener (B) = 3:1 by weight or volume to get 6 kg (A+B) light gray bonding adhesive mixture. Table 3 presents the physical and mechanical properties for the NSM-CFRP strips according to the manufacturer's reports. Table 4 presents the technical data of the epoxy adhesive.

**Table 3. Physical and Mechanical Properties of Sika NSM-CFRP strips (Sika® CarboDur® S1.525).**

|                       |                                    |
|-----------------------|------------------------------------|
| Fiber type            | High strength carbon fibers        |
| Fiber orientation     | 0° (unidirectional)                |
| Strip thickness       | 2.5 mm                             |
| Strip width           | 15 mm                              |
| Tensile E-modulus     | 165000 N/mm <sup>2</sup> (nominal) |
| Mean tensile strength | 3100 N/mm <sup>2</sup>             |
| Strain at break       | > 1.7 % (nominal)                  |

**Table 4. Properties for impregnation resin (Sikadur®-30lp).**

|                        |  |
|------------------------|--|
| Form                   | Resin part A: Paste<br>Hardener part B: Paste                |
| Appearance / Colors    | Part A: white<br>Part B: black<br>Part A+B mixed: light grey |
| Mixed density at 25 °C | 1.8 g/cm <sup>3</sup> (approx.)                              |
| Flashpoint             | N/A  |
| Sag flow               | Non-sag on vertical surface                                  |
| Shrinkage              | 0.04 %   |
| E-Modulus              | 10000 N/mm <sup>2</sup> (compression and tension)            |
| Tensile strength       | 18 N/mm <sup>2</sup> at 7 days                               |
| Flexural strength      | 25 N/mm <sup>2</sup> at 7 days                               |
| Shear strength         | 21 N/mm <sup>2</sup> at 7 days                               |
| Compressive strength   | 85 N/mm <sup>2</sup> at 3 days                               |
| Bond to concrete       | > 4 N/mm <sup>2</sup> at 1 day (concrete fracture)           |

## 2.2. Concrete production

Three sets of concrete mixes were designed according to the ACI-211 mix design procedure [44] with trial mixes, achieving an average cylindrical compressive strength of 37.2 MPa at 28 days. One set was natural coarse aggregate concrete (N), and the other two sets of concrete contained recycled concrete aggregate (RCA) (25 % and 50 % replacement ratios of coarse recycled concrete aggregate, volumetrically) designated as R25 and R50, respectively. All mixtures produced had uniform mixing without segregation, reflecting a good workability. For all concrete sets, the slump values measured according to ASTM C143-00 [45] were approximately in the medium range (80–120 mm). The quantities of materials are summarized in Table 5.

**Table 5. Details of the concrete mixes.**

| Concrete Mix | V <sub>c</sub> /V <sub>a</sub> | N.C.A (kg) | R.C.A (kg) | N.F.A (kg) | N.S (kg) | Cement (kg) | W <sub>net</sub> (kg) | W <sub>eff</sub> (kg) | W <sub>net</sub> /C | W <sub>eff</sub> /C | Slump (mm) |
|--------------|--------------------------------|------------|------------|------------|----------|-------------|-----------------------|-----------------------|---------------------|---------------------|------------|
| N            | 0.575                          | 950.32     | -----      | 533.29     | 185.15   | 372.8       | 234                   | 200                   | 0.63                | 0.54                | 115        |
| R25          | 0.576                          | 712.74     | 208.2      | 527.41     | 183.1    | 391.19      | 237.3                 | 200                   | 0.61                | 0.51                | 110        |
| R50          | 0.577                          | 475.16     | 416.41     | 521.16     | 180.9    | 410.16      | 240.6                 | 200                   | 0.59                | 0.49                | 95         |

V<sub>c</sub> is volume of coarse aggregate, V<sub>a</sub> is total volume of aggregate, N.C.A is natural coarse aggregate, R.C.A is recycled coarse aggregate, N.F.A is natural fine aggregate, N.S is natural silica, W<sub>net</sub> is net water and W<sub>eff</sub> is effective water.

A total of eighteen concrete cylinders (150 mm in diameter and 300 mm in height) were cast and cured. Each concrete mix involved six cylinders subdivided into two subgroups based on the level of heat to be exposed to. Each subgroup contained three cylinders tested according to ASTM [46] to determine the average concrete compressive strength ( $f_c'$ ) at ambient temperature (25 °C) and after being exposed to heat (400 °C) for 3 hours in the electric furnace. In order to get accurate results from the testing machine, the cylinders were capped with sulfur to level surfaces. The average compressive strength was measured and recorded for the cylindrical specimens as illustrated in Table 6.

**Table 6. Average ultimate compressive strength of different concrete mixes at different levels of heat exposure.**

| Concrete Mix | $f'_c$ (MPa) |        |
|--------------|--------------|--------|
|              | 25 °C        | 400 °C |
| N            | 37.1         | 29.92  |
| R25          | 38.2         | 29.81  |
| R50          | 37.5         | 27.80  |
| Average      | 37.6         | 29.2   |

$f'_c$  is 28-day compressive cylinder strength of concrete

### 2.3. Specimens and beam fabrication

The study program involved sixteen reinforced concrete beams (100×150×1150 mm) designed to be under-reinforced by following the guidelines of the ACI committee 318 [47]. All beams were provided with typical longitudinal and transverse steel reinforcements. The bottom (tension) reinforcement consists of two  $\Phi 10$  bars, the same as the top (compression), running along the full span of the beam. Also, the transverse shear reinforcement was roughly designed according to the ACI committee 318 [47] taking into account both the additional rise in ultimate load capacity due to the application of NSM-CFRP strips and the low shear resistance of the heat-damaged recycled aggregate concrete beams. The shear reinforcement consisted of closed 8 mm undeformed steel stirrups, distributed along the shear span and spaced 50 mm centers apart. The steel reinforcements were provided with concrete cover spacers (25 mm) at the bottoms and sides to ensure sufficient cover, then placed in the wooden formworks, as shown in Fig. 1. Specimens were divided into three main groups based on the concrete mix cast. Each group of specimens was cast with a specific concrete mix (N: natural aggregate, R25: 25 % recycled aggregate and R50: 50 % recycled aggregate) and moist-cured for 28 days. Each group was also subdivided into three sets in terms of the level of temperature exposure (25 °C at ambient air, and 400 °C).

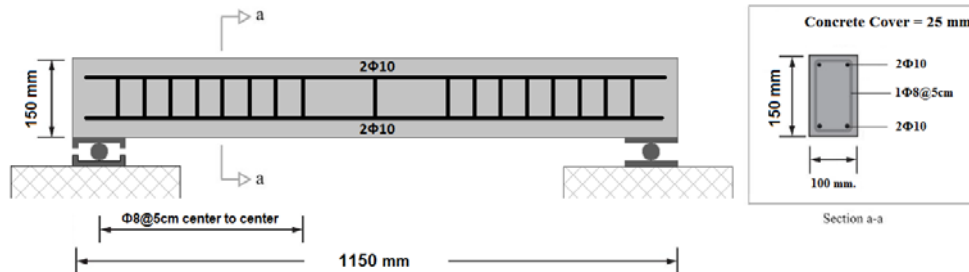


**Figure 1. Specimens and beam fabrication.**

### 2.4. Thermal treatment

Concrete specimens (beams and cylinders) were subjected to elevated temperatures using the electrical furnace available at the structural laboratory. The specimens were exposed to 400 °C (T400) heat for 3 hrs. The rate of heating is shown in Fig. 2.

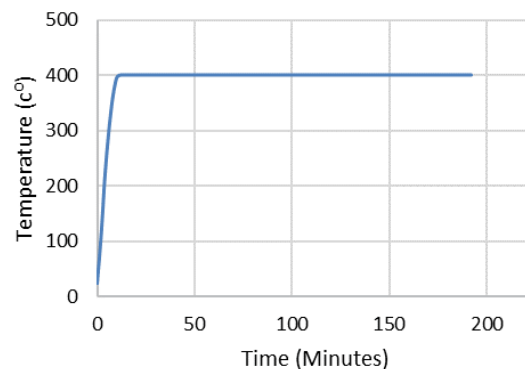


**Figure 2. Temperature history of heated specimens.**

## 2.5. Applying the NSM-CFRP strips

Finally, each set contained an unrepaired beam used as a control specimen, designated with the symbol (C), and a repaired or strengthened beam using NSM-CFRP strips. Two configurations were used for strengthening/repairing: single strip centered at the bottom or double strip at sides (one strip at each side). Each configuration was designated with the symbol S1: One strip at bottom, or S2: Two strips at both sides, respectively. Fig. 3 (a and b) shows a schematic drawing of the repairing configurations. Table 7 illustrates the characteristics of different specimens.

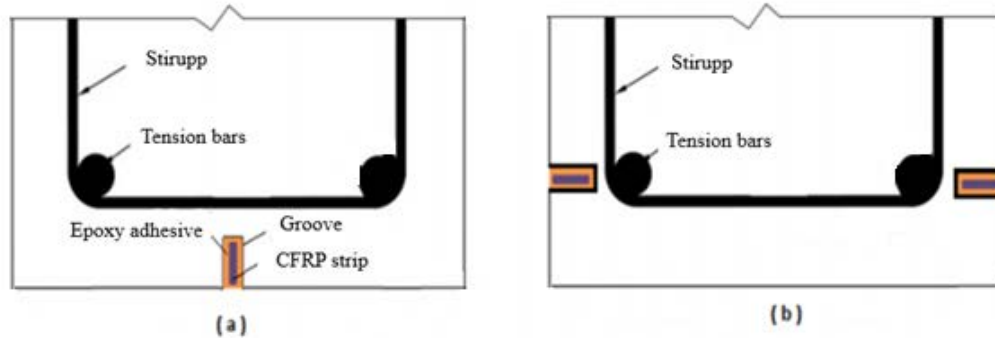


**Figure 3. A schematic drawing of the repairing configurations:**  
**(a) Single concentrated strip at soffit (S1), (b) Two strips at sides, one strip at each side (S2).**

**Table 7. Test program and specimens' designations.**

| Specimen Designation | Type of Concrete | Replacement Ratio % | Temperature (°C) | Repairing Configuration |
|----------------------|------------------|---------------------|------------------|-------------------------|
| B-N-T25-C            | Natural          | 0                   | 25               | Control                 |
| B-N-T25-S1           |                  |                     | 25               | One strip at bottom     |
| B-N-T25-S2           |                  |                     | 25               | Two strips at sides     |
| B-N-T400-C           |                  |                     | 400              | Control                 |
| B-N-T400-S1          |                  |                     | 400              | One strip at bottom     |
| B-N-T400-S2          |                  |                     | 400              | Two strips at sides     |
| B-R25-T25-C          | RAC              | 25                  | 25               | Control                 |
| B-R25-T25-S1         |                  |                     | 25               | One strip at bottom     |
| B-R25-T400-C         |                  |                     | 400              | Control                 |
| B-R25-T400-S1        |                  |                     | 400              | One strip at bottom     |
| B-R50-T25-C          |                  | 50                  | 25               | Control                 |
| B-R50-T25-S1         |                  |                     | 25               | One strip at bottom     |
| B-R50-T25-S2         |                  |                     | 25               | Two strips at sides     |
| B-R50-T400-C         |                  |                     | 400              | Control                 |
| B-R50-T400-S1        |                  |                     | 400              | One strip at bottom     |
| B-R50-T400-S2        |                  |                     | 400              | Two strips at sides     |

## 2.6. Bonding NSM-CFRP strips

For installing the NSM CFRP strips, 25 mm depth and 8 mm width slits were cut using an electric drill for the considered configurations. Slit geometry was considered in this study to fit the dimensions of the CFRP strip employed. The slits were cleaned by an electric air blower before washed with a volatile liquid (thinner) to remove the suspended dust and reduce surface humidity. Later, the bonding adhesive was manually squeezed into the slits filling them completely using a special spatula, then the NSM CFRP strips were pressed into the epoxy up to the full depth of the slits, with the excess epoxy used to finish the surfaces covering the strips. Fig. 4 shows the NSM-CFRP strips installation process.

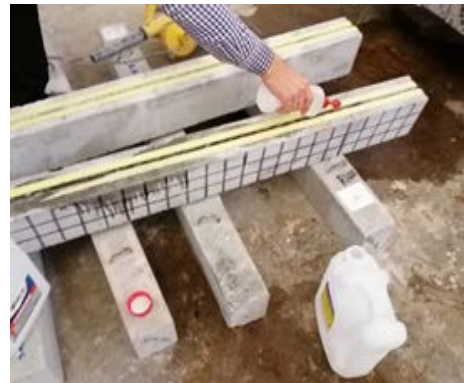
## 2.7. Test setup

All beam specimens were simply supported (one end is a hinge and the other is a roller) over a span of 1.05 m on-center, then subjected to four-point loading applied through a spreader beam. The distance between two point-loads was fixed at 350 mm. Three linear variable displacement transducers (LVDT's) were used. The first one was placed beneath the beam at the mid-span center to measure deflection,

whereas the second one was positioned horizontally to measure the longitudinal strain developed in CFRP strips. The latter was mounted on two short extensions of CFRP strips glued to the main NSM CFRP strips at two points over a gauge length of 350 mm around the center of the beams. Similarly, the third LVDT recorded the end slippage 150 mm apart from the center of support attached to a small piece of CFRP strip glued to the NSM CFRP strip in a pre-cut groove in which the head of the LVDT hits the center of small plastic plate glued to concrete surface. A schematic drawing of test setup is presented in Fig. 5.



(a)



(b) Groove cleaning with thinner



(c) Filling the grooves with "epoxy" paste



(d) Installation of CFRP strips in groove



(e) Finishing the surface



(f) Strengthened/Repaired beams

**Figure 4. NSM CFRP strips installation.**

The load was automatically applied using a universal testing machine of 2000 KN capacity with displacement controlled at 0.041 mm/s loading rate. Using a data acquisition system, instantaneous measurements of load, mid span deflection, elongation in NSM CFRP strip, and relative slippage between the concrete and the bonded CFRP strip were automatically recorded too.



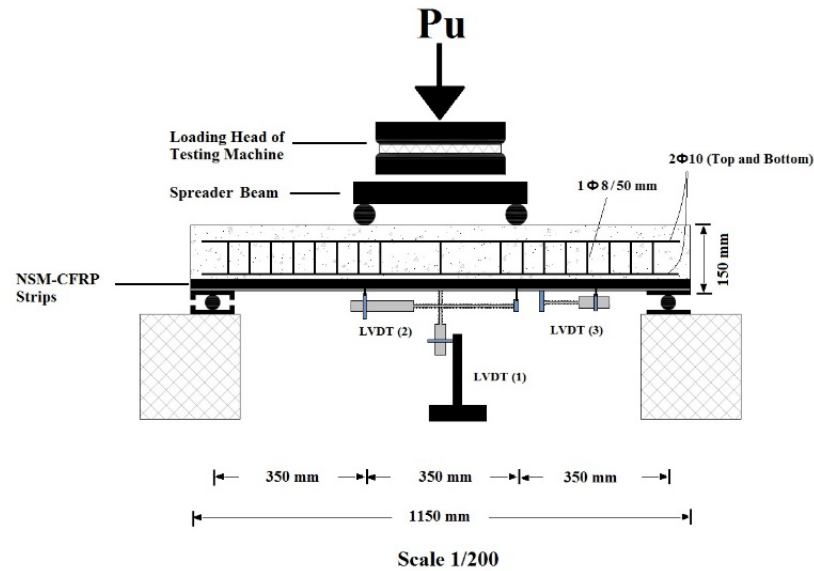


Figure 5. A schematic drawing of the test setup and LVDT's distribution.

### 3. Results and Discussion

The results demonstrate the post heating residual behavior of reinforced RAC beams exposed to elevated temperature and highlight the effect of NSM-CFRP strips as a strengthening/repairing method in increasing/recovering the flexural capacities of intact/heat damaged reinforced RAC beams in terms of ultimate load capacity, mid span deflection, toughness, stiffness, bond slip, and failure modes.

#### 3.1. Load deflection stages

The load–deflection curves presented in Fig. 6, 7 and 8 can be divided into three stages: elastic stage (pre-cracking), post-cracking stage, and yield strengthening stage. In the elastic stage, the specimen's flexural stiffness is given by the uncracked section, resulting in a linear load versus displacement curve. As the load was increased above the  $P_{cr}$ , micro-cracks developed in the specimen, with noticeable cracks appearing in the weak zone of the constant bending moment region. Meanwhile, the slope of the load–displacement curve is decreasing, as can be seen in Table 9, meaning that the beam's bending stiffness is decreasing, indicating that the beam is entering the crack production stage. When the load reaches the yield load, the specimen enters the yield strengthening stage. The load increased slowly at this stage, with a large increase in displacement.

#### 3.2. Summary of the mechanical properties of beams

Mechanical characteristics of different beams are shown below in Table 8 and 9. The results included ultimate load ( $P_u$ ), ultimate deflection at mid span ( $\Delta_u$ ), failure mode (F.M), stiffness, and toughness, and energy adsorption. The stiffness is the slope of the linear part of the load-deflection curve. Energy adsorption is the area under the load deflection curve up to the end of the stage in consideration calculated numerically using the trapezoidal rule.

**Table 8. Test results of beam specimens.**

| Specimen    | $P_u$<br>(kN)                | $\Delta_u$<br>(mm) | $\Delta_y$<br>(mm) | $DI = \frac{\Delta_u}{\Delta_y}$ | F.M       | Max Strain<br>in CFRP | Max Slippage<br>(mm) |
|-------------|------------------------------|--------------------|--------------------|----------------------------------|-----------|-----------------------|----------------------|
| B-N-T25-C   | 45.15<br>(0.0%) <sup>1</sup> | 13.9               | 4.29               | 3.24                             | F         |                       |                      |
| B-N-T25-S1  | 72.65<br>(+61%)              | 17.2               | 5.93               | 2.90                             | HC-PCS-S  | 0.0145                | 1.2519               |
| B-N-T25-S2  | 74.89<br>(+66%)              | 14.3               | 7.37               | 1.94                             | HC-PCS-CC | 0.0045                | 0.9867               |
| B-N-T400-C  | 38.00<br>(-16%)              | 14.5               | 4.98               | 2.91                             | F         |                       |                      |
| B-N-T400-S1 | 63.46<br>(+41%)              | 26                 | 5.3                | 4.91                             | HC-PCS-CC | 0.0111                | 1.3947               |
| B-N-T400-S2 | 65.66                        | 12.5               | 5.08               | 2.46                             | F         | 0.0044                | 0.5540               |



| Specimen      | $P_u$<br>(kN)             | $\Delta u$<br>(mm) | $\Delta y$<br>(mm) | $DI = \frac{\Delta u}{\Delta y}$ | F.M       | Max Strain<br>in CFRP | Max Slippage<br>(mm) |
|---------------|---------------------------|--------------------|--------------------|----------------------------------|-----------|-----------------------|----------------------|
| B-R25-T25-C   | (+45%)<br>44.50<br>(0.0%) | 13.4               | 4.07               | 3.29                             | F         |                       |                      |
| B-R25-T25-S1  | 72.80<br>(+64%)           | 18.2               | 5.19               | 3.51                             | HC-PCS-S  | 0.0128                | 1.2965               |
| B-R25-T400-C  | 36.60<br>(-18%)           | 14.9               | 4.02               | 3.71                             | F         |                       |                      |
| B-R25-T400-S1 | 63.20<br>(+42%)           | 23.5               | 7.11               | 3.31                             | HC-PCS-CC | 0.0107                | 0.7960               |
| B-R50-T25-C   | 44.65<br>(0.0%)           | 14.4               | 4.53               | 3.18                             | F         |                       |                      |
| B-R50-T25-S1  | 71.22<br>(+60%)           | 15.1               | 6.2                | 2.44                             | HC-PCS-S  | 0.0116                | 1.2965               |
| B-R50-T25-S2  | 71.70<br>(+61%)           | 23.1               | 7.25               | 3.19                             | HC-PCS-CC | 0.0043                | 0.3579               |
| B-R50-T400-C  | 34.85<br>(-22%)           | 14.4               | 4.14               | 3.48                             | F         |                       |                      |
| B-R50-T400-S1 | 62.00<br>(+39%)           | 22.1               | 5.9                | 3.75                             | HC-PCS-S  | 0.0090                | 1.6580               |
| B-R50-T400-S2 | 63.67<br>(+43%)           | 16.6               | 6.93               | 2.40                             | HC-PCS-S  | 0.0042                | 0.6200               |

1: Numbers between brackets represent the percentage of control specimens, +ve: increase and -ve: decrease.

F: Flexural type (Steel yielding followed by concrete crushing). DI: Ductility Index

HC-PCS-CC: Horizontal cracks cause partial cover separation with local epoxy-concrete debonding followed by concrete crushing.

HC-PCS-S: Horizontal cracks cause partial cover separation with local epoxy-concrete debonding followed by shear failure.

**Table 9. Stiffness and energy absorption for the pre and post cracking stages.**

| Specimen      | Pre-Cracking<br>stiffness<br>(kN/mm) | Pre-Cracking<br>energy adsorption<br>(kN-mm) | Pre-Yielding<br>Stiffness<br>(kN/mm) | Pre-yielding energy<br>adsorption<br>(kN-mm) | Total Energy<br>adsorption<br>(kN-mm) |
|---------------|--------------------------------------|--|--------------------------------------|--|---------------------------------------|
| B-N-T25-C     | 46.6                                 | 0.78   | 7.21                                 | 100  | 444                                   |
| B-N-T25-S1    | 43.2                                 | 0.93   | 8.65                                 | 177  | 862                                   |
| B-N-T25-S2    | 44.5                                 | 0.85   | 7.73                                 | 255  | 723                                   |
| B-N-T400-C    | 29.0                                 | 0.67   | 6.60                                 | 110  | 376                                   |
| B-N-T400-S1   | 13.6                                 | 1.73   | 7.80                                 | 148  | 562                                   |
| B-N-T400-S2   | 14.3                                 | 2.73   | 8.4                                  | 135  | 417                                   |
| B-R25-T25-C   | 20.6                                 | 0.91   | 7.50                                 | 78   | 430                                   |
| B-R25-T25-S1  | 42.7                                 | 0.95   | 8.90                                 | 135  | 820                                   |
| B-R25-T400-C  | 9.6                                  | 1.06   | 6.30                                 | 67   | 340                                   |
| B-R25-T400-S1 | 33.5                                 | 0.64   | 7.70                                 | 195  | 536                                   |
| B-R50-T25-C   | 31.9                                 | 0.67   | 7.37                                 | 97   | 404                                   |
| B-R50-T25-S1  | 43.9                                 | 1.58   | 8.30                                 | 147  | 721                                   |
| B-R50-T25-S2  | 34.0                                 | 2.50   | 8.97                                 | 306  | 969                                   |
| B-R50-T400-C  | 16.2                                 | 0.91   | 5.9                                  | 69   | 315                                   |
| B-R50-T400-S1 | 18.6                                 | 1.97   | 8.3                                  | 158  | 642                                   |
| B-R50-T400-S2 | 26.5                                 | 0.65   | 9.3                                  | 251  | 446                                   |

### 3.3. Effect of using NSM-CFRP strips on the load-deflection response of heat-damaged beams

According to Table 8 and Fig. 6, the load-deflection curves of specimens (B-N-T400-C, B-R25-T400-C and B-R50-T400-C) showed similar trend behavior. Curves were approximately linear up to certain point before they became non-linear. The deterioration in the mechanical properties is due to the decrease in the value of yield stress for steel and deterioration of bond strength between reinforcing steel and concrete, in addition to the large decrease in the post-heating compressive strength of concrete caused by concrete degradation and thermal cracks. The stiffness of the intact concrete beams was slightly affected by the recycled concrete aggregate content, but for the heat-damaged beams, the recycled concrete aggregate content had a significant effect on the stiffness due to the weaker bond between the damaged recycled aggregate concrete and the reinforcing steel. For beams exposed to an elevated temperature of (400 °C) for three hours, results showed that a significant difference between mixes and the reduction in load capacity was relatively low due to the fact that the strength was controlled by the compressive strength of heat-damaged concrete and the yielding of the steel reinforcement. The last is not significantly affected by temperatures below 700 °C.

Fundamentally, the use of NSM CFRP strips for strengthening and repairing shows a significant enhancement in the beams' behavior including increasing the load carrying capacity as shown in Table 8 and Fig. 6. Strengthened specimens showed a similar and typical mechanical response. For example, the load carrying capacity of specimens B-N-T25-S1 and B-R50-T25-S1 were 61 % and 60 % higher than B-N-T25-C and B-R50-T25-C controlled specimens, respectively. The load-deflection curves were divided into three stages. In the first stage (elastic stage), the load increased linearly up to certain values of load and deflection, causing the initiation of the first crack in the concrete. In this stage, the bond between the CFRP strips, epoxy material, and concrete was good. In the second stage (concrete cracking to steel yielding), the curve changed its slope due to the weaker modulus of CFRP strips and steel yielding, reflecting the linear elastic response of the cracked composite section started by concrete cracking to steel yielding due to increasing bending moment. Finally, the third stage (steel yielding to failure), reflects the nonlinear behavior of the composite section.

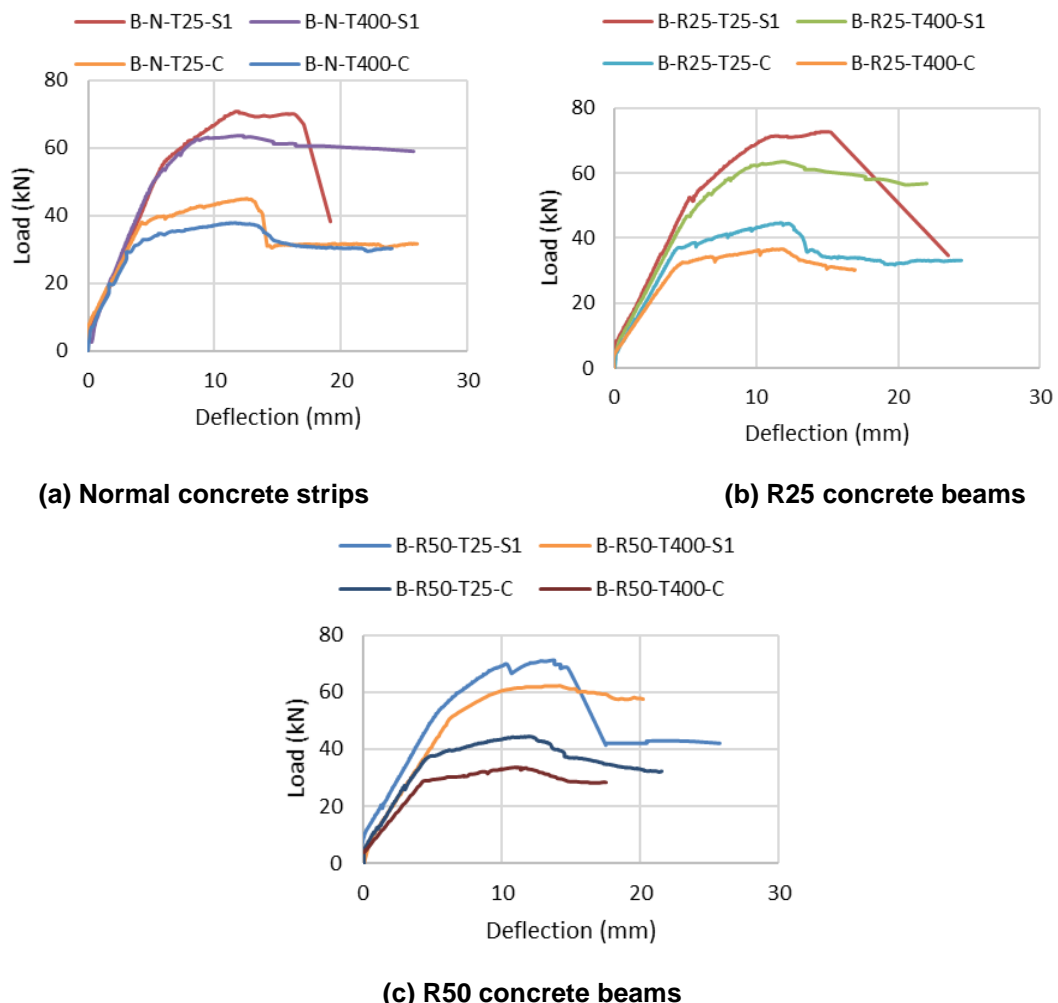


Figure 6. Effect of using NSM-CFRP strips at different levels of heat exposure.

### 3.4. Effect of RAC percentage on the load-deflection response

Results showed typical behavior of beams with different percentages of recycled concrete aggregate as shown in Table 8 and Fig. 7. This is due to the strength of concrete, since all concrete mixes have the same strength regardless the recycled aggregate content indicating that Recycled Concrete Aggregate does not have an effect on the load capacity when the strength of concrete is fixed, but the deflection slightly increases as RCA increases because of the low modulus of elasticity of RAC. From Table 8, the load carrying capacity of specimens B-N-T25-C, B-R25-T25-C, and B-R50-T25-C having different RA content is almost the same.

For heat-damaged specimens at 400 °C, due to the lower tensile strength of RAC and the deterioration in mechanical properties of concrete associated with the heat-damage due to elevated temperatures, the repaired specimens exhibited comparable residual load-carrying capacities but noticeable difference for deflection as the recycled aggregate increased. On the other hand, the stiffness showed a reduction as recycled aggregate increased. For example, from Table 9, the post cracking stiffness of specimens B-N-T400-C, B-R25-T400-C, and B-R50-T400-C were 6.6 kN/mm, 6.3 kN/mm and 5.9 kN/mm, respectively.

This can be related to the significant decrease in bond strength between the damaged concrete and the epoxy adhesive as the recycled aggregate content increases. Heat-damaged recycled aggregate concrete with a high incorporation ratio of recycled concrete aggregate contains a larger amount of damaged mortar surrounding the epoxy leading to a weaker bond as shown in Fig. 7.

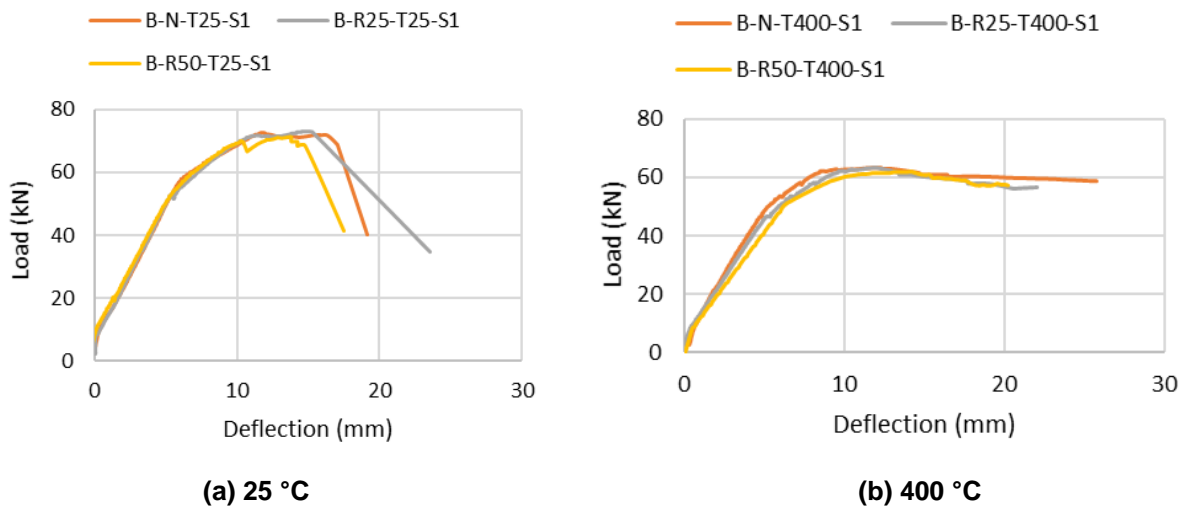
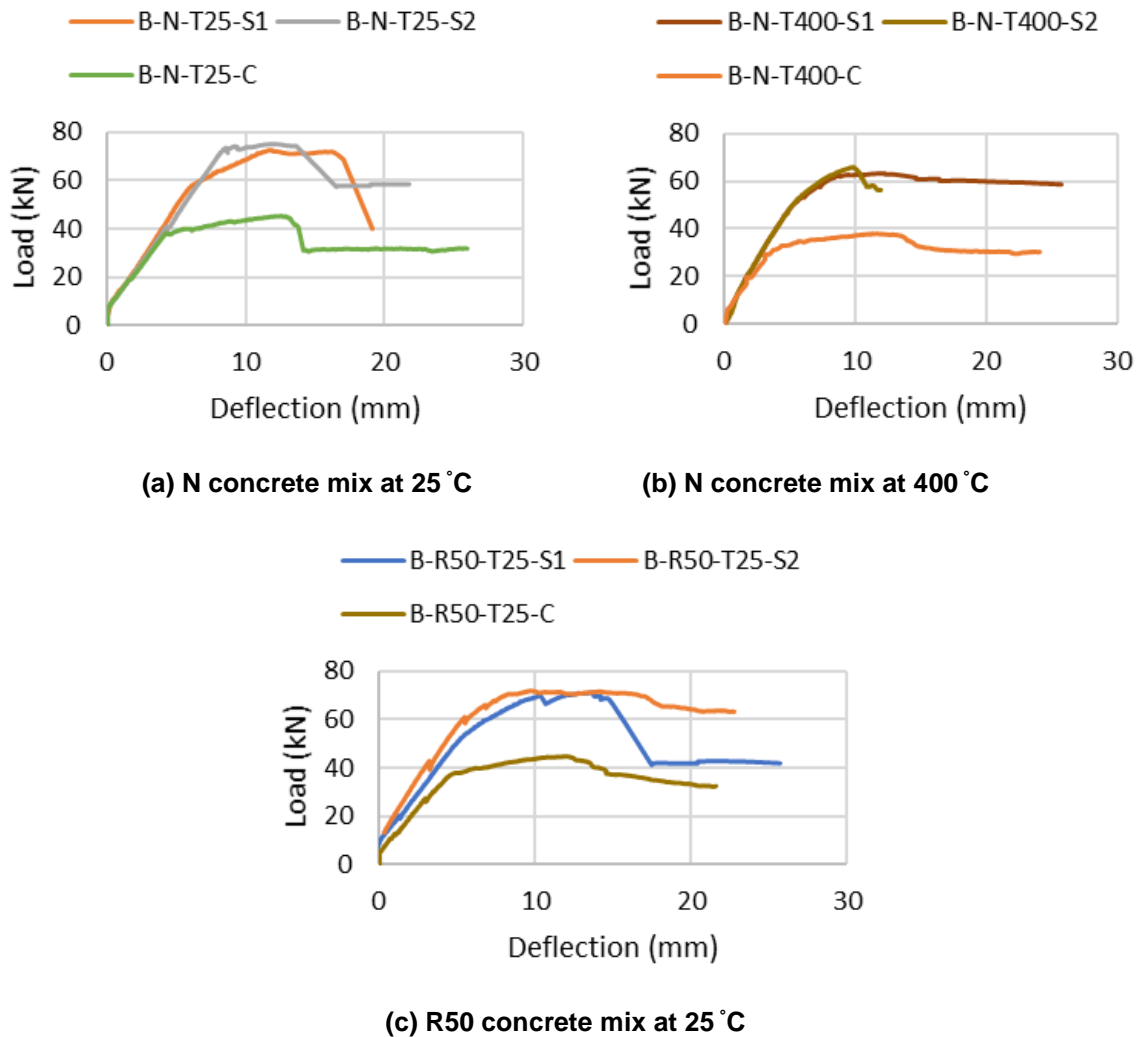


Figure 7. Effect of RAC percentage on the load-deflection response.

### 3.5. Effect of different strengthening/repairing configurations

In this part, the differences between strengthening/repairing configurations are discussed. Fig. 8 shows load-deflection curves of BNSM-CFRP (S1) and SNSM-CFRP (S2) for different percentages of recycled aggregate content and different levels of heat exposure. Table 8 summarizes the other parameters including stiffness and modulus. Generally, specimens strengthened/repared with SNSM-CFRP strips (one strip at each side) showed a significant increase in the cracking load due to a higher ratio of CFRP strips. The load carrying capacity shows a slight change, however, the stiffness significantly increased but toughness decreased. In comparison with the first configuration, the second configuration indicated a significant increase in cracking load and stiffness but a significant reduction in deflection and toughness. Moreover, the ultimate load capacity does not affect the configurations.



**Figure 8. Effect of NSM-CFRP strips strengthening/repairing configuration.**

### 3.6. Strain Development in NSM-CFRP Strips and Bond Slippage

#### 3.6.1. Strain in NSM-CFRP strips

Fig. 9 shows that the induced strain in NSM-CFRP strips is significantly affected by the recycled concrete aggregate; the strain decreases when the RCA percentage increases due to a drop in the bond between CFRP strips and the surrounding concrete. The bond between the NSM-CFRP strips and the concrete cast with natural aggregate is stronger than the bond between the NSM-CFRP strips and the RAC. The reason for the reduction in bond strength is the recycled concrete aggregates consist mostly of cement mortar attached to old virgin aggregate. The mortar itself has lower strength than the virgin aggregate. Using SNSM CFRP in strengthening/repairing specimens significantly reduced the induced strain in NSM-CFRP strips because a larger resisting area available to handle the stresses developed. Fig. 10 shows a comparison between NSM CFRP and SNSM CFRP in terms of strain induced in the CFRP strips.

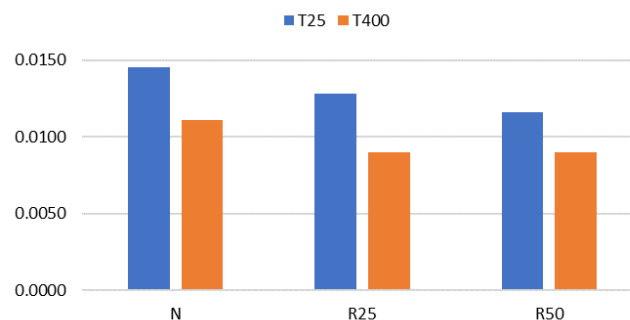


**Figure 9. Strain induced in NSM CFRP strips to ultimate vs. temperature for heat-damaged/repared and unheated/strengthened beams.**

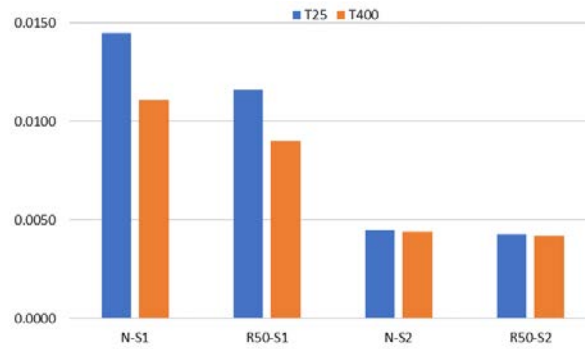


**Figure 10. Strain induced to ultimate vs. temperature for different strengthening/ repairing configurations.**

### 3.6.2 Bond Slippage Between Concrete and CFRP strips

Fig. 11 shows that the bond slippage occurred between CFRP strip and surrounding concrete substrates in the first configuration with one strip at the bottom. The slippage is significantly affected by the recycled concrete aggregate. The maximum slippage at ultimate load increases as the RCA content increases due to lower bond strength between CFRP strips and the surrounding concrete because of the large amount of cement mortar attached to the aggregate in RCA. Fig. 12 indicated that using two strips at the sides helps to minimize the slippage to about 40 % of its value in the first configuration (S1) where a single concentrated strip at the bottom is used.

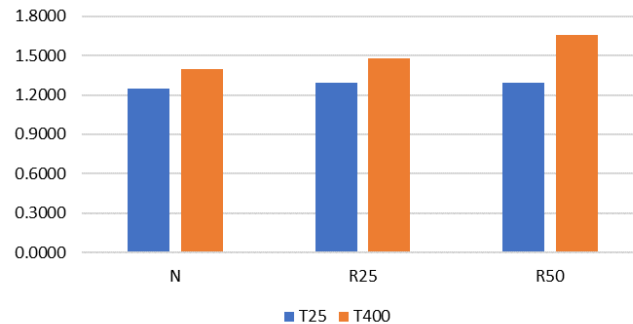


**Figure 11. Bond slippage between NSM CFRP strips vs. temperature for heat-damaged/repaired and unheated/strengthened beams.**

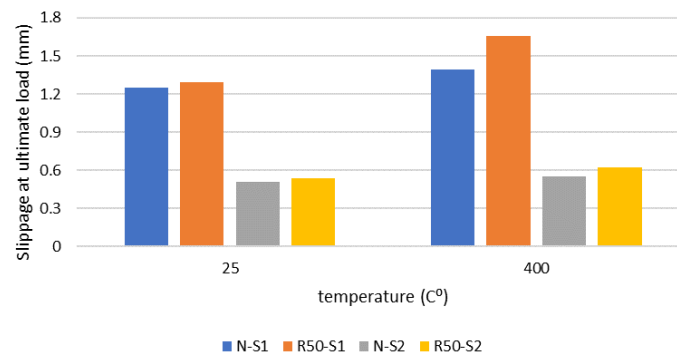
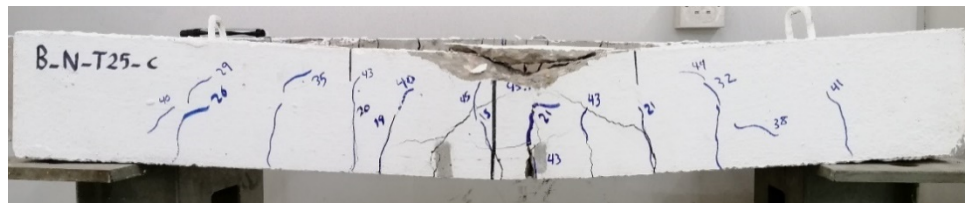


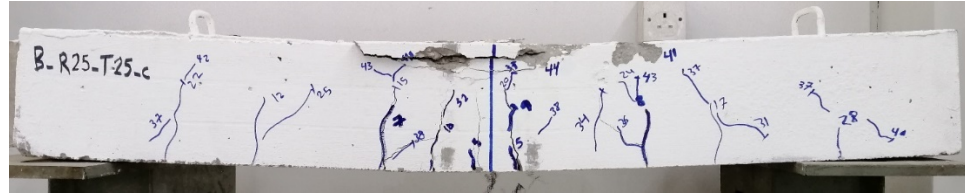
**Figure 12. Bond slippage at ultimate load vs. temperature for different strengthening/ repairing configurations.**

### 3.7. Failure modes

Fig. 13 and Fig. 14 show unheated and heat-damaged control beams at failure. All specimens exhibited a flexural mode of failure. Unheated beams, subjected to four-point loading, showed a typical crack propagation as shown in the pictures of Fig. 13. Cracks initiated within the middle of the span at the tension side when the tensile capacity of concrete was reached. By adding further loads, shear cracks appeared diagonally near the supports in the high shear zones and more flexural cracks became visible and extended to the compression side until failure load. Generally, for the same grade of concrete, the recycled aggregate content did not affect the cracks pattern but reduced the load at which the cracks appeared as the recycled aggregate content increased because the RAC has lower mechanical properties.



a) B-N-T25-C, Loading cracks



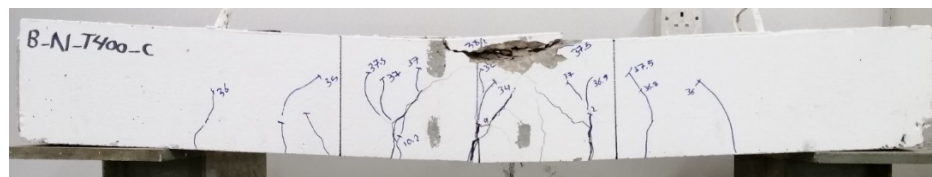
b) B-R25-T25-C, Loading cracks



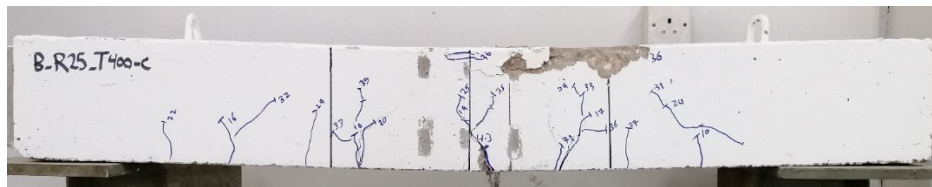
c) B-R50-T25-C, Loading cracks

**Figure 13. Failure mode of unheated control specimens at 25 °C.**

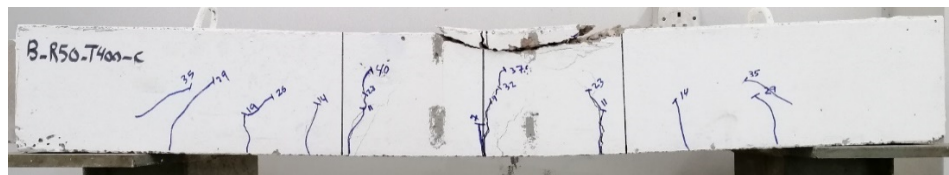
For beams damaged at 400°C, Fig. 14 indicated that failure mode and cracking patterns are similar to those of unheated beams, Cracks initiated at straight vertical profiles in the middle of span in the tension zone before diagonal cracks appeared near the supports. Then more cracks appeared and extended to the compression side, leading to failure. Specimens failed by yielding of tensile steel and then compression failure in concrete at the compression zone with an increase in the number of cracks.



a) B-N-T400-C, Loading cracks



b) B-R25-T400-C, Loading cracks



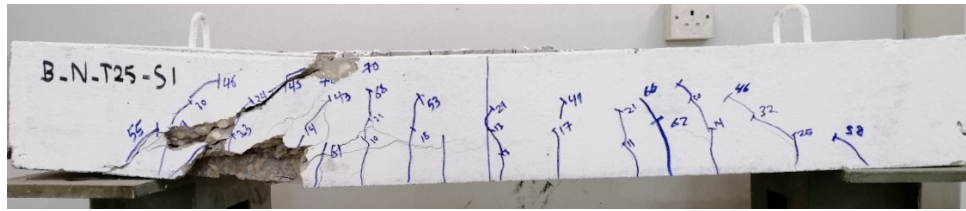
c) B-R50-T400-C, Loading cracks

**Figure 14. Failure mode of control test specimens heated at 400°C for 3 hrs.**

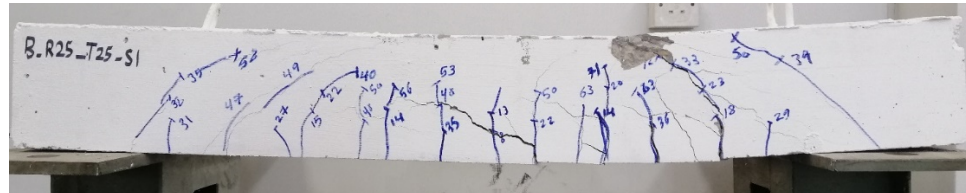
The failure modes of intact specimens strengthened with one NSM-CFRP strip at the bottom are shown in Fig. 15. For specimens B-N-T25-S1, B-R25-T25-S1, B-R50-T25-S1, and B-R100-T25-S1, when the load applied, flexural cracks initiated at the middle zone, and with further application of the load, diagonal cracks initiated near supports in the high shear zone with inclination before the cracks propagated rapidly toward the high-stress zone. Near ultimate load, horizontal cracks at the web appeared and caused a cover separation. The collapse of the beams started with partial concrete cover separation followed by



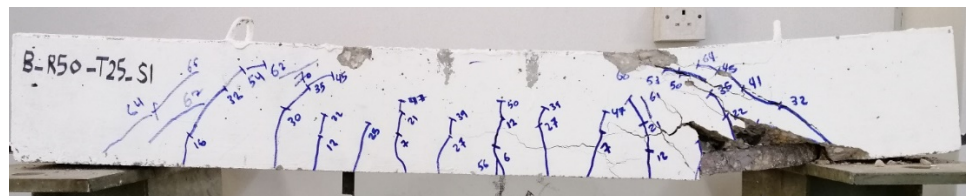
shear failure. On the other hand, specimens strengthened with SNSM CFRP Strips (two strips, one strip at each side), B-N-T25-S2 and B-R50-T25-S2, at ultimate stage, failed by the horizontal cracks that appeared and caused cover separation and then flexural failure followed by concrete crushing. The collapse of the beams started with partial concrete cover separation followed by concrete crushing.



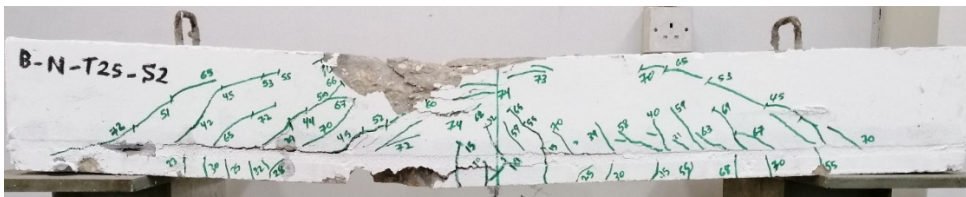
a) B-N-T25-S1, Loading cracks



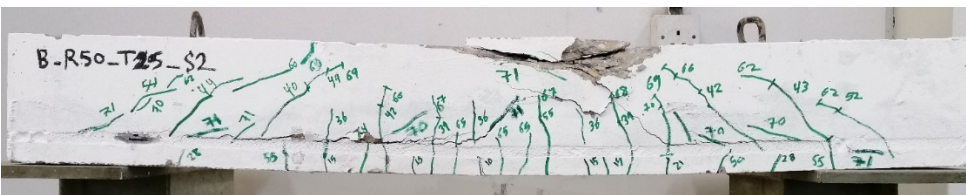
b) B-R25-T25-S1, Loading cracks



c) B-R50-T25-S1, Loading cracks



d) B-N-T25-S2, Loading cracks



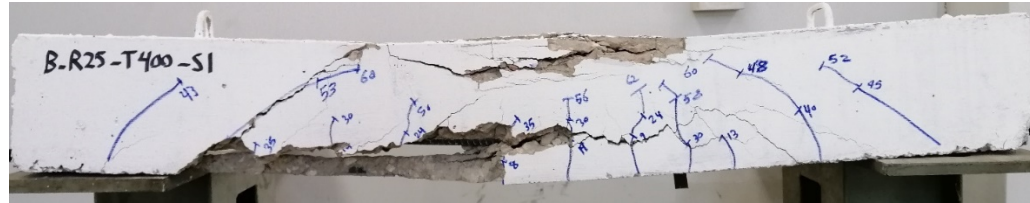
e) B-R50-T25-S2, Loading cracks

**Figure 15. Failure mode of strengthened specimens at 25 °C.**

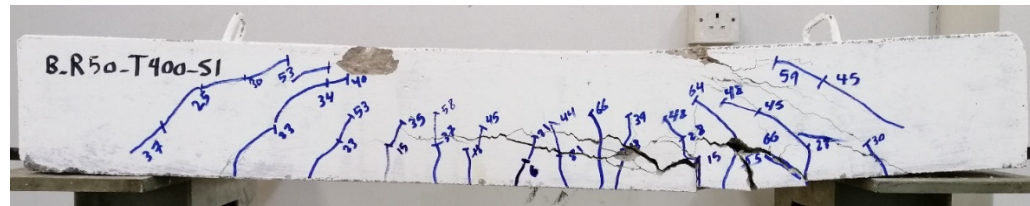
Specimens that heat-damaged at 400 °C and were repaired with one NSM CFRP strip at the bottom are shown in Fig. 16. For specimens B-N-T400-S1, B-R25-T400-S1, B-R50-T400-S1, and B-R100-T400-S1, when the load applied, flexural cracks were initiated at the middle zone, and with further application of the load, diagonal cracks initiated near supports in the high shear zone with inclination before they propagated rapidly toward the high-stress zone. However, near ultimate load, specimens with different concrete mixes showed different failure modes.



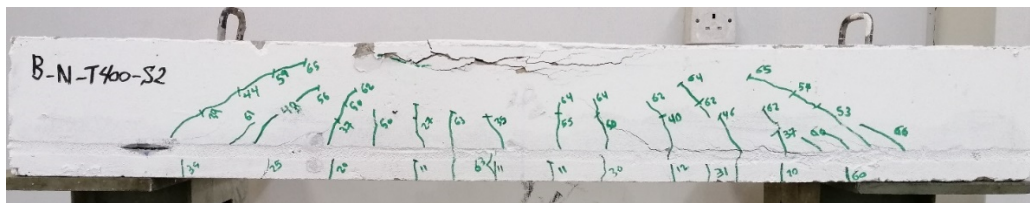
a) B-N-T400-S1, Loading cracks



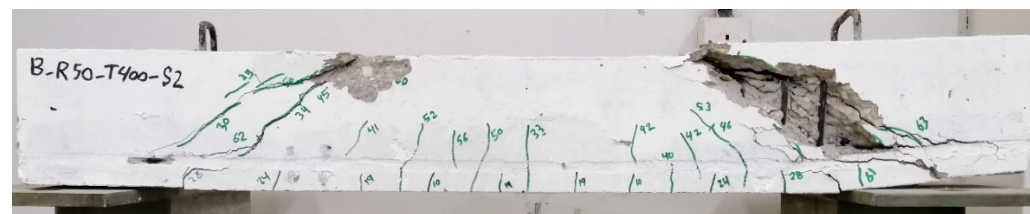
b) B-R25-T400-S1, Loading cracks



c) B-R50-T400-S1, Loading cracks



d) B-N-T400-S2, Loading cracks



e) B-R50-T400-S2, Loading cracks

**Figure 16. Failure mode of repaired test specimens after heating at 400°C for 3 hrs.**

For B-N-T400-S1, partial cover separation with hair-line cracks in the concrete at the compression zone appeared due to concrete crushing. Local splitting of the epoxy cover was noticed. Specimen B-R25-T400-S1 experienced concrete crushing at the same time with partial concrete cover separation. In contrast, B-R50-T400-S1 failed by horizontal cracks that caused partial cover separation followed by shear failure, whereas B-R100-T400-S1 failed by shear. This is because shear capacity is more dependent on concrete than steel in addition to the low shear resistance of RAC as RCA% increases. On the other hand, specimen B-N-T400-S2, repaired with SNSM CFRP Strips (two strips, one strip at each side), failed at the ultimate stage by concrete crushing, whereas B-R50-T400-S2 experienced partial cover separation followed by shear failure. This is because recycled aggregate concrete has a reduction in concrete's mechanical properties including compressive strength and tensile strength in addition to the lower shear resistance of beams cast with RAC.

### 3.8. Comparison with related work in the literature

The optimum replacement ratio of recycled aggregate to enhance the mechanical properties of concrete was reported in [48] as 30 % while based on the current work is about 25 %. In this study, at 50 % RA replacement ratio, the compressive strength drops significantly at 400 °C while [49] reported significant drop in compressive strength for 30 % replacement ratio at 600 °C. Furthermore, the experimental results obtained in this work is consistent with the findings reported in [14–19, 50, 51]. The recycled aggregate



content slightly affects the load – deflection behavior of reinforced concrete beams. The ultimate load, mid-span deflection, stiffness, and toughness for NA beams is almost comparable to ultimate load for RAC beams at room temperature. Heat damaged beams repaired with NSM-CFRP were found to regain the flexural capacity and increase the load capacity and stiffness of damaged beams. The failure mode of repaired specimens with NSM-CFRP was partial concrete cover separation followed by concrete crushing.

#### 4. Conclusions

Based on this study, and its established conception and formulations, the following conclusions can be drawn:

1. Exposing plain RAC to elevated temperatures of 400 °C for three hours created intense cracking on its surface. The cracks intensity increases as the recycled concrete aggregate increases as well as the level of heat exposure. Accordingly, their post-heating mechanical performance degraded as indicated by the reduction in its strength.
2. Recycled concrete aggregate does not have an effect in the ultimate load carrying capacity of unheated reinforced beams when the compressive strength of concrete is fixed whereas exposing reinforced recycled concrete beams to elevated temperatures of 400°C for three hours causes a noticeable damage and degradation on their post-heating mechanical properties and a bond deterioration between the RAC and the steel reinforcement, as indicated by the reduction in the flexural load capacities and stiffnesses.
3. For heat-damaged beams, the reduction in stiffness increases as RCA content increases due to the large amount of decomposed cement mortar in the RAC that leads to a weaker bond with steel.
4. NSM-CFRP strips technique is suitable for the strengthening/repairing of unheated/heat-damaged, reinforced, recycled aggregate concrete beams.
5. Strengthening of intact beams with NSM CFRP strips helped to improve the overall mechanical performance. Specimens cast with different replacement ratios showed a comparable and typical response, based on the load-deflection curves.
6. The stiffness of the repaired beams decreased as the recycled concrete aggregate content increased due to the weaker bond between damaged recycled aggregate concrete and the epoxy adhesive.
7. Using side NSM CFRP with two strips at sides (one strip at each side) for strengthening and repairing of intact/heat-damaged RAC beams helps to achieve slightly higher load carrying capacities
8. The SNSM CFRP strips repairing configuration helps to reduce the induced strain in the CFRP strips to about 40 % of its value when a single concentrated strip at bottom is used. Moreover, it helps to minimize the slippage due to lower stresses and strains in the CFRP strips.

#### 5. Acknowledgement

This research was supported by the Dean of Research at Jordan University of Science and Technology, grant number 162/2019.

#### References

1. El-Nimri, R., Abdel-Jaber, M., Hunaiti, Y., Abdel-Jaber, M. Behavior of light-gauge steel beams filled with recycled concrete. Magazine of Civil Engineering. 2021. 10102–10102. DOI: 10.34910/MCE.101.2
2. Bairagi, N.K., Vidyadhara, H.S., Ravande, K. Mix design procedure for recycled aggregate concrete. Construction and Building Materials. 1990. 4(4). Pp.188–193. DOI: 10.1016/0950-0618(90)90039-4
3. De Brito, J., Saikia, N. Recycled Aggregate in Concrete: Use of Industrial. Construction and Demolition Waste. Green Energy and Technology. Springer-Verlag, London. 2013. DOI: 10.1007/978-1-4471-4540-0
4. Kabir, M.I., Subhani, M., Shrestha, R., Samali, B. Experimental and theoretical analysis of severely damaged concrete beams strengthened with CFRP. Construction and Building Materials. 2018. 178. Pp. 161–174. DOI: 10.1016/j.conbuildmat.2018.05.038
5. Shahidan, S., Azmi, M.A.M., Kupusamy, K., Zuki, S.S.M., Ali, N. Utilizing construction and demolition (C&D) waste as recycled aggregates (RA) in concrete. Procedia engineering. 2017. 174. Pp. 1028–1035. DOI: 10.1016/j.proeng.2017.01.255
6. Rao, M.C. Properties of recycled aggregate and recycled aggregate concrete: effect of parent concrete. Asian Journal of Civil Engineering. 2018. 19(1). Pp. 103–110. DOI: 10.1007/s42107-018-0011-x
7. Salahuddin, H., Nawaz, A., Maqsoom, A., Mehmood, T. Effects of elevated temperature on performance of recycled coarse aggregate concrete. Construction and Building Materials. 2019. 202. Pp. 415–425. DOI: 10.1016/j.conbuildmat.2019.01.011
8. Salau, M.A., Oseafiana, O.J., Oyegoke, T.O. Effects of Elevated Temperature on Concrete with Recycled Coarse Aggregates. In IOP Conference Series: Materials Science and Engineering. 2015. (Vol. 96, No. 1, p. 012078). IOP Publishing. DOI: 10.1088/1757-899X/96/1/012078
9. Sarhat, S.R., Sherwood, E.G. Residual mechanical response of recycled aggregate concrete after exposure to elevated temperatures. Journal of Materials in Civil Engineering. 2012. 25(11). Pp. 1721–1730. DOI: 10.1061/(ASCE)MT.1943-5533.00-00719

10. Yang, H., Lv, L., Deng, Z., Lan, W. Residual compressive stress-strain relation of recycled aggregate concrete after exposure to high temperatures. *Structural Concrete*. 2017. 18(3). Pp. 479–486. DOI: 10.1002/suco.201500153
11. Vieira, J.P.B., Correia, J.R., De Brito, J. Post-fire residual mechanical properties of concrete made with recycled concrete coarse aggregates. *Cement and Concrete Research*. 2011. 41(5). Pp. 533–541. DOI: 10.1016/j.cemconres.2011.02.002
12. Zega, C.J., Di Maio, A.A. Recycled concrete exposed to high temperatures. *Magazine of Concrete Research*. 2006. 58(10). Pp. 675–682. DOI: 10.1680/mac.2006.58.10.675
13. Xiao, J.Z., Zhang, C.Z. Fire damage and residual strengths of recycled aggregate concrete. In *Key Engineering Materials*. 2007. (Vol. 348, Pp. 937–940). Trans Tech Publications. DOI: 10.4028/www.scientific.net/KEM.348-349.937
14. Wardeh, G., Ghorbel, E. Experimental Investigation and Analytical Study on the Flexural Behavior of Reinforced Recycled Aggregate Concrete Beams. *Journal of Modern Mechanical Engineering and Technology*. 2018. 5. Pp. 1–23. DOI: 10.15377/2409-9848.2018.05.1
15. Knaack, A.M., Kurama, Y.C. Service-load deflection behavior of reinforced concrete beams with recycled concrete aggregate. In *Structures Congress 2013: Bridging Your Passion with Your Profession*. 2013. Pp. 2705–2716. DOI: 10.1061/978078-4412848.235
16. Ignjatović, I.S., Marinković, S.B., Mišković, Z.M., Savić, A.R. Flexural behavior of reinforced recycled aggregate concrete beams under short-term loading. *Materials and structures*. 2013. 46(6). Pp. 1045–1059. DOI: 10.1617/s11527-012-9952-9
17. Pan, L.Y., Shao, W.J., Li, G.X., Li, H.F. Experimental Study on Flexural Resistance of Reinforced Recycled-concrete Beams. In *Applied Mechanics and Materials*. 2013. (Vol. 438, Pp. 789–793). Trans Tech Publications. DOI: 10.4028/www.scientific.net/AMM.438-439.789
18. Sato, R., Maruyama, I., Sogabe, T., Sogo, M. Flexural behavior of reinforced recycled concrete beams. *Journal of Advanced Concrete Technology*. 2007. 5(1). Pp. 43–61. DOI: 10.3151/jact.5.43
19. Knaack, A.M., Kurama, Y.C. Behavior of reinforced concrete beams with recycled concrete coarse aggregates. *Journal of Structural Engineering*. 2014. 141(3). p. B4014009. DOI: 10.1061/(ASCE)ST.1943-541X.0001118
20. Duy, N.P., Anh, V.N., Hiep, D.V., Anh, N.M.T. Strength of concrete columns reinforced with Glass fiber reinforced polymer. *Magazine of Civil Engineering*. 2021: 10108–10108. DOI: 10.34910/MCE.101.8
21. Al-Rousan, R., Abo-Msamh, I. Impact of anchored CFRP on the torsional and bending behaviour of RC beams. *Magazine of Civil Engineering*. (2020). DOI: 10.18720/MCE.96.7
22. Kozinetc, K.G., Kaarki, T., Barabanshchikov, Y.G., Lahtela, V., Zotov, D.K. Mechanical Properties Of Sustainable Wooden Structures Reinforced With Basalt Fiber Reinforced Polymer. *Magazine Of Civil Engineering*. 2020. 100(8). Article No. 10012. DOI: 10.18720/Mce.100.12
23. Salakhutdinov, M.A., Gimranov, L.R. Kuznetsov, I.L., Fakhutdinov, A.E., Nurgaleeva, L.M. PFRP structures under the predominately short term load. *Magazine of Civil Engineering*. 2020. DOI: 10.18720/MCE.96.1
24. Al-Rousan, R. Behavior of strengthened concrete beams damaged by thermal shock. *Magazine of Civil Engineering* (2020). DOI: 10.18720/MCE.94.8
25. Travush, V., Konin, D., Krylov, A. Strength of reinforced concrete beams of high-performance concrete and fiber reinforced concrete. *Magazine of Civil Engineering*. 2018. DOI: 10.18720/MCE.77.8
26. Szabó, Z.K., Balázs, G.L. Near surface mounted FRP reinforcement for strengthening of concrete structures. *Periodica Polytechnica Civil Engineering*. 2007. 51(1). Pp. 33–38. DOI: 10.3311/pp.ci.2007-1.05
27. Khalifa, A.M. Flexural performance of RC beams strengthened with near surface mounted CFRP strips. *Alexandria Engineering Journal*. 2016. 55(2). Pp. 1497–1505. DOI: 10.1016/j.aej.2016.01.033
28. Hassan, T., Rizkalla, S. Investigation of bond in concrete structures strengthened with near surface mounted carbon fiber reinforced polymer strips. *Journal of composites for construction*. 2003. 7(3). Pp. 248–257. DOI: 10.1061/(ASCE)1090-0268(2003)7:3(248)
29. Täljsten, B., Carolin, A., Nordin, H. Concrete Structures Strengthened with near Surface Mounted Reinforcement of CFRP. *Advances in Structural Engineering*. 2003. 6(3). Pp. 201–213. DOI: 10.1260/13694330322419223
30. De Lorenzis, L., Nanni, A., La Tegola, A. Flexural and Shear Strengthening of Reinforced Concrete Structures with Near Surface Mounted FRP Rods. *Proceedings of the 3<sup>rd</sup> International Conference on Advanced Composite Materials in Bridges and Structures (ACMBS III)*. 2000. Ottawa. Ontario. Canada. Aug. 15-18. Pp. 521–528.
31. El-Hacha, R., Rizkalla, S., Kotynia, R. Modeling of reinforced concrete flexural members strengthened with near-surface mounted FRP reinforcement. In *7<sup>th</sup> Int. Symp. on Fiber Reinforced Polymer (FRP) Reinforcement for Concrete Structures (FRPRCS-7)*. 2005. (Pp. 1681–1700).
32. Al-Mahmoud, F., Castel, A., François, R., Tourneur, C. Strengthening of RC members with near-surface mounted CFRP rods. *Composite Structures*. 2009. 91(2). Pp. 138–147. DOI: 10.1016/j.compstruct.2009.04.040
33. De Lorenzis, L. and Teng, J.G. Near-surface mounted FRP reinforcement: An emerging technique for strengthening structures. *Composites Part B: Engineering*. 2007. 38(2). Pp. 119–143. DOI: 10.1016/j.compositesb.2006.08.003
34. Teng, J.G., de Lorenzis, L., Wang, B., Li, R., Wong, T.N., Lam, L. Debonding failures of RC beams strengthened with near surface mounted CFRP Strips. *Journal of composites for construction* 2006. 10. no. 2. 92–105. DOI 10.1061/(ASCE)1090-0268;10:2-(92). DOI: 10.1061/(ASCE)1090-0268(2006)10:2(92)
35. Yost, J.R., Gross, S.P., Dinehart, D.W., Mildenberg, J.J. Flexural behavior of concrete beams strengthened with near-surface-mounted CFRP strips. *ACI Structural Journal*. 2007. Vol. 104. Iss. 4. Pp. 430–437.
36. Ferrari, V.J., de Hanai, J.B., de Souza, R.A. Flexural strengthening of reinforcement concrete beams using high performance fiber reinforcement cement-based composite (HPFRCC) and carbon fiber reinforced polymers (CFRP). *Construction and Building Materials*. 2013. 48. Pp. 485–498. DOI: 10.1016/j.conbuildmat.2013.07.026
37. Jadooe, A., Al-Mahaidi, R., Abdouka, K. Behaviour of heat-damaged partially-insulated RC beams using NSM systems. *Construction and Building Materials*. 2018. 180. Pp. 211–228. DOI: 10.1016/j.conbuildmat.2018.05.279
38. Jadooe, A., Al-Mahaidi, R., Abdouka, K. Performance of heat-damaged partially-insulated RC beams strengthened with NSM CFRP strips and epoxy adhesive. *Construction and Building Materials*. 2018. 159. Pp. 617–634. DOI: 10.1016/j.conbuildmat.2017.11.020

39. ASTM, A. C127 Standard Test Method for Relative Density (Specific Gravity) and Absorption of Coarse Aggregate. American Society for Testing and Materials: West Conshohocken, PA, USA. 2015. DOI: 10.1520/C0127-15
40. ASTM, A. C128 Standard Test Method for Relative Density (Specific Gravity) and Absorption of Fine Aggregate. American Society for Testing and Materials: West Conshohocken, PA, USA. 2015. DOI: 10.1520/C0128-15
41. ASTM, C136/C136M-14. (2014). Standard Test Method for Sieve Analysis of Fine and Coarse Aggregates. West Conshohocken, PA, USA. 2014. DOI: 10.1520/C0136-06
42. ASTM C131 / C131M-20. Standard Test Method for Resistance to Degradation of Small-Size Coarse Aggregate by Abrasion and Impact in the Los Angeles Machine, ASTM International, West Conshohocken, PA. 2020. DOI: 10.1520/C0131\_C0131M-20
43. ASTM A370-16. Standard Test Methods and Definitions for Mechanical Testing of Steel Products. American Society for Testing and Materials International, West Conshohocken, United States. 2016. DOI: 10.1520/A0370-20
44. ACI Manual of Concrete Practice. Standard practice for selecting proportions for normal, heavyweight, and mass concrete (ACI 211.1), Part I: Materials and General Properties of Concrete, Detroit, Michigan. 2008.
45. ASTM, C143/C143M. Standard Test Method for Slump of Hydraulic Cement Concrete. West Conshohocken, PA. 2000. DOI: 10.1520/C0143\_C0143M-00
46. American Society for Testing and Materials International (ASTM). West Conshohocken, PA: 2004.
47. American Concrete Institute. Building Code Requirements for Structural Concrete and Commentary (ACI-318), Farmington Hills, Michigan. 2019. DOI: 10.14359/51716937.
48. Ali, R., Hamid, R. Workability and Compressive Strength of Recycled Concrete Waste Aggregate Concrete. Applied Mechanics and Materials. 2015. 754–755, 417–420. DOI: 10.4028/www.scientific.net/amm.754-755.417
49. Salau, M.A., Oseafiana, O.J., Oyegoke, T.O. Effects of Elevated Temperature on Concrete with Recycled Coarse Aggregates. IOP Conference Series: Materials Science and Engineering. 2015. 96, 012078. DOI: 10.1088/1757-899x/96/1/012078
50. Jadooe, A., Al-Mahaidi, R., Abdouka, K. Experimental and numerical study of strengthening of heat-damaged RC beams using NSM CFRP strips. Construction and Building Materials. 2017. 154. Pp. 899–913. DOI: /10.1016/j.conbuildmat.2017.07.202
51. Seara-Paz, S., González-Fontboa, B., Martínez-Abella, F., Eiras-López, J. Flexural performance of reinforced concrete beams made with recycled concrete coarse aggregate. Engineering Structures. 2018. 156, 32–45. DOI: 10.1016/j.engstruct.2017.11.015

**Information about authors:**

**Wasim Barham, PhD**

ORCID: <https://orcid.org/0000-0003-1106-5195>

E-mail: [wsbarham@just.edu.jo](mailto:wsbarham@just.edu.jo)

**Yasmeen Obaidat, PhD**

ORCID: <https://orcid.org/0000-0002-0533-366X>

E-mail: [ytobeidat@just.edu.jo](mailto:ytobeidat@just.edu.jo)

**Huthaifa Alkhatatbeh,**

ORCID: <https://orcid.org/0000-0002-3017-1834>

E-mail: [haalkhatatbeh16@eng.just.edu.jo](mailto:haalkhatatbeh16@eng.just.edu.jo)

*Received 14.09.2020. Approved after reviewing 27.04.2021. Accepted 28.04.2021.*



Research article


UDC 628.168

DOI: 10.34910/MCE.111.7

## Regularities of rapid filter backwash water clarification in reagent-free mode

D.A. Butko , M.S. Volodina 

Don State Technical University, Rostov-on-Don, Russia

 [den\\_111@mail.ru](mailto:den_111@mail.ru)**Keywords:** spent filter backwash water, precipitation, mixing, treated water, water recycling, coagulation

**Abstract.** Discharge of rinsing water from fast filters into surface water bodies as a way of their disposal is unacceptable for environmental reasons, and in some countries it is prohibited by law. Research by Russian and foreign scientists is aimed at studying the schemes for returning wash water to the main stream using reagent methods of clarification, ultrafiltration or filtration on ceramic filters. In this paper, the processes of removing suspended solids from rinsing waters by means of reagent-free clarification under static conditions of sedimentation facilities are considered. In this case, the treated water was exposed to mixing with Camp's criterion obtained as a result of the analysis of the modes of movement in pipelines from the fast filter to the settling facility for the treatment of rinse water, as well as under conditions of additional mixing inside the treatment facilities either by stirrers or by aeroflocculation. Based on the analysis of the results of water clarification under the conditions of reagent-free sedimentation with stirring, mathematical dependences of the clarification effect on the Camp's criterion, water temperature, initial content of suspended solids and clarification time were obtained.

### 1. Introduction

The contamination of surface water bodies (streams and reservoirs) with untreated wastewater under conditions of low water levels in recent year's calls into question their use as a source of water supply to populated areas. An increase in the content of phytoplankton, an increase in the concentration of aluminum, iron and phosphates leads to the fact that water treatment plants cannot cope with the task of preparing water for drinking needs. The volume of untreated wastewater entering surface water bodies in the period from 2010 to 2017 constantly increased from 2503.45 to 3416.60 million m<sup>3</sup> [1]. In 2017, 188645 tons of suspended solids, 504.98 tons of aluminum (as Al<sup>3+</sup>) and 2137.02 tons of iron (as Fe<sup>2+</sup>, Fe<sup>3+</sup> – all water-soluble forms) were discharged into the rivers, which are one of the main components of the pollution from the backwash water of water treatment plants.

For a long time, less attention was paid to the research of systems for reuse of backwash water from rapid filters and water after washing of sedimentation treatment facilities compared with the other aspects of the operation of water treatment plants for municipal and industrial purposes. In Russia (USSR), this problem was explored by V.G. Vodin, V.L. Draginsky [2], V.N. Kuznetsov [3], M.I. Urvantseva [4, 5], and others. In the foreign literature, the topic of backwash water treatment is reflected in the papers [6–10], which offer various technological schemes for treatment and directions for further use of these waters, as well as evaluating the possibility of returning them to the head of structures. The most widely presented results are on the introduction of ultrafiltration into backwash water return schemes [8, 11–14] or on special ceramic filters [14, 15], co-coagulation and ultrafiltration [16], as well as sedimentation in facilities with flotation [9]. The vast majority of publications on the topic of treatment of backwash water rapid filters

Butko, D.A., Volodina, M.S. Regularities of rapid filter backwash water clarification in reagent-free mode. Magazine of Civil Engineering. 2022. 111(3). Article No. 11107. DOI: 10.34910/MCE.111.7

© Butko, D.A., Volodina, M.S., 2022. Published by Peter the Great St. Petersburg Polytechnic University.



This article is licensed under a CC BY-NC 4.0

describe the process of clarification using a coagulant and (or) flocculant [9, 11, 17–20]. A survey of water treatment plants in the United States, where the requirement to recirculate backwash water from rapid filters is legally enforced, showed that 30 % of plants did not provide any treatment of backwash water. Among the plants that were treating 54 % used precipitation, 20 % – equalization, 14 % – precipitation and equalization, and 11 % – other processes [21]. Lilia Mazari and Djamal Abdessemed [19], unlike the others, investigated the possibility of reagentless treatment of backwash water and its use as a coagulant for clarification of feed water in the main flow.

Sedimentation is the cheapest method of treatment, but it is also important to consider that in most cases, constructions for reuse of wash water are located far from filters (the source of waste wash water) and suspended particles are affected by hydrodynamic forces caused by the processes of stirring the volume of water when moving through the pipeline.

The stirring intensity is usually characterized by the root-mean-square (RMS) velocity gradient ( $G$ ) (often referred to simply as the velocity gradient) or its product for the stirring time  $GT$  (Camp criterion).

Babekov E.D. in [22] underlines that the minimum value of the RMS velocity gradient at which the destruction of flocs occurs is  $100 \text{ s}^{-1}$ , and that there is the following dependence between the shear stress  $\tau_s$  in the mixed medium and the velocity gradient:

$$\tau_s = \frac{5}{2} \eta G, \quad (1)$$

where  $\eta$  is the dynamic viscosity of the medium, Pa·s.

In [22], the results of measurements of the shear stress of precipitation conducted by Baryshnikova and amounting to  $1.5\text{--}6 \text{ mg/cm}^2$  ( $0.14715\text{--}0.5886 \text{ Pa}$ ) are presented, and this corresponds to a RMS velocity gradient from  $58.84 \text{ s}^{-1}$  to  $235 \text{ s}^{-1}$ . However, stirring has not only a negative effect on the suspended particles, but also contributes to the strengthening of the suspended solids and their intensive sedimentation. This paper presents the results of studies on the treatment of backwash water with different velocity gradients (with different Camp criteria) in construction for reuse of wash water.

The aim of the study is to obtain the dependencies of reagentless clarification of backwash water in constructions for their reuse. The following tasks contributed to the achievement of the research aim:

- determination of the magnitude of the RMS velocity gradient ( $G$ ) and stirring time ( $T$ ) during the movement of backwash water from rapid filters to their treatment facilities (construction for reuse of backwash water);
- experimental study of clarification processes in modelling the stirring in the pipeline and in the pipeline, followed by the implementation of the second stage of stirring in a flocculation basin, which is part of the construction for reuse of wash water;
- determination of influencing factors on the efficiency of clarification during the stirring and obtaining mathematical dependencies of the clarification effect when modelling stirring in the pipeline and in the pipeline, followed by processing in the flocculation basin.

## 2. Methods

### 2.1. Research objects

The research was conducted at the water treatment plants (WTP) of the Central water supply system of Rostov-on-Don, involving a two-stage reagent scheme of water treatment: sedimentation followed by rapid filtration using the reagent flocculant-coagulant FL 4540 (polyDADMAC). At WTP chlorination (with liquid chlorine or sodium hypochlorite) is used to decontaminate and improve the coagulation properties of the suspended solids. The rapid filters consist of a single-layer filter of  $0.5\text{--}3.0 \text{ mm}$  quartz sand with a coefficient of heterogeneity 1.39 or 1.47. The filters are backwashed with clarified water from the clean water tanks supplied by pumps at an estimated flow rate of  $12 \text{ L/s}\cdot\text{m}^2$ . Currently, waste water is discharged through a system of beams in the Don river.

The quality of waste water after washing the rapid filters throughout the year is characterized by a concentration of suspended solids from  $30$  to  $400 \text{ mg/dm}^3$  and color from  $29$  to  $47 \text{ Pt-Co}$  units, despite the fact that the feed Don water is characterized as "low-color" for most of the year. The indicators "Total alkalinity", "Active reaction of the medium (pH)", "Temperature" in the wastewater were equal to or slightly different from the values in the feed water. Total alkalinity was in the range from  $1.8$  to  $4.9 \text{ mmol/dm}^3$ , active reaction of the medium (pH) was in the range  $6.6\text{--}8.21$  with a predominance of values in the range  $7.0\text{--}$

8.0, and temperature varied from 0.1 °C (winter) to 29.5 °C (summer). Residual concentrations of FL 4540 in the backwash water ranged from less than 0.02 to 0.23 mg/dm<sup>3</sup>.

## 2.2. Description of flocculation process

The formula for calculating the RMS velocity gradient for a gravity pipeline takes the following form:

$$G = \sqrt{\frac{V^2 i g}{\nu}}, \quad (2)$$

where  $V$  is velocity of water movement in the pipeline, m/s;  $\nu$  is kinematic viscosity of water, m<sup>2</sup>/s;  $i$  is pipeline gradient.

Converting the formula (2) and involving the determination of the flow velocity by the Chezy equation, and the Chezy factor included in it by the formula of N.N. Pavlovsky, we obtain

$$G = \frac{i}{n} \sqrt{\frac{g (0.25d)^{1+3\sqrt{n}}}{\nu}}, \quad (3)$$

where  $n$  is friction factor in the Chezy formula, which depends on the pipeline material;  $d$  is internal diameter of the pipeline, m.

In fact, (3) is a linear dependence of the RMS velocity gradient on the pipeline gradient where the angle of the line to the abscissa axis depends on the diameter and material of the pipeline and the temperature of the transported water (Fig. 1). It should be noted that the value of friction factor should be taken from reference data, but not in a consistent manner, as is recommended for hydraulic calculations of gravity ( $n = 0.014$ ) or pressure networks ( $n = 0.013$ ). The design of gravity pipe from filters is usually performed on the calculated flow rate from simultaneous backwash of filters (one or two), while the geodetic gradient coincides with the hydraulic one. The conditions of a real multi-functioning pipelines for drainage of backwash water from rapid filters are characterized by a probabilistic distribution of costs values, coming in it and reduced pipeline capacity due to different factors that can incur an increase in hydraulic gradient and formation of pressure mode with a change in the hydrodynamic mode of motion.

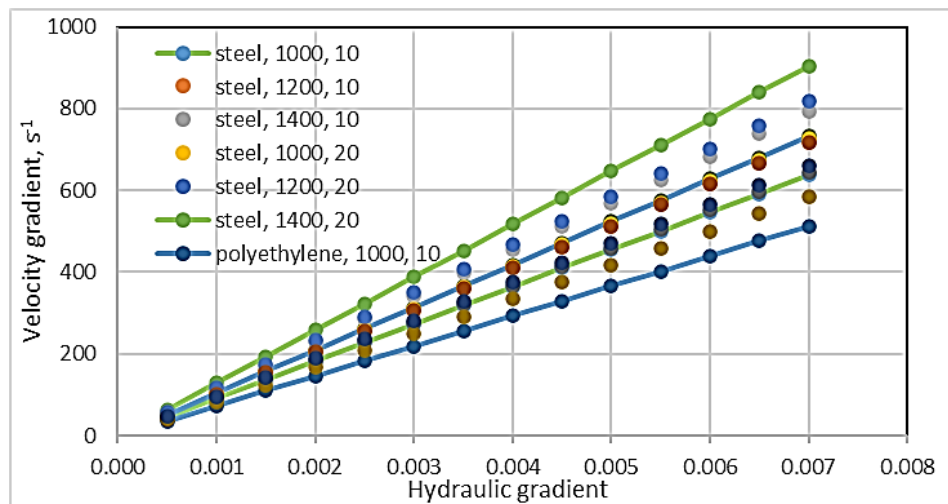


**Figure 1. Changing of the RMS velocity gradient in a gravity pipeline at different hydraulic gradients.**

The recommended value of the RMS velocity gradient for mixers is in the range of 60–300 s<sup>-1</sup>. For flocculation basin they depend on the design and are in the range of 25–60 s<sup>-1</sup> [12]. Analyzing the values of the RMS velocity gradient obtained by the formula (3) (Fig. 1), we can conclude that they are at the level recommended for stirrers or higher, which inevitably causes the impact on the suspended flocs leading to their destruction.

## 2.3. Studies on the sedimentation treatment of wash water

Based on this, two groups of experiments were conducted in the study: clarification of wash water by sedimentation after hydrodynamic impact with RMS velocity gradients characteristic of water movement through the pipeline and clarification by sedimentation after hydrodynamic impact with RMS velocity

gradients characteristic of water movement through the pipeline plus stirring with RMS velocity gradients characteristic of flocculation basins. Water treatment was carried out under laboratory conditions with a sedimentation depth of 0.2, 0.26 and 0.32 m.

Processing of the obtained results was based on the previously derived dependence for sedimentation of backwash water impurities under static conditions [23] and theoretical conclusions from the theory of M.S. Smolukhovskiy. Experimental work to determine the efficiency of water clarification under static conditions was carried out by the author in different periods of the year on the water that was taken directly from quartz sand rapid filters during their washing. The subsequent sedimentation tests were done in the laboratory. As a result of processing the results, an equation is obtained for determining the time of sedimentation for a given clarification effect:

$$Ef = 12.19 \ln(th^{0.51}) - 0.93T + 0.019C_w, \quad (4)$$

where  $t$  is the clarification time of the backwash water to reach the given clarification effect, s;  $Ef$  is given clarification effect, %;  $C_w$  is initial concentration of suspended solids, mg/dm<sup>3</sup>;  $T$  is the temperature of the backwash water in the process of clarification, °C;  $h$  is height of the sedimentation layer, m.

With 95 % confidence, equation (4) can be used in the quality range of backwash water with a suspended solids content from 50 to 400 mg/dm<sup>3</sup> and a water temperature from 5 to 25 °C.

Smolukhovskiy's theory of coagulation states that the velocity (intensity) of coagulation depends on the radius of the sphere of attraction of the particle (approximately equal to two radii of the particle), the intensity of diffusion due to Brownian motion and the initial number of particles in the system. In this case, from the point of view of the efficiency of the collision of particles, the coagulation processes are classified into two types: rapid – each collision ends with the formation of an aggregate and slow – not all collisions end with the formation of aggregates.

For the case of rapid coagulation, the equation describing the change in the number of particles per unit of volume of the system at time  $\tau$  has the form

$$n_\tau = \frac{n_0}{1 + 8\pi D r n_0 \tau} \quad \text{or} \quad n_\tau = \frac{n_0}{1 + \frac{\tau}{T_{1/2}}}, \quad (5)$$

where  $D$  is the diffusion coefficient of single particles;  $r$  is the radius of the particles;  $n_0$  is initial concentration of particles;  $T_{1/2}$  is coagulation time, during which the number of particles per unit volume of sol is halved.

The equation looks similar for slow coagulation with the introduction of the efficiency coefficient of convergence of particle collisions  $\psi$ :

$$n_\tau = \frac{n_0}{1 + \psi 8\pi D r n_0 \tau} \quad \text{or} \quad n_\tau = \frac{n_0}{1 + \psi \frac{\tau}{T_{1/2}}}. \quad (6)$$

In water treatment plants, perikinetic coagulation processes take place, although it is almost impossible to meet their "pure" form due to the constant movement of water and the presence of a minimal RMS velocity gradient. According to the data presented in the monograph [22], orthokinetic coagulation begins to prevail over perikinetic when the particle size is about 1 mcm. The backwash water contains the particles with sizes exceeding 1 mcm (see Fig. 2).



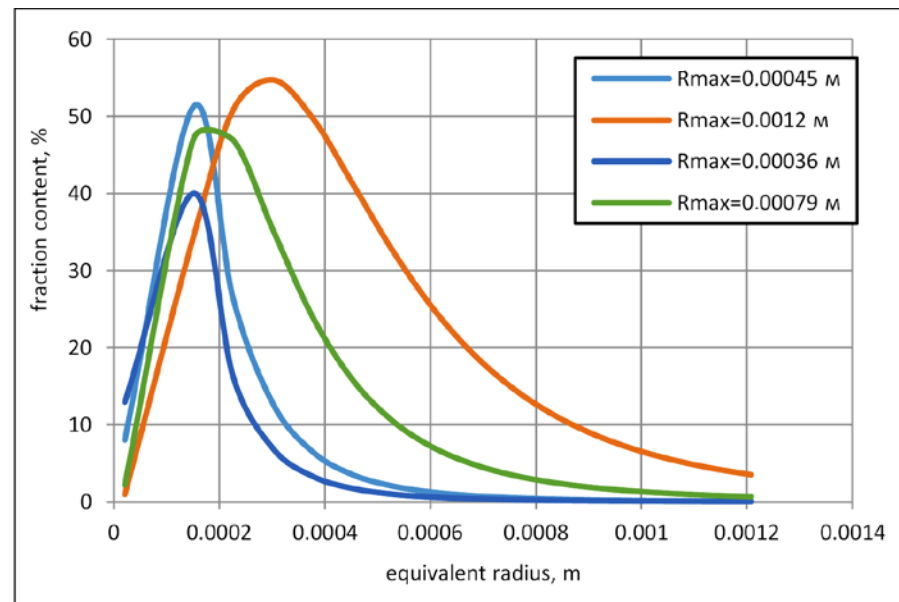


**Figure 2. Derived curve of particle distribution in the backwash water obtained during clarification without mixing [22]. Rmax is maximum radius, m.**

In the research of Harris [24], based on the theory of M.S. Smolukhovsky, the ratio for rapid coagulation was obtained

$$\frac{n_0}{n_\tau} = \exp(KEGn_0\tau), \quad (7)$$

where  $n_0$  is the numerical concentration of particles not coagulated by time  $\tau$ ,  $K$  is coagulation constant;  $E$  is experimentally determined parameter;  $G$  is the RMS velocity gradient.

Based on this ratio and the analysis of a number of other papers on this topic, it may be inferred that the product of  $C_oGT$  ( $C_o$  is the volume concentration of particles in the system,  $GT$  is the Camp criterion) can be used as a parameter that characterizes the conditions for water treatment with hydrolyzing coagulants. Again, it is to be noted that the backwash water is actually a product of coagulation of particles held in the layer of the filter and it contains known concentrations of coagulant (flocculant) (according to our experiment the reagent content is 0.02–0.23 mg/l) used for water treatment. Therefore, the use of the  $C_oGT$  product is acceptable even without the introduction of additional reagents, and when exposed to the backwash water exclusively by stirring. The volume concentration can be replaced by a weight concentration according to the ratio [15]  $C_o = \frac{C_w}{\gamma_0}$ , where  $\gamma_0$  is the amount of solid phase by mass per unit volume of unconsolidated sediment.

The effect of temperature on the process of perikinetic coagulation consists of changes in the intensity of Brownian motion of particles, which, for example, E.F. Kurgaev proposed to express by means of the agglomeration coefficient [25]:

$$\alpha_t = 0.5 + 0.025T. \quad (8)$$

At the same time, a change in temperature entails a change in the viscosity of the medium, and hence the entire heterophase system, which affects both the particle sedimentation velocity and the stirring parameters, in particular, the value of the velocity gradient. Generalizing, we get:

$$Ef = f(C_w, GT, t, T, h), \quad (9)$$

where  $t$  is the sedimentation time, s;  $h$  is depth of the water layer, m.

While investigating natural water treatment of the river Don using WPK-402 (analog of PolyDADMAC) the staff of the Department of water supply and drainage of RISI (Rostov Civil Engineering Institute) obtained the following equation

$$Ef = \text{const} - e^{-kG}. \quad (10)$$

The aforementioned dependencies are involved in obtaining an equation for processing experimental results. The experimental results were processed using MS Excel (Microsoft Corporation) and STATISTICA (StatSoft Inc.) software products. The obtained dependences were checked for the reliability of the approximation using the value of the Pearson correlation squared.

### 3. Results and Discussion

The first group of experiments was conducted by clarification of wash water by sedimentation after hydrodynamic impact with RMS velocity gradients characteristic of water movement through the pipeline. The effect of the velocity gradient applied to backwash water on the subsequent process of water clarification by sedimentation under laboratory conditions at different sedimentation layer depths is shown in the diagrams (Fig. 3, 4). These results presented on these figures are obtained under the clarification of river water during the research. The results of experiments (measurements) were processed using MS Excel with the construction of a trend line using a polynomial equation.

At low values of the velocity gradient (with the Camp criterion  $GT$  from 1200 to 5100), the effect of clarification of backwash water slightly differs from the values obtained in experiments without stirring [23] and does not depend on the value of the Camp criterion (Fig. 3), even if the clarification time is relatively short. Considering the abovementioned results conducted by Baryshnikova [22], under such conditions, the destruction of flocs does not seem to occur, since shear stresses do not reach critical values and the coagulation process occurs with undisturbed partially destabilized suspended particles. It is also important to consider that the suspended solids in the backwash water has a zeta potential closer to the isoelectric point than in the reagentless feed water. Thus, these results prove this idea. This is indicated by No-Suk Parka and his colleagues [26], whose studies show a decrease (in modulus) of the zeta potential of the suspended solids from  $(-19)$  mV in the feed water to  $(-1.4)$  mV in the sediments of sedimentation tanks and in the backwash water up to  $(-4.3)$  mV.

Increasing  $GT$  values in the range from 10000 to 71000, the changes in the clarification effect is slightly increasing. This should be considered a feature for waters with reagent WPK-402 (or PolyDADMAC analog) for feed water treatment. This means that this flocculant was used for clarification river water during the research period (Fig. 4). Previously performed by other soviet scientists studies on river water clarification using WPK-402 as a reagent showed the need for long-term and (or) intensive stirring in order to intensify flocculation and improve the sedimentation properties of the suspended solids in sedimentation tanks.

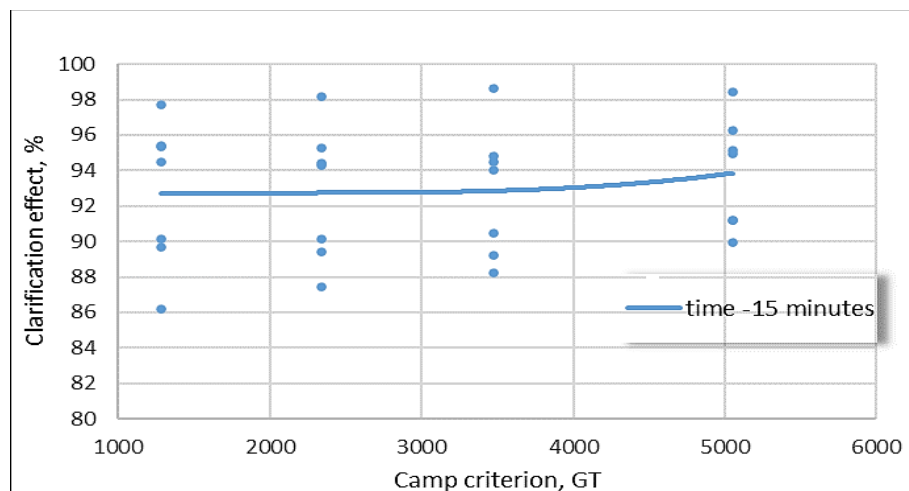


**Figure 3. Change in the clarification effect depending on the  $GT$  values in the range of 1000÷5000 at the depth of the sedimentation layer of 0.32 m (stirring with a constant RMS velocity gradient).**

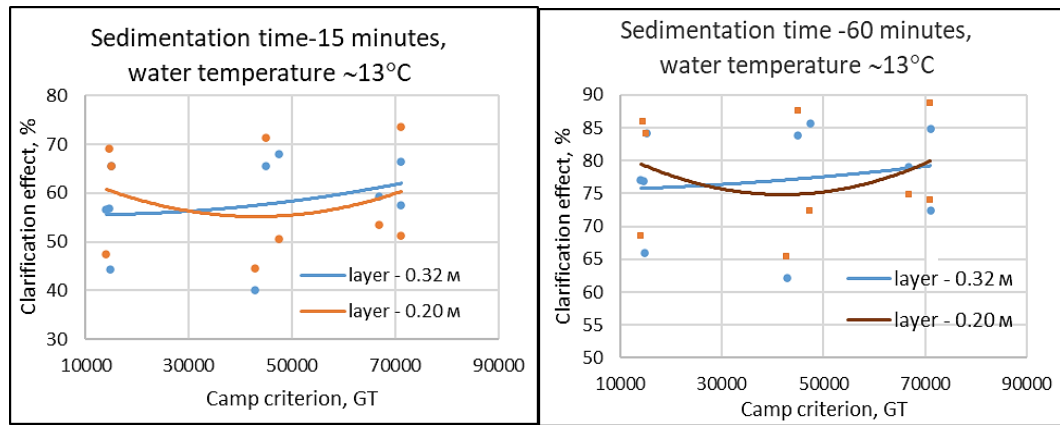


**Figure 4. Change in the clarification effect depending on the  $GT$  values in the range of 10000÷71000 at the depth of the sedimentation layer of 0.20 and 0.32 m (stirring with a constant RMS velocity gradient).**

The Fig. 5 presents the second group of experiments. The study of the treatment of backwash water with a variable velocity gradient was carried out according to the scheme: the first stage – rapid stirring while moving in the pipeline, the second stage – stirring in the flocculation basin. The results obtained in this experiment were different from the above. On the diagrams (Fig. 5) for the sedimentation time of 15 minutes and 60 minutes a minimum at  $GT$  value about 60000 is clearly expressed on the approximating curve. Comparison of the approximating curves in Fig. 4 and 5 shows that with the same sedimentation time, the use of a flocculation basin in a reuse constructions provides the best effect in the ranges of  $GT$  20000÷40000 and 82000÷90000. If the water is stirred with a  $GT$  of 40000 to 82000 when moving through the pipeline, the use of flocculation basin reduces the efficiency of backwash water clarification.

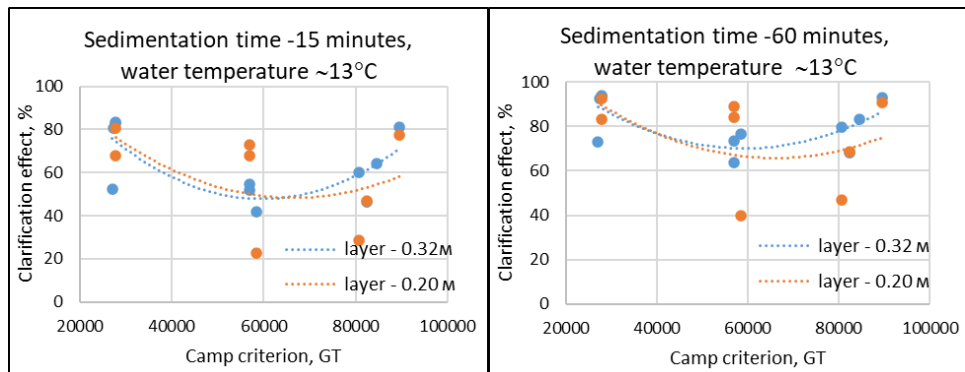


**Figure 5. Change in the clarification effect when modelling the movement of water through a pipeline followed by stirring in the flocculation basin (stirring with a variable RMS velocity gradient).**

Thanks to statistical processing of the results of experimental data obtained in laboratory conditions when modelling the movement of water through the pipeline to construction for reuse of backwash water we have gained an approximating dependence

$$Ef = 100 - t^{0.22} \exp \left( \frac{t^{0.032}}{h^{0.004}} (0.04T - 5.97) - (C_w GT)^{0.007} (0.46 \ln(T) + 0.2) + 10.07 \right), \quad (11)$$

where  $Ef$  is the clarification effect, %;  $t$  is the clarification time (precipitation), s;  $C_w$  is initial concentration of suspended substances in water, mg/dm<sup>3</sup>;  $T$  is water temperature, °C;  $GT$  is Camp criterion.

Stirring with velocity gradients characteristic of flocculation basins for a sufficient duration in the aforementioned intervals of the Camp criterion will contribute to the recovery of flocs without the introduction of additional doses of reagents. As a result of experiments with modelling water stirring in a pipeline followed by stirring in a construction with a lower gradient, the dependence is obtained

$$Ef = 100 - \exp \left( \left( \frac{0.17}{T^{0.03}} \right)^3 \frac{0.01GT + 13085 \left( \frac{0.23}{t^{0.03}} - 0.01 \right) - 6.53}{(C_w h)^{0.02}} \right). \quad (12)$$

Thus, using the obtained approximating equations, it is possible to calculate the clarification effect for various stirring options, both without the use of flocculation basins, and with flocculation basins built into constructions (or devices that restore the sedimentation properties of the suspended solids after the flocs are destroyed when moving through pipelines).

Based on the abovementioned results the most efficient construction for stirring with different velocity gradient should be mechanical stirring devices or air stirring tanks (airflocculators).

## 4. Conclusion

In order to organize reuse of backwash water from rapid filters on drinking water treatment plant the reagentless clarification of such water was studied. The research was conducted at the water treatment plant of the Central water supply system of Rostov-on-Don. Theoretical investigations and experimental results lead to the following conclusions.

1. The clarification of backwash water of water supply system rapid filters should be conducted considering the water removal from filters to the sedimentation facilities. When wash water moves through pipelines from rapid filters to reuse constructions, suspended particles are exposed to shear stresses caused by water stirring under certain conditions that exceed the limit values. Thus, at RMS velocity gradients from 50 to 800 s<sup>-1</sup>, the formed flocs are destroyed and the clarification efficiency is reduced.

2. The authors studied the improving the flocculation properties of suspended particles of backwash water with extra stirring before the sedimentation in laboratories. Experimental studies have made it possible to determine the ranges of the Camp GT criterion, in which it is justified to use additional stirring in the flocculating chambers in reuse constructions (20.000 ÷ 40.000 and 82.000 ÷ 90.000) and the GT ranges in which additional stirring is impractical (from 40.000 to 82.000). Based on the designs of reuse constructions, which are most often used in natural water treatment facilities, we consider it acceptable to embed flocculation basin with mechanical stirring devices or air stirring tanks (airflocculators).

3. Based on the theory of coagulation by M.S. Smolukhovsky and following papers developing its concept, factors affecting the efficiency of clarification in sedimentation constructions are identified and mathematical dependences of the clarification effect are obtained when stirring in the pipeline and in the pipeline with followed by processing in the flocculation basin. The use of the presented mathematical dependencies will make it possible to regulate the effect of backwash water clarification in construction for reuse of wash water at the design stage or during operation, optimizing it in terms of later use of clarified water.

## References

1. Gosudarstvenny doklad «O sostoyanii i ob ochrane okrugayuschei sredy Rossiiskoy federacii v 2017 godu [State report "on the state and protection of the environment in the Russian Federation in 2017"]. [Online] URL: <https://gosdoklad-ecology.ru/2017/> RU (reference date: 31.08.2020) (rus)
2. Draginsky, V.L., Alekseeva, L.P. Obrabotka promywnych wod filtrow wodochistnykh stanzii [Treatment of wash water from water treatment facilities filters]. Water Supply and Sanitary Engineering. 2005. 8. Pp. 25–32. (rus)
3. Kuznesow, W.N. Voswrat promywnoy vody i obrabotka osadkow Zapadnoi filtrowalnoy stancii Ekaterinburga [Return of filter washings and sludge treatment at the western filtration plant of Ekaterinburg]. Water Supply and Sanitary Engineering. 2015. 11. Pp. 28–32. (rus)
4. Urvantseva, M.I. Obrabotka promywnych wod i osadkow wodoprowodnykh stahcii, raspologennykh na istochnikakh maloy i sredney mutnosti i cwetnosti [Treatment of wash water and precipitation from water supply stations located on sources of low and medium turbidity and color]: awtoreferat dis. cand.techn.nauk. [Online] URL: [https://static.freereferats.ru/\\_avtoreferats/01005111383.pdf](https://static.freereferats.ru/_avtoreferats/01005111383.pdf) RU (reference date: 31.08.2020). (rus)
5. Urvantseva, M.I., Artemenok, N.D. Kompleksnaya ocenka processow ochistky promywnych wod wodoprowodnich stanciy v zapadnoy sibiri [Complex assessment of processes of wash water treatment at water supply stations of the western Siberia]. Water Supply and Sanitary Engineering. 2011. 2. Pp. 25a–29. (rus)
6. Vigneswaran, S., Boonthanon, S., Prasanthi, H. Filter backwash water recycling using crossflow microfiltration. Desalination. 1996. 106(1–3). Pp. 31–38. DOI: 10.1016/S0011-9164(96)00089-6
7. Raj, C.B.C., Kwong, T.E., Cheng, W.W., Fong, L.M., Tiong, S.H., Klose, P.S. Wash water in waterworks: contaminants and process options for reclamation. Journal of Environmental Sciences. 2008. 20(11). Pp. 1300–1305. DOI: 10.1016/S1001-0742(08)62225-1. URL: [http://dx.doi.org/10.1016/S1001-0742\(08\)62225-1](http://dx.doi.org/10.1016/S1001-0742(08)62225-1)
8. Brügger, A. Reuse of filter backwash water using ultrafiltration technology. Filtration and Separation. 2000. 37(1). Pp. 22–26. DOI: 10.1016/S0015-1882(00)87607-7
9. Bourgeois, J.C., Walsh, M.E., Gagnon, G.A. Treatment of drinking water residuals: Comparing sedimentation and dissolved air flotation performance with optimal cation ratios. Water Research. 2004. 38(5). Pp. 1173–1182. DOI: 10.1016/j.watres.2003.11.018

10. Hou, B., Lin, T., Chen, W. Evaluation of a drinking water treatment process involving directly recycling filter backwash water using physico-chemical analysis and toxicity assay. RSC Advances. 2016. 6(80). Pp. 76922–76932. DOI: 10.1039/c6ra14912j. URL: <http://dx.doi.org/10.1039/C6RA14912J>
11. Ebrahimi, A., Amin, M.M., Pourzamani, H., Hajizadeh, Y., Mahvi, A.H., Mahdavi, M., Rad, M.H.R. Hybrid coagulation-UF processes for spent filter backwash water treatment: a comparison studies for PAFCl and FeCl<sub>3</sub> as a pre-treatment. Environmental Monitoring and Assessment. 2017. 189(8). DOI: 10.1007/s10661-017-6091-3
12. Reissmann, F.G., Uhl, W. Ultrafiltration for the reuse of spent filter backwash water from drinking water treatment. Desalination. 2006. 198(1–3). Pp. 225–235. DOI: 10.1016/j.desal.2006.03.517
13. Zhang, J., Lin, T., Chen, W. Micro-flocculation/sedimentation and ozonation for controlling ultrafiltration membrane fouling in recycling of activated carbon filter backwash water. Chemical Engineering Journal. 2017. 325. Pp. 160–168. DOI: 10.1016/j.cej.2017.05.077
14. Sardari, R., Osouledini, N. Data in Brief The data on the removal of turbidity and biological agents in spent filter backwash by bed ceramic in water treatment process. Data in Brief. 2018. Pp. 2–6. DOI: 10.1016/j.dib.2018.06.037.
15. Shafiquzzaman, M., Al-Mahmud, A., Al-Saleem, S., Haider, H. Application of a low cost ceramic filter for recycling sand filter backwash water. Water (Switzerland). 2018. 10(2). DOI: 10.3390/w10020150
16. Mahdavi, M., Amin, M.M., Mahvi, A.H., Pourzamani, H., Ebrahimi, A. Metals, heavy metals and microorganism removal from spent filter backwash water by hybrid coagulation-uf processes. Journal of Water Reuse and Desalination. 2018. 8(2). Pp. 225–233. DOI: 10.2166/wrd.2017.148
17. Skolubovich, Y., Voytov, E., Skolubovich, A., Ilyina, L. Cleaning and reusing backwash water of water treatment plants. IOP Conference Series: Earth and Environmental Science. 2017. 90(1). DOI: 10.1088/1755-1315/90/1/012035
18. Kachalova, G.S. Modern coagulants and flocculants in the cleaning of washing waters of water treatment plants. IOP Conference Series: Materials Science and Engineering. 2018. 451(1). DOI: 10.1088/1757-899X/451/1/012226
19. Mazari, L., Abdessemed, D. Feasibility of Reuse Filter Backwash Water as Primary/Aid Coagulant in Coagulation–Sedimentation Process for Tertiary Wastewater Treatment. Arabian Journal for Science and Engineering. 2020. (June). DOI: 10.1007/s13369-020-04597-1.
20. Bourgeois, J.C., Walsh, M.E., Gagnon, G.A. Comparison of process options for treatment of water treatment residual streams. 2005. 4(January).
21. Arora, H., Giovanni, G.D.I., Lechevallier, M. Spent filter backwash water contaminants and treatment strategies. Journal AWWA. 2001. (May) (90832). DOI: 10.1002/j.1551-8833.2001.tb09211.x
22. Babenkow, E.D. Ochistka vody coagulyantami [Water treatment with coagulants]. Moskwa: Nauka, 1977. 356 p.
23. Butko, D.A. Promywnye vody skorych filtrov i ich powtornoe ispolzovanie [Fast filter wash water and reuse]. Rostov-na-Donu: RGSU. 2009. 122 p. (rus)
24. Harris, H.F., Kaufman, W.J., Krone, R.B. Orthokinect flocculation in water purification. J. Sanit. Eng. Div. (1966) Proc. ASCE 92 (SA6) 95-111. (rus)
25. Kurgaew, E.F. Oswetliteli vody [Water clarifiers]. Moskwa: Stroyisdat, 1977. 192 p. (rus)
26. Park, N.S., Kang, M.S., Jeong, W., Kim, J.O. Experimental determination of the characteristics of physico-chemical particles in air-scouring-membrane (microfiltration) backwash water produced during drinking water treatment. Chemical Engineering Research and Design. 2015. 94(October). Pp. 714–720. DOI: 10.1016/j.cherd.2014.10.012. (rus)

### **Information about authors:**

**Denis Butko**, PhD in Technical Science

ORCID: <https://orcid.org/0000-0002-3792-7198>

E-mail: [den\\_111@mail.ru](mailto:den_111@mail.ru)

**Marina Volodina**, PhD in Philology

ORCID: <https://orcid.org/0000-0002-3853-2796>

E-mail: [mclavender1984@gmail.com](mailto:mclavender1984@gmail.com)

*Received 13.10.2020. Approved after reviewing 12.07.2021. Accepted 13.07.2021.*



Research article

UDC 625

DOI: 10.34910/MCE.111.8


## Performance improvement model of cement pavement in seasonal-frost regions

Q.Q. Zhao<sup>a</sup> , Q. Fu<sup>a</sup> , H.T. Zhang<sup>b</sup> , J.W. Wang<sup>c</sup> 

<sup>a</sup> Northeast Agricultural University, Harbin City, Heilongjiang Province, China

<sup>b</sup> China Communications First Public Bureau Highway Survey and Design Institute Co., Urumqi City, China

<sup>c</sup> Harbin Dongan Automobile Engine Manufacturing Co., Harbin, Heilongjiang, China

 2586762756@qq.com

**Keywords:** concrete, pavement management, numerical model, regression analysis, maintenance strategy

**Abstract.** The paper evaluates the performance improvement of cement pavement in seasonal frost regions. The typical diseases of cement concrete pavements in seasonal frost regions are proposed through the analysis of measured data, and the influence factors of pavement performance mutation value in those regions is determined. The application conditions of the model are obtained by the response surface test method; the road performance improvement model is established by the regression analysis method. The goodness-of-fit and significance state of the model were tested, while the validity of the model was verified by comparing it with the evaluation results of the existing model. The results identified the typical diseases of cement concrete pavement in seasonal frost regions: broken slabs, staggered platforms, cracks, exposed aggregates, broken corners and potholes. The mutation value of pavement performance is most sensitive to the impact of road damage index, running quality index and anti-skid performance index before pre-maintenance, that is under pre-curing conditions. The evaluation effect of the model for improving the performance of cement concrete pavement in seasonal frost regions is good, and the interpretable part of the improvement by the model is 99.2 %; the fit of the improved evaluation value and the measured value is 0.991, and the model is high fitting. The evaluation effect of the proposed model is better than the existing model, and the determination of the model is of great significance to the pre-maintenance of cement concrete pavement.

### 1. Introduction

Due to the harsh climate environment and the rapid increase in traffic, the cement concrete pavement inevitably gets cracks, peeling corners, dislocation and other diseases. The diseases not only reduce the quality and life of the cement concrete pavement, but the improper implementation timing of the pre-maintenance can even cause the destruction of the road structure and increase the maintenance cost [1]. Therefore, the accurate prediction of the instantaneous improvement value of pavement performance under preventive maintenance conditions is of great significance for the reasonable determination of the pre-maintenance timing and prolonging the service life of the road surface [2, 3].

Internationally, some studies have been conducted on the evaluation of performance improvement of cement concrete pavement under pre-curing conditions, most of which are analyzing the impact of certain

Zhao, Q.Q., Fu, Q., Zhang, H.T., Wang, J.W. Performance improvement model of cement pavement in seasonal-frost regions. Magazine of Civil Engineering. 2022. 111(3). Article No. 11108. DOI: 10.34910/MCE.111.8

© Zhao, Q.Q., Fu, Q., Zhang, H.T., Wang, J.W., 2022. Published by Peter the Great St. Petersburg Polytechnic University.



This article is licensed under a CC BY-NC 4.0

maintenance measures on the improvement of pavement performance. Sarkar [4, 5] analyzed the improvement degree of pavement performance by different pre-maintenance measures based on road data, and believed that pre-maintenance measures such as thin-layer overlays can effectively improve pavement performance. Yoo [6] made a preliminary evaluation of the test path and obtained the annual growth rate of the flatness index. Idal [7–9] studied a 5000-mile section of Indiana, and evaluated the degree of improvement of pavement performance by different sealing materials. On the basis of tests, Labi [10, 11] established an evaluation model of pavement performance improvement based on the grinding of joints and uplift parts as the basic maintenance measures, and quantified the improvement value of the pavement performance by this maintenance measure. Mandapaka [12–14] compared the advantages and disadvantages of crack sealing methods, and proposed that using waste rubber powder as a sealing material can improve the performance of the road surface to a higher degree.

Existing results on the improvement of pavement performance mainly focuses on pre-curing technology, pre-curing materials, etc. There has not been a large-scale research on the improvement of cement concrete pavement performance, and relatively complete and mature research results have not yet been formed. Farhan [15–18] evaluated different pre-maintenance performance improvement metrics, and determined that the deterioration rate reduction (DRR) and the average annual deterioration rate (AADR) can be used to express the improvement value of road performance. Priya [19, 20] studied the performance deterioration law of cement concrete pavement under the condition of pre-maintenance, and believed that the pavement performance jump value ( $PJ$ ) is the most effective mathematical index for evaluating the effect of road pre-maintenance. Ker [21] established a performance improvement model of cement concrete pavement under pre-curing condition by taking the flatness index as a parameter. However, as a representative parameter of pavement performance evaluation, the flatness index is relatively one-sided, and the impact of climate factors on pre-curing measures is also taken into account. Therefore, the performance improvement model of cement concrete pavement under the pre-curing conditions suitable for the climatic characteristics of seasonal frost regions needs to be further improved.

In this paper, the typical disease types of the pavement are screened through the disease data of the cement concrete pavement in the seasonal frost regions, and the pavement performance indicators that are more sensitive to the pre-maintenance measures are found as parameters. In addition, an improved model for the use of cement concrete pavement under the condition of pre maintenance suitable for seasonal frost regions is established, and the practicability and effectiveness of the model are verified by comparing it with the prediction level of existing models.

## 2. Methods

### 2.1. Screening of maintenance measures

For the types of diseases on cement concrete pavement, domestic and foreign experts have conducted relevant research. Haghnejad [22] evaluated the damage degree and disease distribution of cement concrete pavement by manually drawing the disease distribution map by board, and believed that the most typical diseases are cracks and broken slabs. Saxena [23] proposed broken slabs, cracks, broken corners, staggered platforms, mud, joint filler damage and potholes are the most common types of diseases based on actual engineering data. Jung [24] investigated the pavement damage conditions of several expressways and confirmed that the pavement has corner peeling and arching. Santos [25] detected voids and cracks in the road based on ultrasonic technology. Rao [26] conducted live inspections on cement concrete roads and found that repair measures would also damage the pavement. Based on the research results of the above-mentioned documents, it can be seen that cracks, broken corners, broken slabs, mud, staggered platforms, joint filler damage, repair damage, potholes, corner peeling, arching, voids and exposed aggregates are the diseases that appear on cement concrete pavement.

Cement concrete roads in seasonal frost regions are subject to the coupling effect of traffic load and freeze-thaw cycles. Therefore, in order to screen out the disease types of cement concrete pavement with the characteristics of seasonal frost regions and accurately select the maintenance measures, it is necessary to verify whether the disease status of cement concrete pavement under the influence of seasonal frost regions is different from that of ordinary climate.

Under the environmental conditions that ensure the same disease status as mentioned above, we selected the similar construction year, the same survey year, similar traffic flow, and the pavement performance of the three road sections in the seasonal frost regions, short-term frost regions and non frost regions for testing, and the selected detection index is pavement performance index (PQI). The value range of the pavement performance index is between 0 and 100, and the closer the index value is to 100, the better the pavement performance is. Long-zhou highway section in Guangdong Province, China is selected in non frost regions, Qi-yang expressway section in Jiangsu Province in China is selected in short-term frost regions, Zhao-zhao highway section in Heilongjiang Province, China is selected in seasonal frost



regions. 15 sections are selected for each of the three roads, with piles number of K117-K131. In Fig. 1, the abscissa is piles number, and the ordinate is pavement performance index.

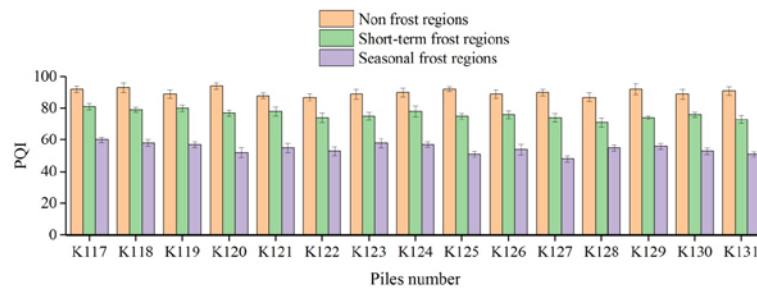


**Figure1. PQI of different regions.**

In Fig. 1, the PQI corresponding to different stake numbers in three different regions are different. For example, at K120, the maximum PQI ratio between the non frost regions and the seasonal frost regions is 1.81, and the ratio of the short-term frost regions to the seasonal frost regions is 1.48, which indicates that the PQI reduction in the seasonal frost regions is significantly higher than that of the short-term frost regions. The decrease of PQI in short-term frost regions is significantly higher than that in non frost regions. Most of the PQI in the non frost regions is between 85 and 100, and the road performance is excellent. The PQI of 15 piles number in the short-term frost regions varies from 70 to 85, because the cement concrete pavement in the short-term frost regions will be affected by freezing and thawing and accompanied by a small amount of snow, the PQI in this case is slightly smaller than the PQI of the non frost regions. The PQI of the road in the seasonal frost regions is significantly lower than that of the other two highways, because the number of annual freeze-thaw cycles in the seasonal frost regions is more than that in the short-term frost regions, and freeze-thaw effects have a greater impact on the performance of concrete, which will cause concrete damage such as deterioration of compactness and strength reduction. Therefore, there are more serious diseases such as cracks inside roads in seasonal frost regions. At the same time, due to the influence of the weather in the seasonal frost regions, the road surface in the cold season is snowy. In order to ensure driving safety, deicing salt or snow melting agent is usually thrown on the road surface, resulting in corrosion of the surface layer of the road. The use of snow shovel will also cause the road surface to wear, so the road performance is relatively low.

Based on the above analysis, the climatic factors in the seasonal frost regions have a significant impact on the road performance. In order to properly maintain the cement concrete pavement in the seasonal frost regions, the types of diseases with the characteristics of the seasonal frost regions should be considered. According to the above analysis, the PQI value of cement concrete pavement in seasonal frost regions is the lowest compared with that in other regions. The reason is that there are many types and severity of diseases of cement concrete pavement in seasonal frost regions under the influence of freeze-thaw, and the pavement performance is poor. At the same time, according to the research results of Haghnejad [22] on freeze-thaw cycle, it is found that under the influence of freeze-thaw, the most sensitive changes of pavement are cracks and exposed aggregates. Therefore, cracks and exposed aggregates are typical diseases of cement concrete pavement in seasonal frost regions. In order to screen out the types of cement concrete pavement diseases with the characteristics of seasonal frost regions, combined with the existing research results above, 12 diseases were finally selected for preliminary screening of the main diseases in seasonal frost regions. The 12 diseases were numbered, and the numbers were D1~D12, as shown in Table 1.

**Table 1. Disease number and name.**

| Number | Disease name   | Number | Disease name        | Number | Disease name       |
|--------|----------------|--------|---------------------|--------|--------------------|
| D1     | cracks         | D5     | staggered platforms | D9     | corner peeling     |
| D2     | broken corners | D6     | joint filler damage | D10    | arching            |
| D3     | broken slabs   | D7     | repair damage       | D11    | void               |
| D4     | mud            | D8     | potholes            | D12    | exposed aggregates |

Using the actual road condition data of Zhao-zhao Highway in Heilongjiang Province, China, group analysis of pavement diseases was carried out, and the key diseases of cement concrete pavement in seasonal frost regions were screened out by using statistical package for Social Sciences (SPSS) software. The principle of group analysis method is to divide many factors into different groups. The factors in the same group have strong similarity, and the differences between the factors in different groups can be reflected, so the characterization of each factor can be observed and analyzed. The specific group analysis process is to calculate the group distance between various factors. The smaller the group distance is, the

stronger the similarity will be, and the more probable is that they fall into the same group. Then, the group distance between different groups is calculated, and the two groups with the smallest group distance are merged into a group again. Repeat this step until the number of groups is reduced to one, and the grouping is completed.

In this study, Euclidean distance method was used to calculate the group distance between the factors, and the group average linkage method was used to calculate the distance between groups, and then the most reasonable number of group was determined according to the silhouette index method. After the analysis and calculation of SPSS software, the 12 factors are finally divided into 5 groups. The diseases in the group with relatively large influence degree and scope on the road condition in the distribution diagram can be determined as the main diseases, and the group classification is shown in Fig. 2.

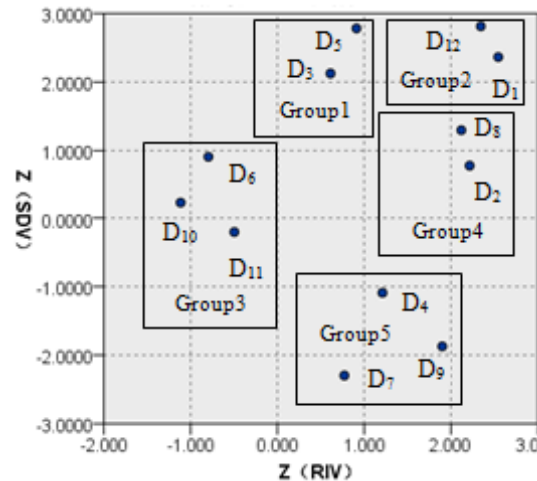


Figure 2. Group distribution.

In the group analysis diagram, RIV represents the average value of the scope of influence and SDV represents the average value of the intensity of influence, both of which are important. In order to eliminate the dimensional relationship between them and make them comparable, the standardized formula proposed by Kaufman and Rousseeuw is used to standardize the two indexes. The standardized two indexes are represented by Z (RIV) and Z (SDV).

In Fig. 2, the abscissa represents the influence scope after standardization, and the ordinate represents the influence intensity after standardization. The larger the Z (RIV) and Z (SDV) values of the disease, the greater the scope and intensity of the influence on the road conditions, indicating that the disease is the main disease affecting the cement concrete pavement in the seasonal frost regions. In Fig. 2, the values of Z (RIV) and Z (SDV) of group 1, group 2 and group 4 are positive, while the values of Z (RIV) and Z (SDV) of group 3 and group 5 are negative. This indicates that the six diseases in group 1, group 2 and group 4 have a wide range and large degree of influence on road conditions, so these six diseases belong to the main diseases. The six factors included in the other two groups have a smaller range and degree of influence than the six diseases in group 1, group 2 and group 4, so they are secondary diseases. After analyzing the group distribution results of 12 disease types, six disease types including broken slabs, staggered platforms, cracks, exposed aggregates, broken corners, and potholes have been identified as the main disease types of cement concrete pavements in seasonal frost regions and the pavement maintenance can be carried out for these six main diseases.

## 2.2. Model parameters

After the maintenance measures are taken for the above-mentioned diseases of cement concrete pavement in the seasonal frost regions, the performance of the pavement will be improved, which is embodied in the immediate performance improvement and the slowing down of the performance deterioration rate. The degree of change of the above indicators is usually characterized by the pavement performance jump value ( $PJ$ ) [19]. According to China's "Highway Technical Condition Evaluation Standards", the evaluation indicators of cement concrete pavement performance include road damage index ( $PCI$ ), road running quality index ( $RQI$ ) and anti-skid performance index ( $SRI$ ). Therefore, under different maintenance conditions, a model between  $PJ$  and  $PCI$ ,  $RQI$  and  $SRI$  can be established to measure the degree of improvement in the performance of cement concrete pavements in seasonal frost regions.

During the implementation of maintenance measures,  $PCI$ ,  $RQI$  and  $SRI$  will change. Therefore, in order to determine the parameters of the performance improvement model of cement concrete pavement

in seasonal frost regions, it is necessary to analyze the correlation between  $PCI$ ,  $RQI$ ,  $SRI$  and  $PJ$  before and after maintenance. The index with strong correlation with  $PJ$  is used as a parameter for model establishment. Pavement performance data refer to Soares's research [27]. The symbols of  $PCI$ ,  $RQI$  and  $SRI$  before and after maintenance are respectively represented as  $PCI_b$ ,  $PCI_a$ ,  $RQI_b$ ,  $RQI_a$ ,  $SRI_b$  and  $SRI_a$ . The correlation between  $PJ$  before and after maintenance and each index is shown in Figs. 3–8.

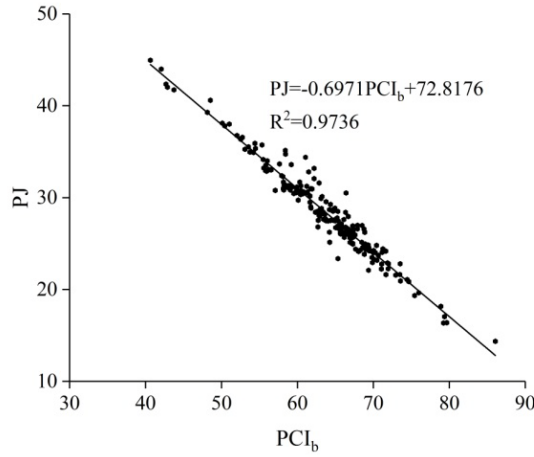


Figure 3. The fitting trend of  $PJ$  and  $PCI_b$ .

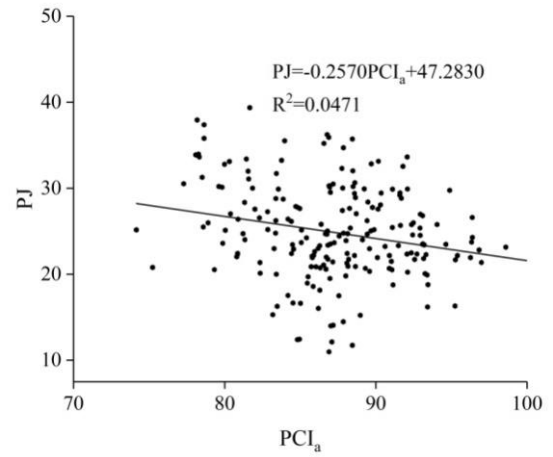


Figure 4. The fitting trend of  $PJ$  and  $PCI_a$ .

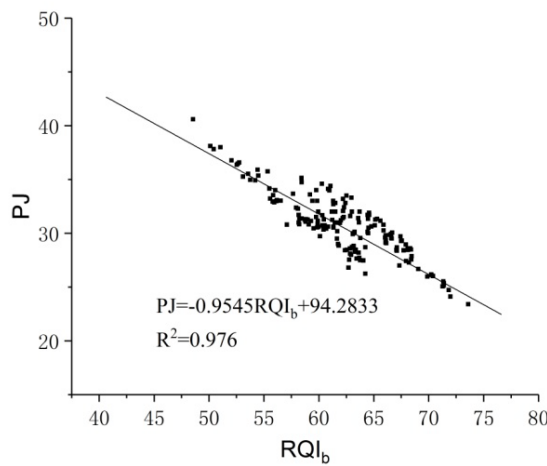


Figure 5. The fitting trend of  $PJ$  and  $RQI_b$ .

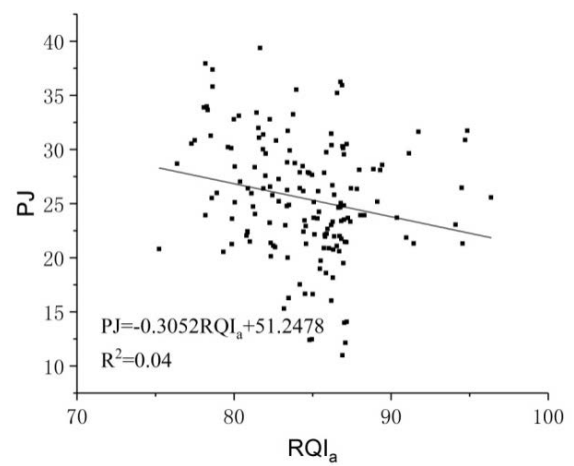


Figure 6. The fitting trend of  $PJ$  and  $RQI_a$ .

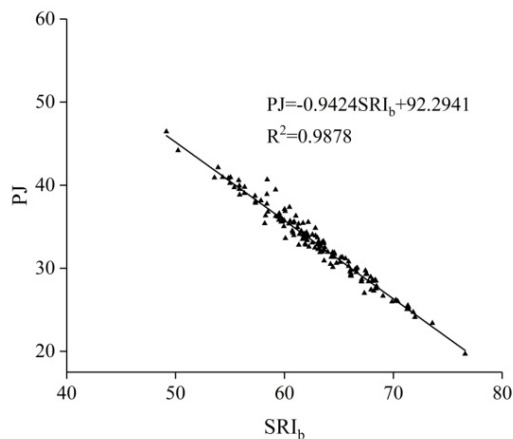


Figure 7. The fitting trend of  $PJ$  and  $SRI_b$ .

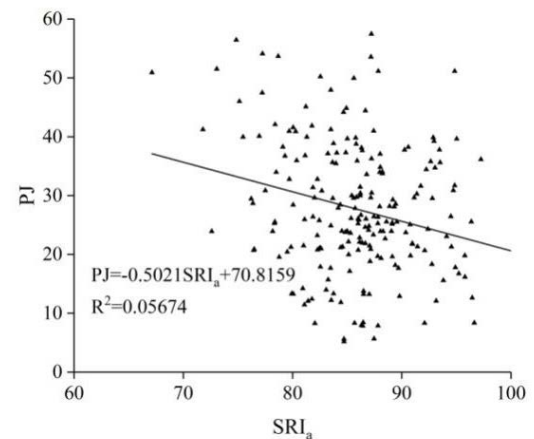


Figure 8. The fitting trend of  $PJ$  and  $SRI_a$ .

From Fig. 3 to Fig. 8, it can be seen that the decisive coefficients ( $R^2$ ) of  $PJ$  and  $PCI_b$ ,  $PCI_a$ ,  $RQI_b$ ,  $RQI_a$ ,  $SRI_b$  and  $SRI_a$  were 0.9736, 0.0471, 0.9928, 0.1312, 0.9878 and 0.0567, respectively, indicating that  $PJ$  was significantly correlated with  $PCI_b$ ,  $RQI_b$  and  $SRI_b$ , and not significantly correlated with  $PCI_a$ ,  $RQI_a$  and  $SRI_a$ . Therefore, the parameters of pavement performance improvement model were determined as  $PCI_b$ ,  $RQI_b$  and  $SRI_b$ .

### 2.3. Model establishment

According to the above research results,  $PCI_b$ ,  $RQI_b$  and  $SRI_b$  are linearly correlated with  $PJ$  respectively. Therefore, the performance improvement model of cement concrete pavement in seasonal frost regions under pre-curing condition is determined as a function form, as shown in Eq. (1):

$$PJ = \lambda_0 + \lambda_1 PCI_b + \lambda_2 RQI_b + \lambda_3 SRI_b, \quad (1)$$

where  $\lambda_0$ ,  $\lambda_1$ ,  $\lambda_2$  and  $\lambda_3$  are constants;  $PCI_b$  is the road damage index before maintenance;  $RQI_b$  is the road quality index before maintenance;  $SRI_b$  is the anti-skid performance index before maintenance.

From the typical road sections in the seasonal frost regions, select 20 road sections of 3 roads, including A, B and C, for disease detection, and apply 140 sets of measurement data of 14 road sections to build the model, and 60 sets of measurement data for the remaining 6 road sections to perform model validation.

According to the obtained data, using SPSS analysis method,  $PJ$  ( $y$ ) as the dependent variable,  $PCI_b$  ( $X_1$ ),  $RQI_b$  ( $X_2$ ) and  $SRI_b$  ( $X_3$ ) as independent variables to perform linear regression analysis of the model. The significance test results of the model are shown in Table 2. The regression mean square value is 345 times the residual mean square value, and the F value is 344.892. The value is large, indicating that the change of the dependent variable is caused by the change of the independent variable rather than the test error. The independent variable has a high degree of interpretation of the dependent variable. The Sig. value is 0.024, which is less than 0.05, indicating that the linear regression of the model is significant, and a regression model can be established between the independent variable and the dependent variable.

**Table 2. Regression model of ANOVAs.**

|            | Sum of Squares | df | Mean Square | F       | Sig.  |
|------------|----------------|----|-------------|---------|-------|
| Regression | 614.206        | 3  | 204.735     | 344.892 | 0.024 |
| Residual   | 0.594          | 1  | 0.594       |         |       |
| Total      | 614.8          | 4  |             |         |       |

After the F test shows that a linear model can be established, it is necessary to determine whether the independent variable has a significant influence on the dependent variable, so the regression coefficient must be tested for significance. The significance test of the regression coefficient is shown in Table 3. In Table 3, the partial regression coefficients corresponding to  $X_1$ ,  $X_2$  and  $X_3$  are all negative values, indicating that  $PCI_b$ ,  $RQI_b$ , and  $SRI_b$  are all negatively correlated with  $PJ$ . The reason is that with the increase of  $PCI$ ,  $RQI$  and  $SRI$ , the  $PJ$  value decreases. Therefore, the better the pavement performance is, the smaller the space for performance improvement after pre maintenance, and the smaller the performance mutation value. The absolute value of the critical value ( $t$ ) of the bilateral test is all greater than the significance level, and the significance value of Sig. is less than 0.05, indicating that the independent variable has a significant influence on the dependent variable, so the two coefficients are all retained in the model.

**Table 3. Coefficient of regression model.**

| Parameter | Partial regression coefficient | Partial regression coefficient standard error | Standardized partial regression coefficient | t      | Sig.  |
|-----------|--------------------------------|---|---|--------|-------|
| Constant  | 86.102                         | 1.491   |   | 6.893  | 0.016 |
| $x_1$     | -1.057                         | 0.059   | 0.489                                       | 4.026  | 0.028 |
| $x_2$     | -2.324                         | 0.143   | 0.348                                       | 5.246  | 0.007 |
| $x_3$     | -1.845                         | 0.032   | -1.149                                      | -3.294 | 0.019 |

The results of the goodness of fit test are shown in Table 4.  $R^2$  is the determining coefficient between the dependent variable and the independent variable, and the adjusted  $R^2$  is the ratio of the mean square deviation to eliminate the influence of the number of independent variables. The closer  $R^2$  and the adjusted  $R^2$  are to 1, the fitting effect of the regression equation the better. The adjusted  $R^2$  of the model is 0.992, which is close to 1, and the error of the standard estimation is only 0.025, indicating that the goodness of fit of the model is relatively high, and the dependent variable can be explained by the model accounting for 99.2 %.

**Table 4. Summary of regression models.**

| $R^2$ | Adjusted $R^2$ | Standard estimated error |
|-------|----------------|--------------------------|
| 0.997 | 0.992          | 0.025                    |

Substituting the coefficient values in Table 2 into Eq. (1) can get an improved model, as shown in Eq. (2):

$$PJ = 86.102 - 1.057PCI_b - 2.324RQI_b - 1.845SRI_b. \quad (2)$$

#### 2.4. Analysis of the applicable conditions of the model

In the climatic environment of the seasonal frost regions, the severity of the disease will affect the values of  $PCI_b$ ,  $RQI_b$  and  $SRI_b$ . Therefore, in order for the model to have a higher evaluation accuracy, it is necessary to determine the applicable conditions for the extent of 6 diseases such as broken slabs, staggered platforms, cracks, exposed aggregates, broken corners, and potholes. The response surface test was designed according to the number of disease types and the degree of quantification range, and the changes of  $PCI_b$ ,  $RQI_b$  and  $SRI_b$  under different disease levels were observed. Taking the impact of six diseases on  $PCI_b$  as an example, a response surface test was designed. The response surface test with 6 factors and 3 levels is selected, and the coding levels are -1, 0 and 1. According to Perez's research [28], the disease degree is quantified. The quantified value of disease degree corresponding to disease number and coding level is shown in Table 5.

**Table 5. 3 factor coding levels and values.**

| Number | Disease name       | - 1 | 0  | 1  |
|--------|--------------------|-----|----|----|
| A      | broken board       | 50  | 72 | 94 |
| B      | staggered platform | 30  | 61 | 92 |
| C      | crack              | 60  | 78 | 96 |
| D      | exposed aggregate  | 63  | 80 | 97 |
| E      | broken corner      | 49  | 72 | 95 |
| F      | hole               | 33  | 57 | 81 |

When the coding level of cracks, exposed aggregates, broken corners and potholes is 0, the response surface of the designed broken slabs and staggered platforms to  $PCI_b$  is shown in Fig. 9. With the increase of the degree of broken slabs and staggered platforms,  $PCI_b$  gradually decreases. When the degree of damage of the broken slabs is between 50 and 72, the decrease of  $PCI_b$  is significantly greater than the decrease when the degree of disease is between 72 and 94. The reason is that there will be traffic flow on the road. Excessive or overload conditions make the internal stress of the slab greater than the maximum bearing capacity of the concrete, and then irregular cracks will cause the slab to break. During this process, the road surface condition drops sharply. At this time,  $PCI_b$  is the most sensitive to changes in the degree of broken slabs and has the highest response. When the disease degree of the staggered platforms is between 30 and 61, the decline of  $PCI_b$  is smaller than that when the degree of the disease is 61 to 92. The reason is that the road can still be used normally when the height difference between adjacent pavement panels is small. When the panel sinks unevenly, it will seriously affect the normal use of the road, and the road condition will quickly drop to the minimum. Therefore, when the degree of staggered platforms is above moderate,  $PCI_b$  has the highest response to the degree of staggered platforms.

When the coding level of broken slabs, staggered platform, broken corners and pothole is 0, the response surface of design cracks and exposed aggregates to  $PCI_b$  is shown in Fig. 10. When the crack degree is above 78, the inclination angle of the response surface increases significantly compared to the angle below 78. The reason is that the freezing and thawing effect of the seasonal frost regions makes the pores of the concrete larger with irregular cracks, and in the late freeze-thaw period, the concrete capillary

pores are seriously damaged, and the cracks expand greatly. At this time,  $PCI_b$  is more responsive to the cracks. When the degree of exposed aggregates is less than 67, the slope of the response surface is greater. The reason is that in the early stage of exposed aggregates, the tires are strongly worn when the vehicle is running, and the road performance has been greatly reduced. As the exposed aggregates gradually deepens, the actual contact area between the tire and the road surface constant, the change range of  $PCI_b$  tends to be gentle, therefore, when the degree of exposed aggregates is below moderate,  $PCI_b$  has a higher responsiveness.

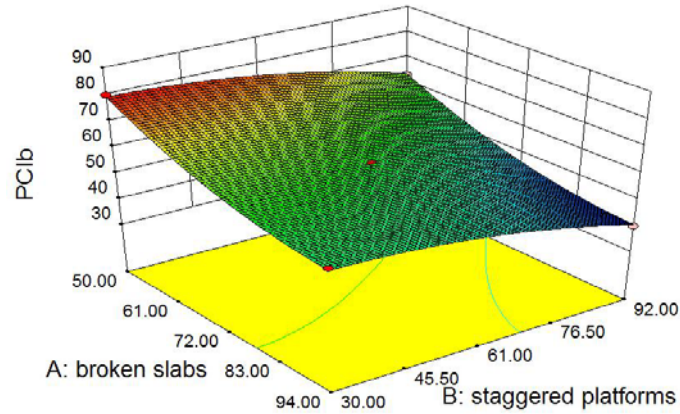


**Figure 9. A and B response surface to  $PCI_b$ .**

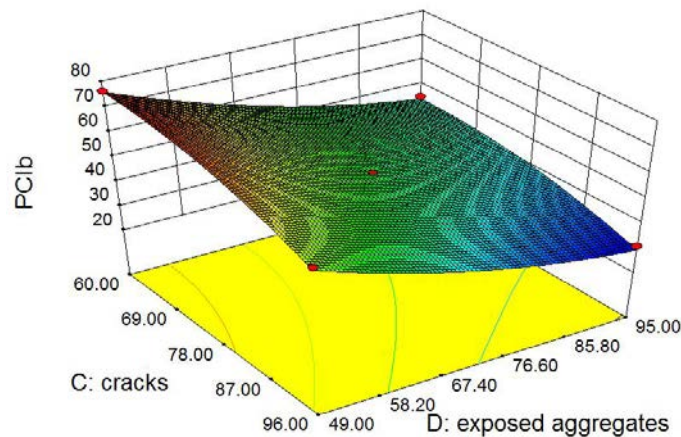


**Figure 10. C and D response surface to  $PCI_b$ .**

When the coding level of broken slabs, staggered platforms, cracks and exposed aggregates is 0, the response surface of design broken corners and potholes to  $PCI_b$  is shown in Fig. 11. When the degree of broken corners exceeds 76, the response surface gradually becomes flat. The reason is that the slab corner is the weakest part of the cement concrete slab. Under the seasonal frost regions climate, it is affected by freezing and thawing, and the compactness of the slab corner becomes worse. If the corner is broken, the road surface condition becomes worse. On this basis, if the corner of the road surface is increased, the road surface condition will not drop significantly. At this time,  $PCI_b$  has a low response to the corner. When the pothole degree is above 37, the slope of the response surface is larger. The reason is that when the pothole degree is large, the pavement will collapse under the load, which seriously affects the normal use of the road surface, indicating that the pothole degree is above medium,  $PCI_b$  is more responsive to the degree of potholes.



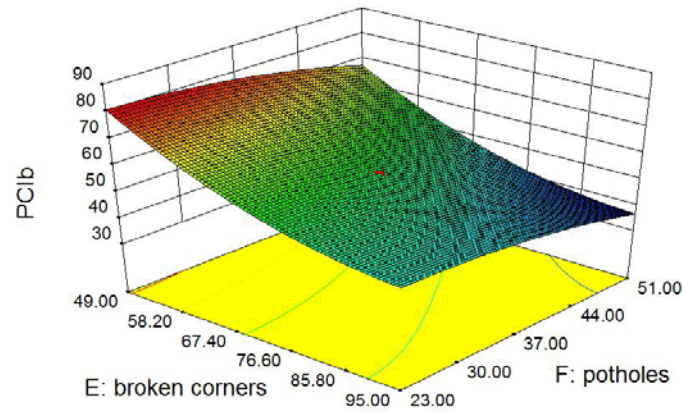


**Figure 11. E and F response surface to  $PCI_b$ .**

Combining the above analyses results of the response surface, we can see that if the response surface becomes flat: it indicates that  $PCI_b$  has a low response to the disease within the disease degree corresponding to the surface. At this time, the accuracy of the performance improvement model for the cement concrete pavement is low. If the slope of the response surface is large, the  $PCI_b$  changes significantly, and the corresponding disease degree will be more suitable for model evaluation. In the same way, the same response surface test is performed on the effects of  $RQI_b$  and  $SRI_b$  on the six diseases to determine the degree of disease that the model is applicable to. L stands for mild, M for moderate, and H for severe. The final test results are shown in Table 6.

**Table 6. Applicable conditions of the model.**

| Disease name        | $PCI_b$ | $RQI_b$ | $SRI_b$ |
|---------------------|---------|---------|---------|
| broken slabs        | L,M     | L,M     | M,H     |
| staggered platforms | M,H     | M,H     | L,M     |
| cracks              | M,H     | M,H     | M,H     |
| exposed aggregates  | L,M     | M,H     | L,M     |
| broken corners      | L,M     | L,M     | M,H     |
| potholes            | M,H     | M,H     | M,H     |

### 3. Results and Discussion

After establishing a model for improving the performance of cement concrete pavement in seasonal frost regions under pre-curing conditions with the  $PCI_b$ ,  $RQI_b$  and  $SRI_b$  model parameters, the practicality of the model needs to be verified. We selected a section of Highway A in the seasonal frost regions, collected the detection data of the road performance mutation value of this section in the past 8 years, and fit the measured value with the evaluation value of the model in this paper and the existing model. Comparing the degree of fit, we judged whether the model established in this paper is better than the existing model. The fitting result is shown in Fig. 12.

In Fig. 12, the abscissa is the actual measured value ( $V_m$ ) of the road performance abrupt change, and the ordinate is the model evaluation value ( $V_p$ ). The model evaluation value of Labi [10] and the measured value fit the determination coefficient ( $R^2$ ) of 0.955, and in Ker's study [21], it is 0.904, while the  $R^2$  of the improved model established in this paper is 0.991, which proves that the performance improvement model established with the  $PCI_b$ ,  $RQI_b$  and  $SRI_b$  parameters has the best fitting effect.

The samples of the same road section will make the test lack randomness, and the test results may have large errors. Therefore, the 6 road sections of the three roads A, B and C are again selected for verification by the actual measured road performance mutation values in the same year, as shown in Fig. 13. In Fig. 13, the edge of the radar chart is clockwise in turn with the numbers of the 6 road segments, and each layer has a fixed range of sudden changes. It can be observed that the broken line of the model evaluation value established in this paper is the closest to the broken line of the measured value, and the broken line of the other two models is relatively far from the broken line of the measured value. The reason is that the model established by Labi did not consider the influence of seasonal frost regions climate on the performance of cement concrete pavement; the parameters of the model established by Ker were not comprehensive enough and the evaluation accuracy was low. Therefore, after comparison and verification,



it can be known that the performance improvement model established with  $PCI_b$ ,  $RQI_b$  and  $SRI_b$  model parameters has a high evaluation level and good practicability.

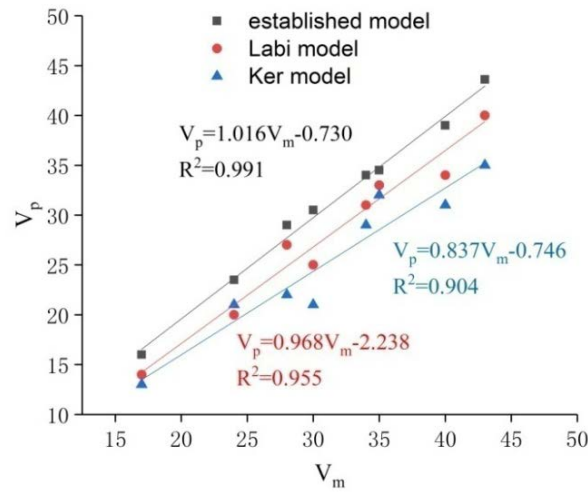


Figure 12. Fitting of  $PJ$  value.

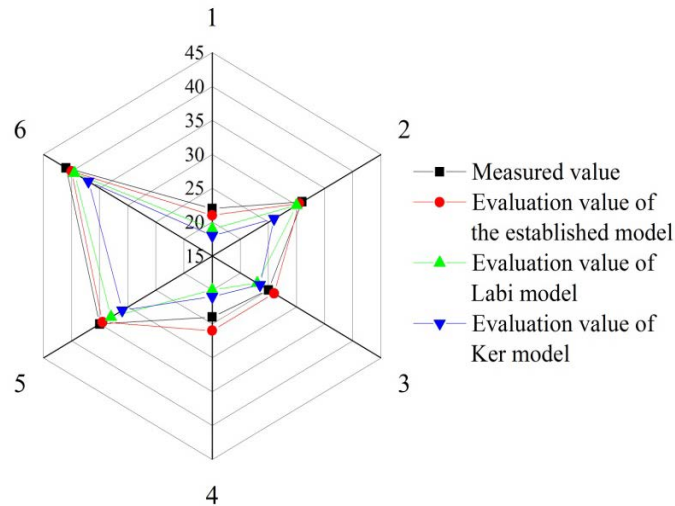


Figure 13. Histogram of  $PJ$  value.

## 4. Conclusions

1. Climatic factors have a significant impact on the performance of cement concrete pavement. The main disease types of cement concrete pavement in seasonal frost regions include broken slabs, staggered platforms, cracks, exposed aggregates, broken corners and potholes. The fitting correlation coefficients of  $PJ$  and  $PCI$ ,  $RQI$  and  $SRI$  before maintenance are 0.9736, 0.9928 and 0.9878, respectively, and the correlation is obvious. The fitting correlation coefficients of  $PJ$  and  $PCI$ ,  $RQI$  and  $SRI$  after maintenance are respectively 0.0471, 0.1312 and 0.0567, and did not show a significant correlation.

2. Using  $PCI$ ,  $RQI$  and  $SRI$  before maintenance as model parameters, a pavement performance improvement model under the pre-cured condition of cement concrete pavement in seasonal frost regions was established. The coefficients after regression analysis were  $-1.057$ ,  $-2.324$ , and  $-1.845$ . The deterministic coefficient of the performance improvement evaluation model is 0.992, and the Sig. value is less than 0.05. The model has a high goodness of fit and a significant regression effect, which has statistical applicability.

3. The applicable conditions of the model for improving the performance of cement concrete pavements in seasonal frost regions under pre-curing conditions are proposed. For  $PCI_b$ , it is lighter for broken slabs, the degree of exposed aggregates and broken corners, and heavier for the staggered platforms, cracks and potholes. For  $RQI_b$ , the degree of broken slabs and broken corners is lighter, and

the degree of staggered platforms, cracks, exposed aggregates and potholes is more severe. For  $SRI_b$ , the degree of staggered platforms and exposed aggregates is lighter, and the degree of broken slabs, cracks, broken corners and potholes is heavier. The extent of the above diseases is the most suitable condition for the model, and the model has the best evaluation effect.

4. The evaluation effect of the established model for improving the performance of cement concrete pavement in seasonal frost regions under pre-curing conditions is better than previous models, and it is more practical. In different periods of the same road section and the same period of different road sections, the performance improvement model and the improvement evaluation value of the existing model are respectively verified with the actual improvement value. The determination coefficient  $R^2$  of the improvement model established in this paper is 0.991. The determination coefficients  $R^2$  of Labi and Ker models are 0.955 and 0.904, respectively, which are lower than the  $R^2$  value of the improved model, with its improvement evaluation value more accurate than that of the existing model as well.

## 5. Acknowledgements

That is funded by the Young Talent Project of Northeast Agricultural University(54978412) and Northeast Agricultural University Postdoctoral Funding Project (88638800).

## References

1. Zhao, Q., Cheng, P., Wang, J., Wei, Y. Damage prediction model for concrete pavements in seasonally frozen regions. Magazine of Civil Engineering. 2018. 84(8). Pp. 57–66. DOI: 10.18720/MCE.84.6
2. Al, Z., Al, B., Daou, A., Chhade, R.H., Chehab, G., Asce, A.M. Experimental and Numerical Assessment of the Behavior of Geogrid-Reinforced Concrete and Its Application in Concrete Overlays. American Society of Civil Engineers. 2018. 30(12). Pp. 1–10. DOI: 10.1061/(ASCE)MT.1943-5533.0002542
3. Fediuk, R.S., Mochalov, A.V., Bituev, A.V., Zayakhanov, M.E. Structuring Behavior of Composite Materials Based on Cement, Limestone, and Acidic Ash. Inorganic Materials. 2019. 55(10). Pp. 1079–1085. DOI: 10.1134/S0020168519100042.
4. Sarkar, A., Hajhosseini, M. The effect of basalt fibre on the mechanical performance of concrete pavement. Road Materials and Pavement Design. 2019. 0(0). Pp. 1–12. DOI: 10.1080/14680629.2018.1561379. URL: <https://doi.org/10.1080/14680629.2018.1561379>
5. Hezhev, T.A., Zhurlov, A.V., Tsipinov, A.S., Klyuev, S.V. Fire resistant fibre reinforced vermiculite concrete with volcanic application. Magazine of Civil Engineering. 2018. 80(4). Pp. 181–194. DOI: 10.18720/MCE.80.16
6. Taylor, P., Yoo, J. Cost-effective selection and multi- period scheduling of pavement maintenance and rehabilitation strategies. Engineering Optimization. 2008. (May 2013). Pp. 37–41. DOI: <http://dx.doi.org/10.1080/03052150701686937>
7. Idal, M.A. V. Rehabilitation Performance Prediction Models for Concrete Pavements. Transportation Research Record. 1999. (99). Pp. 137–146.
8. Zhao, Q., Cheng, P., Wei, Y., Wang, J. Factors effecting the recovery process of self-repairing concrete. Magazine of Civil Engineering. 2019. 88(4). Pp. 52–59. DOI: 10.18720/MCE.88.5
9. Attoh-okine, N.O. Combining Use of Rough Set and Artificial Neural Networks in Doweled-Pavement-Performance Modeling — A Hybrid Approach. Journal of Transportation Engineering. 2002. (June). Pp. 270–275.
10. Labi, S., Sinha, K.C. Life-Cycle Evaluation of Flexible Pavement Preventive Maintenance. Journal of Transportation Engineering. 2005. (October). Pp. 744–751.
11. Klyuev, S.V., Klyuev, A.V., Vatin, N.I. Fiber concrete for the construction industry. Magazine of Civil Engineering. 2018. 84(8). Pp. 41–47. DOI: 10.18720/MCE.84.4
12. Ullidtz, P., Ph, D., Harvey, J.T., Ph, D., Asce, M., Sivaneswaran, N., Ph, D., Asce, M. Mechanistic-Empirical and Life-Cycle Cost Analysis for Optimizing Flexible Pavement Maintenance and Rehabilitation. JOURNAL OF TRANSPORTATION ENGINEERING. 2012. 138(5). Pp. 625–634. DOI: 10.1061/(ASCE)TE.1943-5436.0000367
13. Taylor, P., Bosurgi, G., Trifirò, F. A model based on artificial neural networks and genetic algorithms for pavement maintenance management A model based on artificial neural networks and genetic algorithms for pavement maintenance management. International Journal of Pavement Engineering. 2007. (July 2013). Pp. 37–41. DOI: 10.1080/10298430500195432
14. Fediuk, R.S., Lesovik, V.S., Mochalov, A.V., Otsokov, K.A., Lashina, I.V., Timokhin, R.A. Composite binders for concrete of protective structures. Magazine of Civil Engineering. 2018. 82(6). Pp. 208–218. DOI: 10.18720/MCE.82.19
15. Farhan, J., Fwa, T.F. Pavement Maintenance Prioritization Using Analytic Hierarchy Process. Transportation Research Record. 2009. Pp. 12–24. DOI: 10.3141/2093-02
16. Chootinan, P., Chen, A., Horrocks, M.R., Bolling, D. A multi-year pavement maintenance program using a stochastic simulation-based genetic algorithm approach. Transportation Research Part A. 2006. 40. Pp. 725–743. DOI: 10.1016/j.tra.2005.12.003
17. Klyuev, S.V., Khezhev, T.A., Pukharensko, Y.V., Klyuev, A.V. Experimental study of fiber-reinforced concrete structures. Materials Science Forum. 2018. 945. Pp. 115–119. DOI: 10.4028/www.scientific.net/MSF.945.115
18. Rezaei, M.R., Kordani, A.A., Zarei, M. Experimental investigation of the effect of Micro Silica on roller compacted concrete pavement made of recycled asphalt pavement materials. International Journal of Pavement Engineering. 2020. 0(0). Pp. 1–15. DOI: 10.1080/10298436.2020.1802024. URL: <https://doi.org/10.1080/10298436.2020.1802024>
19. Priya, R., Srinivasan, K.K., Veeraragavan, A. Sensitivity of Design Parameters on Optimal Pavement Maintenance Decisions at the Project Level. Transportation Research Record. 2008. Pp. 47–54. DOI: 10.3141/2084-06
20. Chou, J., Le, T. Reliability-based performance simulation for optimized pavement maintenance. Reliability Engineering and System Safety. 2011. 96(10). Pp. 1402–1410. DOI: 10.1016/j.ress.2011.05.005
21. Ker, H., Lee, Y., Wu, P. Development of Fatigue Cracking Prediction Models Using Long-Term Pavement Performance Database. Journal of Transportation Engineering. 2008. Pp. 477–482.

22. Haghnejad, M., Modarres, A. Effect of freeze-thaw cycles on the response of roller compacted concrete pavement reinforced by recycled polypropylene fibre under monotonic and cyclic loadings. *Road Materials and Pavement Design*. 2020. Pp. 1–17. DOI: 10.1080/14680629.2020.1794942. URL: <https://doi.org/10.1080/14680629.2020.1794942>
23. Saxena, P., Tompkins, D., Khazanovich, L., Balbo, J.T. Evaluation of Characterization and Performance Modeling of Cementitiously Stabilized Layers in the Mechanistic – Empirical Pavement Design Guide. *Transportation Research Record*. 2020. Pp. 111–119. DOI: 10.3141/2186-12
24. Jung, Y.S., Zollinger, D.G. New Laboratory-Based Mechanistic – Empirical Model for Faulting in Jointed Concrete Pavement. *Transportation Research Record*. 2011. Pp. 60–70. DOI: 10.3141/2226-07
25. Santos, J., Ferreira, A. Pavement Design Optimization Considering Costs and Preventive Interventions. *Journal of Transportation Engineering*. 2012. Pp. 911–923. DOI: 10.1061/(ASCE)TE
26. Rao, C., Darter, M.I. Enhancements to Punchout Prediction Model in Mechanistic – Empirical Pavement Design Guide Procedure. *Transportation Research Record*. 2013. (2367). Pp. 132–141. DOI: 10.3141/2367-14
27. Soares, R., Haichert, R., Podborochynski, D., Berthelot, C. Modeling In Situ Performance of Cement-Stabilized Granular Base Layers of Urban Roads. *Transportation Research Record*. 2013. 2363. Pp. 88–95. DOI: 10.3141/2363-10
28. Pérez-acebo, H., Mindra, N., Railean, A., Rojí, E., Mindra, N., Railean, A., Rojí, E. Rigid pavement performance models by means of Markov Chains with half-year step time step time. *International Journal of Pavement Engineering*. 2017. 8436. Pp. 1–14. DOI: 10.1080/10298436.2017.1353390.

**Information about authors:**

**Qianqian Zhao, PhD**

ORCID: <https://orcid.org/0000-0002-0209-4181>

E-mail: [492954791@qq.com](mailto:492954791@qq.com)

**Qiang Fu, PhD**

ORCID: <https://orcid.org/0000-0003-4100-2777>

E-mail: [fuqiang@neau.edu.cn](mailto:fuqiang@neau.edu.cn)

**Hetong Zhang,**

ORCID: <https://orcid.org/0000-0002-0414-9051>

E-mail: [2586762756@qq.com](mailto:2586762756@qq.com)

**Jianwu Wang, Sc.D.**

ORCID: <https://orcid.org/0000-0002-5953-8919>

E-mail: [nihaone@163.com](mailto:nihaone@163.com)

*Received 14.10.2020. Approved after reviewing 28.06.2021. Accepted 29.06.2021.*



Research article

UDC 626.823.91

DOI: 10.34910/MCE.111.9

## Effect of subsoil moisture on filtration through a screen defect

O.A. Baev\* , Yu.M. Kosichenko , V.F. Silchenko

*Russian Scientific Research Institute of Land Improvement Problems, Novocherkassk, Russia*

 [Oleg-Baev1@yandex.ru](mailto:Oleg-Baev1@yandex.ru)

**Keywords:** polymer, geocomposite material, filtration, hydration, numerical model, coating

**Abstract.** The aim of the scientific work is to study the features of filtration under a defect of a polymer screen made of a geomembrane, where the movement of the filtration flow occurs with incomplete saturation of the soil with water. According to the results of experimental studies, local filtration is formed on the filtration tray under the screen defect with incomplete saturation of the soil with water, caused by the action of capillary forces and the presence of trapped air. The article presents the results of studies of a model of a polymer screen with a defect in the form of a slit with a relative width of 0.005 to 0.5. On the basis of studies in a soil flume and experimental pits with film screens, the average moisture content for sandy and loamy soil was established directly under the screen defect. According to the results of the calculations performed, the piezometric pressure along the screen slit significantly decreases with an increase in the permeability of the screen base and reaches negative values at relatively large values of the slit width. The filtration flow through the slit increases with an increase in the permeability of the base soil, and the width of the spreading zone of the filtration flow under the screen decreases. The urgency of solving this problem is due to insufficient study of the influence of moisture saturation of the base soil on filtration through a screen defect.

### 1. Introduction

Filtration through polymer screen damage was studied by a number of researchers, among them: S.V. Solsky and M.G. Lopatina [1], Yu.M. Kosichenko and O.A. Baev [2–6], A.V. Ishchenko [7, 8], M.A. Chernov [9], I.A. Pechenezhskaya [10, 11], J.R. Giroud [12, 13], K. Rowe [14], Touze-Foltz [15], G.R. Koerner [16–18] et alia.

In the work of M.A. Bandurina [19], the software and hardware complex was developed to diagnose the technical condition of water supply facilities of irrigation systems, which provided for the detection of defects in the lining and subsoil base using acoustic and GPR non-destructive testing methods.

In the last 10–20 years geosynthetic materials [20] have been increasingly utilized in small hydraulic engineering. They can successfully be used for environmental facilities industrial and household waste storage facilities, as well as canals and water bodies.

The use of waterproof geosynthetic materials on irrigation canals is considered promising, where losses reach 30 %, of which 80–90 % are due to filtration [4]. Currently, the efficiency of most irrigation canals is 0.75–0.80, and if seepage-control lining used with geosynthetic materials, the efficiency will reach 0.97–0.98 [4]. Thus, the seepage-control effect of geosynthetic materials on the canals can be around 20–30 %.

---

Baev, O.A., Kosichenko, Yu.M., Silchenko, V.F. Effect of subsoil moisture on filtration through a screen defect. Magazine of Civil Engineering. 2022. 111(3). Article No. 11109. DOI: 10.34910/MCE.111.9

© Baev, O.A., Kosichenko, Yu.M., Silchenko, V.F., 2022. Published by Peter the Great St. Petersburg Polytechnic University.



This article is licensed under a CC BY-NC 4.0

Although geosynthetic linings are highly reliable, they can still have various damages during construction and operation. As a result, a significant amount of research was performed on the water permeability of polymer screens and lining.

Among these works, an article by the authors [5] is worth mentioning, where various methods for calculating the water permeability of polymer screens are considered: experimental, theoretical and experimental-theoretical. Based on the results of the theoretical formulas, it was established that calculations according to Yu.M. Kosichenko and V.H. Zhilenkov gives close values of specific filtration flow through a continuous slot, and according to the formula of V.N. Nedriga, a significant discrepancy of up to 30–50 % was obtained. When analyzing the filtration flow through a slot in a polymer geomembrane by a number of design dependencies, including J.P. Giroud [12], the results are consistent with each other. However, using the R.K. Rowe formula [14] a discrepancy of up to 75 % appears, which can be explained by their rather complex appearance and the need to use special functions.

Another article by the authors [6] investigates the problem of water permeability of a polymer screen from a geomembrane through a system of slots. The solution to this problem was obtained using the method of conformal mapping and speed travel time curve. Here a comparison with J.P. Giroud's formula gives a large discrepancy between 67 % and 128 % depending on the slot width, which is fundamentally different from other formulas as it uses the law of non-linear filtration and empirical coefficients from field studies.

In the works of foreign authors [13, 15] an empirical equation for calculating the velocity of fluid flow through the composite lining due to defects in the geomembrane was obtained. Three types of damage were considered (circular, infinite length damage and cracked defects) and three types of contact ("excellent", "good" and "bad").

The forecast of the longevity of geotextiles and geomembranes is discussed in the article [16]. The half-life of unexposed (or coated) high density polyethylene (HDPE) geomembranes with a thickness of 1.5 mm (with a value of 50 % retained strength and elongation) was approximately 450 years. Laboratory tests were conducted over a period of 12 years. The situation is completely different for open geosynthetic materials. They are directly affected by ultraviolet radiation and higher temperatures, which shorten their lifetime. The ratio of unexposed to exposed samples for the HDPE geomembrane is 7 units. Research results for geomembranes range from 47 to 97 years, which took 12 years of laboratory testing to achieve. These results are considered to be the most interesting and were first obtained by the authors.

However, the data given on the durability of closed geomembranes in [17] is considerably overestimated. Thus, according to our calculations [4] (based on the formula derived from the Rice distribution), the predicted (calculated) service life of geomembranes with protective lining made of rubblework is 130 years. As for open geomembranes without protective lining, according to our field observations, their service life may not exceed 25 years. "Similarly", "Texpolimer" guarantees the service life of HDPE and LDPE geomembranes at least 25 years. Carpi's field and laboratory research [21] also showed that permanent open geomembranes have a service life of over 50 years, and for geomembranes under water, 200 years. The Federal Institute for Materials Research in Berlin (BAM) conducted a thorough 365-day life cycle test of bentonitic mats [22]. The test results were then extrapolated using the Arrhenius method, which established a period of 200 years for the use of bentonite coverings, confirming the data previously considered.

Overseas, there is also considerable focus on the application and research of geosynthetic materials (geomembranes) and bentonitic mats (GCL). The article [23] discusses laboratory studies of the capacity of conventional and multi-component geocomposites for five different bentonite clay inserts and a number of different geomembranes (GM). The impact of a 4 mm round defect in the lining of a multi-component geosynthetic material (GCL, geosynthetic clay liner) directly below a 10 mm diameter slot in the geomembrane was investigated.

The canal lining is used to reduce water losses during irrigation [24]. The use of geosynthetic materials, which have been widely used in construction areas, in combination with concrete or as a separate material by replacing concrete with geosynthetic material, is the most economical method for canal lining.

The influence of a defect in the geomembrane on water filtration in groundwater dams and methods of filtering control are discussed in this paper [25]. Defects in the geomembrane can lead to potential hazards for the dam with the geomembrane on its surface, so three-dimensional saturated infiltration fields with different sizes of defects in the geomembrane were simulated using the finite element method. The process of filtering through faulty geomembranes was simulated using methods of removing faulty elements and increasing permeability. The results show that seepage caused by defects have a significant impact on the local seepage field near the defects and have little effect on other parts of the dam.

A general scheme for calculating the flow rate of a liquid through a composite lining (geomembrane + subsoil base) with slots is presented in [14]. Solutions obtained for a round slots and a damaged fold can

be used to interpret field conditions and analyse data on the field seepage. A number of existing solutions have been obtained from the general solution as individual cases.

The durability of open geomembrane lining is discussed in the article [17, 18]. Factors such as ultraviolet radiation, elevated temperatures and oxygen exposure reduce the life of the geomembrane. Ultraviolet fluorescent lamps were used in the studies, where five different geomembranes were evaluated. Each material was examined at temperatures ranging from 60 to 80 °C, with a 50 % reduction in strength and elongation. The results obtained by the authors are similar [17].

It is known that if all base soil pores are completely saturated with water, the filtration flow will be maximised. In case of incomplete soil saturation of the base (according to S.F. Averyanov) the movement of liquids takes place in a three-phase system: soil-liquid-gas skeleton. Water permeability in this case will depend, in addition to the factors determining the filtration coefficient, also on the humidity or saturation degree ( $\omega$ ).

Liquid movement when the ground is not fully saturated is carried out by a partially filled capillary at the walls, so if there is air and water in the ground pores, water will adjoin the skeleton directly and air will be inside the water. Given these circumstances, S.F. Averyanov obtained the following relationship between the filtration coefficient at partial saturation and the filtration coefficient at full saturation as follows:

$$K_{\omega} = K \cdot \left( \frac{\omega - \omega_0}{m - \omega_1} \right)^{3.5} \quad (1.1)$$

where  $K_{\omega}$  and  $K$  are water permeability coefficients, respectively, at partial and full saturation, m/day;  $\omega$  is humidity in the experiments, at which the value of  $K_{\omega}$  was determined, %;  $m$  is humidity corresponding to full porosity, in % of the mass of dry soil, %;  $\omega_1$  is humidity at which the permeability was highest in the experiments, %;  $\omega_0$  is humidity corresponding to bound water, %.

The dependency analysis (1.1) shows that the bracketed expression will always be less than one and will give an even smaller value when raised to 3.5. Based on the above, the value of the filtration coefficient at partial saturation will almost always be lower than at full saturation ( $K$ ).

A review of domestic and foreign sources shows that the study of water permeability was carried out mainly only with full saturation of the filtration area. However, in real conditions, when local filtration is observed through screen defects of a small size, it will occur with incomplete water saturation of the pores of the foundation soil. A number of scientists (S.F. Averyanov, P.Ya. Polubarinova-Kochina, D.F. Shulgin and others) have already proved that for some tasks: drip and subsurface irrigation, incomplete moisture saturation during filtration will be very characteristic.

In this regard, it is urgent to solve the problem of incomplete moisture saturation of the base soil when filtering through a defect in the polymer screen. The aim of the study was to study the features of filtration through a defect in a polymer screen in a soil base with incomplete moisture saturation. Research tasks include:

- description of a soil filtration flume with a screen model made of a polymer geomembrane;
- carrying out experimental studies at different reduced width of the screen slit;
- presentation of the experiments carried out on a filtration pan with incomplete water saturation in the soil base;
- consideration of the theoretical problem of incomplete moisture saturation by the source-runoff method;
- comparison of calculations of filtration from a gap of a polymer screen at full and incomplete moisture saturation.

The object of research is a model of a polymer screen with a defect in the form of a gap, the subject of research is the process of filtration through a defect of a polymer screen in a soil base with incomplete moisture saturation.

## 2. Methods

A soil filtration tray 1.4×2.0×0.47 m was used for the studies. The model of the seepage-control blanket made of a polymer geomembrane with a protective lining was made of a 0.2 mm thick polyethylene

stabilised film at a linear scale of 1:5, which corresponds to a life-size 1.0 mm thick polymer geomembrane. Water was supplied from the pressure tank and drained through the side pockets.

At the bottom of the tray, a drainage layer of 20–40 mm crushed stone was laid to drain water into the side pockets. The use of thin polyethylene film on the model created a tight fit of the screen to the base. Medium sand was used for the protective layer.

Fine sand filtration coefficient in the ground base of the screen at full saturation with water is  $K = 4.8$  m/day, porosity  $n = 39.87\%$ , humidity corresponding to bound water  $\omega_o = 3.7\%$ . Experiments were carried out for two cases:  $\delta_o = 0$  without and with the protective layer  $\delta_o = 10$ . Screen pressure was  $H = 0.2$  m. The given width of the slot in the film screen ( $m/h$ ) was taken from 0.005 to 0.5.

Ground humidity under the screen slot was recorded by laboratory analysis of samples taken immediately after the experience was stopped once the established filtering process had been achieved. Sampling sites were taken under a screen slot at a depth  $h = 0$  and 10 cm.

### 3. Results and Discussion

The results were obtained on the filtration tray at different relative depths of humidity measurement from the screen  $h/H = 0; 0.5$  and at different adduced widths of the slot in the screen  $m/h = 0.005; 0.025; 0.05; 0.25; 0.5$  (Table 3.1).

**Table 3.1. Results of experimental studies on the soil filtration tray.**

| Width<br>Screen slots,<br>$m/h$               |                | $h/H = 0$  |       | $h/H = 0.5$    |            |       |
|---|----------------|------------|-------|----------------|------------|-------|
|   | $\omega_1, \%$ | $\omega^o$ | $\mu$ | $\omega_1, \%$ | $\omega^o$ | $\mu$ |
| Without protective layer ( $\delta_o/H = 0$ ) |                |            |       |                |            |       |
| 0.005   | 14.31          | 0.448      | 0.060 | 15.34          | 0.491      | 0.083 |
| 0.025   | 15.20          | 0.485      | 0.080 | 16.37          | 0.535      | 0.112 |
| 0.05  | 15.58          | 0.501      | 0.089 | 19.31          | 0.659      | 0.233 |
| 0.25  | 19.74          | 0.677      | 0.256 | 22.10          | 0.777      | 0.413 |
| 0.5   | 19.60          | 0.671      | 0.255 | 21.92          | 0.769      | 0.400 |
| With protective layer ( $\delta_o/H = 0.5$ )  |                |            |       |                |            |       |
| 0.005   | 14.10          | 0.439      | 0.056 | 15.04          | 0.479      | 0.076 |
| 0.025   | 15.00          | 0.477      | 0.075 | 15.90          | 0.515      | 0.098 |
| 0.05  | 14.83          | 0.470      | 0.070 | 16.16          | 0.525      | 0.105 |
| 0.25  | 19.20          | 0.654      | 0.226 | 21.69          | 0.759      | 0.382 |
| 0.5   | 19.50          | 0.669      | 0.242 | 20.43          | 0.706      | 0.295 |

The following designations were used in the calculations (except for the above-mentioned):  $\omega$  is ground humidity measured in the experiment, %;  $\omega_1$  is water-saturated ground humidity of the screen base, taking into account a certain amount of pressurized air, %;  $\omega^o = (\omega - \omega_o)/(\omega_1 - \omega_o)$  is relative ground humidity in the experiment;  $\mu = K_{\omega}/K_{\omega_1}$  is ground saturation coefficient of the base; water permeability coefficient of the base ground at humidity  $\omega_1$  was assumed to be equal to  $K_{\omega_1} = 1.10$  m/day; water permeability coefficient at full saturation of the ground pores  $K_{\omega}$  was determined using S.F. Averyanov's formula (1).

From the analysis of the data given in Table 3.1, it can be concluded that the humidity and permeability of the base soil under a screen slot depends on the opening width. As the size of the gap increases, moisture and ground permeability increase [26, 27]. This is because as the width of the slot increases, the flow of water filtered through the slot into the sub-screen base increases, thereby increasing the saturation of the area and thus its permeability. With a protective layer of screen, the permeability of the soil under the screen slot is reduced compared to the case without a protective layer. In all the cases



studied, the saturation coefficient  $\mu$  in relation to the maximum possible ground permeability in the tray near the slot varies from 0.06 to 0.4 and relative humidity  $\omega^0$  from 0.44 to 0.77.

The average value of relative humidity at practically possible slots ( $m/h < 0.05$ ) for sandy ground conditions of the screen model base was 0.45–0.55.

If there are loamy soils at the base of polymer screens, we will determine the relative humidity using the results of "VNIIGIM" (All-Russian Scientific Research Institute of Hydraulic Engineering And Melioration named after A.N. Kostyakov) field observations on open pits. According to these experiments, the maximum humidity of loamy soil under the film screen was 18–22 %; the average humidity at full saturation of the soil was 41 %; and the natural humidity was 5–7 %. According to the provided data, the average relative humidity of loamy soil, taking into account natural humidity, can be assumed to be between 0.35 and 0.45.

On the basis of the experiments carried out, it can be noted that when filtering through a slot in the polymer screen, the following proportions will generally be observed for practically possible sizes ( $m/h < 0.05$ ) in the sub-screen base:

$$\omega_0 < \omega < \omega_1 \leq n \text{ or } K_\omega < K_{\omega_1} < K_\omega, \quad (3.1)$$

i. e. accordingly, the soil humidity and water permeability the coefficient of the filtration zone under the screen slot will be lower than the soil porosity and filtration coefficient at full saturation.

Thus, as a result of experiments on the physical model, it was established that under the slot of the film screen, the movement of water takes place with incomplete water saturation caused by capillary forces and the presence of entrapped air in the ground. The movement of the filtration flow through the small damage is usually accompanied by the formation of two zones in the sub-screen base. The full saturation zone directly at the screen damage and the partial saturation zone surrounding it. Therefore, in order to clarify the calculations of filtration through screen damage, it would be advisable to take into account the incomplete soil saturation of the filtration zone at the sub-screen base.

Let us further consider theoretical solutions using the source-sink method as a justification for experimental models of incomplete water saturation of the base soil with the polymer screen damage [26, 27]. Replacing the slots with linear ones and the slots in the polymer screen with point sources and using a model of water transfer in an unsaturated environment, we will show the possibility of taking into account the incomplete saturation of the filtration area in the calculations of the polymer screen water permeability. For this purpose, we will use theoretical models [27] for non-stationary water transfer tasks in drip and inland irrigation. We assume that the sources are on the surface of the base where the screen is damaged, there is no evaporation from the surface of the base, and the initial moisture distribution in the base soil thickness is homogeneous and equal  $\omega(x, y, z, 0) = \omega_0 = \text{const}$ .

Then the task of distribution of moisture in the sub-screen base through  $N$  sources (screen damage) by the intensity  $q_i(t) = (i = 1, N)$  and located in the plane  $OXY$  coinciding with the surface of the screen will be reduced to the next marginal non-stationary task of moisture transfer [26] in the area  $\Omega = \{(x, y, z, t); z \geq 0; -\infty < x, y < \infty, t \geq 0\}$ :

$$\frac{\partial \omega}{\partial t} = \text{div}[D(\omega) \text{grad} \omega] - \frac{\partial K(\omega)}{\partial Z} + \sum_{i=1}^N q_i(t) \cdot \delta(x - x_i) \cdot \delta(y - y_i) \cdot \delta(Z). \quad (3.2)$$

Under initial and boundary conditions:

$$\omega(x, y, z, 0) = \omega_0; \quad \omega(x, y, z, 0) = \omega_0 (Z_0 \rightarrow \infty), \quad (3.3)$$

where  $\omega(x, y, z, 0)$  is volume humidity;  $D(\omega) = K(\omega) \frac{d\Psi(\omega)}{d(\omega)}$  is capillary diffusion coefficient;

$\Psi(\omega) = \rho/\gamma < 0$  is capillary potential;  $K(\omega)$  is moisture conductivity coefficient;  $\delta$  is dirac delta function.

The last term in equation (3.2) characterises the presence in the plane  $OXY$   $N$  of intensity sources  $q_i(t)$ ;  $x_i, y_i, z = 0$  are coordinates of the  $i$ -th source; the axis  $OZ$  is directed vertically downwards.

The solution of equation (3.3) of a nonsteady problem for a semi-limited region in the presence of a point source, obtained by S.N. Novoselsky [26], is generally presented:

$$\theta(\bar{x}, \bar{y}, \bar{z}, \tau) = \frac{e^{\bar{z}}}{\sqrt{\pi}} \int_0^{\tau} q_1 \left( \frac{\tau - \zeta}{\alpha_0} \right) \cdot \zeta^{-3/2} \cdot \exp \left( -\zeta - \frac{\bar{r}^2}{4\zeta} \right) d\zeta -$$

$$- e^{-2\bar{z}} \int_0^{\tau} \left( \frac{\tau - \zeta}{\alpha_0} \right) \cdot e^{-\frac{\bar{R}^2}{4\zeta}} \cdot \operatorname{erfc} \left( \frac{\bar{z}}{2\sqrt{\zeta}} + \sqrt{\zeta} \right) \cdot \frac{d\zeta}{\zeta}, \quad (3.4)$$

where  $\bar{x} = \beta x$ ;  $\bar{y} = \beta y$ ;  $\bar{z} = \beta z$ ;  $\beta = 0.5 \cdot K_1 = 0.5 \cdot \alpha \cdot n$ ;  $\alpha = 0.02 - 0.1 \text{ cm}^{-1}$ ;  $n = 3 - 5$ ;  
 $\tau = \frac{\bar{D} k_1^2}{4} t = \alpha_0 t$ ;  $\theta = \frac{4}{\beta q^*}$ ;  $\bar{R}^2 = \bar{x}^2 + \bar{y}^2$ ;  $\operatorname{erfc} p = 1 - \operatorname{erf} p$ ;  $\operatorname{erf} p = \frac{2}{\sqrt{\pi}} \int_0^p e^{-\mu^2} d\mu$  are probability integral.

In the case of a linear final length source ( $\bar{z} = 0$ ,  $\bar{x} = 0$ ,  $\bar{y}_1 \leq \bar{y} \leq \bar{y}_2$ ).

$$\theta(\bar{x}, \bar{y}, \bar{z}, \tau) = \frac{e^{-\bar{z}}}{\beta} \int_0^{\tau} q_1 \left( \frac{\tau - \zeta}{\alpha_0} \right) \cdot (\operatorname{erfc} p_1 - \operatorname{erfc} p_2) \cdot$$

$$\cdot \exp \left( -\zeta - \frac{\bar{x}^2 + \bar{z}^2}{4\zeta} \right) d\zeta - e^{-2\bar{z}} \int_0^{\tau} q_1 \left( \frac{\tau - \zeta}{\alpha_0} \right) \cdot$$

$$\cdot (\operatorname{erfc} p_1 - \operatorname{erfc} p_2) \cdot \exp \left( \frac{\bar{x}^2}{4\zeta} \right) \cdot \operatorname{erfc} \left( \frac{\bar{z}}{2\sqrt{\zeta}} + \sqrt{\zeta} \right) \cdot \frac{d\zeta}{\zeta}, \quad (3.5)$$

where  $p_{1,2} = \frac{\bar{y}_{1,2} - \bar{y}}{2\sqrt{\zeta}}$ .

When calculating the dependencies (3.3)–(3.6), the average value of the capillary diffusion coefficient  $D(\omega)$  shall be set using the dependencies of capillary potential  $\Psi(\omega)$  proposed by A.I. Golovanov. Based on a numerical calculation, it is possible to determine the expenditure through screen damage (sources)  $q_1$  at any point in time.

For an approximate assessment of filtration seepage through polymer screen damage, it is sufficient to consider the filtration coefficient at partial saturation  $k_\omega$  instead of the underside of the screen at full saturation  $k_2$  in the previously obtained analytical dependencies:

$$q_{s\omega} = \frac{\pi k_\omega (h_1 + H_c)}{\operatorname{Arsh}(1/\sqrt{\alpha - 1})}; \quad (3.6)$$

$$B_\omega = \frac{2q_{s\omega}}{\pi^2 k_\omega} \cdot \int_0^1 \frac{\operatorname{Arch}(1/\sqrt{\zeta})}{\sqrt{(1-\zeta)(\zeta-\alpha)}} \cdot d\zeta + m; \quad (3.7)$$

$$h_{1\omega} = \frac{\sigma_\omega (h_0 + \delta_0) \cdot \operatorname{Arsh}(1/\sqrt{\alpha - 1}) - H_c \cdot \ln(16\delta_0 / \pi m)}{\sigma_\omega \cdot \operatorname{Arsh}(1/\sqrt{\alpha - 1}) + \ln(16\delta_0 / \pi m)}; \quad (3.8)$$

$$B_\infty = q_{s\omega} / K_\omega; \quad (3.9)$$

where  $q_{s\omega}$  is specific flow rate of filtration through the slot of the polymer screen taking into account the filtration coefficient at partial saturation,  $\text{m}^2/\text{day}$ ;  $B_\omega$  is filtration flow spread width under the screen,  $\text{m}$ ;  $h_{1\omega}$  is piezometric pressure in the slot taking into account partial saturation,  $\text{m}$ ;  $\sigma_\omega = k_1 / K_\omega$  is ratio of the filtration coefficients of the protective layer and the underlying base;  $H_c$  is capillary vacuum of the base soil,  $\text{m}$ ;  $\alpha$  is a parameter determined from the equation of type  $\bar{m} = m / (h_1 + H_c) = F_1(\alpha)$  using a special

table [2];  $m$  is polymer screen slot width, m;  $h_0$  is water depth in the canal (reservoir), m;  $\delta_0$  is thickness of the protective layer of the screen, m.

On the basis of the experiments [5] and available field research data on pilot pits and film screens [2], the average humidity for sandy ground directly under the screen damage shall be set within the limits  $\omega^0 = 0.45 - 0.55$ , and for loamy ground - within the limits  $\omega^0 = 0.35 - 0.45$ .

As an example, filtration calculations from a slot in a polymer screen with a protective coating were performed with the following input data:  $h_0 = 5.0$  m;  $\delta_0 = 0.5$  m;  $k_1 = 0.1$  m/day for the protective ground layer;  $k_2 = 1.0$  m/day for the underlying substrate;  $H_c = 0.3$  m. In addition, calculations were made taking into account the incomplete saturation of soil at  $\omega^0 = 0.5$  in the filtration zone under the polymer screen. The calculation scheme is shown in Fig. 3.1, and the results of the dependencies (3.6)–(3.9) calculations for the different slot widths  $m$  are shown in Table 3.2.

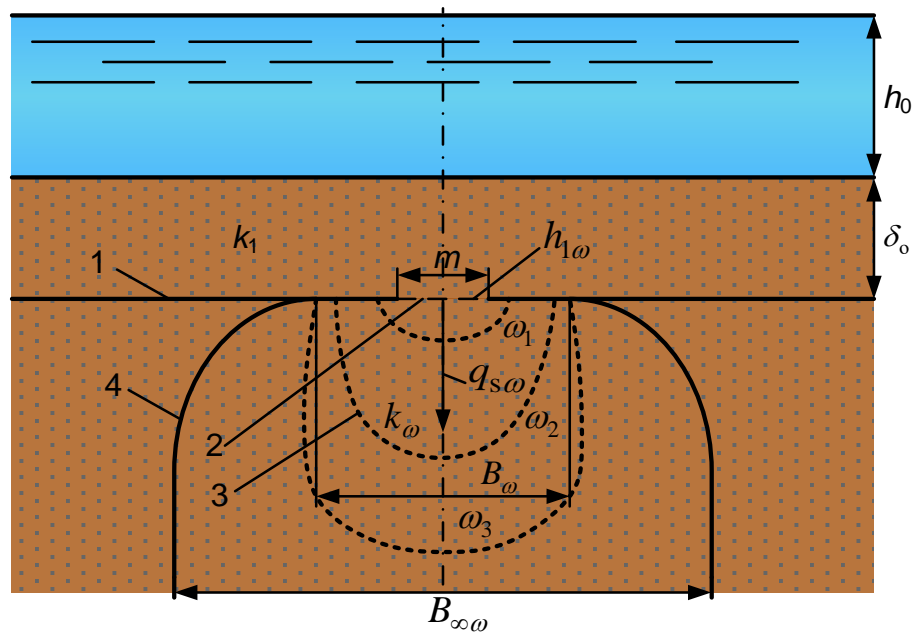


**Figure 3.1. Calculation scheme of filtration through the slot of the screen from the geomembrane taking into account the incomplete saturation of the base soil under the screen: 1 – the screen from the geomembrane; 2 – the slot in the screen; 3 – the contours of different ground humidity of the base soil under the slot in the screen  $\omega_1, \omega_2, \omega_3$ ; 4 – the zone of filtration flow spreading.**

**Table 3.2. The results of the calculation of filtration from a polymer screen slot with a considered complete and incomplete base saturation.**

| $m / h$ | $h_1$ , m   | $h_{1.\omega 1}$ , m | $q_s$ ,<br>m <sup>2</sup> /day | $q_{s\omega}$ ,<br>m <sup>2</sup> /day | $B$ , m      | $B_\omega$ , m | $B_\infty$ , m | $B_{\infty\omega}$ , m |
|---------|-------------|----------------------|--------------------------------|--|--------------|----------------|----------------|------------------------|
| 0.005   | <u>2.27</u> | 4.98                 | <u>0.129</u>                   | 0.0193                                 | <u>0.619</u> | 1.13           | <u>1.29</u>    | 2.37                   |
|         | 0.0615      |                      | 0.218                          |  | 0.104        |                | 0.218          |                        |
| 0.025   | <u>2.30</u> | 5.00                 | <u>0.161</u>                   | 0.0243                                 | <u>0.772</u> | 1.36           | <u>1.61</u>    | 2.83                   |
|         | 0.0388      |                      | 0.275                          |  | 0.131        |                | 0.275          |                        |
| 0.005   | <u>2.32</u> | 5.01                 | <u>0.180</u>                   | 0.0275                                 | <u>0.862</u> | 1.53           | <u>1.80</u>    | 3.17                   |
|         | 0.0187      |                      | 0.311                          |  | 0.151        |                | 0.311          |                        |
| 0.25    | <u>2.37</u> | 5.04                 | <u>0.250</u>                   | 0.0373                                 | <u>1.195</u> | 1.98           | <u>2.50</u>    | 4.19                   |
|         | -0.0346     |                      | 0.422                          |  | 0.213        |                | 0.442          |                        |
| 0.5     | <u>2.43</u> | 5.05                 | <u>0.298</u>                   | 0.0480                                 | <u>1.422</u> | 2.36           | <u>2.98</u>    | 4.98                   |
|         | -0.105      |                      | 0.543                          |  | 0.261        |                | 0.543          |                        |

Note: 1. The numerator shows the values of the calculated parameters at full saturation  $k_1 = 0.1$  m/day and the denominator at full saturation  $k_2 = 1.0$  m/day.

2. Without fractions, the values of the calculated parameters in case of incomplete saturation at the sub-screen base where  $\omega^0 = 0.5$ ;  $k_\omega = k_2(\omega^0)^{3.5} = 0.0884$  m/day.

As can be seen from these calculations, the piezometric pressure along the screen slot ( $h_1$ ) falls significantly as the permeability of the screen base increases and reaches negative values at relatively large slot widths ( $m > 0.01$  m). Apparently, the negative values of piezometric pressure here are related to the phenomenon of capillary suction (vacuum) when the filtration flow moves under the screen slot with incomplete water saturation [32, 33].

Table 2 shows that the filtration flow through the slot increases with both the permeability of the base soil and the size of the slot, while the width of the spreading area of the filtration flow under the screen, in contrast, decreases with increasing permeability. Filtration with full saturation is characterised by a small flow spreading width less than the capillary spreading zone ( $B < 2H_c$ ). This is because there is local filtration underneath the screen slot with incomplete pore saturation and therefore the solid flow zone is narrower than the capillary spreading zone.

At the same time, it should be noted that the filtration flow parameters from the polymer screen slot differ significantly in the case of incomplete saturation of the base soil (the filtration coefficient for incomplete saturation is determined using formula S.F. Averyanov's formula for relative humidity  $\omega^0 = 0.5$ ). The pressure along the slot and the width of the spreading area below the screen more than doubled (Fig. 3.2).

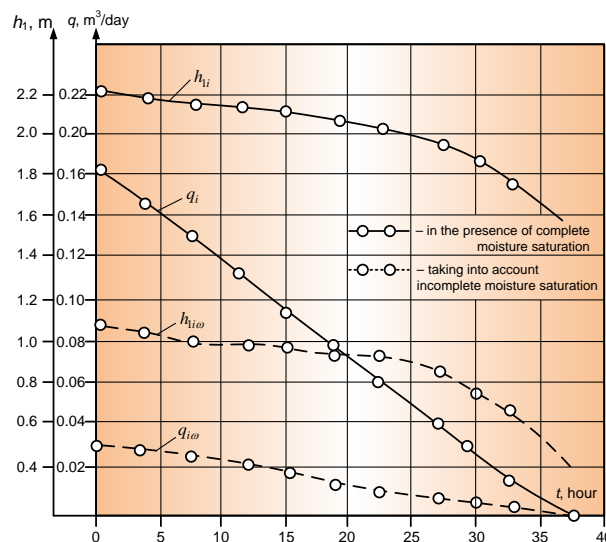


**Figure 3.2. Comparative results of calculations of moisture permeability of bentomats in the presence of defects.**

The graph (Fig. 3.2) shows the change in filtration flow through a single bentonite covering damage at full  $q_i$  and partial  $q_{i\omega}$  water saturation, as well as the change in pressure at the point of damage at full  $h_{1i}$  and partial  $h_{1i\omega}$  saturation, respectively. At full saturation, the cost curve drops from maximum to zero at  $t = 37.5$  hours, while at partial saturation – it drops slowly. In contrast to flow curves, the pressure  $h_1$  at the fault location changes slowly up to  $t = 25$  hour and then drops sharply to some minimum value.

## 4. Conclusions

1. Studies carried out on a soil filtration tray with a geomembrane screen model and slot damage with a fine sand substrate showed that the filtration flow through the slot moves into the sub-screen substrate with incomplete water saturation caused by capillary forces and the presence of entrapped air. With a protective screen layer, the permeability of the soil under the screen slot in the filter area is reduced compared to the case without a protective screen layer. In all the cases studied, the soil saturation coefficient in relation to the maximum possible soil permeability in the tray near the slot varies from 0.06 to 0.40 and relative humidity from 0.44 to 0.77.

2. Using theoretical solutions, the source-drain method and the unsaturated water transfer model, where slots can be replaced by linear ones and the slots in the polymer screen – by point sources, it is shown how solutions can be obtained for non-stationary water transfer tasks under the screen, which are used in drip and subsoilwater irrigation.

3. Specially performed calculations for the example show that the specific filtration flow from a polymer screen slot at partial saturation ( $q_{s0}$ ) decreases compared to full saturation (in the fraction denominator) depending on the width of the slot, the pressure in the slot  $h_1$  increases from 2.27 to 2.43 m, and in the sub-screen base drops from 0.0615 to minus 0.105 m, which is due to the appearance of a vacuum, with the width of the spreading area of the filtration flow directly below the screen  $B_0$  at infinity  $B_{\infty}$  increasing by approximately two times.

4. The results of moisture permeability of bentomat in the presence of defects were also obtained. They show changes in flow rates and pressures at full and incomplete moisture saturation.

## References

1. Solskiy, S.V., Lopatina M.G., Orlova, N.L. Laboratornyye issledovaniya geosinteticheskikh materialov dlya obosnovaniya ikh primeneniya v konstruktsiyakh gruntovykh gidrotekhnicheskikh sooruzheniy [Laboratory research of geo-synthetic materials to justify their application in the structures of soil hydroengineering constructions]. Izvestiya VNIIG B.E. Vedeneeva. 2015. Vol. 276. Pp. 84–89.
2. Kosichenko, Yu.M., Baev, O.A. Matematicheskoye i fizicheskoye modelirovaniye filtratsii cherez малыye povrezhdeniya protivofiltratsionnykh ustroystv iz polimernykh geomembran [Mathematical and physical modeling of seepage through small injuries of anti-seepage devices made of polymeric geo-membranes]. Izvestiya VNIIG B.E. Vedeneeva. 2014. Vol. 274. Pp. 60–74.
3. Kosichenko, Yu.M., Baev, O.A. Multilayer anti-seepage liners based on bentonite mats: comparison of their effectiveness. Power Technology and Engineering. 2019. Vol. 53. Pp. 288–293. DOI: 10.1007/s10749-019-01073-1
4. Kosichenko, Yu.M., Baev, O.A. Highly reliable designs of impervious coatings for channels and reservoirs, the criteria for their efficiency and reliability. Hydraulic Engineering. 2014. No. 8. Pp. 18–25.
5. Kosichenko, Yu.M., Baev, O.A. Water permeability of the polymer screen with a system of slits of hydraulic structures. Magazine of Civil Engineering. 2018. No. 7 (83). Pp. 148–164. DOI: 10.18720/MCE.83.14
6. Baev, O.A., Kosichenko, Yu.M. Gidromekhanicheskoye resheniye zadachi vodopronitsayemosti ekrana narushennoy sploshnosti [Hydromechanical solution to the problem of permeability of the screen of the broken continuity]. Izvestiya Rossiiskoi akademii nauk. Mekhanika zhidkosti i gaza. 2018. No. 4. Pp. 3–11.
7. Ishchenko, A.V. Povysheniye effektivnosti i nadezhnosti protivofiltratsionnykh oblitsovok orositelnykh kanalov: [Improving the efficiency and reliability of anti-filtration partitions of irrigation channels]. Rostov-na-Donu: Izvestiya vysshikh uchebnykh zavedeniy. Severo-Kavkazskiy region. Tekhnicheskoye nauki, 2006. 211 p.
8. Ishchenko, A.V. Gidravlicheskaya model vodopronitsayemosti i effektivnosti protivofiltratsionnykh oblitsovok krupnykh kanalov [Hydraulic model of water resistance and efficiency of anti-filtration lining of large channels]. Izvestiya VNIIG B.E. Vedeneeva. 2010. 258. Pp. 51–64.
9. Chernov, M.A. Obosnovaniye protivofiltratsionnoy effektivnosti oblitsovok kanalov s primeneniym polimernykh materialov. Izvestiya vysshikh uchebnykh zavedeniy [Substantiation of the anti-filtration efficiency of channel linings using polymer materials]. Severo-Kavkazskiy region. Seriya: Tekhnicheskoye nauki. 2011. No. 2. Pp. 108–113.
10. Pechenezhskaya, I.A. Vodopronitsayemost polimernykh protivofiltratsionnykh ekranov dlya usloviy ustanovivshegosya i neustanovivshegosya kharaktera filtratsii [Water resistance of polymer anti-filtration screens for conditions of steady and unsteady filtration]. Avtoreferat dissertatsii na soiskaniye uchenoy stepeni kandidata tekhnicheskikh nauk. Novocherkassk, 1988. 17 p.
11. Pechenezhskaya, I.A. Issledovaniye naporno-beznapornoy filtratsii cherez shchel ekrana metodom filtratsionnykh lotkov [Studies of pressure-free filtration through the screen slit by the method of filtration trays]. Informatsionnyy listok No. 485-98. Rostovskiy TsNTI, 1988. 3 p.
12. Giroud, J.P. Equations for calculating the rate of liquid migration through composite lines due to geomembrane defects. Geosynthetics International. 1997. Vol. 4. Pp. 335–348.
13. Giroud, J.P., Thiel, R.S., Kavazanjian, E. Hydrated area of a bentonite layer encapsulated between two geomembranes. Geosynthetics International. 2004. Vol. 11. Pp. 330–354. DOI: 10.1680/gein.11.4.330.51769
14. Touze-Foltz, N., Rowe, R.K., Duquennoi, C. Liquid flow through composite liners due to geomembrane defects: analytical solutions for axi-symmetric and two-dimensional problems. Geosynthetics International. 1999. Vol. 6. No. 6. Pp. 455–479. DOI: 10.1680/gein.6.0160
15. Touze-Foltz, N., Giroud, J.P. Empirical equations for calculating the rate of liquid flow through composite liners due to geomembrane defects. Geosynthetics International. 2003. Vol. 10. Pp. 215–233. DOI: 10.1680/gein.10.6.215.37243
16. Koerner, R.M., Hsuan, Y.G., Koerner, G.R. Lifetime predictions of exposed geotextiles and geomembranes. Geosynthetics International. 2016. Vol. 24. Pp. 198–212. DOI: 10.1680/jgein.16.00026
17. Koerner, R.M., Koerner, G.R., Hsuan, Y. Exposed geomembrane geosynthetic clay liner composites for solid waste covers, liquid impoundment liners, and canal liners. Geotechnical special publication. 2016. Vol. 274. Pp. 22–35. DOI: 10.1061/9780784480175.002
18. Koerner, G.R., Koerner, R.M. The durability of exposed geomembrane covers. Geotechnical Special Publication Issue. 2017. Vol. 276. Pp. 139–147. DOI: 10.1061/9780784480434.014
19. Bandurin, M.A. Diagnostika tekhnicheskogo sostoyaniya i otsenka ostatochnogo resursa rabotosposobnosti vodoprovodnykh sooruzheniy orositelnykh sistem [Diagnostics of the technical condition and assessment of the residual life

- of the operability of water supply devices of irrigation systems]. Avtoreferat dissertatsii na soiskaniye uchenoy stepeni doktora tekhnicheskikh nauk. Moskva. 2017. 41 p.
20. Glagovskiy, V.B., Solskiy, S.V., Lopatina, M.G., Dubrovskaya, N.V., Orlova, N.L. Geosinteticheskiye materialy v gidrotekhnicheskoy stroitel'stve [Geosynthetic material in hydraulic engineering construction]. Gidrotekhnicheskoye stroitel'stvo. 2014. No. 9. Pp. 23–27.
  21. Skuyero, A.M., Vasketti, G.L. Geomembrany – khorosho zarekomendovavshiye sebya vodopronitsayemye sistemy na gidrotekhnicheskikh sooruzheniyakh. Mezhdunarodnyy dayzhest po gidrotekhnike i poligonam. 2007. Pp. 59–68.
  22. Pryamitskiy, A.V., Shleye, Yu. Bentonitovyye maty kak alternativnyy material dlya protivofiltratsionnykh elementov gidrotekhnicheskikh sooruzheniy [Bentonite materials as an alternative material for anti-filtration elements of hydraulic structures]. Gidrotekhnika XXI vek. 2010. No. 1. Pp. 72–75.
  23. AbdelRazek, A.Y., Kerry Rowe, R. Interface transmissivity of conventional and multicomponent GCLs for three permeants. Geotextiles and geomembranes. 2019. Vol. 47. Pp. 60–74. DOI: 10.1016/j.geotexmem.2018.10.001
  24. Prabakaran, P.A., Sathyamoorthy, G.L., Adhimayan, M. An experimental and comparative study on canal lining exploitation geosynthetic material, cement mortar and material lining. International journal of recent technology and engineering. 2019. Vol. 7. No. 4. Pp. 81–83.
  25. Cen, W., He, H., Li, D. Influence of geomembrane defect on seepage property of earth-rock dams and measures of seepage control. Advances in science and technology of water resources. 2017. Vol. 37. Pp. 61–65. DOI: 10.3880/j.issn.1006-7647.2017.03.010
  26. Novoselskiy, S.N. Teoriya Filipa i yeye obobshcheniye na nestatsionarnyye zadachi vlagoperenosa pri kapel'nom oroshenii [Philippe's theorem and its generalization to non stationary equilibrium problems in a drop collision]. Gidravlika i inzhenernaya gidrologiya. 1981. Pp. 114–120.
  27. Novoselskiy, S.N., Shulgin D.F. Raschet nestatsionarnogo vlagoperenosa pri kapel'nom i vnutripochvennom oroshenii [Calculation of non-stationary moisture transfer during drip and subsurface irrigation]. Izd-vo AN SSSR. Mekhanika zhidkosti i gaza. 1981. No. 4. Pp. 74–81.

#### **Information about authors:**

**Oleg Baev**, PhD in Engineering

ORCID: <https://orcid.org/0000-0003-0142-4270>

E-mail: [Oleg-Baev1@yandex.ru](mailto:Oleg-Baev1@yandex.ru)

**Yuri Kosichenko**, Sc.D. in Engineering

ORCID: <https://orcid.org/0000-0002-9648-6441>

E-mail: [kosichenko-11@mail.ru](mailto:kosichenko-11@mail.ru)

**Victoria Silchenko**,

E-mail: [vika-silchenko@mail.ru](mailto:vika-silchenko@mail.ru)

*Received 08.12.2020. Approved after reviewing 25.05.2021. Accepted 26.05.2021.*



Research article


UDC 628.316

DOI: 10.34910/MCE.111.10

## Removal of heavy metals from wastewater with natural and modified sorbents

S.V. Stepanov , A.K. Strelkov , O.N. Panfilova  

Samara State Technical University, Samara, Russia

 [samoliasgy@yandex.ru](mailto:samoliasgy@yandex.ru)

**Keywords:** water adsorption, heavy metals, wastewater, modified clay, montmorillonite, dolomite, kaolinite, peat

**Abstract.** The paper presents research results of heavy metal ions sorption from a model solution and wastewater of an electroplating enterprise under static conditions. The purpose of this work is to develop a technology of tertiary treatment of electroplating production wastewater from heavy metals to achieve MPC levels for fresh fishery water bodies using local powder sorption materials. The authors examined such sorbents as modified clay (MC) obtained by thermal modification of its natural components (montmorillonite, kaolinite, peat, dolomite), as well as certain primary components and their mixtures without thermal modification. The studies were conducted at low initial concentrations of heavy metals (from 0.002 to 2.8 mg/l) characteristic of wastewater subjected to tertiary treatment. The concentration of heavy metals in wastewater was determined by inductively coupled plasma optical emission spectrometry on Avio™ 200. The research demonstrated that the contact time required to achieve the equilibrium of the treated wastewater and the modified clay sorbent varied from 60 to 120 minutes for the investigated heavy metals. Taking into account the time required to reach the MPCs of heavy metals for fresh fishery water bodies, the estimated contact duration of 90 minutes was recommended. The calculated dose of the modified clay sorbent, sufficient for tertiary treatment of acid-base wastewater of electroplating production to the MPC, was 1 g/l. Experiments with unmodified materials conducted on a multicomponent model solution showed that montmorillonite had the best sorption properties, ensuring the achievement of MPC for all metals, except aluminum, at doses from 0.1 to 0.9 g/l. Peat was the most effective in extracting nickel to MPC with its estimated dose being 0.1 g/l. Dolomite turned out to be the only material that provided the removal of aluminum to MPC at a dose of 1 g/l. The obtained results suggest that it is possible to increase the efficiency of heavy metals removal by selecting sorbent mixture without thermal modification and with mixed sorbent dose of 1–1.6 g/l. The authors recommend a technology of tertiary treatment of acid-base wastewater of electroplating production. This technology is to carry out the sorption process under static conditions using powder sorbents based on local natural materials, followed by separation of the spent sorbent with a precoat cartridge filter.

### 1. Introduction

Contamination of water resources by heavy metals is an enormous environmental problem. For example, the quality of the Kuibyshev reservoir waters in 2009–2018 varied from "polluted" to "dirty". In 2018, compared to the period of 2008–2017, water pollution from copper compounds increased by 47 % in the area below Samara, the excess of contamination for manganese varied from 3 to 6 MPC values of heavy metals for fresh fishery water bodies, and the excess of cadmium reached up to 2 MPC values. The

Stepanov, S.V., Strelkov, A.K., Panfilova, O.N. Removal of heavy metals from wastewater with natural and modified sorbents. Magazine of Civil Engineering. 2022. 111(3). Article No. 11110. DOI: 10.34910/MCE.111.10

© Stepanov, S.V., Strelkov, A.K., Panfilova, O.N., 2022. Published by Peter the Great St. Petersburg Polytechnic University.



This article is licensed under a CC BY-NC 4.0



main part of heavy metal pollution is caused by discharges from electroplating enterprises. Their wastewater is characterized not only by a diverse composition of pollutants, but also by the irregularity of the incoming wastewater. Paper [1] states that the wastewater of electroplating plants contains such elements as cadmium and lead, which are highly dangerous, while aluminum, iron, manganese, copper, nickel, chromium (VI) and zinc are referred to as moderately dangerous substances. Therefore, the degree of purification at local treatment facilities of industrial enterprises should be high, and the technologies used should provide the required efficiency.

The choice of physical and chemical methods of wastewater treatment from heavy metals depends on such initial parameters, as the volume of wastewater, the concentration of metals to be removed, and the total salt content [2–4].

Chemical precipitation is considered the most common method due to its simplicity and low capital costs. This method is widely used for the treatment of highly concentrated wastewater, including industrial wastewater subjected to tertiary treatment. The most frequently used reagents are slaked and quicklime, as well as soda ash. At the same time, even though the reagent method is used everywhere, it does not allow to achieve the required quality of purified water [2]. The purification process is complicated by the fact that each metal has its own pH range, at which the maximum precipitation of insoluble hydroxide occurs. Table 1 shows data on the efficiency of heavy metals precipitation from single- and multicomponent solutions at optimum pH values.

**Table 1. Efficiency of chemical precipitation of heavy metals at optimum pH values.**

| Metals                                       | Initial concentrations, mg/l | Final concentrations after neutralization, mg/l | MPCs of heavy metals for fresh fishery water bodies | Reagents used                            | Optimum pH | References |
|--|------------------------------|---|---|--|------------|------------|
| Cr (III)                                     | 30                           | 0.01  | 0.07  | Ca(OH) <sub>2</sub>                      | 8.7        | [2]        |
| Cu (II)*                                     | 48.51                        | 0.694   | 0.001   | aeration+<br>Ca(OH) <sub>2</sub> or NaOH | 12         |            |
| Zn (II)**                                    | 32                           | 0.22-0.32                                       | 0.01  | CaO                                      | 9–10       | [2]        |
| Cu (II),<br>Zn (II), Cr<br>(III), Pb<br>(II) | 100                          | 0.14<br>0.45<br>0.08<br>0.03                    | 0.001<br>0.01<br>0.07<br>0.006                      | CaO+ ash dust                            | 7–11       | [2]        |
| Fe (III)**                                   | 1.6                          | 0.928   | 0.1   |  |            |            |
| Co (II)                                      | 1.8                          | 0.11  | 0.01  |  |            |            |
| Ni (II)                                      | 6.5                          | 0.05  | 0.01  |  |            |            |
| Cr (III)                                     | 101.6                        | 2.12  | 0.07  | CaO                                      | 8          | [5]        |
| Cu (II)                                      | 4.5                          | 0.079   | 0.001   |  |            |            |
| Zn (II)                                      | 6.9                          | 0.102   | 0.01  |  |            |            |
| Cd (II)                                      | 5.3                          | 0.014   | 0.001   |  |            |            |
| Pb (II)                                      | 1.7                          | 0.1   | 0.006   |  |            |            |
| Al   | 215.9                        | –   | 0.04  | NaOH                                     | 5.5–7.5    | [6]        |

\*Cuprammonium solution

\*\*Multi-component solution

The disadvantages of this method are the large amount of precipitation generated, and, as Table 1 shows, the concentrations after treatment are more than MPCs of heavy metals for fresh fishery water bodies. Thus, an additional wastewater treatment is required afterwards.

The method of ion exchange makes it possible to achieve the MPCs of heavy metals for fresh fishery water bodies during wastewater treatment. The main disadvantages of ion exchange are the competition of metals in multicomponent solutions for active ion exchange centers, the interfering influence of H<sup>+</sup>, K<sup>+</sup>, Na<sup>+</sup>, Ca<sup>2+</sup>, Mg<sup>2+</sup> cations contained in the source water, the need to use chemical reagents for ionite regeneration, and the complexity of spent regenerating solutions treatment [3]. Due to high operating costs, ion exchange is economically feasible only when demineralized water is required.

Membrane filtration technologies with different types of membranes show great promise for heavy metals removal for their high efficiency, easy operation and space saving. When using ultrafiltration, it is

necessary to bind heavy metals into compounds whose particle size exceeds the pore size of ultrafiltration membranes. Two methods of water pre-treatment are used for this purpose. The first method involves surfactant molecules able to aggregate into micelles that can bind metal ions to form large metal-surfactant structures. The second method is based on water-soluble polymers that combine with metal ions and form macromolecules having a higher molecular weight than the molecular weight cut off of the membrane [2]. In reverse osmosis and ultrafiltration, semi-permeable membranes are used to trap hydrated heavy metals. Electrodialysis is another membrane process for the separation of ions across ion-exchange membranes from one solution to another using an electric field as the driving force. However, such disadvantages as high cost, the need for pre-treatment, the large amount of concentrates produced and the cost of their purification, mineral deposits on the surface of the membranes and frequent regeneration with reagents limit their use for the removal of heavy metals [7].

Among electrochemical methods of wastewater treatment from heavy metals, electrocoagulation and electroflotation are most well-known. Electrocoagulation involves the generation of coagulants in situ by electrolytic dissolution of aluminum or iron electrodes. The metal ion generation takes place at the anode, and hydrogen gas is released produced at the cathode. The hydrogen gas can help to float the flocculated particles out of the water. Electroflotation is a solid/liquid separation process that floats pollutants to the water surface by tiny bubbles of hydrogen and oxygen gases generated from water electrolysis. Electrochemical methods of wastewater treatment ~~from~~ are highly effective, especially at high initial concentrations of heavy metals. They are tightly controlled and require fewer chemical substances. Besides, they provide high-quality purification of wastewater with little precipitation. However, high initial investment and significant energy consumption limit the widespread use of electrochemical methods [2, 7].

Over the last years, researchers considered various sorption materials for removal of heavy metals from wastewater. They made use of such sorbents as activated carbon [8, 9], peat [10], dolomite [11], paper-and-pulp industry wastes [12, 13], natural [14–16] and synthetic zeolites [17]. Activated carbons with their high cost are characterized by low efficiency in removing heavy metals [18].

The experiments on using natural and modified clays seem most interesting [18–27]. Clay-based sorbents demonstrated high binding capacity for ions of heavy metals. Clays are widely distributed and inexpensive, and when modified, their sorption capacity increases significantly [23, 24, 27]. Montmorillonite and its modified forms have a higher sorption capacity to metals than kaolinite [24]. Adsorption of heavy metals by clay minerals is explained by ion exchange mechanism, direct binding of metal cations to the surface of the sorbents, as well as surface complexation. Many researchers note an increase in the aluminum concentration in water after its interaction with sorbents containing clay. It is explained by the ion-exchange nature of interaction and release of aluminum contained in clay during it [26, 32]. In the study of acid-modified clays, researchers note a high rate (within 5–10 minutes) of metal adsorption and the achievement of maximum recovery rates after 30 minutes. Thus, maximum values of the exchange capacity at pH = 5.5 for metal ions were as follows: 45 mg/g for iron; 50 mg/g for copper; 48 mg/g for zinc; 89 mg/g for lead [5]. The study of sorption properties was carried out at high initial concentrations, which makes it impossible its application in the calculation of tertiary treatment facilities for low-concentrated wastewater.

This work continues a whole series of studies on the sorption properties of sorbents based on natural materials [29–31]. The purpose of this work is to develop a technology for tertiary treatment of pre-treated wastewater from electroplating production from heavy metals to the MPCs for fresh fishery water bodies using local sorption materials. To do this, the researchers aim to establish the contact time required to achieve the equilibrium between the treated wastewater and the sorbents used; to determine calculated doses of recommended sorbents; to find a solution for separating the suspension of the spent sorbent from the treated water; to develop a schematic diagram of treatment facilities.

## 2. Methods

The sorbents analyzed included a thermally modified mixture of natural materials, mainly clays. Other individual components that are part of this mixture (without thermal modification and binder) included montmorillonite, kaolinite, peat and dolomite as well as a sorbent agent consisting of a composition of these natural components. The composition of sorbents and the methods of their preparation are shown in Table 2.

**Table 2. Composition of sorbents and methods of their preparation and production.**

| Sorbent         | Production method  | Composition, weight by dry mass   | Symbols |
|-----------------|--|---|---------|
| Dolomite powder | Drying to a constant weight at 105 °C and grinding in a ball mill to a particle size less than 0.1 microns   | –   | D       |
| Kaolinite       | The same method  | –   | K       |
| Montmorillonite | The same method  | –   | M       |
| Peat            | The same method  | –   | P       |
| Modified clay   | Preparation of the initial components, as indicated above, mixing with water, thermal modification at 500 °C, grinding to a particle size of less than 0.1 microns | 10 parts montmorillonite, 10 parts kaolinite, 10 part of peat, 1 part of dolomite | MC      |
| Sorbent mixture | A mixture of natural components prepared as described above without thermal modification   | 5 parts of montmorillonite, 4÷10 parts of dolomite, 1 part of peat                | SM      |

When studying the sorption kinetics in each experiment, a sorbent portion of  $0.50 \pm 0.03$  g was added to 200 ml of wastewater (a dose of 2.5 g/l) at a temperature of  $20 \pm 1$  °C, the mixture was mixed with a magnetic stirrer. A water sample was taken after a specified time (5-120 min) of "sorbent-solution" contact and filtered through a paper filter with a pore size of 2-3 microns. Then the concentration of heavy metal ions was determined.

Experiments under static conditions were carried out at a temperature of  $20 \pm 1$  °C by contacting a sample of wastewater with sorbent doses of 0.1–1 g/l while mixing with a magnetic shaker and a contact duration of 90 minutes. Before determining the concentration of heavy metals in purified water, the sample was filtered through a paper filter with a pore size of 2-3 microns.

The effect of coagulation and flocculation on the intensification of the process of sorbent separation from the purified water was studied by the test coagulation. To do this, the suspension of the sorbent after 90 minutes of contact with the wastewater was poured into laboratory cylinders, a 1 % solution of the coagulant was injected into it with a dose of 10-50 mg/l of  $\text{Al}_2\text{O}_3$  and rapid mixing was carried out at a speed of  $500 \text{ min}^{-1}$  for 20 seconds. Then the mixing speed was reduced to  $120 \text{ min}^{-1}$  and slow mixing was carried out for 2 minutes. If the experiment involved the use of flocculant, then after two minutes of slow mixing, a 0.05 % solution of flocculant was added with a dose of 0.4–2 mg/l and slow mixing continued for another 5 minutes. After mixing was completed, settling was carried out in the same cylinders, or the suspension was poured into a Lisenko vessel with a water layer height of 350 mm, in which the kinetics of precipitation and compaction of the suspension were observed. After 30 minutes of settling, samples of purified water were taken.

The studies were carried out on model solution and on real wastewater. A model solution was prepared by dissolving salts  $\text{CuSO}_4 \cdot 5\text{H}_2\text{O}$ ,  $\text{Cd}(\text{CH}_3\text{COO})_2 \cdot 2\text{H}_2\text{O}$ ,  $\text{FeCl}_3 \cdot 6\text{H}_2\text{O}$ ,  $\text{NiCl}_2 \cdot 6\text{H}_2\text{O}$ ,  $\text{ZnCl}_2$ ,  $\text{Pb}(\text{NO}_3)_2$  and  $\text{AlCl}_3 \cdot 6\text{H}_2\text{O}$ , chemical pure (CP) and analytically pure (AP) grades in distilled water. The concentrations of metals in the model solution with pH = 5.5 were, mg/l: copper – 0.0081; cadmium – 0.0211; iron (III) – 1.023; nickel – 0.152; zinc – 0.098; lead – 0.0512; aluminum – 0.9971.

Real wastewater of electroplating production was collected at one of the enterprises of the Samara region. At the existing treatment facilities of this enterprise, chromium (VI) is recovered with sodium sulfite in an acidic environment. After that, chromium-containing wastewater is mixed with acid-base wastewater and the mixture is alkalinized with caustic soda, followed by the separation of the resulting chromium (III), copper, cadmium, iron, nickel, zinc, lead and aluminum hydroxides in the precipitation plant. The treated wastewater is disposed into the city sewer network. Since the existing treatment facilities did not always correctly fulfill wastewater neutralization, the samples of treated wastewater from electroplating production were alkalinized to pH = 8 and then additionally settled for two hours. The resulting clarified water was used in experiments as the original real wastewater. The initial concentrations of metals during the experiment were (mg/l): copper 0.0036 – 0.0389; cadmium 0.0022–0.0561; iron (III) 0.154–3.31; nickel 0.011–0.529; zinc 0.059–0.121; lead 0.008–0.0521; aluminum 0.643–2.81. The total salt content of this wastewater was 834–950 mg/l.

The concentration of heavy metals in wastewater was determined at all treatment stages by Inductively coupled plasma optical emission spectrometry on Avio™ 200 according to Environmental Federative Specification Document (EFSD = [PNDF] in Russian transcription) 14.1:2:4.135-98 "Methods for measuring mass concentration of elements in drinking water and wastewater samples by inductively coupled plasma atomic emission spectrometry". The measurement errors for each element are calculated in the tables depending on the initial concentration.

### 3. Results and Discussion

To study the kinetics of sorption and to determine the duration of contact sufficient to achieve equilibrium in the system "sorbent modified clay–solution", two series of experiments were performed. The experiments were carried out on real wastewater from electroplating production, previously clarified and neutralized to pH = 8.0. The results of the experiments with MC are shown in Fig. 1.

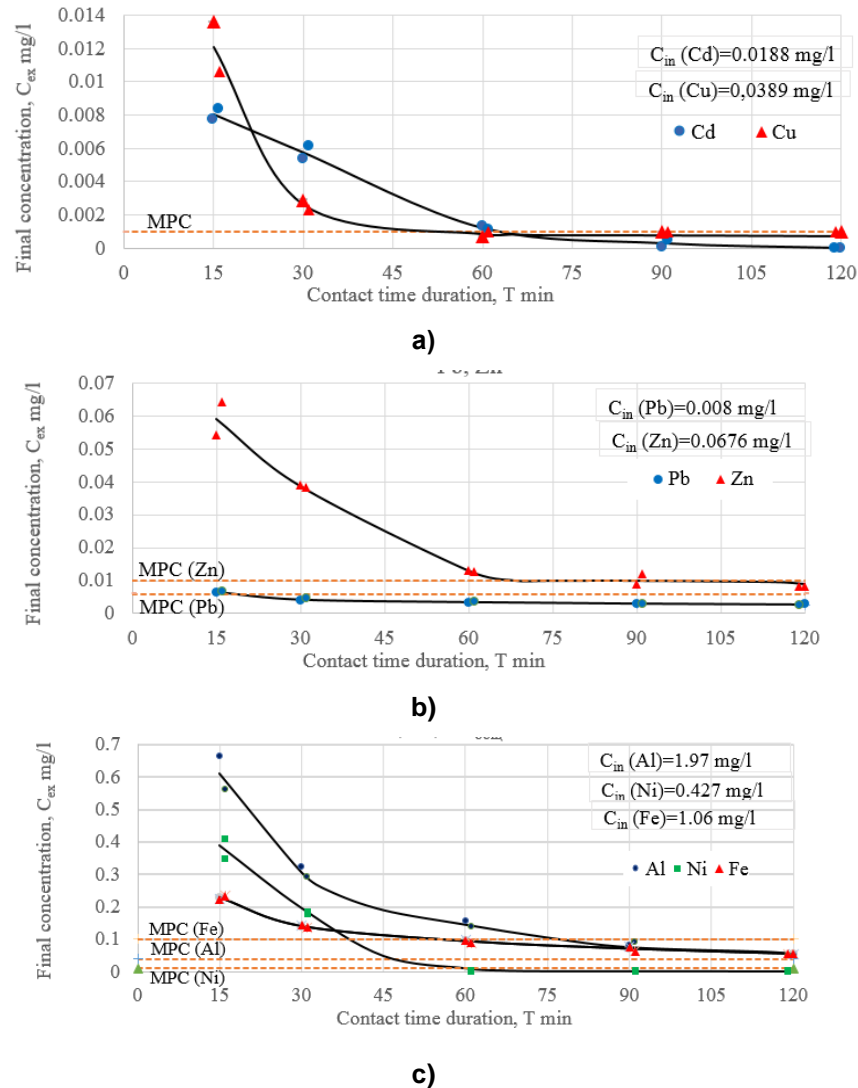


**Figure 1. Kinetics of heavy metals sorption with MC sorbent at a temperature of  $20 \pm 1^\circ\text{C}$ :**  
**a) cadmium, copper; b) lead, zinc; c) aluminum, nickel, iron;**  
 $C_{in}$  is initial heavy metals concentrations

As the graphs in Fig. 1 show, MPC requirements were met in the "sorbent-solution" system after 60–90 minutes of contact. MPC for lead was reached after 20–30 minutes, and it was the fastest time. It took 60 minutes for iron, nickel, copper and cadmium and 90 minutes for zinc to meet MPC requirements. The MPC values for aluminum were not reached; its final concentration after 120 minutes of stirring was 0.051 mg/l. It turned out that the required duration of contact slightly exceeds the time given in Paper [5]. During the time period under study the equilibrium in the "sorbent – solution" system was reached for cadmium, zinc, copper, aluminum and nickel, and it was not reached for lead and iron. According to the results of the experiment, a contact time of 90 minutes was adopted for further experiments on wastewater from electroplating enterprises tertiary treatment.

In order to determine the sorption capacity and the calculated dose of the modified clay sorbent, which under static conditions ensure the achievement of an equilibrium concentration of heavy metals at the level of MPCs for fresh fishery water bodies, a series of experiments was conducted on real wastewater in accordance with the above methodology. For this purpose, a mixture of chromium-containing and acid-base wastewater pre-treated under production conditions was neutralized to pH = 8 and then additionally settled. The results of experiments with different doses of the sorbent are shown in Fig. 2 and Table 3.

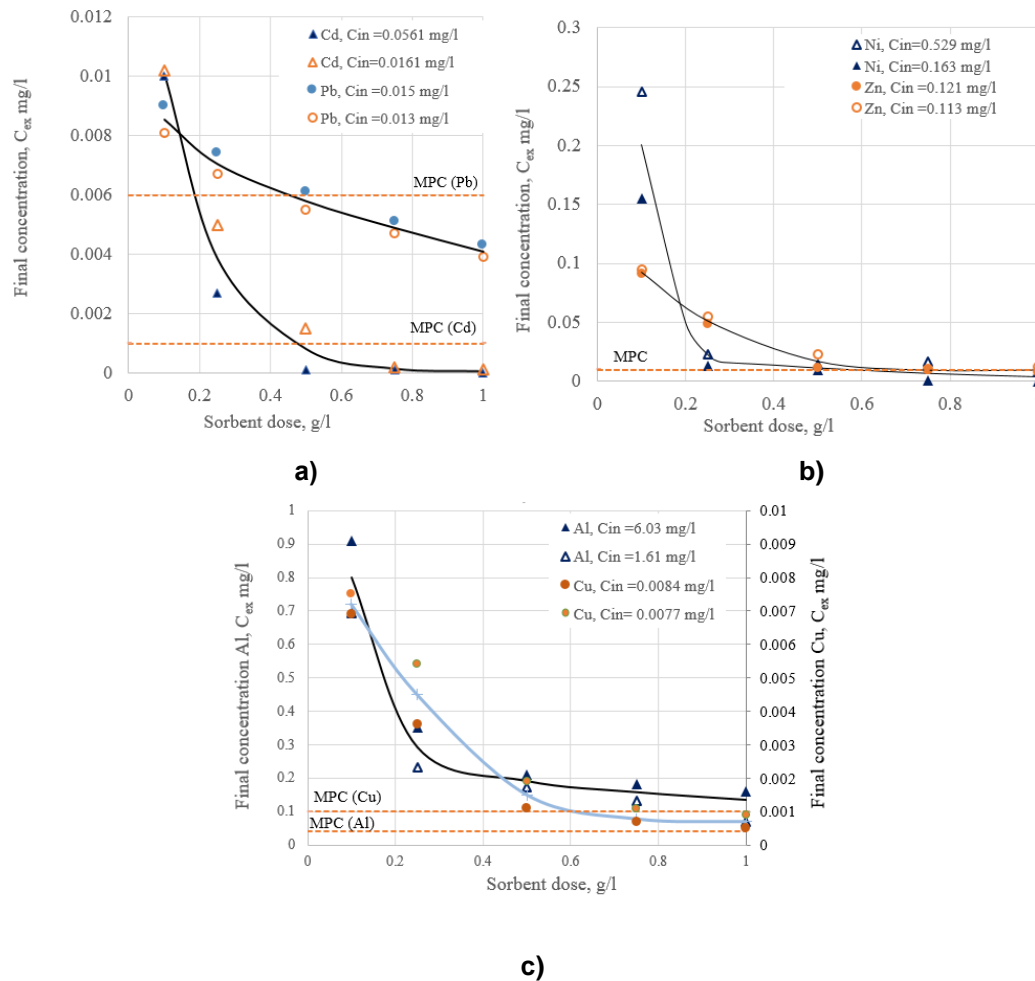


**Figure 2. Dependence of the equilibrium concentration of heavy metals on the modified clay sorbent at a temperature of  $20 \pm 1$  °C: a) cadmium, lead; b) zinc, nickel; c) copper, aluminum;  $C_{in}$  is initial heavy metals concentrations**

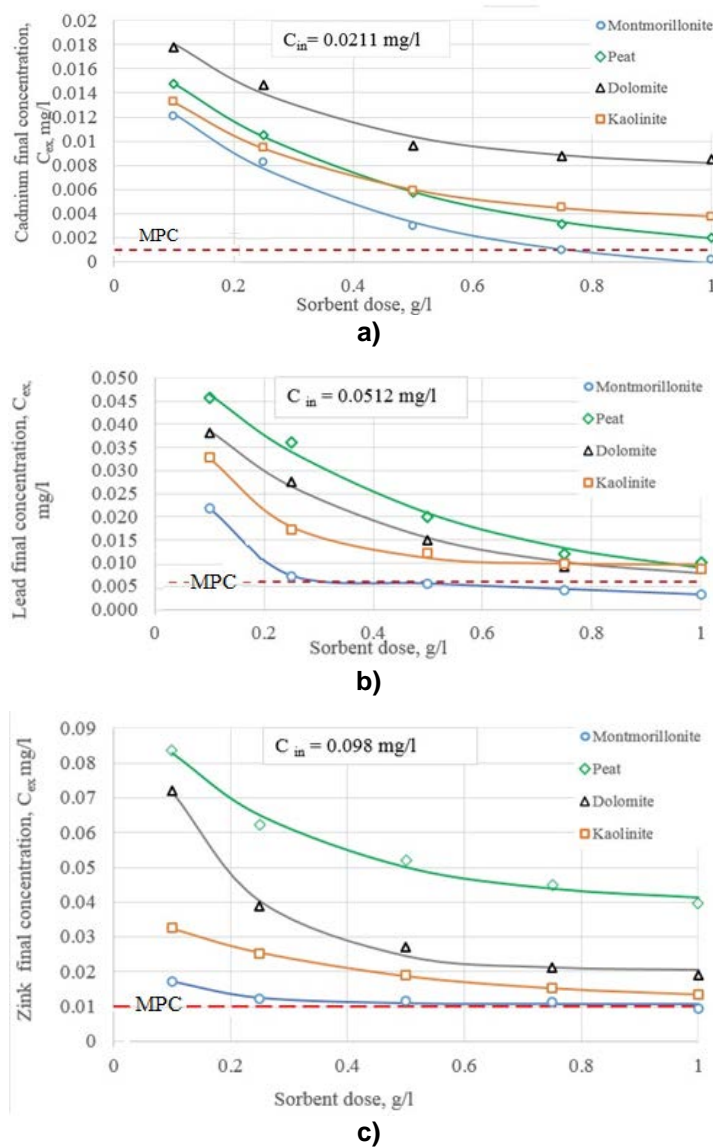
**Table 3. The values of the sorption capacity and the calculated dose of MC sorbent, which ensure the achievement of an equilibrium concentration of heavy metals at the level of the MPCs for fresh fishery water bodies under static conditions during tertiary treatment of wastewater from electroplating production,  $T = 20$  °C.**

| Metal        | Series 1         |                 |                  |                 | Series 2         |                 |                  |                 |
|--------------|------------------|-----------------|------------------|-----------------|------------------|-----------------|------------------|-----------------|
|              | $C_{in}$ , mcg/l | $D_{MPC}$ , g/l | $C_{in}$ , mcg/l | $D_{MPC}$ , g/l | $C_{in}$ , mcg/l | $D_{MPC}$ , g/l | $C_{in}$ , mcg/l | $D_{MPC}$ , g/l |
| Cd           | 56.1±13.5        | 0.5             | 56.1±13.5        | 0.5             | 56.1±13.5        | 0.5             | 56.1±13.5        | 0.5             |
| Pb           | 15.0±6.3         | 0.5             | 15.0±6.3         | 0.5             | 15.0±6.3         | 0.5             | 15.0±6.3         | 0.5             |
| Zn           | 121.0±29.0       | 0.75            | 121.0±29.0       | 0.75            | 121.0±29.0       | 0.75            | 121.0±29.0       | 0.75            |
| Cu           | 8.4±3.53         | 0.75            | 8.4±3.53         | 0.75            | 8.4±3.53         | 0.75            | 8.4±3.53         | 0.75            |
| $Fe_{total}$ | 3310.0±496.5     | 0.25            | 3310.0±496       | 0.25            | 3310.0±496.5     | 0.25            | 3310.0±496.5     | 0.25            |
| Al           | 6030.0±964.8     | 1.0             | 6030.0±964       | 1.0             | 6030.0±964.8     | 1.0             | 6030.0±964.8     | 1.0             |
| Ni           | 529±84.6         | 0.5             | 529±84.6         | 0.5             | 529±84.6         | 0.5             | 529±84.6         | 0.5             |

Note:  $S_{in}$  is initial concentrations of heavy metals;  $D_{MPC}$  is the sorbent dose required to achieve MPC;  $C_{ex}$  is heavy metals equilibrium concentrations in purified water;  $a$  is sorption capacity

Most researchers who studied sorption properties of clays and clay-based sorbents, determined sorption capacity at high initial and equilibrium concentrations of heavy metals [19, 24, 26, 28]. Therefore, it is difficult to compare the results obtained in the experiments described with other research data. Still, a meaningful comparison can be made with the data obtained in Paper [18] when studying the sorption of heavy metals from biologically treated wastewater in Khabarovsk using natural zeolite as a sorbent. At close initial concentrations, the researchers obtained such sorption capacities that correspond to the achievement of the MPCs of heavy metals for fresh fishery water bodies, which are: 0.45 mg/g for aluminum; 0.1 mg/g for zinc and iron; 0.025 mg/g for manganese. We also note that the modified clay sorbent sorption capacity for aluminum and iron was significantly higher than that of zeolite; similar values were obtained for zinc.

To find a more economical option for sorption tertiary treatment of wastewater from electroplating production, the following series of experiments was conducted. The sorption capacity and the calculated dose were determined for the initial unmodified components of sorbents such as montmorillonite, kaolinite, dolomite and peat without their thermal processing. The preliminary preparation of these materials is shown in Table 2. A model solution prepared by dissolving salts of seven heavy metals in distilled water was used as the source water, as indicated in the "Methods" section. In other respects, the method of the experiment was similar to the previous series. The dependences of heavy metals equilibrium concentrations on the sorbent dose are shown in Fig. 3.



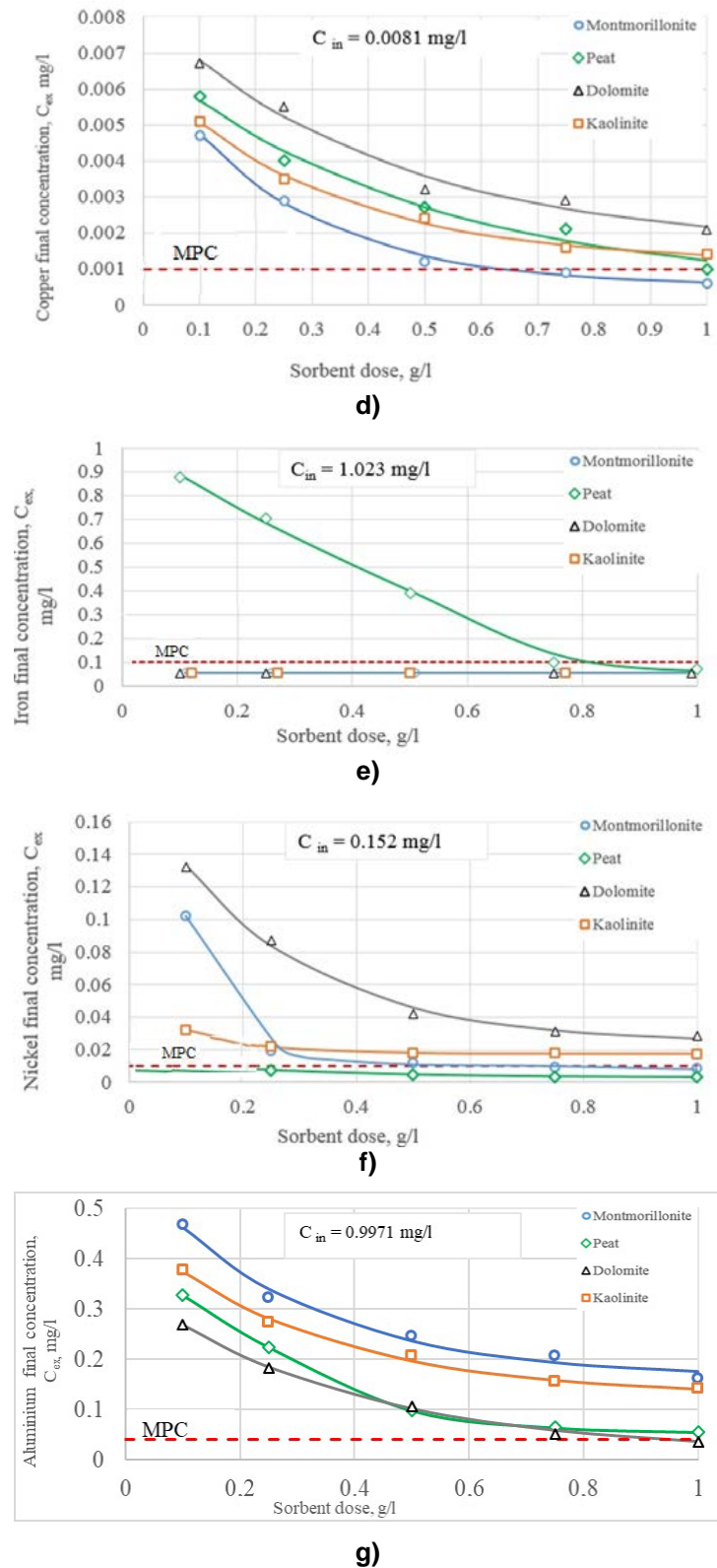


**Figure 3. The dependences of heavy metals equilibrium concentrations on the sorbent dose for the model solution at a temperature of  $20 \pm 1$  °C: a) cadmium; b) lead; c) zinc; d) copper; e) iron; f) nickel; g) aluminum;  $C_{in}$  is initial heavy metals concentrations**

The results of research in static conditions, presented in the form of graphs in Fig. 3, are summarized in Table 4. It specifies the doses of four sorbents sufficient to reduce heavy metals concentration from the initial to the MPCs.



**Table 4. Doses of the initial non-modified sorption materials that ensure the achievement of the equilibrium concentration of heavy metals under static conditions at the level of the MPCs for fresh fishery water bodies during tertiary treatment of wastewater of electroplating production (on a model solution,  $T = 20\text{ }^{\circ}\text{C}$ )**

| Metal                     | Initial concentration, mg/l | The sorbent dose, g/l, required to achieve MPC |                |                |                |
|---------------------------|-----------------------------|--|----------------|----------------|----------------|
|                           |                             | montmorillonite                                | kaolinite      | peat           | dolomite       |
| <i>Cd</i>                 | 0.0211±0.0068               | 0.75   | not registered | not registered | not registered |
| <i>Pb</i>                 | 0.0512±0.0164               | 0.4  | not registered | not registered | not registered |
| <i>Fe<sub>total</sub></i> | 1.023±0.153                 | 0.1  | 0.1            | 0.75           | 0.1            |
| <i>Zn</i>                 | 0.098±0.024                 | 0.9  | not registered | not registered | not registered |
| <i>Ni</i>                 | 0.152±0.040                 | 0.75   | not registered | 0.1            | not registered |
| <i>Al</i>                 | 0.9971±0.1595               | not registered                                 | not registered | not registered | 1              |
| <i>Cu</i>                 | 0.0081±0.003                | 0.65   | not registered | 1              | not registered |

Table 4 shows that montmorillonite has the best sorption properties among all local materials, ensuring the achievement of the MPCs for all metals, except aluminum, at doses varying from 0.1 to 0.9 g/l. These doses turned to be the lowest for cadmium, lead, zinc and copper as compared to other sorbents. The montmorillonite dose of 0.1 g/l needed to remove iron was the same as the doses of kaolinite and dolomite. Peat was most effective in extracting nickel with its estimated dose being 0.1 g/l. Dolomite was the only material that provided aluminum removal at a dose of 1 g/l. The use of kaolinite did not give any advantages for any of the examined heavy metals, which confirmed the data [24, 26] about the significantly higher sorption capacity of montmorillonite compared to kaolinite.

The results obtained suggest that it is possible to increase the efficiency of heavy metals removal by selecting the mixture of natural sorbents. In this case, montmorillonite should make up the bulk of the composition. If there is nickel and aluminum in the composition it is advisable to add peat and dolomite, respectively. The verification of this assumption was carried out on treated wastewater from electroplating production, which was additionally neutralized and clarified, as indicated in the "Methods" section.

Since the addition of sorbent mixture to the treated water formed a suspension, poorly separated by settling, the selection of doses of coagulant and flocculant was further performed to intensify this process. Considering the content of nickel (being 6.3 of MPC) and aluminum (93.3 of MPC) in the source water (see Table 5), a dose of sorbent mixture of 1 g/l was taken with the ratio of the components by weight being montmorillonite: dolomite: peat = 5:4:1. The corresponding sorbent sample was added to a 1.25l of wastewater sample. After 90 minutes of the wastewater and the sorbent mixing, the suspension was poured into five cylinders with a volume of 250 ml each and a trial coagulation was performed at doses of aluminum polyoxychloride 10; 20; 30; 40 and 50 mg/l for  $\text{Al}_2\text{O}_3$  in accordance with the procedure presented in the "Methods" section. According to the minimum turbidity of the clarified water, the optimal dose of the coagulant was determined as 40 mg/l for  $\text{Al}_2\text{O}_3$ . Then the experiment was repeated under the same conditions, but with the same dose of aluminum polyoxychloride – 40 mg/l for  $\text{Al}_2\text{O}_3$ . Additionally, the flocculant MagnaflocLT20 with doses of 0.4; 0.8; 1.2; 1.6 and 2 mg/l were introduced. According to the minimum turbidity of the clarified water, the optimal dose of the flocculant was determined as 0.4 mg/l.

The main experiment of this series was carried out in a glass cup with a volume of 1000 ml, a dose of sorbent mixture (SM) being 1 g/l, with the following ratio of components by weight – montmorillonite: dolomite: peat = 5:4:1. The final suspension was mixed with a magnetic stirrer at a temperature of 20 °C. After 90 minutes of contact, in accordance with the above-mentioned procedure, a coagulant – aluminum polyoxychloride with a dose of 40 mg/l for  $\text{Al}_2\text{O}_3$  and a flocculant MagnaflocLT200 with a dose of 4 mg/l were successively introduced into the glass. After mixing was completed, the suspension was poured into a Lisenko vessel, in which the kinetics of precipitation and compaction of the suspension were observed. After 30 minutes of settling, the sediment settled down to 8.1 ml/l. The efficiency of heavy metals removal in this experiment was determined twice: after settling and after filtering the clarified water through a paper filter with pores of 2-3 microns.

The experiment results are shown in Table 5.

**Table 5. Efficiency of tertiary treatment of wastewater from electroplating production with sorbent mixture (sorbent dose – 1 g/l, aluminum polyoxochloride dose – 40 mg/l for  $Al_2O_3$ , flocculant Magnafloc LT20 dose – 0.4 mg/l, temperature 20 °C).**

| Metal                     | Concentration in wastewater, mg/l |               |                | Efficiency, %                        |         | Adsorption capacity, mg/g |
|---------------------------|-----------------------------------|---------------|----------------|--------------------------------------|---------|---------------------------|
|                           | source                            | purified      |                | the degree of sorption-sedimentation | general |                           |
|                           |                                   | unfiltered    | filtered       |                                      |         |                           |
| <i>Cd</i>                 | 0.0014±0.0005                     | 0.0007±0.0003 | 0.00048±0.0002 | 51.4                                 | 66.7    | 0.0010                    |
| <i>Pb</i>                 | 0.0064±0.0027                     | 0.0018±0.0008 | 0.0008±0.0003  | 71.9                                 | 87.5    | 0.0056                    |
| <i>Fe<sub>total</sub></i> | 0.123±0.032                       | 0.073±0.018   | 0.058±0.014    | 40.7                                 | 52.8    | 0.0650                    |
| <i>Zn</i>                 | 0.0326±0.014                      | 0.0142±0.005  | 0.0101±0.003   | 56.4                                 | 69.0    | 0.0225                    |
| <i>Ni</i>                 | 0.0631±0.016                      | 0.0075±0.003  | 0.0057±0.002   | 88.1                                 | 91.0    | 0.0574                    |
| <i>Cu</i>                 | 0.0028±0.0012                     | 0.0017±0.0007 | 0.0016±0.0007  | 39.3                                 | 42.9    | 0.0012                    |
| <i>Al</i>                 | 3.73±0.597                        | 0.643±0.103   | 0.313±0.075    | 82.8                                 | 91.6    | 3.4170                    |

The data given in Table 5 show that the assigned task of reducing the concentration of heavy metals to MPC was almost completed. Only copper and aluminum exceeded the permitted concentrations. At the same time, the efficiency of aluminum removal as well as its sorption capacity were both high (91.6 % and 3.417 mg/g, respectively). The data given in Fig. 3d and 3g indicate that to meet the standards for copper and aluminum for a given concentration of heavy metals in the source wastewater, it is sufficient to increase the proportion of dolomite in sorbent mixture to the ratio of components being montmorillonite: dolomite: peat = 5:10:1 and take a 1.6 g/l dose of sorbent mixture. It is also important to note that the main part of heavy metals is removed from the treated wastewater at the settling stage, with the share of filtration in the overall cleaning effect varying from 3 to 15 %.

The research results make it possible to recommend the described technology for the treatment of wastewater containing heavy metals as well as acid-base wastewater from electroplating production. This technology includes correction of the pH of water to the range corresponding to the lowest solubility of heavy metal hydroxides, depending on the composition of the initial wastewater in each specific case (see Table 1) and sorption tertiary treatment with the use of sorbents based on local natural materials.

The authors elaborated two schemes of treatment plants that can be used to remove heavy metals from wastewater. The continuous operation scheme (see Fig. 4a) provides equalization of the source wastewater (1) in the equalization basin (2). Wastewater neutralization takes place in a flow reactor (4) equipped with a mixing device. The supply of the alkaline reagent solution is carried out from the alkali dosing unit (3) in accordance with the pH-meter signals. The resulting suspension of heavy metal hydroxides sediments in the settler (5). Clarified wastewater enters a flow sorption reactor with a mixing device (6). The sorbent is dosed into the adsorber in a dry form using a sorbent dispenser (7). At the exit from the reactor to the channel equipped with a mixing device, a coagulant solution is introduced into it from the coagulant dosing unit (8). The spent sorbent is separated in the tertiary settler (9), and the clarified water enters the transfer tank (10). The water supply for filtration is carried out by the feed pump (11). For final purification of wastewater from the residual amount of suspension, which is a spent sorbent, the installation with a precoat cartridge filter (12) is used. Treated wastewater (19) enters the clean water tank (13). A mixture of sediments containing heavy metal hydroxides and spent sorbent with removed heavy metals is collected in the sludge tank (14). To improve the dewatering process, a flocculant (18) is introduced before the mechanical dewatering unit (15). The drainage (16) obtained after dewatering is returned to the equalization basin, and the dewatered sludge (17) is taken to landfill sites for deposit.

In the batch treatment plant (see Fig. 4b), the same processes are carried out, but the wastewater neutralization, settling and removing of metal hydroxides, contact with the sorbent and its settling are carried out in the batch reactor (20), alternating in time. Wastewater treated at these stages is collected in the transfer tank (10). The operation of the precoat filter and mechanical dewatering units is similar to the operation of the corresponding units of the continuous operation scheme.

It is obvious that with an increase in capacity, the technical and economic advantages of continuous-acting plants increase in comparison with batch treatment plants. The choice of the treatment scheme is recommended to be carried out on the basis of a technical and economic calculation.

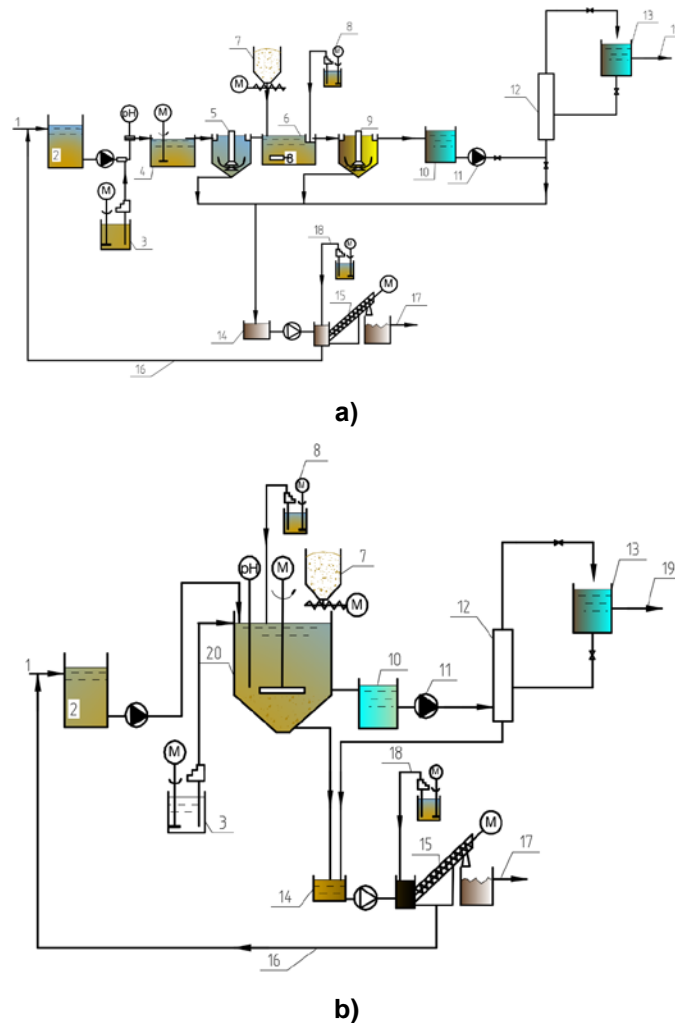


**Figure 4. Wastewater treatment plant from heavy metal ions: a) continuous operation; b) batch operation; 1 – source wastewater; 2 – equalization basin; 3 –alkali dosing unit; 4 – reactor-neutralizer; 5 – settler; 6 – adsorber with mixer; 7 – sorbent dispenser; 8 – coagulant dosing unit; 9 – tertiary settler ; 10 – transfer tank; 11 – feed pump of filtration unit; 12 – precoat filtration unit; 13 – treated water tank; 14 – sludge tank; 15 – mechanical dewatering unit; 16 – drainage; 17 – dewatered sludge; 18 – flocculant dosing unit; 19 – treated wastewater; 20 – batch reactor**

## 4. Conclusions

This paper considers using sorbents based on natural materials for post-treatment of wastewater from electroplating production. The experiments were carried out on a model solution containing a mixture of cadmium, lead, iron, zinc, nickel, copper and aluminum salts, as well as on wastewater from Samara electroplating plant treated at existing facilities by neutralization and sedimentation methods. The authors used local natural materials (that it montmorillonite, kaolinite, dolomite, peat and their mixtures obtained by thermal modification and without thermal modification) as sorbents. The research yielded the following conclusions:

1. Heavy metals initial concentrations in acid-base wastewater of electroplating production subjected to tertiary treatment after its neutralization to pH values corresponding to the minimum solubility of metal hydroxides, with account of the discrepancy between the optimal pH intervals, are 0.002–2.8 mg/l.
2. The contact time required to achieve the equilibrium of the treated wastewater and the modified clay sorbent (MC) varied from 60 to 120 minutes for the investigated heavy metals. Considering the time required to reach the MPCs of heavy metals for fresh fishery water bodies, the estimated contact duration of 90 minutes is recommended.
3. The calculated dose of the modified clay sorbent (MC), sufficient for tertiary treatment of pre-neutralized and clarified acid-base wastewater of electroplating production to the MPCs of heavy metals for fresh fishery water bodies, is 1 g/l.

4. The experiments demonstrated that montmorillonite had the best sorption properties among the studied natural materials, non-modified with temperature exposure, ensuring the achievement of MPC for all metals, except aluminum, at doses varying from 0.1 to 0.9 g/l. Peat was most effective in extracting nickel with its estimated dose being 0.1 g/l. Dolomite was the only material that provided aluminum removal at a dose of 1 g/l. For additional treatment of wastewater of electroplating plants from heavy metals, it is proposed to use a sorbent mixture made up of an unmodified mixture of components by the following ratio: montmorillonite: dolomite: peat = 5:4÷10:1 with its dose being 1–1.6 g/l.

5. The researchers put forward two schemes of tertiary treatment of pre-neutralized and clarified acid-base wastewater of electroplating production. The first-scheme is based on a continuous treatment process and the second is based on a batch treatment process. They consist in carrying out the sorption process under static conditions using powder sorbents based on local natural materials, followed by separation of the spent sorbent suspension by coagulation, tertiary sedimentation and filtering it with a precoat cartridge filter.

## References

1. Sorme, L., Lagerkvist, R. Sources of heavy metals in urban wastewater in Stockholm. *Sci. Total Environ.* 2002. 298. Pp. 131–145.
2. Fu, F., Wang, Q. Removal of heavy metal ions from wastewaters: A review. *Journal of Environmental Management.* 2011. 3(92). Pp. 407–418.
3. Bobade, V., Eshtiagi, N. Heavy Metals Removal from Wastewater by Adsorption Process: A Review. *APCCHE 2015 Congress Incorporating Chemeca.* 2015. 6(6). Pp. 312–317.
4. Kurniawan, T.A. 2003. Physico-chemical treatment techniques for wastewater laden with heavy metals. *Chemical Engineering Journal.* 118. 2006. Pp. 83–98. DOI: 10.1016/j.cej.2006.01.015
5. Ramazanov, A.Sh., Qasim, E.G. Heavy metals removal from waste water in electroplating industry with the use of montmorillonite clay. *Ecology and Industry of Russia.* 2015. Vol. 19. Iss. 12. Pp. 11–15. DOI: 10.18412/1816-0395-2015-12-11-15
6. Le, V.G., Vo, T.D.H., Nguyen, B.S., Vu, C.T. Recovery of iron(II) and aluminum(III) from acid mine drainage by sequential selective precipitation and fluidized bed homogeneous crystallization (FBHC). *Journal of the Taiwan Institute of Chemical Engineers.* 115. 2020. Pp. 135–143. doi.org/10.1016/j.jtice.2020.10.007
7. Barakat, M.A. New trends in removing heavy metals from industrial wastewater. *Arabian Journal of Chemistry.* 2011. № 4 (4). Pp. 361–377.
8. Sheng-Fong Lo, Song-Yung Wang, Ming-Jer Tsai, Lang-Dong Lin. Adsorption capacity and removal efficiency of heavy metal ions by Moso and Ma bamboo activated carbons. *Chemical Engineering Research and Design.* 2012. 90. Iss. 9. Pp. 1397–1406.
9. Tounsadi, H., Khalidi, A., Farnane, M., Abdennouri, M., Barka, N. Experimental design for the optimization of preparation conditions of highly efficient activated carbon from *Glebionis coronaria* L. and heavy metals removal ability. *Process Safety and Environmental Protection.* 2016. 102. Pp. 710–723.
10. Gogoi, H., Leiviskä, T., Heiderscheidt, E., Postila, H., Tanskanen, J. Removal of Metals from Mining Wastewaters by Utilization of Natural and Modified Peat as Sorbent Materials. *Mine Water and Circular Economy IMWA.* 2017. Pp. 218–225.
11. Kocaoba, S. Comparison of Amberlite IR 120 and dolomite's performances for removal of heavy metals. *Journal of Hazardous Materials.* 2007. Vol.147. Pp. 488–496. DOI: 10.1016/j.jhazmat.2007.01.037
12. Shan-Shan Li, Yi-Li Song, Hua-Rong Yang, Qing-Da An., Zuo-Yi Xiao, Shang-Ru Zhai, Carboxymethyl cellulose-based cryogels for efficient heavy metal capture. Aluminum-mediated assembly process and sorption mechanism. *International Journal of Biological Macromolecules.* 2020. 164. Pp. 3275–3286.
13. O'Connell, D.W., Birkinshaw, C., O'Dwyer, T.F. Heavy metal adsorbents prepared from the modification of cellulose: a review. *Bioresource Technology.* 2008. 99 (15). Pp. 6709–6724. https://doi.org/10.1016/j.biortech.2008.01.036
14. Vatin, N.I., Chechevichkin, V.N., Chechevichkin, A.V., Shilova, E.S. Application of clinoptilolite zeolites for natural water purification. *Civil Engineering.* 2013. No. 2. Pp. 81–88.
15. Aziz, H.A., Adlan, M.N., Ariffin, K.S. Heavy metals [Cd, Pb, Zn, Ni, Cu and Cr (III)] removal from water in Malaysia: Post treatment by high quality limestone. *Bioresource Technology.* 2008. 99(6). Pp. 1578–1583. DOI: 10.1016/j.biortech.2007.04.007
16. Erdem, E., Karapinar, N., Donat, R. The removal of heavy metal cations by natural zeolites. *Journal of Colloid and Interface Science.* 2004. 280. Pp. 309–314. DOI: 10.1016/j.jcis.2004.08.028
17. Chen, M., Nong, S., Zhao, Y., Sohail Riaz, M., Xiao, Y., Molokeev, M. S., Huang, F. Renewable P-type zeolite for superior absorption of heavy metals: Isotherms, kinetics, and mechanism. *Science of The Total Environment.* 2020.726. Pp. 138535. DOI: 10.1016/j.scitotenv.2020.138535
18. Shvetsov, V.N., Morozova, K.M. Extraction of heavy metal ions from biologically treated municipal wastewater. *Water Supply and Sanitary Engineering.* 2012. 7. Pp. 59–63.
19. Kashifuddin, M. A review on the adsorption of heavy metals by clay minerals, with special focus on the past decade. *Chemical Engineering Journal.* 2017. 308. Pp. 438–462. https://doi.org/10.1016/j.cej.2016.09.029
20. Zacaroni, L.M., Magriotis, Z.M., Cardoso, Md-G., Santiago, W.D. et al. Natural clay and commercial activated charcoal: properties and application for the removal of copper from cachaça. *Food Control.* 2015. 47. Pp. 536–544. https://doi.org/10.1016/j.foodcont.2014.07.035
21. Bentahar, Y., Hurel, C., Draoui, K., Khairoun, S., Marmier, N. Adsorptive properties of Moroccan clays for the removal of arsenic(V) from aqueous solution. *Applied Clay Science.* 2016. 119. Pp. 385–392. https://doi.org/10.1016/j.clay.2015.11.008
22. Alemayehu, D.D., Singh, S.K., Tessema, D.A. Assessment of the adsorption capacities of fired clay soils from JIMMA (Ethiopia) for the removal of Cr (VI) from aqueous solution. *Universal Journal of Environmental Research and Technology.* 2012. 2 (5). Pp. 411–420.
23. Abollino, O., Acetob, M., Malandrino, M., Sarzaninia, C., Mentastia, E. Adsorption of heavy metals on Na-montmorillonite. Effect of pH and organic substances. *Water Research.* 2003. 37. Pp 1619–1627. DOI: 10.1016/S0043-1354(02)00524-9

24. Bhattacharyya, K.G., Gupta, S.S. Adsorption of a few heavy metals on natural and modified kaolinite and montmorillonite: A review. *Advances in Colloid and Interface Science*. 2008. 140 (2). Pp. 114–131. DOI: 10.1016/j.cis.2007.12.008
25. Churchman, G.J., Gates, W.P., Theng, B.K.G., Yuan, G., Bergaya, F., Theng, B.K.G. Lagaly, G. (Eds.). *Clays and Clay Minerals for Pollution Control. Development in Clay Science*. Vol. 1. Elsevier Press. 2006.
26. Srinivasan, R. *Advances in Application of Natural Clay and Its Composites in Removal of Biological, Organic, and Inorganic Contaminants from drinkingwater*. Hindawi Publishing Corporation *Advances in Materials Science and Engineering*. 2011. Article ID 872531, 17 p. DOI: 10.1155/2011/872531
27. Abdugaffarova, K.K., Dorogov, M.V., Vikarchuk, A. A. New sorption materials on the basis of aluminosilicates for wastewater treatment. *Nano Hybrids and Composites*. 2017. 13. Pp. 190–196.
28. El-Maghrabi, H.H., Mikhail S. Removal of heavy metals via adsorption using natural clay material. *Journal of Environment and Earth Science*. 2014. 4 (19).
29. Stepanov, S.V., Panfilova, O.N., Abdugaffarova K.K. Post-treatment of wastewater from heavy metal ions with a new sorbent based on modified clays. *Water Supply and Sanitary Engineering*. 2018. 1. Pp. 46–50.
30. Stepanov, S., Panfilova, O.N. Removal of heavy metal ions with clay-based sorbent. *IOP Conference Series: Earth and Environmental Science*. 2019. 272. DOI: 10.1088/1755-1315/272/2/022248
31. Stepanov, S.V., Panfilova, O.N., Abdugaffarova, K.K. Physico-chemical properties of the new sorbent on the basis of sand. *Urban Construction and Architecture*. 2019. No. 1. Pp. 52–56. DOI: 10.17673/Vestnik.2019.01.9
32. Li X., Li H., Yang G. Electric fields within clay materials: How to affect the adsorption of metal ions. *Journal of Colloid and Interface Science*. 2017. (501). Pp. 54–59. DOI: 10.1016/j.jcis.2017.04.040

**Information about authors:**

**Sergey Stepanov**, Sc.D. in Technical Science

ORCID: <https://orcid.org/0000-0002-9139-680X>

E-mail: [stepanovsv3@yandex.ru](mailto:stepanovsv3@yandex.ru)

**Alexander Strelkov**, Sc.D. in Technical Science

ORCID: <https://orcid.org/0000-0002-0419-4231>

E-mail: [a19400209@yandex.ru](mailto:a19400209@yandex.ru)

**Olga Panfilova**,

ORCID: <https://orcid.org/0000-0002-1383-1271>

E-mail: [samoliasgsy@yandex.ru](mailto:samoliasgsy@yandex.ru)

*Received 23.12.2020. Approved after reviewing 12.07.2021. Accepted 13.07.2021.*



Research article

UDC 69.059.4

DOI: 10.34910/MCE.111.11

## Structural health monitoring by merging dynamic response data

L. Gaile , L. Pakrastins\* , L. Ratnika 

Riga Technical University, Riga, Latvia

 [leonids.pakrastins@rtu.lv](mailto:leonids.pakrastins@rtu.lv)

**Keywords:** structural health monitoring, modal analysis, damage detection, finite element method, dynamic response, natural frequencies, structural analysis, temperature, vibration analysis, structural dynamics, buildings

**Abstract.** The process of Structural Health Monitoring aims to detect changes in material and/or geometric properties, boundary conditions or member connectivity of a structural system in time. However, the transfer of research results into engineering practice poses several challenges, especially for stiff structures with very diverse geometry that could not be well dynamically excited like low and medium-rise structures under ambient vibration conditions. Noise in modal parameters from output-only modal analysis due to variable environmental and operational conditions is considered one of the most problematic aspects of detecting structural damage using a vibration-based method. This research proposes a new way to reduce environmental noise in vibration data and dynamic parameters by merging dynamic response data from two similar shear wall buildings. The object of the study is a three-story reinforced concrete building. First, the damage features as natural frequencies and zero-order temporal moment of the vibration response are studied. Further, those feature changes are explored by means of modelling wall removal/opening introduction into the finite element models. It is established that the variation in the base excitation spectrum has more impact on dynamic response than introduced structural changes. Therefore, a time-domain feature like a zero-order temporal moment of the vibration response is not applicable for the proposed method. The appropriate damage sensitive feature vector for this approach is the difference of natural frequencies from two monitored buildings. The proposed method for fusion of vibration information from several buildings that share the same environmental and operational conditions filter out environmental noise effectively and give a clear advantage in reducing false alarm possibility during continuous and automated structural health monitoring process.

### 1. Introduction

Structural Health Monitoring (SHM) is a process of implementing a damage detection strategy that involves the observation of a structure over time using periodically spaced or continuous dynamic response measurements. The extraction of damage-sensitive features from those measurements and the statistical analysis of these features are used to determine the current state of the system health. One of the SHM strategies is to use the vibration-based monitoring (VBM) global method by extracting the information about lower vibrational modes of the structure. Although VBM damage identification techniques are suitable for global damage assessment of large and flexible structures [1], recent advances in various technology branches allow developing new cost-effective methodologies for low and medium-rise structures. These include sensing equipment, signal acquisition and transmission, data processing and analysis, as well as

Gaile, L., Pakrastins, L., Ratnika, L. Structural health monitoring by merging dynamic response data. Magazine of Civil Engineering. 2022. 111(3). Article No. 11111. DOI: 10.34910/MCE.111.11

© Gaile, L., Pakrastins, L., Ratnika, L., 2022. Published by Peter the Great St. Petersburg Polytechnic University.



This article is licensed under a CC BY-NC 4.0

numerical modelling. Examples of successful dynamic parameter identification for medium-rise buildings under ambient vibration excitation (AVT) can be found in the literature [2–4].

One of the most problematic aspects of implementing an SHM system in practice is that real structures undergo the changing operational and environmental variables (EOV) [5]. The changes in natural frequency estimates due to environmental and operational variables are often of the same order of magnitude as those caused by damage [6]. Still, only a few researchers incorporate the consequences of these effects on their proposed SHM system. The most common environmental effects are temperature and moisture changes, but the operational effect changes mass and ambient loading conditions. These effects may disguise the changes in modal parameters from structural damage. In their seminal work in 2007, Hoon Sohn provided an extensive review of the effects of environmental and operational variations on real structures [7]. Many structures exhibit daily and seasonal temperature variations that cause the expansion or contraction of structures and boundary conditions changes. These effects mostly investigated in bridge monitoring research (e.g. [8–11]) because bridge structures experience more severe conditions than insulated buildings.

Realistic and direct modelling of the influence of environmental and operational variables on the structure's response is an almost impossible task. Therefore, it is common to build mathematical models from experimentally measured environmental data. Vibration-based damage sensitive features of healthy structure [12–16] obtained using different techniques, e.g. from simplest linear regression models to neural networks and support vector machines. The limitation of those methods is the restricted use of only those structures on which model has been created. Also, a training period that covers the range of environmental changes is needed to filter their influence, e.g. it is about one year for temperature variations [17].

Rainieri et al. [6] presents the Second-Order Blind Identification technique and demonstrates that it can model the variability of natural frequency estimates in operational conditions and give a fundamental insight in determining the causes of such variability.

Other techniques aim to obtain the variability of natural frequencies without measuring environmental or operational variables. These algorithms, e.g. principal component analysis (PCA) [5], Mahalanobis-squared distance (MSD), auto-associative neural network (AANN), factor analysis (FA), singular value decomposition (SVD) [18] rely only on response time-series data acquired under changing operating conditions. Recently a novel distance-based anomaly detection method based on adaptive Mahalanobis-squared distance and one-class kNN rule called AMSD-kNN has been proposed to detect early damage under the environmental variability conditions [19]. The authors of the paper performed comparative studies and concluded that the proposed AMSD-kNN method is superior to the conventional MSD, PCA, and AANN based anomaly detection techniques in detecting damage and distinguishing the damaged state from the normal condition properly.

Sohn in [7] points out that data normalisation procedures need to be more focused on specific applications. For example, industries and research should focus more on tests of real structures in their operating environment than laboratory tests of representative structures. The structural monitoring case of the “Cardarelli” Hospital in Campobasso [20] is one of the rare cases of longitudinal research on frequency dependency on building temperature changes. It shows clear frequency dependency for all four closely spaced modes on daily temperature changes. The first two are transversal and longitudinal bending modes, but the other two are torsional modes. The estimates' swing systematically recurs every day, with a sudden drop in the night and a gradual increase in the morning up to the maximum value reached in the afternoon.

Yuen and Kuo [21] utilise a one-year daily measurement of a 22-storey reinforced concrete building to trace the variation of its modal frequencies, which is identified using the Bayesian spectral density approach with the ambient vibration data. Their work investigates the ambient temperature variation and fundamental frequency variation during the year, and the results of the research highlight that the relative humidity could be essential for long-term structural health monitoring. Coletta et al. [19] use cointegration theory to remove environmental effects from dynamic data of the Sanctuary of Vicoforte in Italy. Their investigation showed that the different nature of the effects imposed by operational and environmental variations on structural response requires an extension of cointegration theory.

Gentile and Ruccolo [20] describe findings from one-year monitoring of EOV effects on the first six modes of Milan Cathedral. Authors conclude that the variations observed in the resonant frequencies are mainly driven by temperature, with the effect of thermal changes being very peculiar as the mode shapes in opposite do not exhibit appreciable fluctuations associated with the environmental changes.

Compiling the results from case studies mentioned above, it follows that environmental effects for building structures may introduce a variation of first natural frequencies up to 8 % depending on building structure and exposure level to those effects. On the contrary, variations in mode shapes due to EOV's seems to be less sensitive.



The recent development of the Internet of Things (IoT) rapidly expands the possibilities for the implementation of state-of-the-art SHM systems. IoT solutions for SHM purposes are commonly based on four principal components: sensor devices, gateway, Remote Control and Service Room, and Open Platform Communications server [19, 20, 22]. In the near future, low-cost sensor devices for sensor networks will be able to gather lots of vibration data remotely and aggregate it. After that, a critical analysis will be possible both for one structure and several buildings at once. Advancements of sensors with noise level as low as 60 ng/ $\sqrt{\text{Hz}}$  for the frequency band of interest [21] has already been reached.

This paper investigates the ways to reduce environmental noise in vibration data and dynamic parameters by merging vibration data from two similar buildings under ambient vibration conditions with variable operational and environmental situations. This work presents an approach for data fusion and verifies it by FEM simulations of two three-story buildings with very similar but not identical structural parameters nor ambient excitation. Furthermore, damage sensitive feature changes due to EOVS effects is investigated.

It is found that the fusion of vibration information from several buildings that share the same environmental and operational conditions gives clear benefits in reducing false alarm possibility during continuous and automated structural health monitoring process. The advantage of the presented approach includes: filtering out damage sensitive feature variations due to EOVS; potential reduction of training data required when machine algorithms applied for damage detection; no necessity for developing a reference model of a building, or gathering previous information on building dynamic response.

## 2. Research methods

There are four recognised paths to deal with EOVS effects in SHM:

1. Development of mathematical models from experimental measurements;
2. Monitoring of structure in an undamaged state and extracting feature vectors that are later compared with damaged state feature vectors;
3. Machine learning approaches trained on the undamaged state;
4. Damage detection by using features that are insensitive to EOVS effects.

However, almost all of the approaches require gathering experimentally or via model simulations vast amounts of information before the actual in-service monitoring due to the well-known SHM axiom that states:

*"The assessment of damage requires a comparison between two system states"* [23].

The authors also propose to use a reference state for damage detection—not the same building or its model in the undamaged state but rather a similar building nearby that generally share the same EOVS conditions. An example of such structures might be mass housing. Fig. 1 shows three buildings with similar structural composition and materials are located near ambient vibration source – regular traffic. These kinds of buildings often have reached their intended design life. SHM system that could detect an illegal structural change like new openings in walls or entire wall removals would enhance such buildings' structural safety.

The basic underlying assumptions of the proposed method are:

- Very unlikely that the exact damage occurs simultaneously at both buildings;
- Both buildings have a similar structure and share the same environmental and operational conditions (e.g. temperature, moisture and vibration source);
- The monitored feature vector changes due to the damage event;
- Properties of the soil only slightly modify modal frequencies of the building;
- The chosen monitoring system is capable of recording a time series of sensor network located in both buildings simultaneously and extract feature vectors with a precision higher than its value changes due to the damage event;
- Preferably, at least one damage sensitive feature is extracted from the frequency domain and one from the time domain to cross-check the identified damage event to reduce false alarm situations.

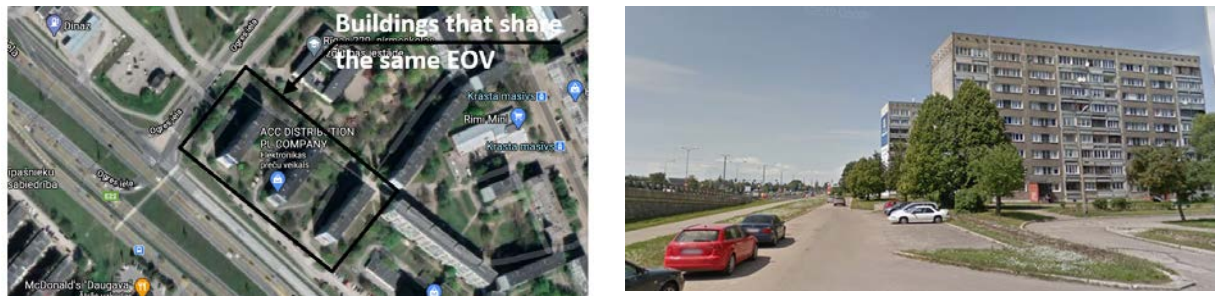


**Figure 1. Example of mass house buildings that share the same EOV and ambient vibration conditions [24, 25].**

To find out appropriate damage sensitive features of medium-rise shear wall structure 60 FEM simulation cases were performed. In all these simulations, the previously outlined method for structural damage identification was applied to filter out the effects of variable environmental and operational conditions. These simulations correspond to 30 experimental measurements per year per building.

Generally, EOV effects might be sources of variations in the following structural elements and parameters: stiffness changes of the foundation base (cause: groundwater changes, freezing and defrosting of the soil); the variable inertial mass of the structure (cause: snow, rain, varying material densities, variable load etc.); the variable stiffness of the structure (cause: temperature, moisture, change in boundary conditions of elements).

Stiffness changes in the foundation base affect natural frequency values, but this dynamic parameter change does not characterise the damage of the structure. Therefore, in performed simulations, building bases are taken as fixed.

Other EOV effects are implemented in the model through variable elastic modulus and material density. A total change of natural frequencies due to EOV are in the range of 3 %. EOV deviations have a harmonic component and a stochastic component. Due to seasonal temperature fluctuations, changes represent a harmonic function of elastic modulus  $E$  (see Fig. 2), but the stochastic component of EOV effects considered by changes in material density (see Fig. 3).

Variations in the excitation signal from building to building were realised through randomly generated signal following the Gaussian distribution in the frequency domain. In calculations, mean and standard deviation values of excitation frequencies varied but remained equal for both buildings per simulation. At the same time, randomly generated amplitudes of frequencies simulate discrepancies in the excitation spectrum per building. The range of those simulation parameters was chosen based on typical spectral characteristics of sites exited by regular traffic and reported in the literature [26, 27] Input parameters for FEM simulations are presented in Table 1, and the example of generated signal  $a(t)$  is shown in Fig. 4.

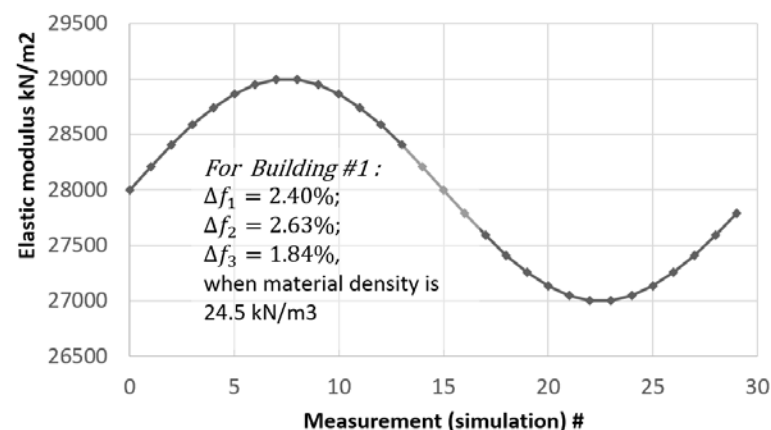


**Figure 2. Applied deviations in elastic modulus  $E$  in FEM simulations ( $\Delta f$  – change of natural frequency).**

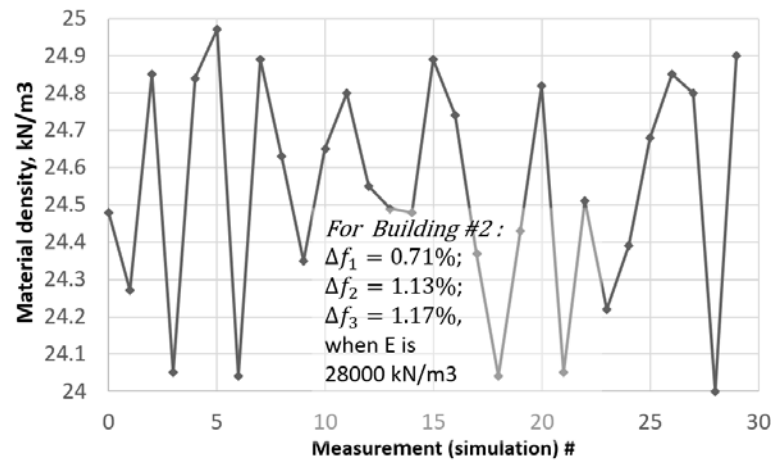


**Figure 3. Applied deviations in material density in FEM simulations ( $\Delta f$  – change of natural frequency).**

**Table 1. Input parameters for FEM simulation.**

| Case* | Gaussian kernel parameters of the excitation signal (frequency domain) |                              | Obtained RMS of the base excitation signal (time domain), m/s <sup>2</sup> |                      | Parameters for modelling of EOV effect                       |        |   |       |
|-------|--|------------------------------|--|----------------------|--|--------|---|-------|
|       | (Max; min) of Standard deviation, Hz                                   | (Max; min) of Mean value, Hz | Max  | Min                  | Elastic modulus (for stiffness variation), kN/m <sup>2</sup> |        | Density (for mass variation), kN/m <sup>3</sup> |       |
|       |  |                              |  |                      | Max  | Min    | Max   | Min   |
| A + B | (3.75; 2.03)   | (13.32; 8.13)                | $2.69 \cdot 10^{-4}$   | $1.81 \cdot 10^{-4}$ | 28 995   | 28 000 | 24.95   | 24.00 |
| A + C | (3.91; 2.04)   | (13.69; 9.18)                | $2.76 \cdot 10^{-4}$   | $1.87 \cdot 10^{-4}$ | 28 866   | 27 257 | 25.00   | 24.11 |
| D + B | (3.86; 2.42)   | (13.92; 8.43)                | $2.72 \cdot 10^{-4}$   | $1.88 \cdot 10^{-4}$ | 27 792   | 27 005 | 24.99   | 24.01 |

\* A+B is the case when Building #1 and Building #2 is undamaged; A+C is the case when Building #1 is undamaged, and Building #2 is damaged by damage case I; D+B is the case when Building #1 is damaged by damage case II and Building #2 is damaged before by Case I.

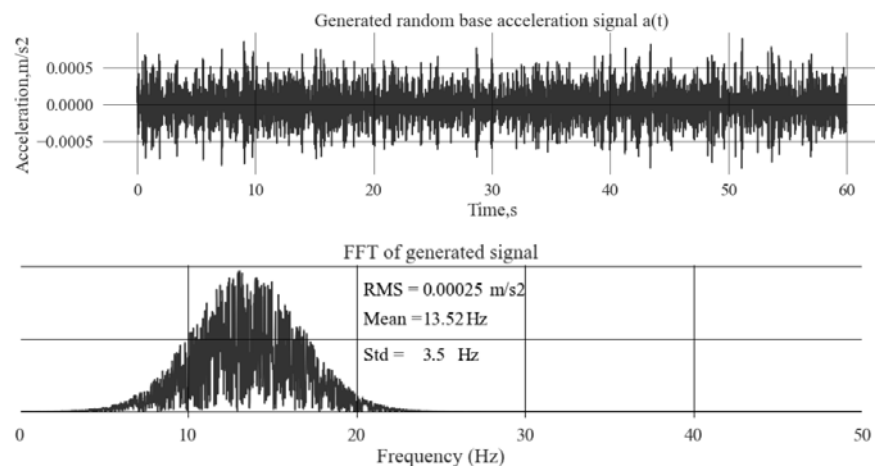


**Figure 4. Example of generated and applied base excitation signal to FEM model.**

Four FE models of three-story RC shear buildings were developed. Model A and B correspond to undamaged states of building. Model C corresponds to the damage state of building B, but model D corresponds to the damaged state of building A. Dimensions, stiffness of springs that models shear walls, and measurement point locations are presented in Fig. 5. Model B (Building #2) is not an exact copy of model A (Building #1) because to simulate differences in applied base excitation amplitudes, model B is turned by 15 degrees in the plane. It has shear walls in all directions for the middle axis of the building and has reduced stiffness due to different opening composition in one of the building's outer walls. These structural differences from model to model are highlighted in the drawing of Fig. 5.

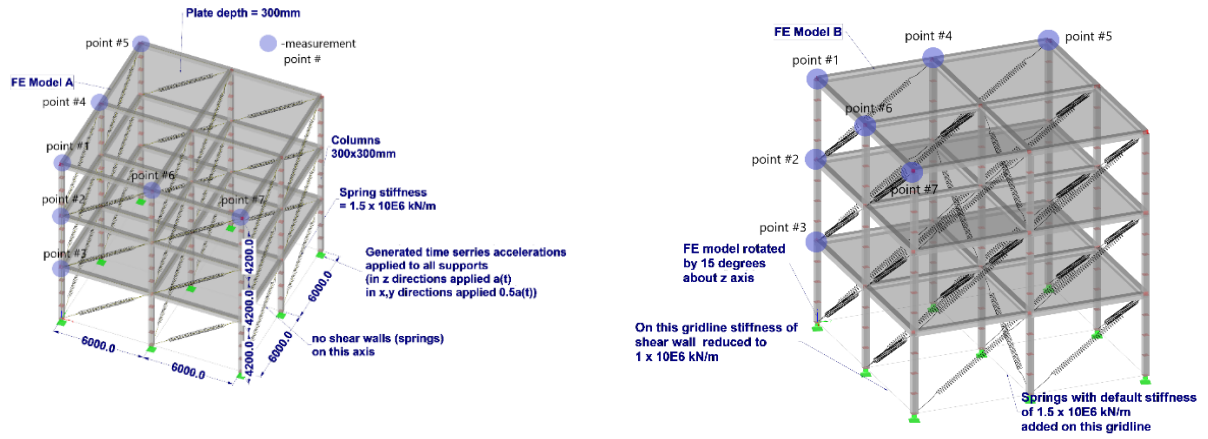


**Figure 5. FE Models of buildings for the undamaged state with response measurement point notation (for model B highlighted only structural differences in the drawing).**

Structural damage generally causes changes in structural parameters, and it affects the dynamic behaviour of the building. Deviation from the structure's original geometry and changes in element boundary conditions mostly affect the local/global stiffness of the structure. Therefore it introduces variations in natural frequencies of elements/structure. The deviations in material properties, such as cracks, may change all modal parameters: natural frequencies, mode shapes and damping. In this research, damage state assumed shear wall removal or shear wall stiffness reduction due to the new opening that does not cause changes in the damping parameter. All building models damping ratio is taken as 5 %. Introduced structural changes for Building #1 (FE Model A) and Building #2 (FE Model #B) is presented in Fig. 6.

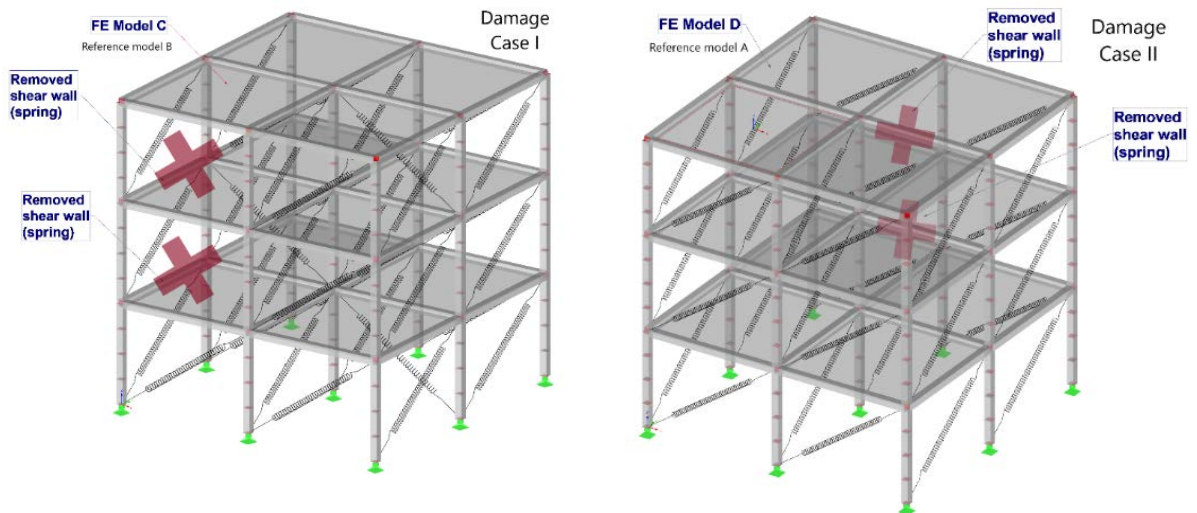


**Figure 6. FE Models of buildings for damaged state (highlighted only introduced structural differences due to damage).**

The difference between first natural frequencies (first transverse, first longitudinal and torsional) between both buildings is proposed as the damage identification feature vector from the frequency domain analysis:

$$\{\Delta f_i\} = \frac{\{f_{2i}\} - \{f_{1i}\}}{\{f_{2i}\}} \cdot 100\%, \quad (1)$$

$\Delta f_i$  is natural frequency difference for mode shape  $i$ ;  $f_{2i}$  is natural frequency of monitored building for mode shape  $i$ ;  $f_{1i}$  is natural frequency of reference building for mode shape  $i$ .

As mentioned before, it is useful to have also a damage sensitive feature vector from the time-domain analysis. The output-only modal identification process's errors could be identified if the statistic parameters of the response signal are used as the damage-sensitive features. An example of such metrics is the temporal statistics of signals developed by Smallwood [28]. One of the temporal statics' metrics is temporal

moment  $m_n(t_s)$  of a time history  $a(t)$  about a time location  $t_s$  and is defined as the square of a time history:

$$m_n(t_s) = \int_{-\infty}^{+\infty} (t - t_s)^n a(t)^2 dt, \quad n = 0, 1, 2, 3, \dots, \quad (2)$$

$a(t)$  is acceleration time series;  $t_s$  is reference time;  $n$  is order of the temporal moment.

As the zero-order temporal moment is independent of the time shift  $t_s$  and taking to account that all experimentally obtained data from sensors are discrete, the data equation (2) can be rewritten as:

$$m_0 = \sum_{i=1}^{k-1} \frac{\Delta t}{2} (a_j^2 + a_{j+1}^2), \quad (3)$$

$a_j$  is data point  $j$  in acceleration time series;  $\Delta t$  is time step in acceleration time series.

The square of the time history is used to avoid the problem of negative amplitudes, and this definition allows it to relate it with an energy  $E$ .

Ambient response time series are not unimodal, i.e., they have more than one maximum. Therefore, kurtosis obtained from 4<sup>th</sup> order central moment normalised by energy  $E$  is another potentially useful metrics. For further details, see reference [26]. Different mode shapes respond differently to the same structural change due to the discrepancies in generalised mass and generalised stiffness per mode shape. This property might also be utilised for damage detection purpose.

Linear modal analysis based on the structure's eigenvalues and mode shapes is used to decouple the system and obtain building response to simulated base excitation. It is appropriate because experimental research, e.g. [29], shows that buildings under ambient vibrations due to very small vibration amplitudes behave elastically.

### 3. Results and Discussion

Thirty data points are obtained for each of the building, which simulates 30 measurements during the year by recording acceleration time series with a sample rate of 100Hz under variable EOV, base excitation and two damage scenarios: Case I is damaged Building #2; Case II is damaged Building #1. Acceleration time series of transversal and longitudinal directions is obtained from seven points best-suited to represent the first translational, longitudinal, and torsional vibration modes. As these are results from simulations, no additional data processing is required. However, data detrending due to sensor inaccuracies, for example, sensitivity to temperature changes, should be performed in practice before the dynamic parameter identification process.

It is found that for a three-story shear wall building with three bays in each direction is possible to identify changes in wall stiffnesses due to the wall removal or implementation of openings by analysing first frequency (transverse, longitudinal and torsional) changes. The fusion of modal information from two buildings gives a clear advantage to filter out frequency variations due to environmental and operational conditions when properties of the soil only slightly modify modal frequencies of the building. The building could behave as a dependent unit against ground response as one rigid mass for the soft-soil condition [30]. Then method could be used for the identification of changes in the building support conditions.

Figure 7 represents the traditional way of showing the frequency changes where the negative effects of EOV can be easily identified. Similar graphs could be found in experimental works of other authors, e.g. Fig. 3 in [20] and Fig. 2 in [20]. Variations in natural frequencies of buildings due to these effects are presented in Table 2. In contrast, Fig. 8 has "flat" regions, and jumps occur only due to introduced building damage scenarios. Thus, variations due to EOV effects are successfully filtered out.

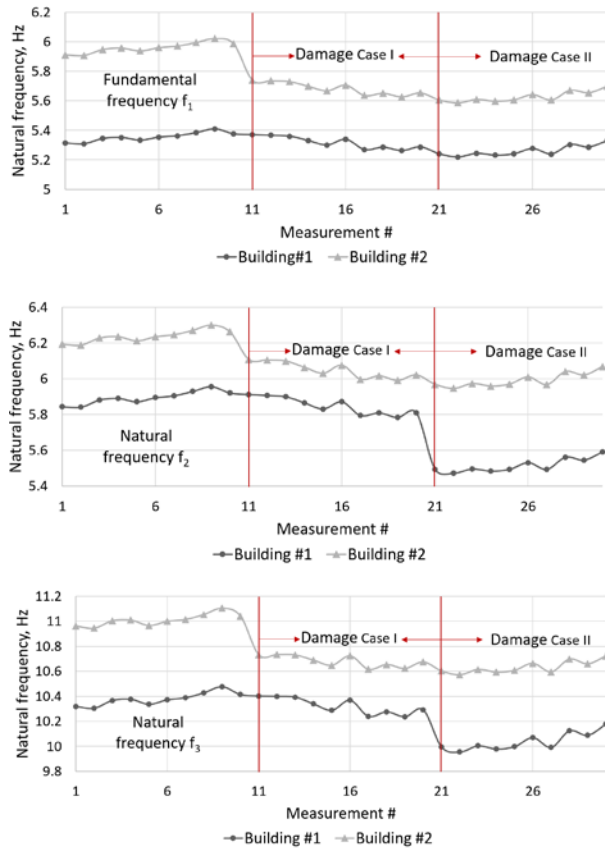


**Figure 7. Building frequencies due to EOV and introduced damages.**

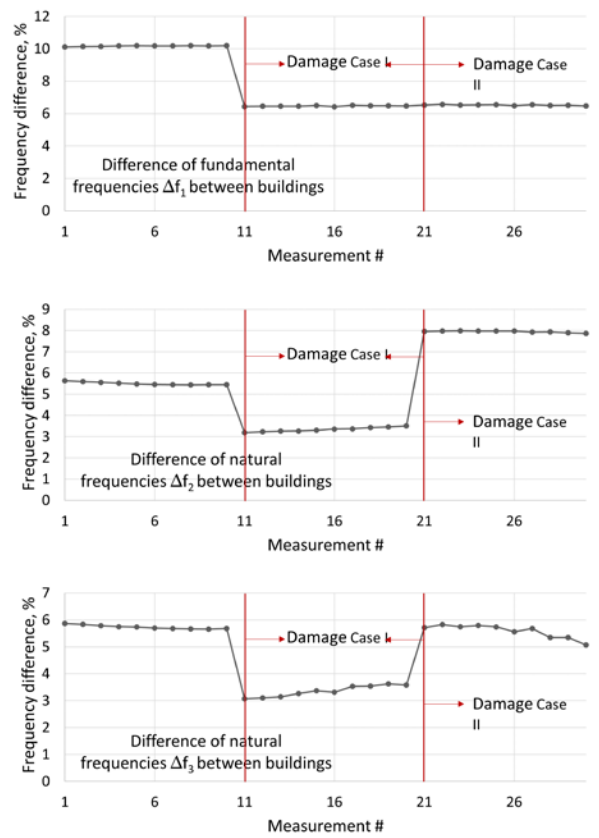


**Figure 8. Building frequency difference plots due to EOV and introduced damages.**

By exploring three frequency difference plots together, partial damage localisation might be done. For example, in damage Case II structural changes do not affect the first transverse frequency. Therefore, it follows that structural changes are not introduced in this direction. Potentially characteristic frequency jumps could be mapped for typical shear wall building structures, and machine learning algorithms applied for further damage localisation.

The required precision of dynamic parameter structural identification from the ambient response signal is dependent on the detection capability of a particular change point algorithm. This problem is not in the scope of the article but will be considered in further investigations.

**Table 2. Natural frequency changes due to change in EOV simulation parameters.**

| Case                                  |             | Frequency changes due to EOV<br>$((f_{\max} - f_{\min}) / f_{\max}) \cdot 100$ |                             |                          |
|---------------------------------------|-------------|--|-----------------------------|--------------------------|
|                                       |             | Transverse mode ( $f_1$ )  | Longitudinal mode ( $f_2$ ) | Torsional Mode ( $f_3$ ) |
| Non damaged case (measurement # 1-10) | Building #1 | 1.85 %   | 1.93 %                      | 1.63 %                   |
|                                       | Building #2 | 1.89 %   | 1.78 %                      | 1.44 %                   |
| Damage case I (measurement # 11-20)   | Building #1 | 2.01 %   | 2.18 %                      | 1.60 %                   |
|                                       | Building #2 | 1.97 %   | 1.92 %                      | 1.10 %                   |
| Damage case II (measurement # 21-30)  | Building #1 | 2.08 %   | 2.15 %                      | 2.19 %                   |
|                                       | Building #2 | 1.98 %   | 2.03 %                      | 1.41 %                   |

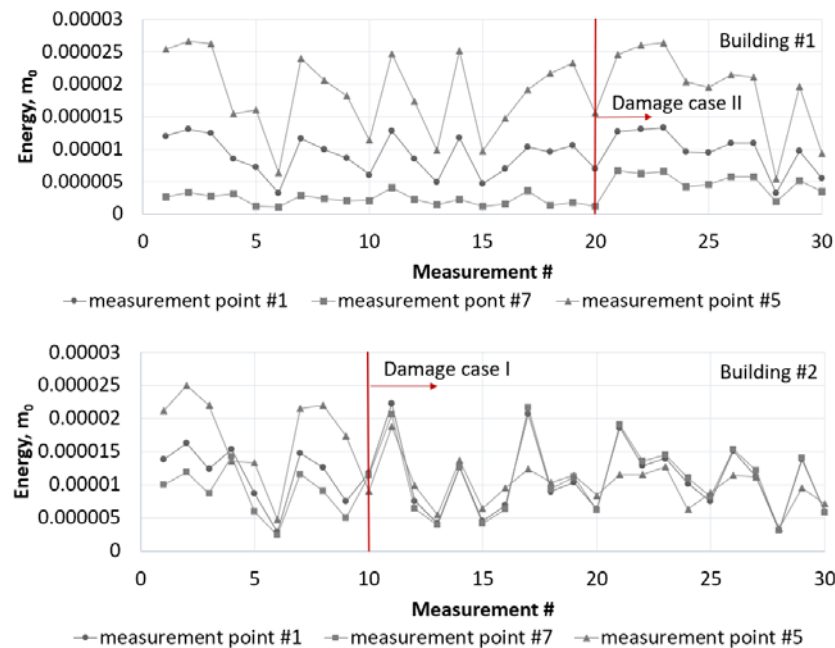
While performing result analysis, all variable and first mode frequency pairwise Pearson correlations were found. The main results are presented in Table 3. The results indicate that frequency domain damage sensitive feature i.g., mode frequency, are more sensitive to elastic modulus changes than mass changes.



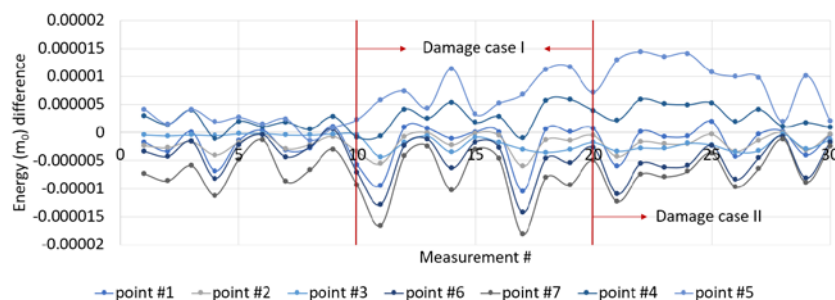
**Table 3. Correlations between 1<sup>st</sup> frequencies of buildings and EOVS simulation parameters.**

| EOV parameter              | Building #1 natural frequencies |        |         | Building #2 natural frequencies |        |         |
|----------------------------|---------------------------------|--------|---------|---------------------------------|--------|---------|
|                            | Transv.                         | Long.  | Torsion | Transv.                         | Long.  | Torsion |
| Elastic modulus $E$        | +0.905                          | +0.921 | +0.854  | +0.913                          | +0.896 | +0.774  |
| Material density, $\gamma$ | -0.486                          | -0.450 | -0.577  | -0.536                          | -0.568 | -0.738  |

Time-domain feature for cross-checking of damage identification is also explored, namely change of vibration energy amplitude (first temporal moment) at sensor locations that measures the overall building dynamic response strength. It is found that the first temporal moment (energy) of each measurement time series may represent the distinct dynamic behaviour of each building due to the variable excitation and EOVS (see Fig. 9).

**Figure 9. Energy changes due to variations of base excitation and EOVS.**

However, for damage detection, this is not an appropriate feature. Visually some disparities in energy difference for various damage situations might be spotted (see Fig. 10). Still, there is not simulated additional sensor self-noise in this research that could reduce the possibility of identifying damages from this feature.

**Figure 10. The energy difference between the response of buildings to the base excitation variations.**

The steady linear growth in the cumulative sum plot (Fig. 11) of functions presented in Fig. 10 confirms that damage identification using pure statistics of time series is not feasible. For both buildings, variations of the base excitation spectrum have more impact on dynamic response than structural changes due to introduced damage scenarios.



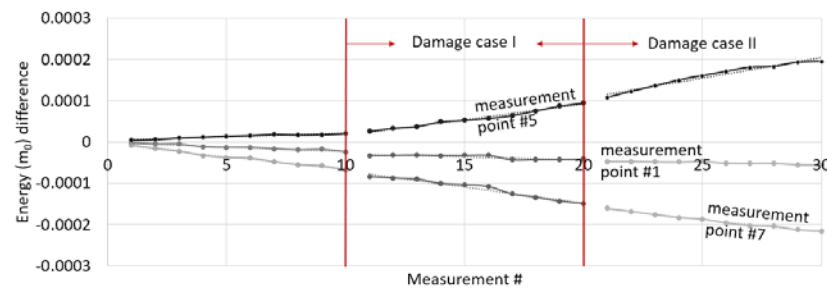


**Figure 11. The energy difference between the response of buildings to the base excitation variations (cumulative sum plot).**

## 4. Conclusion

This research proposed a new approach to reduce environmental noise in experimentally obtained vibration data and dynamic parameters by data fusion of dynamic response of two similar buildings under ambient vibration and variable operational and environmental conditions referred to as EOVS. Data fusion capabilities are investigated by using FEM simulations of two three-story shear wall buildings with very similar but not exact structural parameters or ambient excitation.

By utilising one of the buildings as a reference state instead of the same building, it is possible to identify shear wall removal or new opening implementation from the damage sensitive feature vector taken as natural frequency differences of both buildings. In this way, successfully filtered out natural frequency variations due to EOVS effects, leaving the jumps in a data which cause is a damage introduction in one of the structures. Implementation of natural frequencies differences series for damage detection potentially significantly reduce training data required when machine learning analysis is used on data which is one of the distinctive advantages of this data fusion approach. Also, outliers from erroneous output-only modal identifications might be easily spotted, and different novelty detection algorithms can be applied for damage recognition.

The required accuracy of the dynamic parameter structural identification from ambient vibration testing depends on the effectiveness of the chosen change-point algorithm for the damage state detection. Investigation of the time-series data statistics showed that the approach is not effective for the time-domain analysis. Variations in base excitation signal influence more the dynamic response of building than structural changes due to introduced damage scenarios for medium-rise buildings.

The fusion of building dynamic response data from several buildings that share the same environmental and operational conditions give a clear advantage in reducing false alarm possibility during continuous and automated structural health monitoring process. Further full-scale experimental investigations are planned to assess the proposed approach's effectiveness for real structures in their operating environment.

## 5. Acknowledgement

This work has been supported by the European Regional Development Fund within the Activity 1.1.1.2 "Post-doctoral Research Aid" of the Specific Aid Objective 1.1.1 "To increase the research and innovative capacity of scientific institutions of Latvia and the ability to attract external financing, investing in human resources and infrastructure" of the Operational Programme "Growth and Employment" (No.1.1.1.2/VIAA/3/19/393).

## References

1. Belostotsky, A.M., Akimov, P.A. Adaptive Finite Element Models Coupled with Structural Health Monitoring Systems for Unique Buildings. *Procedia Engineering*. 2016. 153. Pp. 83–88. DOI: 10.1016/j.proeng.2016.08.084
2. Kamarudin, A.F., Mokhtar, S.N., Zainal Abidin, M.H., Daud, M.E., Rosli, M.S., Ibrahim, A., Ibrahim, Z., Md Noh, M.S. Structural health monitoring on medium rise reinforced concrete building using ambient vibration method. *IOP Conference Series: Earth and Environmental Science*. 2018. DOI: 10.1088/1755-1315/140/1/012152
3. Michel, C., Guéguen, P., Bard, P.Y. Dynamic parameters of structures extracted from ambient vibration measurements: An aid for the seismic vulnerability assessment of existing buildings in moderate seismic hazard regions. *Soil Dynamics and Earthquake Engineering*. 2008. DOI: 10.1016/j.soildyn.2007.10.002
4. Capraro, I., Pan, Y., Rollins, K., Gao, W., Ventura, C.E. Ambient vibration testing of a 4-storey parking garage. *Conference Proceedings of the Society for Experimental Mechanics Series*. 2015. DOI: 10.1007/978-3-319-15248-6\_3
5. Soo Lon Wah, W., Chen, Y.T., Roberts, G.W., Elamin, A. Separating damage from environmental effects affecting civil structures for near real-time damage detection. *Structural Health Monitoring*. 2018. DOI:10.1177/1475921717722060
6. Rainieri, C., Magalhaes, F., Gargaro, D., Fabbrocino, G., Cunha, A. Predicting the variability of natural frequencies and its causes by Second-Order Blind Identification. *Structural Health Monitoring*. 2019. DOI: 10.1177/1475921718758629

7. Sohn, H. Effects of environmental and operational variability on structural health monitoring. Philosophical Transactions of the Royal Society A: Mathematical, Physical and Engineering Sciences. 2007. DOI: 10.1098/rsta.2006.1935
8. Peeters, B., De Roeck, G. One year monitoring of the Z24-bridge: Environmental influences versus damage events. Proceedings of the International Modal Analysis Conference – IMAC. 2000.
9. Alampalli, S. Influence of in-service environment on modal parameters. Proceedings of the International Modal Analysis Conference – IMAC. 1998.
10. Cross, E.J., Koo, K.Y., Brownjohn, J.M.W., Worden, K. Long-term monitoring and data analysis of the Tamar Bridge. Mechanical Systems and Signal Processing. 2013. DOI: 10.1016/j.ymssp.2012.08.026
11. Moser, P., Moaveni, B. Environmental effects on the identified natural frequencies of the Dowling Hall Footbridge. Mechanical Systems and Signal Processing. 2011. DOI: 10.1016/j.ymssp.2011.03.005
12. Peeters, B., Maeck, J., De Roeck, G. Vibration-based damage detection in civil engineering: Excitation sources and temperature effects. Smart Materials and Structures. 2001. DOI: 10.1088/0964-1726/10/3/314
13. Zhou, H.F., Ni, Y.Q., Ko, J.M. Eliminating temperature effect in vibration-based structural damage detection. Journal of Engineering Mechanics. 2012. DOI: 10.1061/(ASCE)EM.1943-7889.0000273
14. Ni, Y.Q., Hua, X.G., Fan, K.Q., Ko, J.M. Correlating modal properties with temperature using long-term monitoring data and support vector machine technique. Engineering Structures. 2005. DOI: 10.1016/j.engstruct.2005.02.020
15. Hua, X.G., Ni, Y.Q., Ko, J.M., Wong, K.Y. Modeling of temperature-frequency correlation using combined principal component analysis and support vector regression technique. Journal of Computing in Civil Engineering. 2007. DOI: 10.1061/(ASCE)0887-3801(2007)21:2(122)
16. Finotti, R.P., Souza Barbosa, F. De, Cury, A.A., Gentile, C. A novel natural frequency-based technique to detect structural changes using computational intelligence. Procedia Engineering. 2017. DOI: 10.1016/j.proeng.2017.09.438
17. Limongelli, M.P., Çelebi, M. Seismic Structural Health Monitoring. From Theory to Successful Applications. 2019. ISBN: 978-3-030-13976-6
18. Figueiredo, E., Park, G., Farrar, C.R., Worden, K., Figueiras, J. Machine learning algorithms for damage detection under operational and environmental variability. Structural Health Monitoring. 2011. DOI: 10.1177/1475921710388971
19. Sarmadi, H., Karamodin, A. A novel anomaly detection method based on adaptive Mahalanobis-squared distance and one-class KNN rule for structural health monitoring under environmental effects. Mechanical Systems and Signal Processing. 2019. DOI: 10.1016/j.ymssp.2019.106495
20. Gargaro, D., Rainieri, C., Fabbrocino, G. Structural and seismic monitoring of the “cardarelli” Hospital in Campobasso. Procedia Engineering. 2017. DOI: 10.1016/j.proeng.2017.09.244
21. Yuen, K.V., Kuok, S.C. Ambient interference in long-term monitoring of buildings. Engineering Structures. 2010. DOI: 10.1016/j.engstruct.2010.04.012
22. Emelianov, M. Considering the information technology for structural health monitoring (SHM) systems. E3S Web of Conferences. 2019. 97. DOI: 10.1051/e3sconf/20199703011
23. Worden, K., Farrar, C.R., Manson, G., Park, G. The fundamental axioms of structural health monitoring. Proceedings of the Royal Society A: Mathematical, Physical and Engineering Sciences. 2007. DOI: 10.1098/rspa.2007.1834
24. Google Maps. (2019). [Google maps of Riga city, Latvia] [Satellite map]. Retrieved January 10, 2021, from <https://www.google.com/maps/@56.9250334,24.1645615,144m/data=!3m1!1e3>
25. Google Maps. (2019). [Google maps of Riga city, Latvia] [Street map]. Retrieved January 10, 2021, from <https://goo.gl/maps/KKr5y3YhUH4AqqvX6> .
26. Hao, H., Ang, T.C., Shen, J. Building vibration to traffic-induced ground motion. Building and Environment. 2001. DOI: 10.1016/S0360-1323(00)00010-X
27. Gaile L; Sliseris J; Ratnika L. Towards SHM of medium-rise buildings in non-seismic areas. Proceedings of 10<sup>th</sup> International Conference on Structural Health Monitoring of Intelligent Infrastructure - SHMII 10 (submitted), 2021.
28. Smallwood, D.O. Characterization and Simulation of Transient Vibrations Using Band Limited Temporal Moments. Shock and Vibration. 1994. DOI: 10.1155/1994/940635
29. Ivanovic, S., Trifunac, M., Todorovska, M. Ambient vibration tests of structures-a review. ISET Journal of Earthquake Technology. 2000.
30. Kamarudin, A.F., Zainal Abidin, M.H., Mokhtar, S.N., Daud, M.E., Ibrahim, A., Ibrahim, Z., Md Noh, M.S. Identification of Natural Frequency of Low Rise Building on Soft Ground Profile using Ambient Vibration Method. Journal of Physics: Conference Series. 2018. DOI: 10.1088/1742-6596/995/1/012100

#### **Information about authors:**

**Liga Gaile, Sc.D.**

ORCID: <https://orcid.org/0000-0002-7292-0821>

E-mail: [liga.gaile\\_1@rtu.lv](mailto:liga.gaile_1@rtu.lv)

**Leonids Pakrastins, PhD**

ORCID: <https://orcid.org/0000-0002-8367-7927>

E-mail: [leonids.pakrastins@rtu.lv](mailto:leonids.pakrastins@rtu.lv)

**Lasma Ratnika,**

E-mail: [lasma.ratnika@rtu.lv](mailto:lasma.ratnika@rtu.lv)

*Received 08.02.2021. Approved after reviewing 22.06.2021. Accepted 01.07.2021.*

Gaile, L., Pakrastins, L., Ratnika, L.



Research article

UDC 629.563.2:004.942:626/627

DOI: 10.34910/MCE.111.12

## Mooring system optimization for marine floating hydrotechnical structures

A. Bolshev , S.A. Frolov , E.V. Shonina  

Peter the Great St. Petersburg Polytechnic University, St. Petersburg, Russia

 [shonina\\_ev@spbstu.ru](mailto:shonina_ev@spbstu.ru)

**Keywords:** offshore structure, mooring system, multi-objective optimization, penalty function method, optimization, semi-submersible platform, mooring, tension force, method of golden section

**Abstract.** Existing offshore areas require development and mining using floating structures. The article presents design issues and settings of anchor mooring systems for marine floating structures. Improving and optimization methods for mooring systems, presented in publications of Russian and foreign authors, are discussed. The parameters influencing the safety of floating marine structures operation are identified. The parameters that are advisable to take as criteria are discussed. The restrictions imposed on non-criteria parameters are considered. The optimization criterion of the marine floating structures mooring systems in extreme operating modes is formulated. An optimization method for mooring systems is suggested in accordance with the proposed criterion. The study gives an example of mooring system optimization in the storm mode for a platform operated in ice-free seas. A similar methodology can be used for mobile ice-resistant platforms, conceptual variants of which are being developed for operation in Arctic conditions. Research results were obtained by the method of mathematical modeling.

### 1. Introduction

The development tasks of the global ocean resources lead to the need of the construction and operation of various structures that have been functioning for a long time in offshore waters. Many of these structures have ability to move in offshore waters and positioning in the targeted water area using an anchor mooring system. Such floating objects include semisubmersible drilling platforms, floating cranes, floating berths, floating power structures, offshore pipelay vessels, submerged floating tunnels, etc. [1].

Operation of offshore structures is always associated with the risk of serious accidents due to extreme environmental loads. Often such structures operate in offshore waters, where the impact of wind loads and extreme storm waves can lead to irreversible effects. High cost of structures, their isolated location from coastal bases and the availability of operating personnel constantly working at these structures determines highest requirements for reliability and structure safety.

One of the most important factor determining safety of the considered floating structures is mooring system failure-free operation. It must ensure the upholding of all restrictions due to the continuation of normal operation or survival preservation of the marine structure under any environmental loads [2, 3].

At the design phase of an offshore floating structures or at the design phase of positioning it in offshore waters, it is always necessary to solve the issues of the composition and configuration of its mooring system, the azimuthal orientation of the floating anchored structure, the selection of the lengths and tension of mooring lines, influence of mooring angle, etc. This task leads to different solutions

Bolshev, A., Frolov, S.A., Shonina, E.V. Mooring system optimization for marine floating hydrotechnical structures. Magazine of Civil Engineering. 2022. 111(3). Article No. 11112. DOI: 10.34910/MCE.111.12

© Bolshev, A., Frolov, S.A., Shonina, E.V., 2022. Published by Peter the Great St. Petersburg Polytechnic University.



This article is licensed under a CC BY-NC 4.0

depending on the floating structure characteristics, the intensity of the expected environmental loads, the depth of the marine waters, etc.

Searching for the best decision for the mooring system parameters presume the ensure of the highest level of the structure safety within the prescribed operating conditions.

### *1.1. Problems of mooring systems design and floating structures positioning*

The problems that appear at the design stage of the mooring system for the floating structure are associated with the uncertainty of the environmental conditions for its practical use. The offshore floating mooring structures are mobile. In prospect they can be used in different seas, at different depths, in water areas where the parameter of wind-wave conditions differs very significantly. Designing of a newly created mooring system requires parametrization: number of lines of the mooring system, their maximum length, caliber of the chains or cables of these lines, location of the hawser hole on the structural body, linear weight and elasticity-strength characteristics of the elements of the mooring line, mooring line type, mass and the holding force of the anchors.

Selection of parameters usually depends on the maximum permissible values of wind velocity, height and wave period, sea depth due to the uncertainty of the environmental conditions in the water area of the structure position. This ensures the safety of structure positioning during usage of the mooring systems. In any case the process of creating a mooring system is associated with ranging the values of numerous parameters and searching for such combinations of these parameters at which the structure is capable of safely functioning under extreme environmental loads.

The problems that appear at the stage of structure positioning in certain water area look more precise. In this case the external conditions, the number and configuration of the mooring lines, their elastic-weight characteristics, the parameters of the floating structure anchors are already known. It is necessary to determine the best orientation of the structure, mooring lines layouts, their length and tension to ensure the unconditional safety of the structure during the period of extreme storms expected in a certain water area. It is also necessary to find the best combination of the listed characteristics that ensure the highest safety level of the structure's functioning under the worst external conditions.

Commonly it is possible to change the tension of the lines of the structure with an already deployed mooring system during its operation. This ensures that the conditions for the operability of the structure are met. In this mode it is necessary to select the tension of the lines to fulfill the constraints of the structure's operability (more severe than in the storm mode) or to select the extreme external conditions under which the operation of the structure is permissible.

The problem of optimization of the mooring systems for keeping floating anchored structures in a storm (survival) mode is considered in this article. This task is wider in comparison with the task of optimization in operation mode. At the same time, this task is one of the main elements of the optimization of the mooring systems at the stage of its initial design.

### *1.2. Mooring systems design experience*

The experience of designing mooring systems and methods for determining the parameters of these systems are presented in a number of Russian and foreign publications.

In particular, the regulatory document of the Russian Maritime Register of Shipping ND 2-020201-015 "Rules for the classification, construction and equipment of mobile offshore drilling units and fixed offshore platforms" for floating drilling units contains recommendations on the choice of mooring lines for use at the stage of driving the platforms to the positioning point: estimating the length of mooring lines method, their caliber and mass of anchors based on the given displacement of floating structures and its surface exposed to the wind. This method is very approximate, applicable for a limited range of wave and wind velocity. It does not take into account the mooring lines position, so its application to the analysis of the platform mooring system in operation or storm modes is problematic. In the same regulatory document, it is proposed to study behavior of the mooring systems in various modes of operation to select their parameters, to determine the extreme forces in the elements of the mooring system, to compare them with safety criteria and, on this basis, to improve the configuration of the mooring system. However, the organization procedure for improving the parameters of the mooring system, parameter determination procedure of this system is not stated in the regulatory document.

Nevertheless, the engineering practice of Russian design organizations in the design of the offshore anchored structures complies with the provisions of the regulatory document of the Register of Shipping. For example, in [4], the authors show the mooring system design, performed using the "POSITION" software package in accordance with ND 2-020201-015 "Rules for the classification, construction and equipment of mobile offshore drilling units and fixed offshore platforms". The results of the work make it

possible to determine the main parameters of the mooring system and to make a conclusion that the mooring system provides a reliable position of the platform with a permissible displacement.

The influence of various loads on the movement of a floating structure and on the mooring system was studied in [5]. The authors also consider the horizontal stiffness of the system as the main parameter characterizing the operational safety. But during the preliminary design of the mooring system the following safety criterion is taken into account: the maximum tension of the mooring line should not exceed the allowed values. Dynamic analysis for three different depths was performed in time domain using Simo-Riflex-AeroDyn software packages.

Similar criteria are discussed in article [6]. The authors presented the results of the mooring analysis of semisubmersible platform Scarabeo 7 according to the rules of two classification societies: American Petroleum Institute (API) and Det Norske Veritas (DNV). The aim of the study was to compare the obtained results. During positioning of an offshore object the main criteria must be observed. The authors also include maximum displacement of the object limited to avoid damage or breaking of riser and the maximum tension in lines, determined by the safety factor.

The requirements for the safety factor as a criterion for assessing the positioning system are also considered by the authors in [7]. Safety factors represent the ratio of breaking load to maximum force in the most loaded mooring line. Numerical modeling was carried out in software package "Anchored Structures". The calculation analysis had given a high convergence of the results with real processes.

Similarly, the requirements of the "Rules for the classification, construction and equipment of mobile offshore drilling units and fixed offshore platforms" are taken as the main criteria for determining the parameters of mooring lines in article [8]. The authors performed a series of preliminary calculations to determine the effective length of the mooring line and chose the length of the line at which the vertical force transmitted to the anchor equals zero. Mooring parameters were assessed using the POSITION and "Anchored Structures" software packages.

The study of a floating structure movement and the selection of a suitable mooring system are discussed in [9, 10]. Seven symmetrical mooring systems were modeled, consisting of four or eight mooring lines to find the best mooring system. The results of the analysis show that the optimal mooring system is a variant with eight lines and 60° angle between two adjacent lines (the criterion for comparison is the smallest horizontal displacements). Second variant is the one with eight lines and 30° angle between two adjacent lines (the criterion is the lowest tension values).

The authors of the listed articles perform the design and analysis of the mooring systems operation, choosing various parameters of the system as an evaluation criterion. Mainly mooring systems selected for the calculation are not further optimized because they are sufficient for the normal operation of the structure. Due to the high computational efforts associated with modeling of the mooring systems, optimization algorithms are not used in the design cycle. Without the use of formal optimization approaches the design of mooring systems is limited to an iterative engineering and design approach based on experience and search for an acceptable engineering solution.

In a number of foreign articles, the authors approach the issue of optimization in more detail using heuristic methods [11–15]. One such method is the genetic algorithm. A genetic algorithm is a type of evolutionary computation that solves optimization problems using natural evolution methods. The algorithm is an incomplete enumeration of mooring systems variants, which improves the value of the objective function. For example, in [16] the goal of optimization is to minimize the displacement of the structure. The minimum value of the objective function is calculated using an iterative genetic algorithm. The result is optimized anchor positions. In this case the set of environmental conditions (waves, winds loads and sea currents) is converted into equivalent external static force acting on the floating structure. Dynamic analysis of the floating structure behavior is not used in the calculation of mooring systems.

The genetic algorithm is used in the article [17], which describes the procedure of developing the code aimed at solving the problems of optimization of the mooring pattern. The author defines the optimal mooring system as the one that minimizes the constraint force of the floating structure (platform) itself. In this case, the author, in addition to the displacement of the structure, takes into account the following aspects affecting the choice of the optimal system: angle of the structure position, the platform mooring system, distribution of external loads; the length and tension of each line for selection of materials and sizes. The objective function which takes into account the displacement of the structure, is calculated in the MIMOSA software package, while the genetic algorithm is executed using the MatLab language. The genetic algorithm is also successfully applied in works [18–20].

Adequate results of the optimization process can be shown by the particle swarm method. It considers calculating a large number of mooring system variations to create a point cloud, within which it is possible to search for the best value of the objective function. This approach is used to solve the problem

of floating platforms positions in [21, 22]. In [21] modeling was carried out for deep-water systems in the PROSIM software for the operating mode, taking into account the maximum allowable offset of the structure in order to avoid riser breakdown, as well as taking into account the safety factor. This algorithm has already been successfully used by the authors for another OtimRiser software package in [23].

A review of existing works by Russian authors suggests that most of the modeling and calculation methods allow calculating pre-selected mooring lines, but the issue of choosing the optimal position system and its adjustment is not solved. Because of this an engineer has to select a mooring system based on design experience, model and calculate its parameters. Then it's necessary to iteratively improve the parameters to values satisfying the safety criteria.

As for foreign studies, works with the use of fuzzy logic are presented on the issue of optimization of mooring systems. The approaches make it possible to form a fuzzy set, and the optimization problem implies the choice of the «middle» variant that satisfies the given constraints. The result is not an optimal solution, but a close to optimal one. In addition, in the considered solutions modeling the behavior of an anchored structure and the operation of its mooring system are considered separately from the optimization procedure. Processes are executed in different software environments. This approach excludes the possibility of obtaining an exact optimal solution.

It is therefore possible to conclude that the development of methods that allow obtaining an accurate optimal solution for the parameters of the mooring system for marine floating anchored structures is a logical completion of the ideology of Russian regulatory documents (for example, ND 2-020201-015 "Rules for the classification, construction and equipment of mobile offshore drilling units and fixed offshore platforms"), develops methods for finding optimal solutions based on planning numerical experiments [24, 25] and allows to abandon approximate solutions of fuzzy logic in a number of practical problems.

### *1.3. Problem definition*

In the scope of this article the following tasks are set:

- Identify the parameters affecting the floating structure safety in general and mooring system in particular.
- Determine a parameter that can be accepted as a criterion value.
- Identify constraints in the design of mooring systems.
- Formulate an optimality criterion for the survival mode.
- Develop a method for optimization of the mooring system of a floating anchored structure in survival mode.

There are a number of parameters characterizing the behavior of an anchored structure under the influence of static and dynamic environmental loads, which affect its safety:

1. The mooring lines tension, which must not exceed the ultimate breaking load at any time.
2. Horizontal displacement of the structure, which must not lead to damage to its structural elements.
3. Vertical displacement of the structure, which must not lead to the climb of waves on the deck of the structure.
4. Angular displacement of the structure, which must not obstruct the functioning of the structure and the crew life.
5. Lack of the anchors movement, which guarantees the preservation of the initial characteristics of the structure mooring system.

To solve the optimization problem, it is necessary to determine which of the listed parameters have the greatest impact on the behavior and operation of the entire structure. To do this it is necessary to take into account the consequences to which they can lead:

1. Lines break can certainly lead to emergency situations.
2. Horizontal movements during operation mode can lead to riser break. This could be the cause of the oil spill. However, the risers are usually detached in survival mode (extreme storm) and this parameter becomes insignificant.
3. Vertical movements of the structure, which can lead to the climb of waves on the deck, are an undesirable event. But it does not necessarily lead to emergency consequences.
4. Large angular displacements of the structure are usually undesirable, but do not lead to emergency consequences.

5. Due to the anchors movements, the floating structure may have displaced and the properties of the mooring system may change. Movements of anchors are usually not allowed in the operating mode of an anchored structure. However, in survival mode, when there are no restrictions on the linear movement of the structure, the movement of the anchors will not lead to an accident. After the storm is over, the mooring lines tension and the settings of the mooring system can be reset.

Thus, the lines tension can be taken as the criterion that mostly determines the safety of a floating structure. The remaining parameters can be considered as constraints that will be taken into account during mooring system optimization according to the selected criterion.

## 2. Methods

### 2.1. Formulating of the criterion for the mooring system optimization in survival mode

Floating structure must be positioned in the water area and must be held by an anchor mooring system in survival mode. In this case, the orientation of the structure, which is characterized by the azimuth angle  $\beta$ , is the subject of research in the optimization process.

The mooring lines of the floating structure have a known maximum possible length, and their elastic-weight characteristics are presented in the technical passport. The length of the lines can be calculated during the optimization process and it is limited by the following formula:

$$H \leq L \leq L_{max}, \quad (1)$$

where  $L$  is the line length used in the mooring system,  $H$  is the sea depth,  $L_{max}$  is the maximum possible line length.

The number of mooring lines  $N$  is known; the inclination angles are selected during the optimization process.

The initial lines tension including the margin of safety should not exceed the breaking force. This safety factor is determined by ND 2-020201-015 and depends on the selection mode (survival, operation, emergency mode), as well as on the method of analyzing the behavior of the structure (quasi-static or dynamic). Thus, the formal constraint on the initial tension is:

$$0 < F_0 < F_b / k_n, \quad (2)$$

where  $k_n$  is the standard safety factor for the mooring lines tension,  $F_b$  is the breaking force of the mooring lines,  $F_0$  is the initial tension of the mooring lines.

Commonly a floating anchored structure which is positioned in the offshore waters is exposed to wind, currents and waves. These external loads are time-dependent and can impact in different combinations and from different directions. Usually, combinations of loads are taken during the analysis of extreme impacts. These loads combinations are typical for each force direction taking into account the wind rose, currents and waves. In prospect, the force direction will be designated by the index  $k$  (for example,  $k = 1, 2 \dots 8$ ).

Formalizing the idea of the greatest safety of a structure from the point of view of the tension margin, the best variant will be: such a variant of the mooring system when the most tension margin in the most tensioned anchor line is retained (on the worst combination of external loads (the worst load direction) in extreme storm). The mathematical formulating of this criterion is presented below:

$$\max_{F_0, L_i, \beta, \alpha_i} \min_k \left[ \frac{F_b}{\max_i F_{i,k}(F_0, L_i, \beta, \alpha_i)} \right], \quad (3)$$

where  $F_0$  is the initial tension of the mooring lines,  $L_i$  is the length of the line with the number  $i$  ( $i = 1, 2, \dots, n$ ),  $\alpha_i$  is the plan inclination angle of the line,  $\beta$  is the azimuth angle of the structure.

The proposed criterion assumes that certain parameters of the lines are defined. The line tension and the azimuth angle of the structure are known, line length and the plan inclination angle of the line are



defined. Further, the behavior of the structure under storms from different directions ( $k$ ) should be modeled. The maximum tension  $\left( \max_i F_{i,k} (F_0, L, \beta, \alpha) \right)$  calculated in any line is determined for each direction. The safety factor for this “worst” line is calculated. The safety factor for the “worst” line under the external loads from the “worst” direction  $\left( \min_k \right)$  is determined as the result of such numerical experiment. Then, changing the parameters  $F_0, L, \beta, \alpha$  it is necessary to find such combinations for which the “worst” safety factor will be the maximum possible.

## 2.2. Solution procedure

Mathematically the task solution is minimizing the functional  $J$  subject to series of restrictions:

$$\left\{ \begin{array}{l} J(F_0, L_i, \beta, \alpha_i) = \max_{F_0, L_i, \beta, \alpha_i} \min_k \left[ \frac{F_b}{\max_i F_{i,k} (F_0, L_i, \beta, \alpha_i)} \right] \\ \min_k \Delta_k > \Delta_0 \\ \max_k \varphi_{x,k} < \varphi_{xmax} \\ \max_k \varphi_{y,k} < \varphi_{ymax} \\ \max_i F_{i,k} < \frac{F_b}{k_n} \\ L_{min} < L_i \leq L_{max} \\ \alpha_{i-1} < \alpha_i \leq \alpha_{imax} \end{array} \right. , \quad (4)$$

where  $\Delta_0$  и  $\Delta_k$  are the minimum permissible clearance of the floating structure and the minimum clearance recorded during modeling an extreme storm from the “ $k$ ” direction;  $\varphi_{x,k}$  and  $\varphi_{xmax}$  are the maximum angle of roll of the structure during modeling an extreme storm from the “ $k$ ” direction and the maximum permissible angle of roll;  $\varphi_{y,k}$  and  $\varphi_{ymax}$  are the maximum trim angle of the structure during modeling an extreme storm from the “ $k$ ” direction and the maximum permissible trim angle;  $F_{i,k}$  is maximum line tension with number  $i$  under the impact of a storm from the “ $k$ ” direction.

The initial values of the optimized parameters are determined as follows. The initial tension of all mooring lines is equal in value within the limits (2). The tension of all lines changes during implementing the optimization procedure, but it also remains equal in all lines to ensure a symmetric constraint force from the multidirectional loads.

The azimuth angle of the structure varies within  $(0, \pi)$  in the process of optimization because of the symmetrical form of floating structures about the direct axis. The initial angle value is arbitrary within the definition limits.

The plan inclination angles of the lines are set and changed for each line with the number  $i$  ( $i = 1, 2, \dots, n$ ). To start the optimization process, the initial values of the lines plan inclination angles  $\alpha_i$  can be presented as follows:  $\alpha_1 = \alpha_0$ ,  $\alpha_{i+1} = \alpha_i + 2\pi/N$ , where  $\alpha_0$  is an arbitrarily assigned angle, index  $i$  determines the number of the line,  $N$  is the number of mooring lines. To keep the symmetric constraint reactions of the mooring system, the plan inclination angles of the lines that are in the first quadrant are considered as independent. The remaining plan inclination angles are determined by symmetry about the X-axis and Y-axis. The initial values of independent angles are set in the range  $(0, \pi/2)$  so that the plan inclination angle of every next line will be greater than the previous one.

The initial line lengths are set the equal based on constraint (1). The lengths of the lines located in the first quadrant are considered as independent to ensure the equal constraint force in mooring lines under the multidirectional loads during further optimization. The remaining lengths are taken equal to them by symmetry about X-axis and Y-axis.

Thus, to solve the problem it is necessary to perform a multiparameter optimization of functional (4) with known initial values of the variables and with a number of constraints.

First, it is necessary to discuss the nature of the functional  $J$ . The functional must be convex, continuously differentiable and must have continuous first and second derivatives to apply most of the methods for finding an extremum. Unfortunately, this functional is specified implicitly and it cannot be investigated formally (analytically) from the point of view of the indicated requirements. However, from physical considerations, it can be assumed that it is convex. The formal accounting of existing constraints written in the form of inequalities is a separate issue. Unfortunately, these constraints also have no analytical form and specified implicitly. In this regard, it is difficult to use, for example, gradient methods with a gradient projection onto the constraint zone [26], because the zone of constraints is unknown in advance and it is update during the research.

In prospect it is proposed to form a functional that would include all constraints by using the penalty function [26] taking into account the features of the functional and constraints (4):

$$J_f(F_0, L_i, \beta, \alpha_i) = \max_{\alpha_i, \beta, L_i, F_0} \min_k \left[ \frac{F_b}{\max_i F_{i,k}(F_0, L_i, \beta, \alpha_i)} \right] - \sum S_q, \quad (5)$$

where  $S_q$  is the penalty function generated for each constraint from (4).

In functional (5) compared to (4) all constraints are presented in the form of penalty functions  $S_q$ . Each of them is responsible for the penalty for constraint violation with number  $q$ . If all constraints are met, we will get the same functional (4).

The penalty function for an arbitrary parameter  $x(a < x < b)$  is proposed to be entered by following formulas:

$$S = p \frac{a - x + |a - x|}{a}, \quad (6)$$

$$S = p \frac{x - b + |x - b|}{b}.$$

The penalty function in the form (6) takes zero value in the zone where the constraint is fulfilled. It has a positive numerical value in the zone where the constraint is violated. The  $p$  factor is used to scale the penalty function.

To find the extremum of the functional (5), the method of sequential optimization of the functional with respect to each of the arguments is used. In this case, optimization (5) for the parameters  $F_0, \beta, \alpha_i, L_i$  is sequentially carried out until the value of the objective function stabilizes in the zone of the extreme value. The problem is deemed to be solved if the extremal value of functional (5) is found, and the formula  $\sum S_q = 0$  is satisfied.

The procedure is implemented for one current variable  $F_0, \beta, \alpha_i$  or  $L_i$  at each step of the coordinatewise optimization. For optimization (5), the method of dividing the interval is used. At the first step of the optimization procedure the initial interval is divided into three parts by two new control points insertion. Then the values of the functional at these new points are calculated. And then, for further research, the interval is left where the control point with the extreme value of the functional is located. The procedure is repeated cyclically. The interval where the extremum is located is reduced at each step. The procedure stops when the size of the uncertainty interval becomes comparable to the permissible error.

There are three similar approaches that implement this idea. These are the half-interval method, the Fibonacci method and the golden section search method [26]. All of them differ only in the way the interval is divided into parts. The errors of these methods are comparable, but the golden section method and Fibonacci method have a noticeable advantage. This is due to the special method of dividing the interval,

when one of the two control points that divide the interval is used in the next iteration. In this research the golden section method has found practical application. It requires “ $M$ ” numerical experiments ( $M = -4.82 \log \varepsilon$ ) (relative result error  $\varepsilon$  of the extremum search). The “ $M$ ” value in practical tasks was within limits of 10 ones.

### 3. Results and Discussion

The stated methodology was implemented in software package [27], which allows modeling in the time domain the behavior of offshore floating anchored structures under the loads of wind, current, waves and ice. The software implementation of the methodology and the capabilities of the software package made it possible to perform parallel modeling of the behavior of anchored structure on a personal computer while simultaneously solving eight problems in the time domain associated with the storm loads from different directions. The researched works mainly propose the use of foreign software systems to model the behavior of anchored structures, such as Simo, Riflex [5], MIMOSA [17], MOSES [18], ANSYS Aqwa [28] and next working with optimizing program to select an anchor mooring system. It is difficult to find a rigorous solution to the optimization problem with such division of functions. An integrated optimization procedure, an element of which is a comprehensive mathematical modeling of the behavior of the investigated object, is proposed in this work.

Mooring system optimization for a semisubmersible floating platform MOSS CS50 MK2, installed at a depth of 90 m in the area of the Kirinskoye gas condensate field to the East of the Sakhalin Island is considered as an example.

The platform is positioned at the drilling location by mooring system that includes 8 mooring lines. The mooring system is represented by 84 mm chains with a total length of 2130 m; the studded chain with NV P5 category with a breaking load of 8381 kN. The linear weight of the chain is 1.6 kN/m, Young's modulus is  $0.58 \times 10^8$  kN/m. 3D geometrical model of the platform was prepared for the numerical modeling in software package “Anchored Structures”. It is shown in Fig. 1.

The external loads typical for a storm with 100-year return period were taken from Reference data on the regime of wind and waves of the Barents, Okhotsk and Caspian seas (The Russian Maritime Register of Shipping) to study the behavior of the platform in survival mode. The external conditions were accepted for extreme load mode in accordance with ND 2-020201-015 “Rules for the classification, construction and equipment of mobile offshore drilling units and fixed offshore platforms”. The rose of external loads has an asymmetry. Hull resistance coefficients were taken from the platform technical passport. Next, multiple time domain modeling of an extreme storm duration of 6 hours and from 8 different directions was performed. The behavior of the platform and extreme tensions in the mooring lines were investigated based on the modeling. On this basis, the mooring system was optimized using criterion (5).

In the initial position it was assumed that the azimuth angle of platform was  $45^\circ$ , the length of all mooring chains had maximum possible value of 2100 m. The mooring lines on the plan had the similar degree step of  $45^\circ$  and the first line has an angle of  $22.5^\circ$  with the longitudinal axis of the platform.

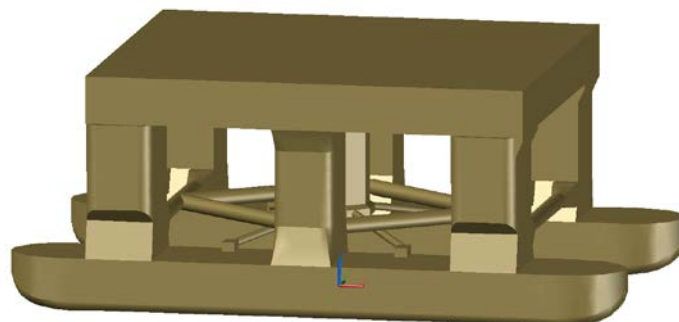


**Figure 1. General view of platform geometrical model.**

The first optimization step, associated with the search for the best tension of the lines (Fig. 2), showed that in the initial position the initial tension of 500 kN is the best value. The safety factor of the mooring lines with the initial configuration is on the edge of the permissible value ( $K_n = 1.5$ ) according to ND 2-020201-015. The second optimization step (Fig. 3) showed that the maximum possible length of mooring lines is the minimum allowable one. Negative values in Fig. 2 and Fig. 3 appear when any of the restrictions from (4) are violated, which reduces the functional  $J_f$  so much that its value cannot pretend to be an extremum. The  $135^\circ$  azimuth angle of the platform was found to be the best based on the comparison of storms from

different directions. Next the search for the best plan inclination angle of the line was performed. Only the first two angles are independent that is why the best values of the first two angles were determined:  $\alpha_1 = 10.5$ ,  $\alpha_2 = 77.5$  (other ones are determined on the basis of symmetry). The mooring system parameters which provide the safety factors for the tension of the mooring lines were obtained after the first cycle of the optimization procedure.

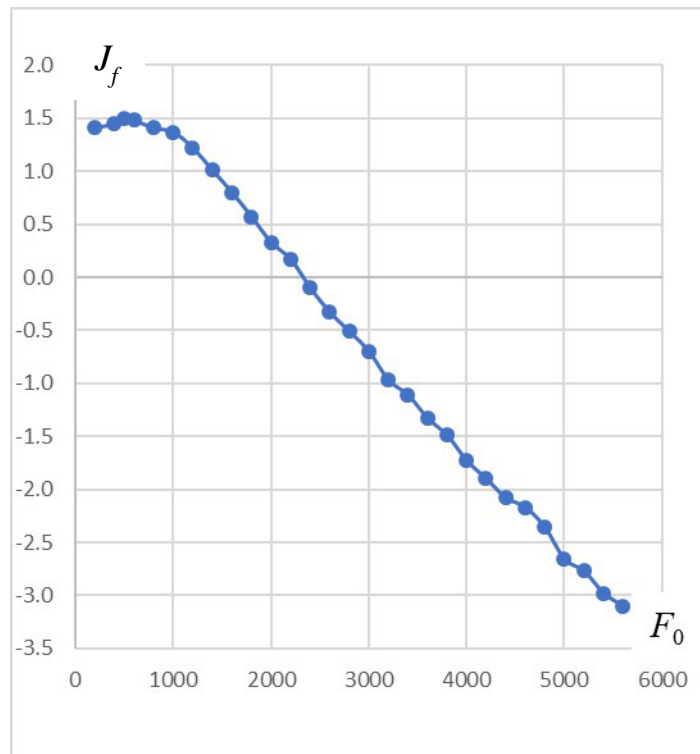


Figure 2. The value of the functional  $J_f$  at the first step of the initial tension optimization.

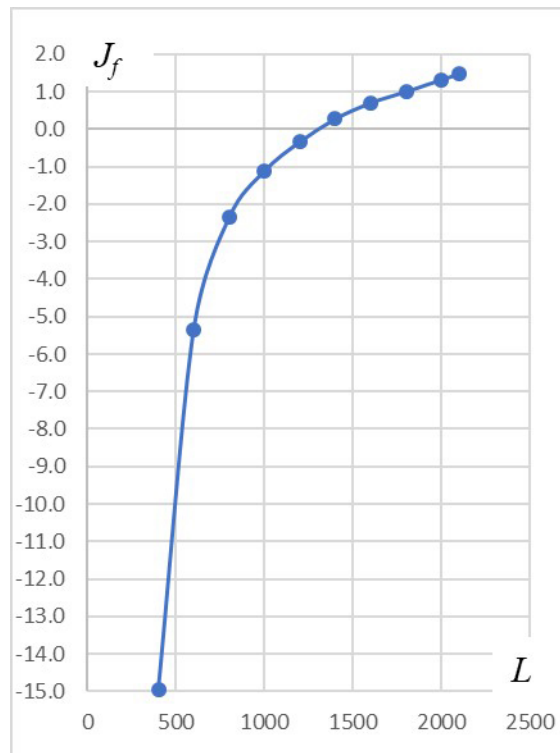
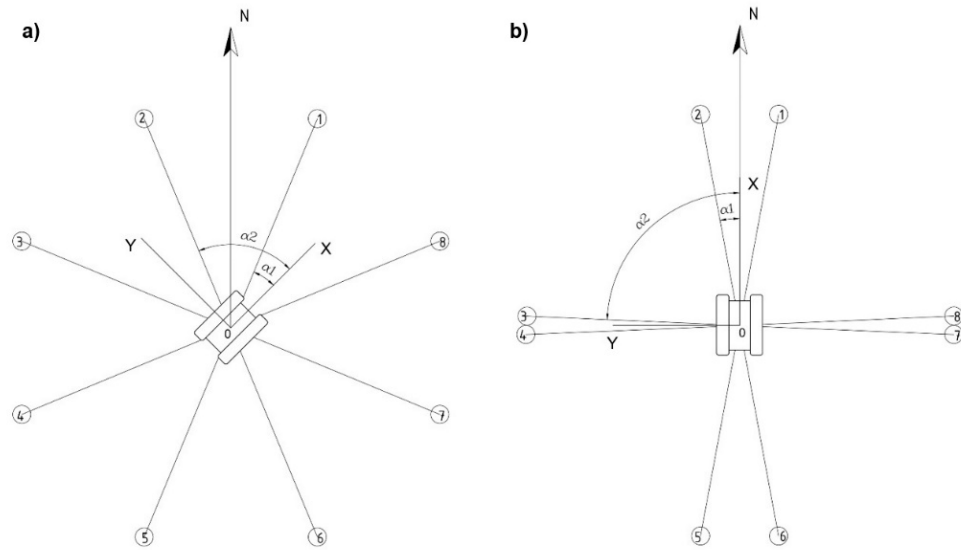


Figure 3. The value of the functional  $J_f$  at the first step of the line length optimization.

The initial values of the parameters obtained in the previous cycle were used in the second cycle of optimization. The newly obtained parameters of the platform positioning were determined by the following parameter values: the platform azimuth angle from  $0^\circ$  or  $180^\circ$  (the azimuth angle had little effect on the

value of the optimality criterion: the worst safety factor for the lines tension varied within 1 % in the range of azimuth angles variation). The optimal initial tension is 450 kN, the length of the lines is 2100 m, the values of the independent plan inclination angles of the lines are  $\alpha_1 = 10.5$ ,  $\alpha_2 = 87.5$ . Fig. 4 presents the comparison between the initial location of mooring lines and optimized one.



**Figure 4. Location of mooring lines: a) — initial case; b) — optimized case.**

According to the results of the second optimization cycle, the safety factors for the lines tension were obtained. Comparison of safety factors values are shown in Table 1.

**Table 1. The lowest safety factor for tension in anchor lines.**

| Direction | Initial safety factors | Safety factors at the first optimization step | Safety factors at the second optimization step |
|-----------|------------------------|---|--|
| N         | <b>1.46</b>            | 1.66  | <b>1.66</b>                                    |
| E         | 1.53                   | 1.68  | 1.67   |
| S         | 1.50                   | 1.68  | 1.80   |
| W         | 1.62                   | 1.75  | 1.79   |
| NE        | 1.68                   | 1.74  | 1.82   |
| SE        | 1.75                   | 1.64  | 1.82   |
| SW        | 1.90                   | 1.96  | 2.10   |
| NW        | 1.70                   | <b>1.62</b>                                   | 1.81   |

Thus the optimization procedure in this example made it possible to determine the characteristics of the mooring system, when the initial value of the criterion safety parameter is improved by 10 % on the average, as well as made it possible to leave the boundary of the minimum permissible values of the safety factors for the tension of the mooring lines. The performed test calculation also confirmed the convexity of functional (5) and the convergence of the optimization procedure. The performed optimization procedure based on numerical experiments in the time domain, implemented in software package, makes it possible to abandon the fuzzy logic tasks presented in a number of works [14–17].

## 4. Conclusions

The problem of choosing the parameters of the mooring system that ensure the highest safety of the structure in operation is always emerge at the design phase of an offshore floating anchored structures or at the design phase of positioning it in offshore waters.

The problem of choosing the best parameters of mooring systems can be formulated in various ways, which can lead to multicriteria and multiparameter optimization problems. The solution of the problems of choosing the mooring systems parameters in the most complex formulation is possible using the methods of fuzzy logic, which allows finding acceptable solutions.

A variant of the formulation of mooring system optimization problem for floating anchored structure in survival mode is proposed in this article. This allows to find an exact optimal solution for the main

parameters of the mooring system. A method for solving the problem of multiparameter optimization of the mooring system characteristics is proposed, which is implemented using existing software products that modeling the dynamics of offshore floating structures under the environmental loads.

## 5. Acknowledgements

The research is partially funded by the Ministry of Science and Higher Education of the Russian Federation as part of World-class Research Center program: Advanced Digital Technologies (contract No. 075-15-2020-934 dated 17.11.2020).

## References

1. Shkhinek, K.N. and other. *Gidrotekhnicheskie sooruzheniya na kontinentalnom shelfe* [Hydraulic structures on the continental shelf]. *Gidrotekhnika*. [Hydraulic engineering. XXI century]. 2013. 4 (16). Pp. 48–56.
2. Elistratov, V.V. and others. The investigation of conceptual approaches to the creation of marine ice-resistant floating wind power plant. *Proceedings of the International Offshore and Polar Engineering Conference*. 2019. Vol. 1. Pp. 428–434.
3. Elistratov, V.V. and others. *Proektirovanie i nauchnoe obosnovanie morskikh vetroelektricheskikh stancij* [Design and scientific rationale of offshore wind power stations]. *Nauchno-tehnicheskii sbornik RMRS* [Research Bulletin of the Russian Maritime Register of Shipping]. 2014. No. 37. Pp. 77–85.
4. Tertyshnikova, A.S., Blagovidova, I.L., Kushnir, V.M. Parameters of the position system for the deep-water drilling platform. *Vestnik SevNTU* [Bulletin of SevNTU]. 2010. No. 106. Pp. 164–167.
5. Xu, K., Gao, Z., Moan, T. Effect of hydrodynamic load modelling on the response of floating wind turbines and its mooring system in small water depths. *Journal of Physics: Conference Series*. 2018. Vol. 1104. DOI:10.1088/1742-6596/1104/1/012006
6. Kolacio, I., Prpić-ORŠIĆ, J., Kurilić, K. Analiza sidrenja poluuronjive platforme scarabeo 7 [Analysis for Semisubmersible platform Scarabeo 7]. *Brodogradnja* [Shipbuilding]. 2010. 61 (1). Pp. 34–41.
7. Naumenko, A.A., Blagovidova, I.L., Pyanov, A.V., Ivanova, O.A. Numerical simulation of the positioning process of complex floating objects when performing offshore operations. *Transactions of the Krylov state research center*. 2019. No. S2. Pp. 239–247. DOI: 10.24937/2542-2324-2019-2-S-I-239-247
8. Ivanova, O.A., Kushnir, V.M., Blagovidova, I.L. Physical models of TLP and SPAR deepwater drilling platforms for experimental researches of the dynamics in the experimental basin. *Vestnik SevNTU* [Bulletin of SevNTU]. 2014. No. 153. Pp. 72–79.
9. Sabziyan, H., Ghassemi, H., Azarsina, F., Kazemi, S. Effect of Mooring Lines Pattern in a Semi-submersible Platform at Surge and Sway Movements. *Journal of Ocean Research*. 2014. Vol. 2, No. 1. Pp. 17–22. DOI:10.12691/jor-2-1-4
10. Sabziyan, H., Ghassemi, H., Azarsina, F., Kazemi, S. Appropriate Model for Mooring Pattern of a Semi-Submersible Platform. *Journal of Subsea and Offshore*. 2015. Vol. 1. Pp. 18–25.
11. Iqbal, M., Azam, M., Naeem, M., Khwaja, A.S., Anpalagan, A. Optimization classification, algorithms and tools for renewable energy: A review. *Renewable and Sustainable Energy Reviews*. 2014. No. 39. Pp. 640–654. DOI: 10.1016/j.rser.2014.07.120
12. Wu, B., Cheng, X., Chen, Y., Ni, X., Zhang, K. Design Automation of Mooring Systems for Floating Structures. *Practical Design of Ships and Other Floating Structures*. 2020. No. 65. Pp. 579–594. DOI: 10.1007/978-981-15-4680-8\_40
13. Montasir, O.A., Yenduri, A., Kurian, V.J. Mooring System Optimisation and Effect of Different Line Design Variables on Motions of Truss Spar Platforms in Intact and Damaged Conditions. *China Ocean Engineering*. 2019. 33 (4). Pp. 385–397. DOI: 10.1007/s13344-019-0037-1
14. Monteiro, B.F., de Pina, A.A., Baioco, J.S., Albrecht, C.H., de Lima, B.S.L.P., Jacob, B.P. Toward a methodology for the optimal design of mooring systems for floating offshore platforms using evolutionary algorithms. *Marine Systems and Ocean Technology*. 2016. 11 (3-4). Pp. 55–67. DOI: 10.1007/s40868-016-0017-8
15. de Pina, A.C., de Pina, A.A., Albrecht, C.H., Leite Pires de Lima, B.S., Jacob, B.P. ANN-based surrogate models for the analysis of mooring lines and risers. *Applied Ocean Research*. 2013. No. 41. Pp. 76–86. DOI: 10.1016/j.apor.2013.03.003
16. Carbone, A., Menezes, I., Martha, L.F. Mooring Pattern Optimization using Genetic Algorithms. *6<sup>th</sup> World Congresses of Structural and Multidisciplinary Optimization*. Brazil. Rio de Janeiro, 2005.
17. Shafieefar, M., Rezvani, A. Mooring optimization of floating platforms using a genetic algorithm. *Ocean Engineering*. 2007. 34 (10). 1413–1421. DOI: 10.1016/j.oceaneng.2006.10.005
18. Mirzaei, M., Maimun, A., Priyanto, A., Fitriady, A. Mooring Pattern Optimization Using A Genetic Algorithm. *Jurnal Teknologi* (Sciences and Engineering). 2014. 66 (2). 189–193. DOI: 10.11113/jt.v66.2519
19. Jin, H.Z., Su, X.Y., Yu, A.C., Lin, F. Design of automatic mooring positioning system based on mooring line switch. *Dianji Yu Kongzhi Xuebao* [Electric Machines and Control]. 2014. 18 (5). 93–98.
20. Xu, S.W., Liang, M.X., Wang, X.F., Ding, A.B. A Mooring System Deployment Design Methodology for Vessels at Varying Water Depths. *China Ocean Engineering*. 2020. Vol. 34, No. 2. Pp. 1–13. DOI: 10.1007/s13344-020-0018-4
21. Monteiro, B.D.F., Albrecht, C.H. and others. Optimization of mooring systems for floating offshore platforms considering seabed obstacles. *Proceedings of the ASME 2017 36th International Conference on Ocean, Offshore and Arctic Engineering*. Norway. Trondheim, 2017. DOI: 10.1115/OMAE2017-61482
22. Monteiro, B.D.F., Baioco, J.S., Albrecht, C.H., de Lima, B.S.L.P., Jacob, B.P. Optimization of mooring systems in the context of an integrated design methodology. *Marine Structures*. 2021. Vol. 75. DOI: 10.1016/j.marstruc.2020.102874
23. de Pina, A.A., Albrecht, C.H., de Lima, B.S.L.P., Jacob, B.P. Tailoring the Particle Swarm Optimization Algorithm for the Design of Offshore Oil Production Risers. *Optimization and Engineering*. 2010. No. 12. Pp. 215–235. DOI: 10.1007/s11081-009-9103-5
24. Teslyaruk, I., Bolshev, A. Numerical analysis of behavior offshore anchored structures and improvement of systems of their holding. *Proceedings of the Second International Conference on Mathematics and Computers in Sciences and in Industry*. Malta. Sliema, 2015. Pp. 188–190. DOI: 10.1109/MCSI.2015.45
25. Teslyaruk, I., Bolshev, A. Technique optimization of holding systems of marine floating objects on the basis of numerical modeling of their behavior. *International Journal of Mathematics and Computers in Simulation*. 2016. Vol. 10. Pp. 72–76.

26. Amosov, A.A., Dubinskij, Y.A., Kopchenova, N.V. Vychislitelnye metody dlya inzhenerov [Computational methods for engineers]. Moscow: Vysshaya shkola. 1994. 543 p.
27. Bolshev, A.S., Kuteinikov, M.A., Frolov, S.A. Matematicheskoe modelirovanie povedeniya morskikh plavuchih obyektov v programnom komplekse «Anchored Structures» [Mathematical modeling of offshore floating objects in the software package «Anchored Structures»]. Nauchno-tekhnicheskii sbornik RMRS [Research Bulletin of the Russian Maritime Register of Shipping]. 2013. No. 36. Pp. 68–90.
28. Gogin, A., Kantarzi, I. Numerical Study of the Floating Gravity Base Structure Mooring. Proceedings of ECE 2019. Lecture Notes in Civil Engineering. 2020. Vol. 70. 205–219. DOI: 10.1007/978-3-030-42351-3\_18

**Information about authors:**

**Alexander Bolshev**, Sc.D. in Technical Science

ORCID: <https://orcid.org/0000-0002-0177-8389>

E-mail: [bolshev\\_as@spbstu.ru](mailto:bolshev_as@spbstu.ru)

**Sergey Frolov**, PhD in Technical Science

ORCID: <https://orcid.org/0000-0002-1811-7712>

E-mail: [frolov\\_sa@spbstu.ru](mailto:frolov_sa@spbstu.ru)

**Ekaterina Shonina**,

ORCID: <https://orcid.org/0000-0001-5292-7295>

E-mail: [shonina\\_ev@spbstu.ru](mailto:shonina_ev@spbstu.ru)

*Received 15.02.2021. Approved after reviewing 04.06.2021. Accepted 16.06.2021.*






Research article

UDC 691.3, 628.51, 661.25

DOI: 10.34910/MCE.111.13

## Production of Portland cement using fluorine gypsum – hydrofluoric acid waste

M.P. Kuz'min<sup>a,b,\*</sup> , L.M. Larionov<sup>b</sup> , M.Yu. Kuz'mina<sup>b</sup> , A.S. Kuz'mina<sup>b</sup> , J.Q. Ran<sup>c</sup> ,  
A.E. Burdonov<sup>b</sup>, E.V. Zenkov<sup>b,d</sup> 

<sup>a</sup> Baikal State University, Irkutsk, Russia

<sup>b</sup> Irkutsk National Research Technical University, Irkutsk, Russia

<sup>c</sup> Shenzhen University, Shenzhen, China

<sup>d</sup> Irkutsk State Transport University, Irkutsk, Russia

 Mike12008@yandex.ru

**Keywords:** gypsum, fluorogypsum, concrete, by product, waste management, gypsum stone, Portland cement clinker, microstructure

**Abstract.** Introduction. The purpose of the research was to explore the possibility of making PC400–D20 Portland cement, as the gypsum stone was replaced with fluorogypsum during the milling process. The study deals with physical and mechanical properties of Portland cement obtained by mixing milled Portland cement clinker, fly ash (consisting of nanosized particles of SiO<sub>2</sub> and Al<sub>2</sub>O<sub>3</sub>) and sulphate additives (gypsum stone or fluorogypsum). Methods. In accordance with the quality indicators set by Russian State Standard GOST 4913–82 (EN 13279–2), Angarsk Electrolysis Chemical Plant (JSC AECP) fluorogypsum is significantly superior to the gypsum stone mined in the Nukutsky Gypsum Quarry (Irkutsk Region). The use of high-quality fluorite concentrate in the production of the hydrofluoric acid can be accounted for exceptional characteristics of fluorogypsum found at the sludge fields of JSC AECP. Results and Discussion. The composition of sludge fields of Angarsk Electrolysis Chemical Plant has been investigated. The quality of its main component, fluorogypsum, has been determined with accredited classification. The studies of chemical composition and physical properties of fluorogypsum deposited at the sludge fields of JSC AECP proved that it can serve as a first-grade raw material in accordance with Russian State Standard GOST4913–82 for the production of high-grade gypsum. Laboratory tests confirmed the practicability of using fluorogypsum as a substitute for natural gypsum stone in cement production process (when grinding cement clinker). A technology and parameters for the production of high-grade gypsum production from the fluorogypsum have been developed. Conclusions. Laboratory tests confirmed the possibility of using fluorogypsum as a setting regulator in cement production when grinding cement clinker. The exact quantity of fluorogypsum when grinding cement clinker was determined, which ensures the production of high-quality cement in compliance with Russian State Standard GOST 10187–85. The prospects of using fluorogypsum as a raw material for the production of high-quality gypsum as well as a wide range of building mixtures based on it has been identified.

Kuz'min, M.P., Larionov, L.M., Kuz'mina, M.Yu., Kuz'mina, A.S., Ran, J.Q., Burdonov, A.E., Zenkov, E.V. Production of portland cement using fluorine gypsum – hydrofluoric acid waste. Magazine of Civil Engineering. 2022. 111(3). Article No. 11113. DOI: 10.34910/MCE.111.13

© Kuz'min, M.P., Larionov, L.M., Kuz'mina, M.Yu., Kuz'mina, A.S., Ran, J.Q., Burdonov, A.E., Zenkov, E.V., 2022. Published by Peter the Great St. Petersburg Polytechnic University.



This article is licensed under a CC BY-NC 4.0

## 1. Introduction

Millions of tons of solid by-product materials are produced every year by chemical industries all over the world. The accumulation of these materials causes substantial societal costs for containment and disposal, including environmental pollution and related economic losses [1]. Therefore, finding new beneficial applications for these large reserves of unused and/or underutilized materials is of great interest and provides important opportunities for sustainable economic development. At the same time, the construction industry is always searching for alternative supplies of usable materials in order to curb its carbon footprint, reduce the cost of new projects, and ensure long term sustainability of the industry itself.

Gypsum binders have increasingly been used in the construction industry due to their relatively low production energy intensity as well as such important properties as short curing time, which, in turn, reduces the duration of technological operations and ensures good formability and workability of the material, volume stability, and no necessity for compaction. Gypsum chemical composition is non-toxic, so its processing does not cause carbon dioxide emissions into the environment [1–3].

Gypsum raw materials are extracted predominantly from open pit mines. Gypsum mining enterprises are mainly large, highly mechanized industries whose production volume reaches 2 million tons of stone per year. The stone is usually shipped to the consumer after primary crushing and grading into 0–300, 0–60, and 60–300 mm fractions. Unfortunately, gypsum deposits in quarries and mines are not subjected to enrichment.

Gypsum-containing waste, including phosphogypsum, borogypsum, fluorogypsum, as well as wastes resulted from citric acid production in chemical, food and other manufacturing, represents an important part of the raw material base in the gypsum industry of the country.

Hydrofluoric acid was a key product of Angarsk Electrolysis Chemical Plant (JSC AECP). The production process was commenced in the fifties of the last century and had successfully been conducted up until 2015. However, due to the logistical concerns, the line for hydrofluoric acid production was closed by the top-management of Rosatom State Atomic Energy Corporation.

Hydrofluoric acid was produced by treating fluorite  $\text{CaF}_2$  with sulfuric acid in an externally heated rotary kiln at temperature of 450–500 °C ( $\text{CaF}_2 + \text{H}_2\text{SO}_4 \rightarrow \text{CaSO}_4 + 2\text{HF}$ ). This way, fluorogypsum or industrial gypsum ( $\text{CaSO}_4$ ) was formed as a by-product. Upon undergoing the lime neutralization, fluorogypsum was stored in the form of calcium sulphate dihydrate  $\text{CaSO}_4 \cdot 2\text{H}_2\text{O}$  in the sludge dumps on the territory of JSC “AIECP”. The diffractogram of the fluorogypsum sample taken from the sludge dumps shows peaks indicative of calcium sulphate (Fig. 1). The peaks pointing at fluorite are represented in fewer numbers ( $2\theta = 27.3^\circ; 55.2; 61.3; 68.8^\circ$ ) and are characterized by low intensity.

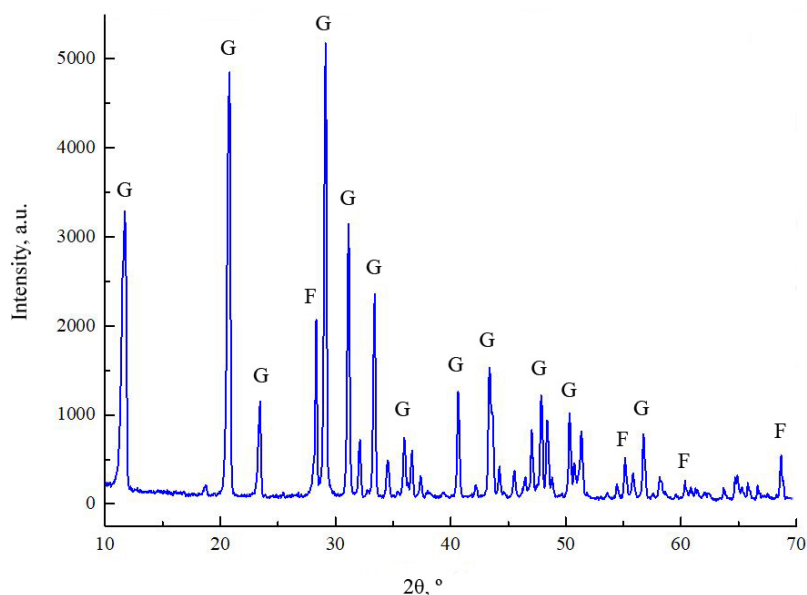


**Figure 1. The diffractogram of the fluorogypsum sample taken from the sludge dumps of JSC AECP (G – gypsum  $\text{CaSO}_4 \cdot 2\text{H}_2\text{O}$ ; F – fluorite  $\text{CaF}_2$ ).**

During the production process, up to a total millions of cubic meters of the material was accumulated. It remained discarded of a long time (Fig. 2) owing to a misconception that fluorogypsum might be radioactive (due to the activity of the enterprise). Therefore, the first stage of the studies was the

assessment of radioactivity of the sludge fields. During the course of the research, several samples were collected from the different points of the mass.



**Figure 2. Sludge Dumps of JSC AECP.**

According to the results of the radiation safety monitoring, administered in the certified laboratory pursuant to the existing standards and specifications, including Russian State Standard GOST 30108–94, fluorogypsum was recognized as a first class radiation-proof material ( $SA = 88 < Bq/kg$ ) suitable for all types of construction (certificate 31/10; dd. October 14, 2010).

In respect of the quality indicators set by Russian State Standard GOST 4913–82 (EN 13279–2), JSC AECP fluorogypsum is significantly superior to the gypsum stone mined in the Nukutsky Gypsum Quarry (Irkutsk Region). The gypsum stone, however, enjoys wide application due to the perceived lack of alternatives (as there exist only one gypsum stone quarry in the Eastern Siberia). The use of high-quality fluorite concentrate in the production of the hydrofluoric acid can be accounted for exceptional characteristics of fluorogypsum found at the slurry fields of JSC AECP.

Fluorogypsum has already been considered a raw material for the production of mineral binders and, when fused with cement, a component of dry building mixes [16]. In addition, fluorogypsum treated with sulfuric acid was viewed as an initial product for manufacturing mineral fertilizers [7].

Along with fluorogypsum, there exist the materials exhibiting similar chemical properties and physical characteristics [8–25]:

- phosphogypsum, a by-product of phosphoric acid production;
- borogypsum, a by-product of boric acid production.

Some attempts were made to produce gypsum-cement-pozzolana binders with phosphogypsum [3, 4, 7]. Investigations revealed that a gypsum binder made of a phosphogypsum anhydrite and blast furnace slag mixture 70–24 % with appropriate activators achieved 23 MPa strength after 28 d curing at 27 °C under high humidity and a mixture composed of 75 % gypsum, 20 % OPC and 5 % microsilica as cementitious binder developed a strength of up to 17 MPa after 200 days under water [17].

Addition of wastes containing boron in cement based materials causes mostly decrease in strength parameters and increase in setting times. Researchers agree that impurities and  $B_2O_3$  in the wastes are the most influencing parameters effecting strength reduction and retardation of setting time [18].

Fluorogypsum can be used as:

1. a set-controlling admixture for the clinker milling [2–5];
2. a raw material in production of high-quality gypsum [11, 16].

The purpose of the research is to explore the chemical composition and physical properties of fluorogypsum (the waste of hydrofluoric acid production) as well as the possibility of making PC400–D20 Portland cement (according to Russian State Standard GOST10178–85), as the gypsum stone was replaced with fluorogypsum during the milling process.

## **2. Material and Methods**

Fluorogypsum is a light gray paste where the particle size does not exceed 0.08 mm, and the true density equals  $2.35 \text{ g/cm}^3$ . The range of water content of the average sample taken from the settled sludge is 15–20 %. The dried sample is a powder with a specific surface area of  $480 \text{ m}^2/\text{kg}$ . The chemical

composition of the samples was determined by the flame atomic absorption spectrophotometry: the method was finalized by the bulletins № 61 and № 172–S issued by the Scientific Committee on Analytical Research Methods in 2016 and October 27, 2015 respectively, approved by The Federal Methodical Center for Laboratory Research and Certification of Mineral Raw Materials of the Ministry of Natural Resources and Environment of the Russian Federation, and revised by the Federal State Unitary Enterprise “All-Russian Research Institute of the Mineral Raw Materials named after N.M. Fedorovsky”.

A flame photometer based on a DFS–12 spectrometer and the PerkinElmer 403 atomic absorption spectrophotometer were used for the chemical analysis of the fluorogypsum which is presented in Table 1.

**Table 1. Chemical analysis of fluorogypsum.**

| Content, %                         | SiO <sub>2</sub> | Al <sub>2</sub> O <sub>3</sub> | Fe <sub>2</sub> O <sub>3</sub> | CaO   | MgO   | K <sub>2</sub> O | SO <sub>3</sub> | Other<br>vapor<br>impurities |
|------------------------------------|------------------|--------------------------------|--------------------------------|-------|-------|------------------|-----------------|------------------------------|
| Max.                               | 2.07             | 0.64                           | 0.429                          | 31.88 | 0.768 | 0.073            | 44.25           | 21.29                        |
| Min.                               | 1.93             | 0.58                           | 0.422                          | 31.56 | 0.731 | 0.071            | 44.13           | 22.25                        |
| Average<br>(based on 3<br>samples) | 1.97             | 0.61                           | 0.426                          | 36.63 | 0.745 | 0.072            | 44.19           | 21.76                        |

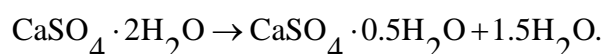
*Note: Chemical analysis of the fluorogypsum was conducted in the analytical department of Vinogradov Institute of Geochemistry SB RAS.*

Based on the acquired data, the fluorogypsum can be classified as the premium grade material as set by Russian State Standard GOST 4013–82. In the course of establishing the quantitative composition of the trace elements, the absence of harmful and dangerous impurities was determined as well.

This makes it possible to organize a production of high-quality gypsum, as the deposits of the slurry fields of JSC AECP can be used to create gypsum of grades G 10 and higher according to Russian State Standard GOST 12579. Likewise, the material can be referred to as the first category in terms of whiteness – a factor proven to be especially valuable for the producers of dry construction mixtures.

Currently there is no production of high-quality gypsum in Irkutsk region. The established fields of high-quality raw materials used to manufacture gypsum are mainly located in European part of Russia, but the reserves are limited and do not satisfy the needs of the entire country. This shortage is fulfilled by means of external supply. Angarsk Gypsum Plant produces gypsum that does not exceed G5, as the plant's production lines are designed to process the raw materials of the Nukutsky Gypsum Quarry.

Processing fluorogypsum of the slurry fields of JSC AECP relies on the removal of hygroscopic moisture from the material before converting calcium sulphate dihydrate into its end product – hemihydrate. At the temperatures of 100–140 °C, the process of transformation of calcium sulphate dihydrate into hemihydrate takes places according to the following reaction:



Despite its simplicity, the production of high-quality gypsum requires special conditions. There are two structurally different modifications of calcium sulphate hemihydrate, namely,  $\alpha$ - and  $\beta$ -modifications. Alpha-hemihydrate, which is formed at a temperature slightly above the initial boiling point under the increased pressure of water vapor, is considered the most valuable. The production process is carried out in the autoclave under certain pressure, so that the removal of internal water from the gypsum does not cause loosening and destruction of the grains (particles). Dense hemihydrate smooth surfaced crystals are formed. In this case, the compliance with such technological parameters as vapor pressure, temperature, and processing time serves as a prerequisite.

The second form,  $\beta$ -hemihydrate, is produced under the atmospheric pressure: during the dehydration process, the water comes out in the form of the steam which results in strong mechanical dispersion of grains and the formation of a rough surface, “pitted” with a large number of cracks and capillaries. The higher the temperature and the lower the water vapor pressure, the finer the surface of the crystals are.

Structural differences determine the properties of  $\alpha$ - and  $\beta$ -modifications of calcium sulphate hemihydrate.  $\beta$ -hemihydrate is distinguished by its increased solubility and higher hydration rate; however, to obtain a so-called rolling gypsum paste, it requires more water (50–70 wt. % of gypsum compared to 30–45 % for the  $\alpha$ -hemihydrate). A result, it possesses less strength.

The production of high-quality gypsum opens up the prospects for the manufacturing a wide range of building mixtures. Currently, the construction market is 80 % filled with materials of the foreign origin represented by a wide range of products for all types of work and of various complexity. Upon conducting an in-depth study, it can be concluded that the production technology of the imported building mixtures sold on the Russian market is quite simple and based upon:

- strict selection of inert aggregate grain-size distribution
- high-quality binder;
- optimum input of special additives.

Special additives are classified into plasticizing, hydrophobic, air-retraining, as well as organic and non-organic substances.

All things considered, given the availability of high-quality gypsum of our own production, it becomes possible to manufacture building mixtures of the enhanced properties. This will secure the share on the market of construction materials.

### 3. Results and Discussion

#### 3.1. *The use of fluorogypsum as a set-controlling admixture for the clinker milling*

The process applied in large-scale cement production based on the traditional technology of burning cement clinker in tubular rotary kilns at the grinding stage. In this case, calcium sulphate dihydrate serves a regulator of the setting time and is added in the amount of 3–5 % of the clinker weight during the grinding process (in accordance with the adopted technology).

During the study, the raw materials used by Angarsk Cement Plant (i.e. the gypsum stone mined at the Nukutsky Gypsum Quarry) were replaced with the fluorogypsum deposited in the sludge dumps of JSC AECP. The needs of the cement plant for this type of the raw materials amounted to 3000 tons per month.

The purpose of the research was to explore the possibility of making PC400–D20 Portland cement (according to Russian State Standard GOST 10178–85 (EN 197–1), as the gypsum stone was replaced with fluorogypsum during the milling process. The object of the study dealt with physical and mechanical properties of Portland cement obtained by mixing milled Portland cement clinker, active mineral additives (fly ash) and sulphate additives (gypsum stone or fluorogypsum).

##### Properties of the test materials:

a) *Portland cement clinker (PCC)* of the specified mineral composition manufactured by the Cement Factory “Angarsk Cement” in the form of the dark gray particles of 3 to 40 mm each;

b) *fly ash (FA)* of Irkutsk Thermal Power Plant – 1 in the form of light gray powder (density of 2.3–2.4 g/cm<sup>3</sup>, bulk density of 780–820 kg/m<sup>3</sup> CaO absorption activity 40–50 mg);

c) *gypsum stone (GS)* in the form of white crushed gypsum stone of particles of 20 mm each, used as a sulphate-containing additive in the production of the Portland cement (according to Russian State Standard GOST 4013);

d) *fluorogypsum (FG)*, waste deposits in the form of suspension (mass humidity 12–15 %) containing solid particles not exceeding 0.08 mm and possessing true density of 2.35 g/cm<sup>3</sup>;

e) *standard quartz uniformly graded sand* used to prepare cement mortar according to Russian State Standard GOST 310–4 (ENG 196–1).

All the materials with the exception of the clinker were dried in order to obtain constant weight [18, 21]. The drying of fly ash and sand was carried out at the temperature of 105±5 °C. Gypsum stone and fluorogypsum were dried at the temperature of 68±2 °C to avoid dehydration.

Upon the drying, all the materials with the exception of fluorogypsum were ground in the ball mill to the required particle size (residue on sieve No. 008 not exceeding 15 wt. %) and then subjected to drying for one more hour before being placed in hermetically sealed containers. The containers then were stored in the chamber with low relative air humidity as ensured by calcium chloride placed on the tin. The materials were stored that way up until being used in the experiment.

The materials were used to determine the quality indicators of two compositions of cement, where either gypsum stone or the fluorogypsum of JSC AECP slurry fields were used as set regulators. The qualitative composition of such types of the cement conforms to the standards accepted at “Angarsk Cement” plant, namely:

- Portland cement clinker (PCC);
- active mineral additive fly ash: 18 % of the total clinker mass;
- gypsum additive (GS or FG): 5.2 % of the total clinker mass.

The components of each type of the cement in the quantities required for the experiments in accordance with Russian State Standard GOST 310.2–76 and Russian State Standard GOST 25328 (EN 2061) were mixed in a laboratory mill for two hours as the metal balls were replaced with rubber and plastic “grinding elements”. The property values of two composition of the cement ( $PCC = 1.0 + FA = 0.18 + GS = 0.052$  and  $PCC = 1 + FA = 0.10 + FG = 0.052$ ) are summarized in the Table 2.

**Table 2. Property values of cement produced with addition of either the gypsum stone or the fluorogypsum.**

| No. | Properties                                       | Property values         |                       |   |
|-----|--|-------------------------|-----------------------|---|
|     |  | Cement:<br>PCC + FA+ GS | Cement:<br>PCC+FA+ FG | According to<br>Russian State<br>Standard GOST<br>10178–85      |
| 1   | Density, g/cm <sup>3</sup>                       | 3.05                    | 3.02                  | 2.9–3.1   |
| 2   | Fineness: residue on sieve № 008, wt. %          | 13.5                    | 14.2                  | ≤ 15.0  |
| 3   | Fineness: surface area, m <sup>2</sup> /kg       | 371                     | 356                   | ≥ 250   |
| 4   | Consistency, wt. %                               | 26                      | 27                    | 25–30   |
| 5   | Initial Setting                                  | 3 hours 05min           | 3 hours 10 min        | ≥ 45 min  |
| 6   | Final Setting                                    | 7 hours 25 min          | 7 hours 50 min        | ≤ 10 hours  |
| 7   | Strength of the 1-day steam-cured samples, MPa:  |                         |                       | 1 <sup>st</sup> group > 27.0                                    |
|     | a) bending strength;                             | 3.72                    | 3.97                  | 2 <sup>nd</sup> group: 24–27                                    |
|     | b) compression strength                          | 20.20                   | 23.13                 | 3 <sup>d</sup> group ≤ 24                                       |
| 8   | Strength of the 7-day water-cured samples, MPa:  |                         |                       |   |
|     | a) bending strength;                             | 3.83                    | 4.02                  | not standardized  |
|     | b) compression strength                          | 23.19                   | 24.18                 |   |
| 9   | Strength of the 28-day water-cured samples, MPa: |                         |                       |   |
|     | a) bending strength;                             | 6.15                    | 6.31                  | > 5.9   |
|     | b) compression strength                          | 41.20                   | 42.2                  | > 39.2  |
| 10  | Bulk density, kg/m <sup>3</sup>                  | 1100                    | 1080                  |   |
| 11  | Bleeding, vol. %                                 | 32                      | 30                    | According to<br>Russian State<br>Standard GOST<br>25328–82 ≤ 30 |

The results of the study demonstrate that physical and mechanical properties of the produced cement samples satisfy the technical requirements set by Russian State Standard GOST 10187–85 (EN197–1). Thus, the samples can be classified as PC400–D20 cement brand.

Substitution of a gypsum additive from natural gypsum stone to the one of fluorogypsum did not present to have any significant effect on the quality of the cement. However, adding fluorogypsum to Portland cement resulted in a slight increase in the water requirement for the material. This is reflected both in the consistency and in the reduction of water release (a positive effect from the increased dispersity of fluorogypsum).

Increase in the setting time of the cement paste is one of the potential positive impacts of using the fluorogypsum. This, in turn, makes the cement more effective in concrete to be subjected to electrical heating in winter. As a result, this phenomenon allows for reclassifying Portland cement from group 3 to group 2 (with regard to the curing).

However, replacing the Nukut gypsum [18, 19] with fluorogypsum may prove complicated due to the increased hygroscopic moisture in the latter (15–25 %). The moisture removal procedure conducted in the usual manner is not cost-effective. According to the conservative estimate, the energy cost of the water

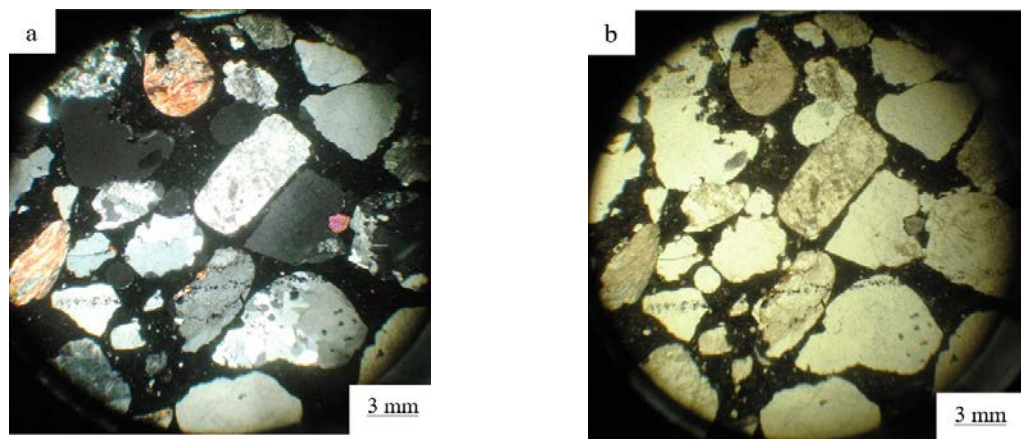


removal is 156.4 kWh per ton of fluorogypsum, and with the usual 50 % efficiency of using thermal units, these costs would double.

In this regard, an original and economical method of water removal was designed and then tested under the laboratory conditions. The method is a combination of chemical absorption of hygroscopic moisture by the hemihydrate, with the subsequent transformation of the latter into the dihydrate of normative humidity. This technology allows to reduce the cost of bringing fluorogypsum to the normalized humidity by 25 %.

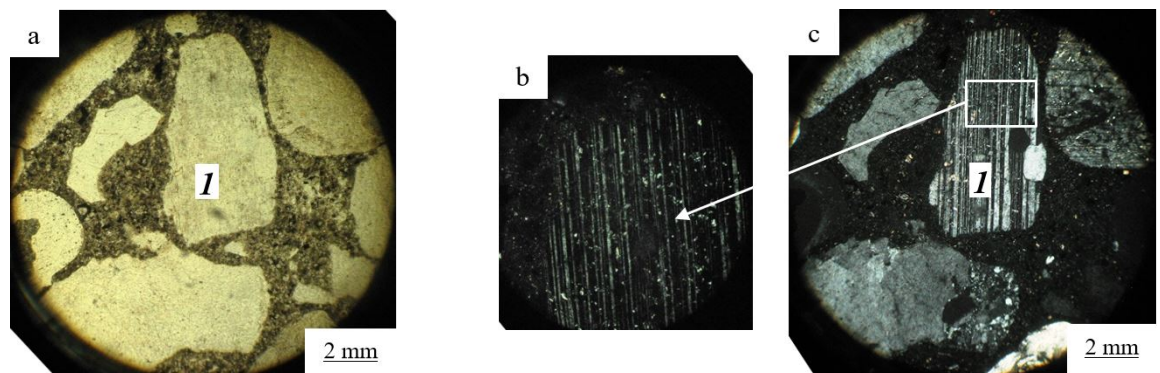
Another requirement to be met for the use of fluorogypsum in the cement industry deals with the loading and transportation of the material as it should not create dust areas. Hence, the process of moisture removal must be combined with the refining the fluorogypsum through the rotary drum granulator or the roller press. The particles (granules or pellets) formed this way will possess the necessary strength to retain their shape during loading and transportation.

The nature of incorporating fluorogypsum additives in the structure of the cement stone is revealed by crystal-optical examination. Filamentous contact points between the fluorogypsum and the cementing mass are clearly defined (Fig. 3).



**Figure 3. Cement with fluorogypsum as an additive: general layout (a – transmitted light, b – polarized light).**

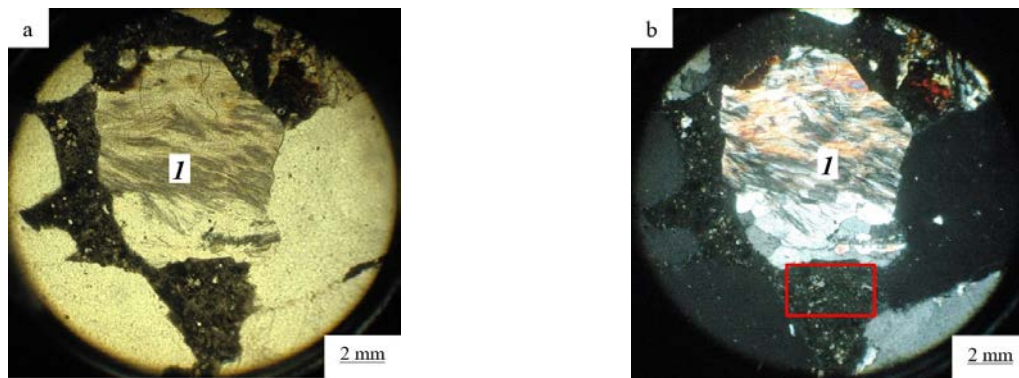
Fig. 4 demonstrates the processes of ettringite particles thin shells formation. Contact points between the grain and the cementing material are clearly defined.



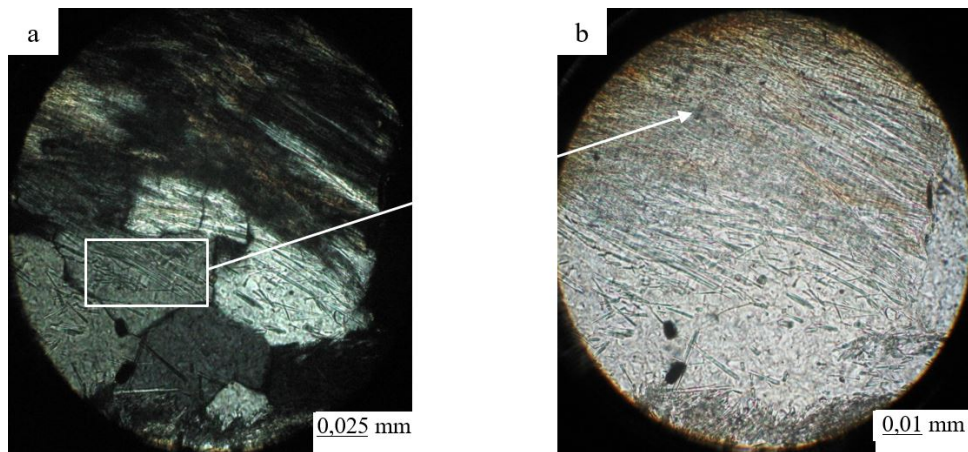
**Figure 4. The processes within an ettringite grain (1) (a – transmitted light, b and c – polarized light).**

Fig. 5 shows a crystallographic image of a fluorogypsum grain, as well as the processes of ettringite shells formation between the clinker grains. It should be noted that replacements are observed only within a given grain. Fig. 6 shows a cementing mass, in individual grains of which recrystallization of the shell is observed (1), and needle-shaped formations bind cement particles into a monolith.





**Figure 5. Fluorogypsum grain (1)**  
a – transmitted light, b – polarized light.



**Figure 6. Element from Fig. 3. Cementing mass: recrystallization of the shell is observed in individual grains (1).**

This study corroborates a classical scheme of cement stone formation as fluorogypsum is used to prevent false setting [3–4].

When mixing cement containing fluorogypsum and water, film-like ettringite  $\text{Ca}_6\text{Al}_2(\text{SO}_4)_3(\text{OH})_{12}\cdot 26\text{H}_2\text{O}$  is formed on the surface of the clinker grains. The ettringite inhibits the interaction of cement and water which leads to a so-called induction period, or a dormant period. Subsequently, the shielding shells are gradually destroyed and the dormant period ends after 3–6 hours. Cement starts interacting with water, and the structural strength of the system increases.

Within a few hours after mixing cement containing fluorogypsum and water, ettringite particles recrystallize on the clinker grains of the shell to form elongated crystals that gradually bind the cement particles to each other. This creates a setting effect. Due to recrystallization, the shells become more permeable to water, which leads to its increased interaction with cement and further strengthening of the structure.

## 4. Conclusions

1. The in-depth studies of chemical composition and physical properties of fluorogypsum deposited at the slurry fields of JSC AECP proved that it can serve as a first-grade raw material in accordance with Russian State Standard GOST 4913–82 for the production of high-grade gypsum.

2. Laboratory tests confirmed the possibility of using fluorogypsum as a setting regulator in cement production when grinding cement clinker. Crystal-optical studies have proved the classical scheme of the behavior of gypsum during the formation of cement stone as well as its role in the setting of cement paste. The exact quantity of fluorogypsum when grinding cement clinker was determined, which ensures the production of high-quality cement the corresponding to the requirements set by Russian State Standard GOST 1018785 (EN 197–1).

3. The prospects of using fluorogypsum as a raw material for the production of high-quality gypsum as well as a wide range of building mixtures based on it has been identified. That, in turn, makes it possible to firmly gain a foothold in the market of high-quality dry building mixtures.

## References

1. Levchenko, Ye.A., Vorobchuk, V.A., Peshkov, A.V. Ispolzovaniye ftorgipsa dlya polucheniya mineralnogo vyazhushchego [The use of fluorogypsum to obtain a mineral binder]. Vestnik IrGTU. 2014. 6. Pp. 123–125. (rus)
2. Bigdeli Y., Barbato, M., Gutierrez-Wing, M.T., Lofton, C.D. Use of slurry fluorogypsum (FG) with controlled pH-adjustment in FG-based blends. Construction and Building Materials. 2018. 163. Pp. 160–168. DOI: 10.1016/j.conbuildmat.2017.12.099
3. Bigdeli, Y., Barbato, M., Gutierrez-Wing, M.T., Lofton, C.D., Rusch, K.A. Jongwon, Jung, Jungyeon, Jang. Development of new pH-adjusted fluorogypsum-cement-fly ash blends: Preliminary investigation of strength and durability properties. Construction and Building Materials. 2018. 182. Pp. 646–656. DOI: 10.1016/j.conbuildmat.2018.06.086
4. Xuquan, H., Mingming, J., Xiaorong, Z., Cilai, T. Mechanical properties and hydration mechanisms of high-strength fluorogypsum-blast furnace slag-based hydraulic cementitious binder. Construction and Building Materials. 2016. 127. Pp. 137–143. DOI: 10.1016/j.conbuildmat.2016.09.152
5. Garg, M., Pundir, A. Investigation of properties of fluorogypsum-slag composite binders – Hydration, strength and microstructure. Cement and Concrete Composites. 2014. 45. Pp. 227–233. DOI: 10.1016/j.cemconcomp.2013.10.010
6. Yan, P., Yang, W., Qin, X., Yi, Y. Microstructure and properties of the binder of fly ash-fluorogypsum-Portland cement. Cement and Concrete Research. 1999. 29. Pp. 349–354. DOI: 10.1016/S0008-8846(98)00214-2
7. Sadiqul Islam, G.M., Chowdhury, F.H., Raihan, M.T., Sikder Amit, S.K., Rafiqul, M.I. Effect of Phosphogypsum on the Properties of Portland Cement. Procedia Engineering. 2017. 171. Pp. 744–751. DOI: 10.1016/j.proeng.2017.01.440
8. Singh, M. Role of phosphogypsum impurities on strength and microstructure of selenite plaster. Construction and building materials. 2005. 19 (6). Pp. 480–486. DOI: 10.1016/j.conbuildmat.2004.07.010
9. Akin, A.İ., Sert, Y. Utilization of weathered phosphogypsum as set retarder in Portland cement. Cement and Concrete Research. 2004. 34 (4). Pp. 677–680. DOI: 10.1016/j.cemconres.2003.10.017
10. Cárdenas-Escudero, C. Procedure to use phosphogypsum industrial waste for mineral CO<sub>2</sub> sequestration. Journal of Hazardous Materials. 2011. 196. Pp. 431–435. DOI: 10.1016/j.jhazmat.2011.09.039
11. Mehta, P.K., Monteiro, J.M. Concrete, Structure, Properties and Materials (4<sup>th</sup> Edition). McGraw-Hill Education. New York City, NY, USA, 2013. 684 p.
12. Colombani, J., Bert, J. Holographic interferometry study of the dissolution and diffusion of gypsum. Water Geochimica et Cosmochimica Acta. 2007. 71. Pp. 1913–1920. DOI: 10.1016/j.gca.2007.01.012
13. Gorlanov, E.S., Bazhin, V.Yu., Fedorov, S.N. Carbide formation at a carbon-graphite lining cathode surface wettable with aluminum. Refractories and Industrial Ceramics. 2016. 57. Pp. 292–296. DOI: 10.1007/s11148-016-9971-0
14. Hasan-Nattaj, F., Nematzadeh, M. The effect of forta-ferro and steel fibers on mechanical properties of high-strength concrete with and without silica fume and nano-silica. Construction and Building Materials. 2017. 137. Pp. 557–572. DOI: 10.1016/j.conbuildmat.2017.01.078
15. Nagrockienė, D., Girskas, G., Skripkiūnas G. Properties of concrete modified with mineral additives. Construction and Building Materials. 2017. 135. Pp. 37–42. DOI: 10.1016/j.conbuildmat.2016.12.215
16. Singh, M., Garg, M. Activation of fluorogypsum for building materials. Journal of Scientific and Industrial Research. 2009. 68. Pp. 130–134.
17. Bigdeli, Y., Barbato, M., Gutierrez-Wing, M.T., Lofton C.D. Use of slurry fluorogypsum (FG) with controlled pH-adjustment in FG-based blends. Construction and Building Materials. 2018. 163. Pp. 160–168. DOI: 10.1016/j.conbuildmat.2017.12.099
18. Kuz'min, M.P., Larionov, L.M., Kondratiev, V.V., Kuz'mina, M.Yu., Grigoriev, V.G., Kuz'mina, A.S. Use of the burnt rock of coal deposits slag heaps in the concrete products manufacturing. Construction and Building Materials. 2018. 179. Pp. 117–124. DOI: 10.1016/j.conbuildmat.2018.05.222
19. Emrullahoglu Abi, C.B. Effect of borogypsum on brick properties. Construction and Building Materials. 2014. 59. Pp. 195–203. DOI: 10.1016/j.conbuildmat.2014.02.012
20. Garg, M., Pundir, A. Investigation of properties of fluorogypsum-slag composite binders – Hydration, strength and microstructure, Cement & Concrete Composite. 2014. 45. Pp. 227–233. DOI: 10.1016/j.cemconcomp.2013.10.010
21. Kuz'min, M.P., Larionov, L.M., Paul K. Chu, Abdul M. Qasim, Kuz'mina, M.Yu., Kondratiev, V.V., Kuz'mina, A.S., Jia Q. Ran New methods of obtaining Al–Si alloys using amorphous microsilica. International Journal of Metalcasting. 2020. 14. Pp. 207–217. DOI: 10.1007/s40962-019-00353-w
22. Kuz'min, M.P., Paul K. Chu, Abdul M. Qasim, Larionov, L.M., Kuz'mina, M.Yu., Kuz'min, P.B. Obtaining of Al–Si foundry alloys using amorphous microsilica – Crystalline silicon production waste. Journal of Alloys and Compounds. 2019. 806. Pp. 806–813. DOI: 10.1016/J.JALLCOM.2019.07.312
23. Kuz'min, M.P., Kondrat'ev, V.V., Larionov, L.M., Kuz'mina, M.Y., Ivanchik, N.N. Possibility of preparing alloys of the Al–Si system using amorphous microsilica. Metallurgist. 2017. 61. Pp. 86–91. DOI: 10.1007/s11015-017-0458-0
24. Kuz'min, M.P., Kuz'mina, M.Yu., Kuz'mina, A.S. Production and properties of aluminum-based composites modified with carbon nanotubes. Materials Today: Proceedings. 2019. 19 (5). Pp. 1826–1830. DOI: 10.1016/j.matpr.2019.07.021
25. Golewski, G.L. An assessment of microcracks in the Interfacial Transition Zone of durable concrete composites with fly ash additives. Composite Structures, 2018. 200. Pp. 515–520. DOI: 10.1016/j.compstruct.2018.05.144

### Information about authors:

**Mikhail Kuz'min**, PhD in Technical Science

ORCID: <https://orcid.org/0000-0002-8714-5004>

E-mail: [Mike12008@yandex.ru](mailto:Mike12008@yandex.ru)

**Leonid Larionov**,

ORCID: <https://orcid.org/0000-0003-3878-9820>

E-mail: [larionov59@rambler.ru](mailto:larionov59@rambler.ru)

**Marina Kuz'mina**, PhD in Chemical Science  
ORCID: <https://orcid.org/0000-0001-7215-5501>  
E-mail: [kuzmina.my@yandex.ru](mailto:kuzmina.my@yandex.ru)

**Alina Kuz'mina**, PhD in Physics and Mathematics  
ORCID: <https://orcid.org/0000-0003-3878-9820>  
E-mail: [kuzmina.istu@gmail.com](mailto:kuzmina.istu@gmail.com)

**Jia Q. Ran**, PhD  
ORCID: <https://orcid.org/0000-0003-0685-0420>  
E-mail: [ranjiaqi26@gmail.com](mailto:ranjiaqi26@gmail.com)

**Alexander Burdonov**, PhD in Technical Science  
E-mail: [slimbul@rambler.ru](mailto:slimbul@rambler.ru)

**Evgeniy Zenkov**, PhD in Technical Science  
ORCID: <https://orcid.org/0000-0003-4414-0307>  
E-mail: [jovanny1@yandex.ru](mailto:jovanny1@yandex.ru)

*Received 15.02.2021. Approved after reviewing 05.07.2021. Accepted 06.07.2021.*



Research article

UDC 624.04:531.391.3


DOI: 10.34910/MCE.111.14

## Analytical estimation of the first natural frequency and analysis of a planar regular truss oscillation spectrum

M.N. Kirsanov<sup>1</sup> , V.S. Safronov<sup>2</sup> 

<sup>1</sup>National Research University "Moscow Power Engineering Institute", Moscow, Russia

<sup>2</sup> Voronezh State Technical University, Voronezh, Russia

 [c216@ya.ru](mailto:c216@ya.ru)

**Keywords:** truss, natural vibrations, lower frequency estimate, vibration spectrum, kinematic variability, Dunkerley's method

**Abstract.** A statically determinate truss of a beam type with a triple lattice with short descending and long ascending braces is considered. The mass of a truss is modeled by concentrated loads at its nodes. For the first natural frequency, the Dunkerley's method derives a formula for the dependence of its lower boundary on the number of panels. The calculation of the efforts in the truss required to obtain the stiffness value according to the Maxwell-Mohr formula is performed in the Maple computer mathematics system by cutting out the nodes. It is shown that for a certain number of panels the proposed scheme of the truss has the property of kinematic variability. For admissible numbers of panels, by induction, the sequence of solutions for trusses with different numbers of panels is generalized to an arbitrary case. The coefficients of the required dependence are obtained as solutions of linear homogeneous recurrent equations. To obtain and solve recurrent equations, the operators of the Maple system are used. The found solution is compared with the minimum frequency of the spectrum obtained numerically. It is shown that the accuracy of the analytical assessment monotonically increases with the increase in the number of panels. Multiple frequencies and the independence of several higher frequencies from the number of panels were found in the frequency spectrum.

### 1. Introduction

Although one of the most important characteristics of a structure for practice is its lowest natural frequency, for many engineering problems it is also necessary to know the entire frequency spectrum of the structure. Such tasks, in particular, include the tasks of seismic resistance of structures [1–3]. In most cases, the frequency spectrum is calculated numerically in a linear [4, 5] or nonlinear [6–10] setting. In rare cases, the first frequency is determined analytically [11–16]. Particularly effective are formulas for the vibration frequencies of regular structures, depending on their order (the number of periodicity elements, for example, panels). General questions of the existence of statically determinate regular rod systems were studied in [17–19]. Formulas for the deflection of planar regular trusses for various types of lattices and supports are obtained in handbooks [20, 21], and [22–24]. The formulas for deflection make it possible to calculate the stiffness of the truss and calculate the natural frequencies based on it. Methods for calculating natural frequencies are reviewed in [25, 26].

In this paper, we derive the analytical dependence of the lower boundary of the first natural vibration frequency of a regular truss and analyze its spectrum. In contrast to the known similar problems, the

---

Kirsanov, M.N., Safronov, V.S. Analytical estimation of the first natural frequency and analysis of a planar regular truss oscillation spectrum. Magazine of Civil Engineering. 2022. 111(3). Article No. 11114. DOI: 10.34910/MCE.111.14

© Kirsanov, M.N., Safronov, V.S., 2022. Published by Peter the Great St. Petersburg Polytechnic University.



This article is licensed under a CC BY-NC 4.0

proposed truss scheme has a special feature. For some values of the number of panels, the design allows kinematic variability. This complicates the derivation of the formula for the desired dependency. In addition, this study takes into account both degrees of freedom of each mass in the truss node. The solution is compared with the numerical one obtained for a refined (non-uniform) distribution of masses over nodes.

## 2. Methods

### 2.1. Calculation of forces. Kinematic analysis

The symmetric truss of a beam type with a triple diagonal lattice is considered (Fig. 1). Ascending and descending braces have different angles of inclination. The inertial properties of the structure are modeled by the same masses concentrated in all hinges. In this case, the rods themselves are assumed to be devoid of masses. The truss has  $2n$  panels, length  $a$  and  $2h$  high. The truss consists of  $n_e = 8(n+1)$  elements, including three rods, simulating a movable left and fixed right hinge support.

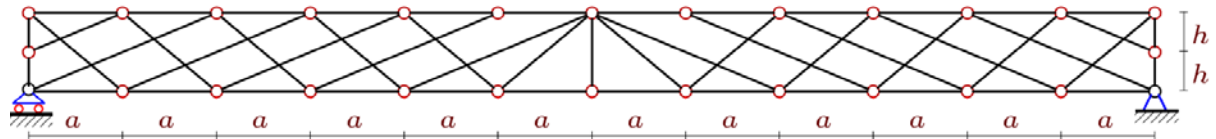


Figure 1. Truss,  $n = 6$ .

To calculate the forces in the structural members, the program [27], written in the language of symbolic mathematics Maple [28], is used. The algorithm used in this program also allows you to use other similar systems: Mathematica, Maxima, Reduce, etc. The coordinates of the hinges are entered into the program, assuming that the origin is located in the left support:

$$x_i = x_{i+2n+2} = a(i-1), \quad y_i = 0, \quad y_{i+2n+2} = 2h, \quad i = 1, \dots, 2n+1,$$

$$x_{2(n+1)} = 0, \quad x_{4(n+2)} = 2na, \quad y_{2(n+1)} = y_{4(n+1)} = h.$$

The lattice structure is defined by ordered lists of the vertices of the rods  $T_i, i = 1, \dots, n_e$ . For the rods of the lower belt, for example, we have:

$$T_i = [i, i+1], \quad i = 1, \dots, 2n.$$

The equilibrium equations of all nodes of the truss constitute a system, the solution of which gives the values of the forces in symbolic form, depending on the given number of panels. The matrix of the system of equations consists of the direction cosines of the forces, determined by the values of the coordinates of the nodes of the rods. The matrix is filled in a cycle along all the bars of the truss  $i = 1, \dots, n_e$

$$L_1 = x_{T[i,2]} - x_{T[i,1]}, \quad L_2 = y_{T[i,2]} - y_{T[i,1]},$$

$$l_i = \sqrt{L_1^2 + L_2^2},$$

$$G_{\alpha j} = -L_j / l_i, \quad \alpha = 2T[i,2] + j - 2 \leq n_e,$$

$$G_{\alpha j} = L_j / l_i, \quad \alpha = 2T[i,1] + j - 2 \leq n_e, \quad j = 1, 2.$$

The system of equilibrium equations is written in matrix form  $\mathbf{GS} = \mathbf{P}$ , where  $\mathbf{S}$  is the vector of unknown forces in the rods and supports,  $\mathbf{P}$  is the vector of loads.

Trial calculations of the forces in the rods from the action of arbitrary loads have shown that for some numbers of panels, for example  $n = 2, 5, 8, 11, \dots$ , or  $n = 3k - 1, k = 1, 2, 3, \dots$ , the determinant of the system of equilibrium equations vanishes. This is possible in the case of instantaneous change of the design, which, of course, is completely unacceptable here. This fact is confirmed by the diagram of possible velocities (Fig. 2). This is not the only scheme of possible velocities. Its asymmetric variants are also admissible when all nodes in one of the truss halves are stationary or the directions of the velocities are asymmetric. There is a connection between the values of the velocities  $v/h = u/a$ .



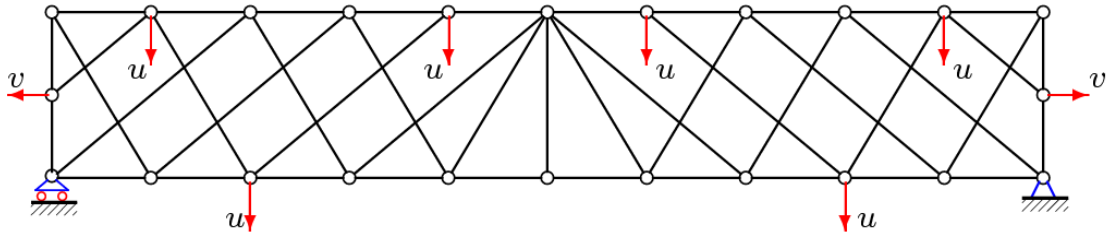


**Figure 2. Scheme of possible velocities of truss nodes,  $n = 5$ .**

Eliminating the unacceptable values of  $n$  from the calculations, we set the following sequence of panel numbers used to display the dependence of the vibration frequency on the number of panels:

$$n = \left( 6k + 5 - (-1)^k \right) / 4, \quad k = 1, 2, \dots \quad (1)$$

In what follows, by the order of the truss, we mean the number  $k$ . The dependence of the deflection of this truss on the number of panels at various loads is given in the handbook [21].

## 2.2. First frequency. The analytical solution according to the Dunkerley's method

Since each node endowed with mass has two degrees of freedom, the number of degrees of freedom of the considered truss is equal to  $N_s = 2N$ , where  $N = 4n + 2$  is the number of masses. The formula for determining the lower (first) frequency by the Dunkerley's method [29, 30], which gives an estimate of this value from below, has the form

$$\omega_D = \left( \sum_{j=1}^N 1/\omega_{h,j}^2 + 1/\omega_{v,j}^2 \right)^{-1/2}, \quad (2)$$

where  $\omega_{h,j}$ ,  $j = 1, \dots, N$  is partial frequencies of horizontal vibrations, and  $\omega_{v,j}$  is partial frequencies of vertical ones. Partial frequencies are calculated from the analysis of the differential equation of motion of one mass fixed at node  $j$  of the truss

$$m\ddot{u}_j + D_j u_j = 0,$$

where  $u_j$  is the vertical displacement of the mass,  $\ddot{u}_j$  is the acceleration,  $D_k$  is the stiffness coefficient ( $j$  is the mass number). The frequency of vibration of the load is  $\omega_j = \sqrt{D_j/m}$ . The stiffness coefficient is calculated using the Maxwell – Mohr formula under the assumption that the stiffness of all the rods are the same

$$\delta_j = 1/D_j = \sum_{\alpha=1}^{n_e-3} \left( S_{\alpha}^{(j)} \right)^2 l_{\alpha} / (EF).$$

Here it is indicated  $S_{\alpha}^{(j)}$  is the forces in the element number  $\alpha$  from the action of a unit vertical or horizontal force applied to the node where the mass numbered  $k$  is located. According to (2) we have

$$\omega_D^{-2} = m \sum_{j=1}^{N_s} \delta_j = m(\Delta_h + \Delta_v). \quad (3)$$

Sequential calculation of trusses with an increasing number of panels shows that the expression for the coefficient  $\Delta_v$  has a constant form

$$\Delta_v = \left( C_1 a^3 + C_2 c^3 + C_3 d^3 + C_4 h^3 \right) / \left( h^2 n EF \right), \quad (4)$$

where  $c = \sqrt{a^2 + h^2}$ ,  $d = \sqrt{a^2 + 4h^2}$  are the lengths of the braces.

The coefficients  $C_1, \dots, C_4$ , as functions of the number  $k$ , related to the number of panels  $n$  in half the span by formula (1), are found by the induction method with the involvement of the Maple system operators.

Using the operator *rgf\_findrecur*, we make sure that the sequence of coefficients  $C_1$  satisfies the linear homogeneous recurrent equation of the ninth order

$$C_{1,k} = C_{1,k-1} + 4C_{1,k-2} - 4C_{1,k-3} - 6C_{1,k-4} + \\ + 6C_{1,k-5} + 4C_{1,k-6} - 4C_{1,k-7} - C_{1,k-8} + C_{1,k-9}.$$

The *rsolve* operator solves this equation

$$C_1 = (k+1) \left( 54k^4 + 9 \left( 19 - 5(-1)^k \right) k^3 + 3 \left( 123 - 35(-1)^k \right) k^2 + \right. \\ \left. + 3 \left( 92 - 45(-1)^k \right) k - 40(-1)^k + 50 \right) / 40.$$

The remaining coefficients are found as solutions to similar equations of the sixth and seventh orders:

$$C_2 = (k+1) \left( 78k^2 + 3 \left( 27 - 11(-1)^k \right) k - 14(-1)^k + 14 \right) / 12, \\ C_3 = \left( 78k^3 + 3 \left( 77 - 17(-1)^k \right) k^2 + \left( 233 - 101(-1)^k \right) k - 53(-1)^k + 77 \right) / 96, \\ C_4 = \left( 9 \left( 5 - (-1)^k \right) k^2 + 12 \left( 11 - 3(-1)^k \right) k - 35(-1)^k + 83 \right) / 6.$$

Similarly, we obtain the sum related to the partial frequencies of horizontal vibrations:

$$\Delta_h = \left( C_5 a^3 + C_6 c^3 + C_7 d^3 + C_8 h^3 \right) / \left( a^2 n^2 EF \right), \quad (5)$$

where

$$C_5 = \left( 648k^4 + 54 \left( 47 - 8(-1)^k \right) k^3 + 9 \left( 425 - 157(-1)^k \right) k^2 + \right. \\ \left. + 3 \left( 893 - 505(-1)^k \right) k - 547(-1)^k + 731 \right) / 32, \\ C_6 = \left( 36k^3 + 6 \left( 19 - 2(-1)^k \right) k^2 + 4 \left( 29 - 10(-1)^k \right) k - 29(-1)^k + 37 \right) / 4, \\ C_7 = (k+1) \left( 18k^2 - \left( 15(-1)^k - 57 \right) k - 8(-1)^k + 52 \right) / 16, \\ C_8 = \left( 18k^2 + 12 \left( 5 - 3(-1)^k \right) k - 47(-1)^k + 55 \right) / 4.$$

As a result, we obtain the desired lower estimate of the first frequency in analytical form

$$\omega_D = \sqrt{\frac{nEF}{m \left( \left( C_1 a^3 + C_2 c^3 + C_3 d^3 + C_4 h^3 \right) / h^2 + \left( C_5 a^3 + C_6 c^3 + C_7 d^3 + C_8 h^3 \right) / (na^2) \right)}}. \quad (6)$$

If we do not take into account the horizontal fluctuations of loads, then the solution turns out to be much simpler

$$\tilde{\omega}_D = h \sqrt{\frac{nEF}{m \left( C_1 a^3 + C_2 c^3 + C_3 d^3 + C_4 h^3 \right)}}. \quad (7)$$



### 3. Results and Discussion

#### 3.1. Numerical calculation of the spectrum of natural frequencies

Let us estimate the accuracy of the obtained dependence by comparing it with the result of the numerical solution. To calculate the forces in the rods, which are used to calculate the stiffness of the structure, you can use the same program used to calculate the estimate (6).

The system of differential equations for the movement of loads has the form

$$\mathbf{M}_N \ddot{\mathbf{U}} + \mathbf{D}_N \mathbf{U} = 0, \quad (8)$$

where  $\mathbf{U} = [x_1, \dots, x_N, y_1, \dots, y_N]^T$  is the displacement of the masses,  $\mathbf{D}_N$  is the stiffness matrix,  $\mathbf{M}_N$  is the diagonal inertia matrix of size  $N \times N$ , and  $\ddot{\mathbf{U}}$  is the acceleration vector. Multiplying (8) by the compliance matrix  $\mathbf{B}_N$ , we reduce the problem of finding natural frequencies to the problem of the eigenvalues of the matrix  $\Phi_N = \mathbf{B}_N \mathbf{M}_N$ . Indeed, taking into account the ratio  $\ddot{\mathbf{U}} = -\omega^2 \mathbf{U}$ , where  $\omega$  is the natural frequency of oscillations, we obtain  $\Phi_N \mathbf{U} = \lambda \mathbf{U}$ , where  $\lambda = 1/\omega^2$  is the eigenvalue of the matrix  $\Phi_N$ . Maple has an *Eigenvalues* operator from the *LinearAlgebra* package for calculating eigenvalues and vectors of matrices.

**Example.** The elastic modulus of steel  $E = 2 \cdot 10^5$  MPa. The rods have a cross-section of  $F = 40.5 \text{ cm}^2$  and a linear mass of  $\rho = 31.8 \text{ kg/m}$  (channel-shaped cross-section No. 30). Dimensions  $a = 3 \text{ m}$ ,  $h = 1 \text{ m}$  are accepted. The mass of each node in the analytical solution (6) is calculated by the formula  $m = \rho L_0 / N$  where  $L_0 = 4an + 4(n-1)c + (2n-1)d + 6h$  is total length of all truss rods. In the numerical solution, the masses of the nodes depend on the lengths of the rods connected to the nodes. The mass of each rod is divided in half between the nodes at its ends. For the assumed cross-section of the rods and the dimensions of the truss at  $n = 3$ , the corresponding mass distribution is given in Fig. 3. In an analytical solution designed for equal masses, each node has a mass in this case  $m = 203 \text{ kg}$ .

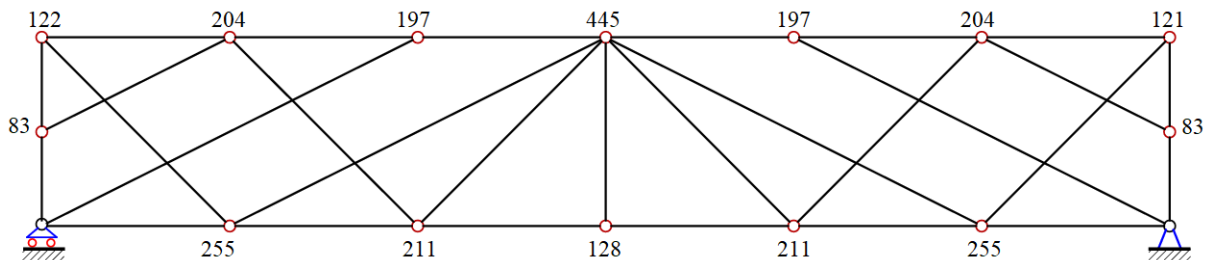


**Figure 3. Mass distribution over the truss nodes in the numerical solution of the problem (kg).**

Graph 4 compares the analytical estimate (6) and the lowest frequency of the spectrum of the truss, obtained numerically.

With an increase in the number of panels, the vibration frequency decreases, and the degree of approximation of the analytical estimate also increases. More precisely, you can trace the dependence of the error on the number of panels, if you enter the value  $\varepsilon = (\omega_1 - \omega_D) / \omega_1$  of the relative discrepancy. For  $k > 12$ , the discrepancy of solution (5) decreases to a quite acceptable value of several percent (Fig. 4). An increase in the accuracy of the solution with a decrease in the height  $h$  of the structure is also noticeable.

With an increase in the number of panels, the vibration frequency decreases, and the degree of approximation of the analytical estimate increases. More precisely, you can trace the dependence of the error on the number of panels, if it corresponds to the relative discrepancy  $\varepsilon = (\omega_1 - \omega_D) / \omega_1$ . For  $k > 12$ , the discrepancy of solution (5) decreases to a quite acceptable value of several percent (Fig. 5). An increase in the accuracy of the solution with a decrease in the height of the structure is also noticeable.

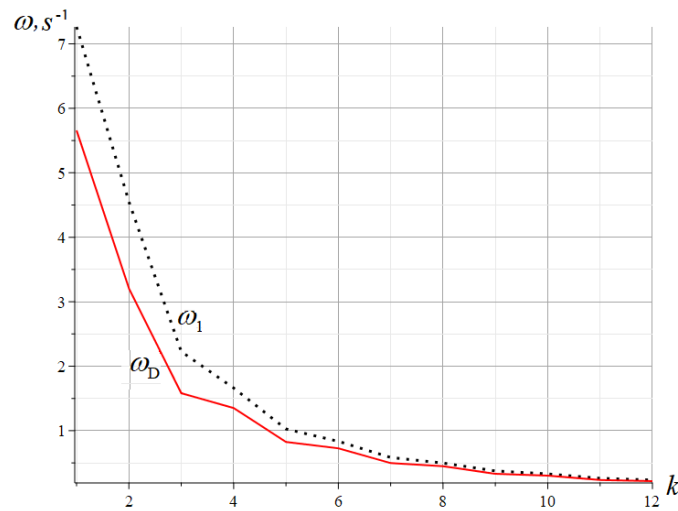


**Figure 4. Dependence of the lower Dunkerley's estimate  $\omega_D$  and the first frequency  $\omega_1$  obtained numerically on the number of panels.**

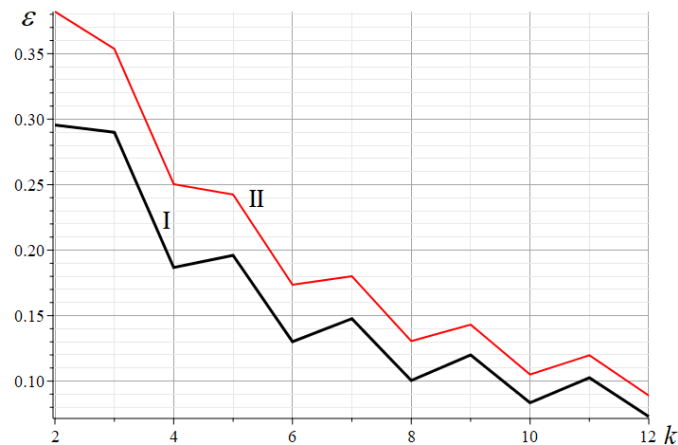


**Figure 5. Solution (6) discrepancy depending on the number of panels and the height of the truss; I –  $h = 1$  m; II –  $h = 2$  m.**

Increasing analytical accuracy with the increasing number of panels is of fundamental importance to practice. The "curse of dimension" is known, according to which with an increase in the complexity of the design, associated, for example, with an increase in the number of panels, the accuracy of solving a system of algebraic equations inevitably decreases, and the calculation time increases. Of course, the high bit depth and power of modern computing technology overcome this difficulty to some extent, but there can always be a design of such complexity that the power of the computing system and the amount of memory may not be enough. An analytical solution gives a simple solution and an increase in the order of the calculated system only goes to increase its accuracy. Note, however, that the effect of increasing the accuracy of the lower Dunkerley's estimate is not valid for all structures. For spatial systems, for example, the error grows with an increase in the number of panels, asymptotically approaching a value of the order of 30–40 %.

Note that without taking into account the horizontal fluctuations in the Dunkerley's formula (3), the result does not change much.

The corresponding frequency ratio according to the formula (6) and (7) decreases with an increase in the number of panels and a decrease in the height of the truss (Fig. 6).

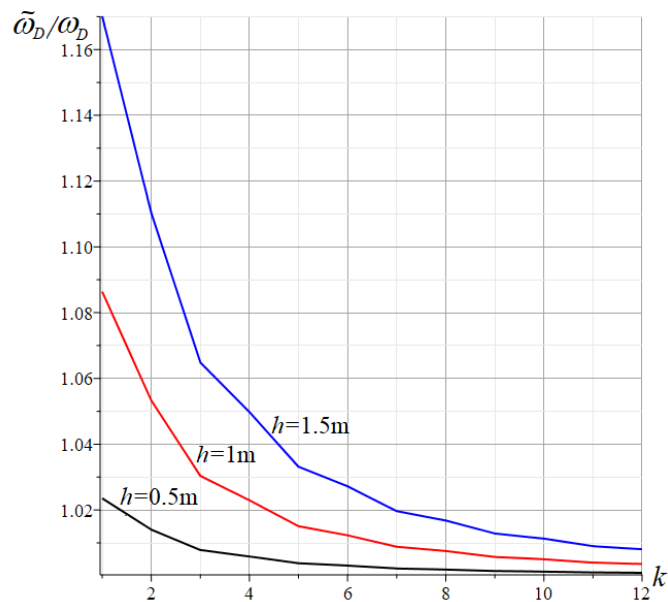


Figure 6. Comparison of frequencies obtained by formulas (6) and (7).

### 3.2. Natural frequency spectrum

An analysis of the entire frequency spectrum of the truss revealed interesting features. In Fig. 7, with the same data as for Fig. 3, the spectra of trusses with  $k = 1, 2, \dots, 8$  are plotted. Horizontal mass fluctuations are not taken into account here. Each broken curve corresponds to a truss of order  $k$ , the abscissa shows the numbers of frequencies in the spectrum. The characteristic independence of the last five higher frequencies in each spectrum from the order of the system is noticeable. Here, the equality of frequencies is taken within the framework of a certain accuracy. Let us denote  $\omega_j^{(k)}$  is frequencies with number  $j$  in the spectrum of a truss of the order of  $k$ , ordered in ascending order. According to (1), the number of degrees of freedom of a truss of the order of  $k$  is equal to  $N = 6k + 7 - (-1)^k$ ,  $k = 1, 2, \dots$ . The higher frequencies in the spectra of the truss under consideration are multiples of pairs and do not depend on accuracy  $\delta_\omega$  on the order of  $k$ . For example, for  $h = 1$  m, we have higher frequencies  $\omega_j^{(8)} = 119.138 \text{ c}^{-1}$ ,  $j = N = 6k + 7 - (-1)^k$ , that are multiple and equal to each other for different  $k$  with a relative accuracy of  $\delta_\omega = \left( \omega_j^{(8)} - \omega_j^{(1)} \right) / \omega_j^{(8)} = 1.26 \cdot 10^{-5}$ , and for  $h = 2$  m the frequency and error of equality of conditionally multiple frequencies are less:  $\omega_j^{(8)} = 88.885 \text{ s}^{-1}$ ,  $\delta_\omega = 0.643 \cdot 10^{-5}$ .

The same pattern also applies to the second and third frequencies from the end of the spectrum:  $j = N - 2$ ,  $j = N - 3$ . The lowest frequencies in the spectra are located more chaotically.

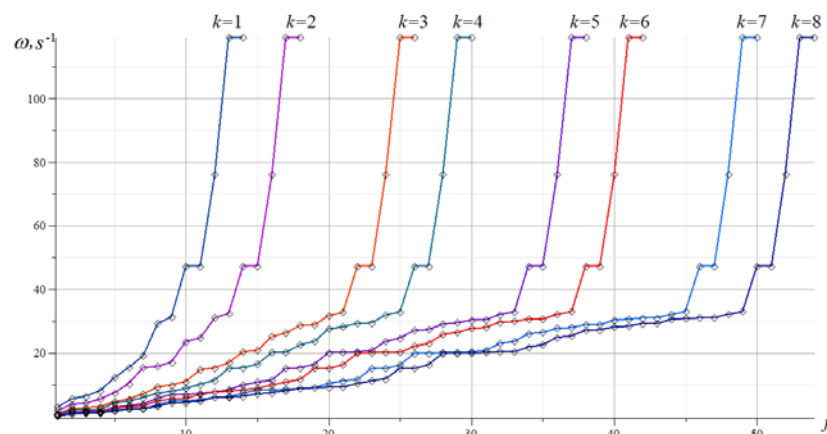


Figure 7. Spectra of natural frequencies of trusses of orders 1-8.

## 4. Conclusion

1. For the considered planar truss, an analytical lower estimate of the first frequency is obtained for an arbitrary number of panels. The coefficients of the resulting formula have the form of polynomials no higher than the fifth order in the number of panels.
2. It is noted that for a certain number of panels, the truss allows instantaneous kinematic variability. This is confirmed by the distribution pattern of possible node velocities.
3. A comparison of the analytical estimate with the numerical result shows that with an increase in the number of panels, the accuracy of the estimate increases.
4. It is shown that the highest frequency in the truss spectrum and several higher frequencies do not depend on the order of the truss. Multiple frequencies are found.

## 5. Acknowledgments

This research has been supported by the Interdisciplinary Scientific and Educational School of Moscow University "Fundamental and Applied Space Research".

## References

1. Resatalab, S., Ahmadi, M.T., Alembagheri, M. Seismic response sensitivity analysis of intake towers interacting with dam, reservoir, and foundation. *Magazine of Civil Engineering*. 2020. 98(7). Pp. 9901–9901. DOI: 10.18720/MCE.99.1.
2. Pekcan, G., Itani, A.M., Linke, C. Enhancing seismic resilience using truss girder frame systems with supplemental devices. *Journal of Constructional Steel Research*. 2014. 94. Pp. 23–32. DOI: 10.1016/j.jcsr.2013.10.016.
3. Vatin, N., Ivanov, Ay., Rutman, Y., Chernogorskiy, S., Shvetsov, K. Earthquake engineering optimization of structures by economic criterion. *Magazine of Civil Engineering*. 2017. 8(76). Pp. 67–83. DOI: 10.18720/MCE.76.7
4. Siriguleng, B., Zhang, W., Liu, T., Liu, Y.Z. Vibration modal experiments and modal interactions of a large space deployable antenna with carbon fiber material and ring-truss structure. *Engineering Structures*. 2020. 207. Pp. 109932. DOI: 10.1016/j.eng-struct.2019.109932
5. Liang, L., Li, X., Yin, J., Wang, D., Gao, W., Guo, Z. Vibration characteristics of damping pad floating slab on the long-span steel truss cable-stayed bridge in urban rail transit. *Engineering Structures*. 2019. 191. Pp. 92–103. DOI: 10.1016/j.eng-struct.2019.04.032
6. Khodzhaev, D., Abdikarimov, R., Vatin, N. Nonlinear oscillations of a viscoelastic cylindrical panel with concentrated masses. *MATEC Web of Conferences*. 2018. 245. DOI: 10.1051/mateconf/201824501001
7. Santana, M.V.B., Gonçalves, P.B., Silveira, R.A.M. Closed-form solutions for the symmetric nonlinear free oscillations of pyramidal trusses. *Physica D: Nonlinear Phenomena*. 2021. 417. Pp. 132814. DOI: 10.1016/j.physd.2020.132814
8. Liu, M., Cao, D., Zhang, X., Wei, J., Zhu, D. Nonlinear dynamic responses of beamlike truss based on the equivalent nonlinear beam model. *International Journal of Mechanical Sciences*. 2021. 194. Pp. 106197. DOI: 10.1016/j.ijmecsci.2020.106197
9. Ufimtcev, E. Dynamic Calculation of Nonlinear Oscillations of Flat Trusses Part 2: Examples of Calculations. *Procedia Engineering*. 2017. 206. Pp. 850–856. DOI: 10.1016/j.proeng.2017.10.562.
10. Ufimtsev, E., Voronina, M. Research of Total Mechanical Energy of Steel Roof Truss during Structurally Nonlinear Oscillations. *Procedia Engineering*. 2016. 150. Pp. 1891–1897. DOI: 10.1016/j.proeng.2016.07.188.
11. Kirsanov, M.N., Petrichenko, E.A., Vorobev, O.V. The formula for the lower estimate of the fundamental frequency of natural vibrations of a truss with an arbitrary number of panels. *Construction of Unique Buildings and Structures*. 2021. 94(1). Pp. 9403–9403. DOI:10.4123/CUBS.94.3. URL: <https://unistroy.spbstu.ru/article/2021.94.3> (date of application: 6.03.2021)
12. Vorobyev, O. About methods of obtaining analytical solution for eigenfrequencies problem of trusses. *Structural mechanics and structures*. 2020. 1(24). Pp. 25–38. URL: [http://vuz.exponenta.ru/PDF/NAUKA/elibrary\\_42591122\\_21834695.pdf](http://vuz.exponenta.ru/PDF/NAUKA/elibrary_42591122_21834695.pdf)
13. Vorobev, O.V. Bilateral Analytical Estimation of the First Frequency of a Plane Truss. *Construction of Unique Buildings and Structures*. 2020. 92(7). Pp. 9204–9204. DOI: 10.18720/CUBS.92.4.
14. Kirsanov, M.N., T.D.V. Analysis of the natural frequencies of oscillations of a planar truss with an arbitrary number of panels. *Vestnik MGSU*. 2019. 14(4). Pp. 284–292. DOI: 10.22227/1997-0935.2019.3.284-292. URL: <http://vuz.exponenta.ru/1/kt.pdf> (date of application: 11.03.2021)
15. Kirsanov, M.N., Vorobyev, O.V. Calculating of a spatial cantilever truss natural vibration frequency with an arbitrary number of panels: analytical solution. *Construction of Unique Buildings and Structures*. 2021. 94. Pp. 9402. DOI: 10.4123/CUBS.94.2
16. Petrichenko, E.A. Lower bound of the natural oscillation frequency of the Fink truss. *Structural Mechanics and Structures*. 2020. 26(3). Pp. 21–29.
17. Hutchinson, R.G., Fleck, N.A. Microarchitected cellular solids - The hunt for statically determinate periodic trusses. *ZAMM Zeitschrift für Angewandte Mathematik und Mechanik*. 2005. 85(9). Pp. 607–617. DOI: 10.1002/zamm.200410208
18. Hutchinson, R.G., Fleck, N.A. The structural performance of the periodic truss. *Journal of the Mechanics and Physics of Solids*. 2006. 54(4). Pp. 756–782. DOI: 10.1016/j.jmps.2005.10.008
19. Zok, F.W., Lattice, R.M., Begley, M.R. Periodic truss structures. *Journal of the Mechanics and Physics of Solids*. 2016. 96. Pp. 184–203. DOI: 10.1016/j.jmps.2016.07.007.
20. Kirsanov, M.N. *Planar trusses: Schemes and Formulas*. Cambridge Scholars Publishing Lady Stephenson Library. Newcastle upon Tyne, GB, 2019.
21. Kirsanov, M. *Trussed Frames and Arches: Schemes and Formulas*. Cambridge Scholars Publishing Lady Stephenson Library. Newcastle upon Tyne, GB, 2020.

22. Ovsyannikova, V.M. Dependence of deformations of a trapezous truss beam on the number of panels. *Structural Mechanics and Structures*. 2020. 26(3). Pp. 13–20.
23. Ilyushin, A.S. The formula for calculating the deflection of a compound externally statically indeterminate frame. *Structural mechanics and structures*. 2019. 22(3). Pp. 29–38.
24. Rakhmatulina, A.R., Smirnova, A.A. Analytical calculation and analysis of planar springel truss. *Structural mechanics and structures*. 2018. 17(2). Pp. 72–79. URL: <http://vuz.exponenta.ru/PDF/NAUKA/Rahm-Smirn2018-2.pdf> (date of application: 27.02.2021)
25. Kreith, K. *Oscillation Theory*. 324. Springer Berlin Heidelberg. Berlin, Heidelberg, 1973.
26. Liu, X., Li, Y., Lin, Y., Banerjee, J.R. Spectral dynamic stiffness theory for free vibration analysis of plate structures stiffened by beams with arbitrary cross-sections. *Thin-Walled Structures*. 2021. 160. Pp. 107391. DOI: 10.1016/J.TWS.2020.107391
27. Buka-Vaivade, K., Kirsanov, M.N., Serdjuk, D.O. Calculation of deformations of a cantilever-frame planar truss model with an arbitrary number of panels. *Vestnik MGSU*. 2020. (4). Pp. 510–517. DOI: 10.22227/1997-0935.2020.4.510-517
28. Rapp, B.E. *Introduction to Maple. Microfluidics: Modelling, Mechanics and Mathematics*. Elsevier, 2017. Pp. 9–20.
29. Trainor, P.G.S., Shah, A.H., Popplewell, N. Estimating the fundamental natural frequency of towers by Dunkerley's's method. *Journal of Sound and Vibration*. 1986. 109(2). Pp. 285–292. DOI: 10.1016/S0022-460X(86)80009-8
30. Low, K.H. Modified Dunkerley's formula for eigenfrequencies of beams carrying concentrated masses. *International Journal of Mechanical Sciences*. 2000. 42(7). Pp. 1287–1305. DOI: 10.1016/S0020-7403(99)00049-1

**Information about authors:**

**Mikhail Kirsanov**, Sc.D. in Physics and Mathematics

ORCID: <https://orcid.org/0000-0002-8588-3871>

E-mail: [c216@ya.ru](mailto:c216@ya.ru)

**Vladimir Safronov**, Sc.D. in Technical Science

E-mail: [vss22@mail.ru](mailto:vss22@mail.ru)

*Received 26.03.2021. Approved after reviewing 12.07.2021. Accepted 12.07.2021.*



Research article

UDC 666.9.03

DOI: 10.34910/MCE.111.15

## 3D-printable artificial marble

**G.S. Slavcheva** , **E.A. Britvina**   
Voronezh State Technical University, Voronezh, Russia  
 [gslavcheva@yandex.ru](mailto:gslavcheva@yandex.ru)

**Keywords:** additive manufacturing, 3d-printable material, rheological behavior, compressive strength, setting time

**Abstract.** This paper presents the rheological and hardened properties of novel 3D-printable materials imitating structures of marble. The effects of mixed proportion on rheological behavior, kind of texture, setting time, density, compressive strength, water absorption, drying shrinkage, frost resistance are presented together. Two kinds of squeezing tests were used to evaluate the extrusion ability and shape stability of the fresh mixture. A high compression speed test using constant plate speed of 5 mm/s was implemented to simulate the behavior of the system in the process of extrusion. The squeezing test was conducted with a constant strain rate of 0.5 N/s as to model the behavior of the system in the process of multi-layer casting. Properties of the 3D-printable artificial marble were determined by Russian standards. The fresh mixtures of 3D-printable artificial marbles had plastic yield value of 1.2–3.5 kPa, structural strength of 1.2–3.3 kPa, the value of plastic deformations was 0.05–0.06 mm/mm. This defined the ability of these mixtures to plastically deform without structure destruction and hold their form, resist the deformation under compressions load during multi-layer casting. The received specimens of artificial marble resemble six kinds of textures of white and color marble. The 3D-printable artificial marble had high compressive strength (36–48 MPa and 55–68 MPa at 1 day and 28 days after production respectively), low water absorption (0.75 %), drying shrinkage (1.3–1.9 mm/m), high frost resistance and short setting time that determine the effectiveness of 3D-printed structures life cycle.

### 1. Introduction

The idea of scaling up additive manufacturing techniques for automated building construction has been a topic of research for several years [1–8]. Research to date can be classified into the next groups:

- pumpability, extrusion ability, printability, buildability, open time of 3D-printable mixture [9–14];
- component design, properties, and durability of 3D-printed composite materials [15–19];
- modeling, mechanics, and control of the 3D-printing process [10, 11, 20–22];
- demonstrating the viability of 3D-printed structures [23–26].

According to review [18, 19], the component design is the interdependent factor affecting mechanics and control of the 3D-printing process and viability of 3D-printed structures. The material is typically a high cement content mortar, which contains a different kind of aggregates with a maximum particle size in the order of 2 mm to 3 mm, plasticizer, viscosity modifying additive, fiber.

At the same time, the typical viable 3D-printed structures are printed shells watch that have a function of permanent formwork. All known and used compositions of 3D-printed materials are produced by using grey cement and plain, monochrome aggregates. As a result, 3D-printed structures are grey and plain too and need finishing and painting in order to provide their architectural expressiveness. It is obvious that the

Slavcheva, G.S., Britvina, E.A. 3D-printable artificial marble. Magazine of Civil Engineering. 2022. 111(3). Article No. 11115. DOI: 10.34910/MCE.111.15

© Slavcheva, G.S., Britvina, E.A., 2022. Published by Peter the Great St. Petersburg Polytechnic University.



This article is licensed under a CC BY-NC 4.0

finishing requires a lot of handwork that would discredit the idea of robotic 3D-printing technology. The solution to this problem can be the usage of decorative concrete, whose properties would be adapted to the printing process.

However, all known kind of color decorative concretes are used in traditional concrete casting technology [27–30]. Therefore, the development of 3D-printable decorative concrete would allow the 3D-printed structures to obtain architectural expressiveness without additional costs for their finishing.

This paper aims to contribute to this promising line of research, and reports on outcomes of a research program aimed to develop a novel 3D-printable decorative concrete.

## 2. Materials and Methods

Six types of 3D-printable cement pastes were studied (Table 1). The initial components were used of the system:

- white Portland cement CEM I 52.5 R (EN 197 – 1: 2011),
- the plasticizer of Sika trademark based on polycarboxylate ethers,
- complex viscosity modifying additive,
- three kinds of aggregates, limestone filler ( $\text{CaCO}_3$  content ~ 95%; a particle size distribution ranging from 1 to 75  $\mu\text{m}$ ),
- polypropylene fiber ( $l = 12 \text{ mm}$ ,  $d = 0.022 - 0.034 \text{ mm}$ ),
- pigments ( $\text{Fe}_2\text{O}_3$  content ~ 80%).

**Table 1. Tested cement paste composition and specimen identification.**

| Specimen ID | Components/ mass cement (%) |                                      |                     |            |                  |             | W/C  | kind of aggregates   |
|-------------|-----------------------------|--------------------------------------|---------------------|------------|------------------|-------------|------|----------------------|
|             | plasticizer                 | complex viscosity modifying additive | polypropylene fiber | aggregates | limestone filler | pigment     |      |                      |
| T1          | 1.2                         | 0.4                                  | 0.5                 | 125        | -                | -           | 0.32 | sand                 |
| T2          | 1.2                         | 0.4                                  | 0.5                 | 125        | -                | -           | 0.35 | granite              |
| T3          | 1.2                         | 0.4                                  | 0.5                 | 100        | 25               | -           | 0.39 | slate                |
| T4          | 1.2                         | 0.4                                  | 0.5                 | 125        | -                | 0.2 (red)   | 0.35 | granite + slate      |
| T5          | 1.2                         | 0.4                                  | 0.5                 | 125        | -                | 0.2 (green) | 0.35 | granite + serpentine |
| T6          | 1.2                         | 0.4                                  | 0.5                 | 100        | 25               | -           | 0.38 | granite + slate      |

The aggregates had a particle size distribution ranging from 0 to 5 mm (Table 2). The white Portland cement and aggregates with different colors and particle sizes have been used to achieve the imitation structure of marble. W/C- ratio, concentration, and the particle size range of aggregates, the concentration of limestone filler was assumed as the main factors for the change of rheological behaviour of the 3D-printable cement pastes. Content of plasticizer, complex viscosity modifying additives, polypropylene fiber were assumed as a fixed factor for the experiments.

**Table 2. The particle size distribution of limestone filler.**

| kind of aggregates | color      | particle size range    |                         |
|--------------------|------------|------------------------|-------------------------|
|                    |            | volume of particles, % | size (d), $\mu\text{m}$ |
| sand               | white      | 13.2                   | 630                     |
|                    |            | 49.3                   | 315                     |
|                    |            | 37.5                   | 160                     |
|                    |            | 67.0                   |                         |
| granite            | yellow     | 13.0                   | 1250                    |
|                    |            | 20.0                   | 630                     |
|                    |            |                        |                         |
| slate              | terracotta | ~ 98                   | 2500                    |
| serpentine         | green      | 65.4                   | 5000                    |
|                    |            | 34.6                   | 2500                    |



To evaluate the extrusion ability and firm stability of fresh mixture, the different kinds of squeezing tests were used following the methodology developed in the works [10, 20–22, 31, 32].

Cylindrical samples of fresh cement paste with radius  $R$  equal to their height  $h_0 = 25$  mm were used for the implementation of the experiment. For the squeezing test, the sample was put between two smooth plates diameter of which corresponded to the size of the sample and was loaded into the testing system “INSTRON Sates 1500 HDS”. The test was conducted on a fresh sample for all mixtures directly after their molding.

High compression speed test using constant plate speed  $v = 5$  mm/s was implemented as the behaviour of the system in the process of extrusion is most adequately modeled with this speed. The curves “compression force  $N$  is displacement  $\Delta_{pl}$ ” were obtained during the experiments were interpreted as influence curves of reduced compression load  $F^*$  from a relative change of height of the sample  $h_i/R$ :

$$F_i^* = \frac{Ph_i}{\pi R^2}, \quad (1)$$

where  $h_i = (h_0 - \Delta)$ ,  $h_0$  is the initial height of the sample,  $\Delta$  is transferred in the point of time, value  $R$  was taken as constant and equal to the radius of the sample at the beginning of the experiment.

According to the results of the analysis of the received experimental curves for the studied system's values  $K_i$ , called plastic yield value by N. Roussel and C. Lanos [20, 21], was calculated at the inflection point of the  $F^*(h_i/R)$  curves ( $h_i/R = 0.9$ ):

$$K_i \left( \frac{h_i}{R} \right) = \frac{\sqrt{3}F^*}{2} \quad (2)$$

The squeezing test was conducted with a constant strain rate  $v = 0.5$  N/s was implemented as the behaviour of the system in the process of multi-layer casting [32]. The strain rate conforms to the average speed of load increase during multi-layer casting of building sites by industrial printers. The methodology of its implementation corresponds to the approaches of A. Perrot [10, 22] to the evaluation of the buildability of the 3D printable mixtures. Squeezing was conducted until the rupture of the samples. The curves “displacement  $\Delta_{pl}$  – time  $\tau$ ”, “displacement  $\Delta$  is compression force  $N$ ” were recorded as the result of the experiments. Based on the obtained experimental curves, structural strength ( $\sigma_0$ ) of fresh mixtures was calculated for the moments corresponding to the start of deformation ( $\Delta_{pl} = 0.1$  mm), and plastic strength ( $\sigma_{pl}$ ) was calculated at the beginning of cracking. The value of plastic deformations  $\Delta_{pl}$  at the start of cracking was determined as a ratio of the displacement  $\Delta$  of the plates in the squeezing test to the initial height of the sample  $h_0$ .

Properties of the 3D-printable artificial marble were determined by Russian standards:

- water absorption according to Russian State Standard GOST 12730.3 “Concretes. Method of determination of water absorption”;
- setting time according to Vicat method (Russian State Standard GOST 310.3 “Cements. Methods for determination of standard consistency, times of setting and soundness”);
- compressive strength according to Russian State Standard GOST 10180 – 12 “Concretes. Methods for strength determination using reference specimens” using the universal 4-column static hydraulic testing system “INSTRON Sates 1500 HDS”;
- frost resistance according to Russian State Standard GOST 10060-2012 “Concretes. Methods for determination of frost-resistance” (the first basic method for repeated freezing and thawing);
- drying shrinkage according to Russian State Standard GOST 24544-2020 “Concretes. Methods of shrinkage and creep flow determination”.

### 3. Results and Discussion

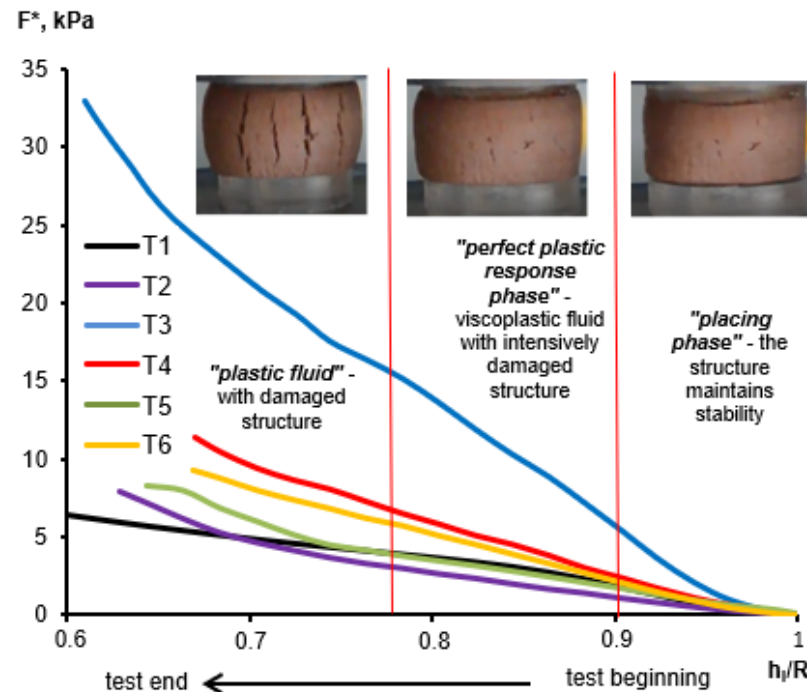
#### 3.1. Rheological behaviour

The rheological properties of fresh mixtures for 3D-printable artificial marble are listed in Table 3. Results of two kind of squeezing tests are shown in Figure 1, 2.

**Table 3. Rheological properties of 3D-printable artificial mixtures.**

| Specimen ID | Plastic yield value $K_i$ , kPa | Strength, kPa         |                       | Value of plastic deformations $\Delta_{pl}$ , mm/mm |
|-------------|---------------------------------|-----------------------|-----------------------|---|
|             |                                 | structural $\sigma_0$ | plastic $\sigma_{pl}$ |   |
| T1          | 2.38                            | 0.74                  | 45.78                 | 0.06  |
| T2          | 1.23                            | 1.42                  | 42.25                 | 0.08  |
| T3          | 4.70                            | 0.41                  | 51.41                 | 0.06  |
| T4          | 3.49                            | 1.95                  | 40.71                 | 0.05  |
| T5          | 1.72                            | 3.29                  | 35.13                 | 0.05  |
| T6          | 2.35                            | 1.19                  | 28.54                 | 0.06  |

As a result of the interpretation of the squeezing test with constant plate speed, we received experimental curves  $F^* = f(h_i/R)$  (Fig. 1) which correspond to the similar curves of N. Roussel [21]. Analysis of experimental curves  $F^* = f(h_i/R)$  for the description of rheological behavior of fresh artificial marble paste during squeezing was conducted based on approaches of fundamental structural rheology of disperse systems [31].

**Figure 1. Tested artificial marble  $F^*(h_i/R)$  curves.**

Under the action of low compression stress on the first section of the curve within deformation range  $\sim 0.9 < h_i/R < 1$  the structure maintains stability ("placing phase" according to N. Roussel's terminology). According to point of view structural rheology of disperse systems, the "placing phase" can be characterized as a viscoplastic fluid with undisturbed structure. When the stress on the second section increases with  $0.8 < h_i/R < 0.9$ , the system is plastically deformed while its structure loses its stability ("perfect plastic response phase" according to N. Roussel). This section can be correlated with a viscoplastic fluid with intensively damaged structure in conformity with the structural rheology approach.

The experimental results show similar kinds of  $F^*(h_i/R)$  curves for 5 studied systems (T1, T2, T4, T5, T6). They have expressed a horizontal section of plastic deformation. For the systems transfer from stable condition to plastic flow is estimated by load  $F^*$  for  $\sim 2.0 \div 3.0$  kPa, transfer into the condition of the flow with damaged structure happens with  $F^* > 5.0$  kPa. These mixtures can be extruded through an extruder nozzle with low squeezing force. The system T3 does not have the horizontal section of plastic deformation, transfer from stable condition to plastic flow is estimated by load  $F^*$  for  $\sim 6.0$  kPa.

The systems T1, T2, T4, T5, T6 have rational values plastic yield value  $K_i = 1.2 - 3.5$  kPa (Table 3), which is determined at the beginning of the viscoplastic fluid of disperse system with undisturbed structure.

These values  $K_i$  ensure the best extrudability due to their sufficient plasticity and capacity for viscoplastic flow without the structure damage under the influence of extrusion stress [32]. At the same time, the system T3 having the highest plastic yield value ( $K_i = 4.5$  kPa) can not have a capacity for viscoplastic flow in the extrusion process due to high rigidity.

Analysis of the received experimental data of the curves “displacement  $\Delta$  – time  $\tau$ ”, “displacement  $\Delta$  – compression force  $N$ ” (Fig. 2) shows three typical zones of rheological behavior.

The first one is the zone of phase stability. The structural strength  $\sigma_0$  is calculated based on the quantity load  $N$  at the beginning of deformation of viscoplastic mixtures can be considered as the main criterion of their buildability. The structural strength  $\sigma_0$  characterizes the ability of the system to maintain stability without deformation during loading. The second one is the zone of the plastic phase. The system’s ability to deform without destruction is evaluated by the quantity of plastic strength  $\sigma_{pl}$  calculated based on the quantity load  $N$  at the beginning of cracking. To characterize buildability, it seems reasonable to evaluate the number of plastic deformations on this section  $\Delta_{pl}$ , which have to be minimized for 3D printable materials. The third one is the cracking phase and intensively destruction of the structure. The curves “ $\Delta - \tau$ ” shows that all studied system displays the similar phase stability and plastic phase zone. However, the structural strength for system T3 is less in  $\sim 2 - 3$  times comparing with the systems T1, T2, T4, T5, T6 (see Table 3).

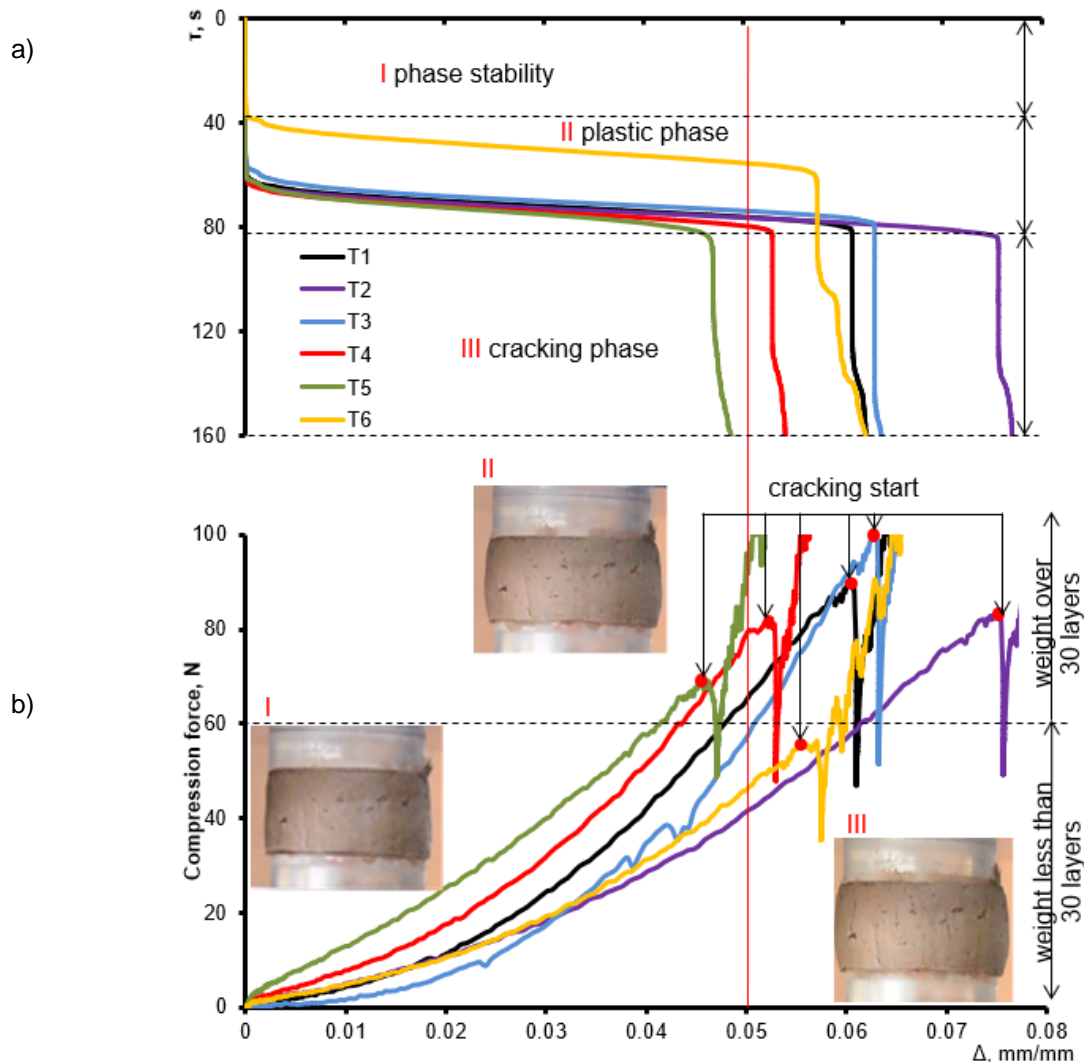


**Figure 2. Tested artificial marble “displacement  $\Delta$  – time  $\tau$ ” (a) and “displacement  $\Delta$  – compression force  $N$ ” (b) experimental results.**

The transition between plastic yield value  $K_i$ , the value of structural  $\sigma_0$  and plastic  $\sigma_{pl}$  strength, plastic deformations  $\Delta_{pl}$  is linked to the concentration and a particle size distribution of the aggregates and filler. At the same time, the inclusion of pigments does not have a significant influence on the rheological properties of mixtures.

Change of rheological characteristics of mixture depends on kind of distribution of particle size. If aggregates have different particle sizes, their particles rationally locate between cement particles. As a result, dense spatial packing of solid particles into cement paste structure is ensured. Such structuring of the mixture solid-phase ensures the increase of their firm stability and consequently buildability. By contrast, aggregates having equal particle size loosen fresh mixture structure. This effect of decreasing plasticity and firm stability of mixtures is logically related to the influence of aggregates. Introduction of aggregates into dispersing system “cement + water” as a regulating factor of solid-phase properties changes packing density and molecular interactions between solid particles. As a result, flow under stress becomes difficult for coarser systems containing aggregates. For systems T1, T2, T4, T5, T6 (aggregates with different particle sizes (see Table 2)) plastic yield value  $K_i$ , corresponding to the beginning of the plastic flow, is in the range from 1.23 to 2.49 kPa. At the same time, these systems have enough firm stability ( $\sigma_0 = 1.2 - 3.3$  kPa,  $\Delta_{pl} = 0.05 - 0.06$ ). The system T3 (aggregates with equal particle size) is characterized by the highest rigidity ( $K_i = 4.70$  kPa) and the least firm stability ( $\sigma_0 = 0.41$  kPa,  $\Delta_{pl} = 0.06$ ). Therefore, usage of aggregates with different particle sizes allows the fresh mixture to obtain plasticity and firm stability but usage of aggregates with equal particle size would not be possible to ensure that.

### 3.2. Properties of 3D-printable artificial marble

As shown in Figure 3, all the specimens of received 3D-printable composites resemble the structures of marble. System T1 imitates the structure of white marble; the systems T2 – T6 imitate the different structures of color marble.

Table 4 shows the properties of specimens of received 3D-printable artificial marble. The average density of all the specimens is 2150 kg/m<sup>3</sup>, the average water absorption is 0.75 %, frost resistance 200 cycles, drying shrinkage 1.3–1.9 mm/m. The compressive strength of 3D-printable artificial marble specimens is in the range from 36.5 to 47.7 MPa at 1 day after production; from 54.5 to 67.9 MPa at 28 days after production. In 1 day of hardening 3D-printable artificial marble occurs the most intensive growth of the strength. It is important to emphasize that in this period the strength receives 75 -80 % from 28 days strength.

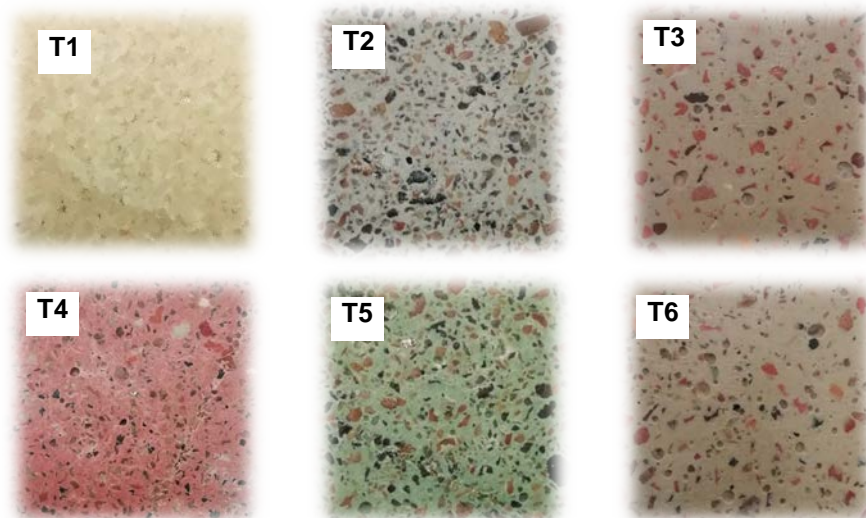


Figure 3. The structures of 3D-printable artificial marble.

Table 4. Properties of 3D-printable artificial marble.

| Specimen ID | Density, kg/m <sup>3</sup> | Water absorption, % | Setting time, min | Compressive strength, MPa |         | Frost resistance, cycle | Drying shrinkage, mm/m |
|-------------|----------------------------|---------------------|-------------------|---------------------------|---------|-------------------------|------------------------|
|             |                            |                     |                   | 1 day                     | 28 days |                         |                        |
| T1          | 2250                       | 0.2                 | 105               | 47.7                      | 67.9    | 200                     | ≤ 1.6                  |
| T2          | 2200                       | 0.3                 | 105               | 44.8                      | 60.9    | 200                     | ≤ 1.4                  |
| T3          | 2150                       | 1.7                 | 120               | 47.5                      | 66.6    | 200                     | ≤ 1.7                  |
| T4          | 2250                       | 0.8                 | 75                | 41.6                      | 63.8    | 200                     | ≤ 1.4                  |
| T5          | 2150                       | 0.9                 | 60                | 36.5                      | 54.5    | 200                     | ≤ 1.3                  |
| T6          | 2150                       | 0.6                 | 120               | 42.2                      | 63.6    | 200                     | ≤ 1.9                  |

These results indicate that changing the kind of aggregates, the inclusion of pigments does not have a significant influence on the properties of materials. On the other hand, the inclusion of pigments has a positive influence on the setting time of mixtures. The systems without pigments (T1, T2, T3, T6) are characterized by setting time 105–120 min, the systems with pigments (T4, T5) are characterized by setting time 60–75 min. That is due to the pigment content directly related to the hydration process despite the aggregates kind and ratio varies.

The high early-age strength, short setting time, low water absorption and drying shrinkage, high frost resistance are very important attributes to 3D-printable materials because they determine the effectiveness of building technology and durability of 3D-printed structures.

## 4. Conclusion

Six kinds of structures of 3D-printable artificial marbles have been received using white Portland cement, pigments, and aggregates with different colors and particle sizes.

The fresh mixtures of 3D-printable artificial marbles had plastic yield value  $K_i \cong 1.2 - 3.5$  kPa that is defined the ability of these mixtures to plastically deform without structure destruction and maintain stability during extrusion. At the same time, these systems had enough firm stability (structural strength  $\sigma_0 = 1.2 - 3.3$  kPa, the value of plastic deformations  $\Delta_{pl} = 0.05 - 0.06$  mm/mm) that is characterized the system's ability to hold its form, resist the deformation under compressions load during multi-layer casting.

The optimal rheological characteristics of fresh mixtures can be achieved with the usage of aggregates with different particle sizes. The fresh mixtures having aggregate's particle size range from 0.15 to 5 mm are characterized by the optimal plasticity, structural strength, and deformability under the load. Using aggregates with equal particle size impairs these characteristics of mixtures.

The 3D-printable artificial marble had high compressive strength (36–48 MPa and 55–68 MPa at 1 day and 28 days after production respectively), low water absorption (0.75 %) and drying shrinkage (1.3–1.9 mm/m), high frost resistance and short setting time that determine the effectiveness of 3D-printed structures life cycle.

## 5. Acknowledgments

The experimental studies have been carried out using the facilities of the Collective Research Center named after Professor Yu.M. Borisov, Voronezh State Technical University, which is partly supported by the Ministry of Science and Education of the Russian Federation, Project No 075- 15-2021-662

## References

1. Lim, S., Buswell, R.A., Le, T.T., Austin, S.A., Gibb, A.G.F., Thorpe, T. Developments in construction-scale additive manufacturing processes. *Automation in Construction*. 2012. 21(1). Pp. 262–268. DOI:10.1016/j.autcon.2011.06.010
2. Zhang, J., Wang, J., Dong, S., Yu, X., Han, B. A review of the current progress and application of 3D printed concrete. *Composites Part A: Applied Science and Manufacturing*. 2019. 125. Pp. 105533. DOI:10.1016/j.compositesa.2019.105533
3. Labonnote, N., Rønnquist, A., Manum, B., Rüther, P. Additive construction: State-of-the-art, challenges and opportunities. *Automation in Construction*. 2016. 72. Pp. 347–366. DOI:10.1016/j.autcon.2016.08.026
4. Buswell, R.A., Leal de Silva, W.R., Jones, S.Z., Dirrenberger, J. 3D printing using concrete extrusion: A roadmap for research. *Cement and Concrete Research*. 2018. 112. Pp. 37–49. DOI:10.1016/j.cemconres.2018.05.006
5. Ngo, T.D., Kashani, A., Imbalzano, G., Nguyen, K.T.Q., Hui, D. Additive manufacturing (3D printing): A review of materials, methods, applications and challenges. *Composites Part B: Engineering*. 2018. 143. Pp. 172–196. DOI: <https://doi.org/10.1016/j.compositesb.2018.02.012>
6. Shakor, P., Nejati, S., Paul, G., Malek, S. Review of emerging additive manufacturing technologies in 3d printing of cementitious materials in the construction industry. *Frontiers in Built Environment*. 2019. 4(85). Pp. 1–17. DOI:10.3389/fbuil.2018.00085
7. Wangler, T., Roussel, N., Bos, F.P., Salet, T.A.M., Flatt, R.J. Digital Concrete: A Review. *Cement and Concrete Research*. 2019. 123. Pp. 105780. DOI: <https://doi.org/10.1016/j.cemconres.2019.105780>
8. Khan, M.S., Sanchez, F., Zhou, H. 3-D printing of concrete: Beyond horizons. *Cement and Concrete Research*. 2020. 133. Pp. 106070. DOI: 10.1016/j.cemconres.2020.106070
9. Liu, Z., Li, M., Weng, Y., Wong, T.N., Tan, M.J. Mixture Design Approach to optimize the rheological properties of the material used in 3D cementitious material printing. *Construction and Building Materials*. 2019. 198. Pp. 245–255. DOI: 10.1016/j.conbuildmat.2018.11.252
10. Perrot, A., Rangeard, D., Pierre, A. Structural built-up of cement-based materials used for 3D-printing extrusion techniques. *Materials and Structures/Materiaux et Constructions*. 2016. 49. Pp. 1213–1220. DOI: 10.1617/s11527-015-0571-0
11. Roussel, N. Steady and transient flow behaviour of fresh cement pastes. *Cement and Concrete Research*. 2005. 35. Pp. 1656–1664. DOI: 10.1016/j.cemconres.2004.08.001
12. Nerella, V.N., Näther, M., Iqbal, A., Butler, M., Mechtcherine, V. Inline quantification of extrudability of cementitious materials for digital construction. *Cement and Concrete Composites*. 2019. 95. Pp. 260–270. DOI: 10.1016/j.cemconcomp.2018.09.015
13. Charrier, M., Ouellet-Plamondon, C. Testing Procedures on Materials to Formulate the Ink for 3D Printing. *Transportation Research Record*. 2020. 2674(2). DOI: 10.1177/0361198120907583

14. Le, T.T., Austin, S.A., Lim, S., Buswell, R.A., Gibb, A.G.F., Thorpe, T. Mix design and fresh properties for high-performance printing concrete. *Materials and Structures/Materiaux et Constructions*. 2012. 45(8). Pp. 1221–1232. DOI: 10.1617/s11527-012-9828-z
15. Le, T.T., Austin, S.A., Lim, S., Buswell, R.A., Law, R., Gibb, A.G.F., Thorpe, T. Hardened properties of high-performance printing concrete. *Cement and Concrete Research*. 2012. 42(3). Pp. 558–566. DOI: 10.1016/j.cemconres.2011.12.003
16. Feng, P., Meng, X., Chen, J.F., Ye, L. Mechanical properties of structures 3D printed with cementitious powders. *Construction and Building Materials*. 2015. 93. Pp. 486–497. DOI: 10.1016/j.conbuildmat.2015.05.132
17. Ma, G., Wang, L. A critical review of preparation design and workability measurement of concrete material for largescale 3D printing. *Frontiers of Structural and Civil Engineering*. 2018. 12(3). Pp. 382–400. DOI: 10.1007/s11709-017-0430-x
18. N.I. Vatin, L.I. Chumadova, I.S. Goncharov, V.V. Zykova, A.N. Karpenya, A.A. Kim, E.A. Finashenkov. 3D-Pechat V Stroitelstve. *Stroitelstvo Unikalnykh Zdaniy I Sooruzheniy*. 2017. 1(52). Pp. 27–46. DOI: 10.18720/CUBS.52.3
19. Lu, B., Weng, Y., Li, M., Qian, Y., Leong, K.F., Tan, M.J., Qian, S. A systematical review of 3D printable cementitious materials. *Construction and Building Materials*. 2019. 207. Pp. 477–490. DOI: 10.1016/j.conbuildmat.2019.02.144
20. Roussel, N., Lanos, C. Plastic fluid flow parameters identification using a simple squeezing test. *Applied Rheology*. 2003. 13(3). Pp. 132–141. DOI: 10.1515/arh-2003-0009
21. Toutou, Z., Roussel, N., Lanos, C. The squeezing test: A tool to identify firm cement-based material's rheological behaviour and evaluate their extrusion ability. *Cement and Concrete Research*. 2005. 35(10). Pp. 1891–1899. DOI: 10.1016/j.cemconres.2004.09.007
22. Perrot, A., Mélinge, Y., Rangeard, D., Micaelli, F., Estellé, P., Lanos, C. Use of ram extruder as a combined rheo-tribometer to study the behaviour of high yield stress fluids at low strain rate. *Rheologica Acta*. 2012. 51(8). Pp. 743–754. DOI: 10.1007/s00397-012-0638-6
23. Buswell, R.A., Soar, R.C., Gibb, A.G.F., Thorpe, A. Freeform Construction: Mega-scale Rapid Manufacturing for construction. *Automation in Construction*. 2007. 16. Pp. 224–231. DOI: 10.1016/j.autcon.2006.05.002
24. Khoshnevis, B. Automated construction by contour crafting - Related robotics and information technologies. *Automation in Construction*. 2004. Pp. 5–19. DOI: 10.1016/j.autcon.2003.08.012
25. Cesaretti, G., Dini, E., De Kestelier, X., Colla, V., Pambaguian, L. Building components for an outpost on the Lunar soil by means of a novel 3D printing technology. *Acta Astronautica*. 2014. 93. Pp. 430–450. DOI: 10.1016/j.actaastro.2013.07.034
26. Gosselin, C., Duballet, R., Roux, P., Gaudillière, N., Dirrenberger, J., Morel, P. Large-scale 3D printing of ultra-high performance concrete - a new processing route for architects and builders. *Materials and Design*. 2016. 100. Pp. 102–109. DOI: 10.1016/j.matdes.2016.03.097
27. López, A., Guzmán, G.A., Di Sarli, A.R. Color stability in mortars and concretes. Part 1: Study on architectural mortars. *Construction and Building Materials*. 2016. 120. Pp. 617–622. DOI: 10.1016/j.conbuildmat.2016.05.133
28. López, A., Guzmán, G.A., Di Sarli, A.R. Color stability in mortars and concretes. Part 2: Study on architectural concretes. *Construction and Building Materials*. 2016. 123. Pp. 248–253. DOI: 10.1016/j.conbuildmat.2016.06.147
29. Bazhenova, O., Kotelnikov, M. Operational features of decorative concrete. *E3S Web of Conferences*. 2018. Pp. 02021. DOI: 10.1051/e3sconf/20183302021
30. Kopecskó, K. Self-compacting concrete produced with limestone waste. *IOP Conference Series: Materials Science and Engineering*. 2018. Pp. 012006. DOI: 10.1088/1757-899X/442/1/012006
31. Slavcheva, G.S., Artamonova, O.V. The rheological behavior of disperse systems for 3D printing in construction: the problem of control and possibility of «nano» tools application. *Nanotechnologies in Construction: A Scientific Internet-Journal*. 2018. 10(3). Pp. 107–122. DOI: 10.15828/2075-8545-2018-10-3-107-122
32. Slavcheva, G.S., Artamonova, O. V. Rheological behavior of 3D printable cement paste: Critical evaluation. *Magazine of Civil Engineering*. 2018. 84(8). Pp. 97–108. DOI: 10.18720/MCE.84.10

### **Information about authors:**

**Galina Slavcheva, Sc.D. in Technical Science**

ORCID: <https://orcid.org/0000-0001-8800-2657>

E-mail: [gslavcheva@yandex.ru](mailto:gslavcheva@yandex.ru)

**Ekaterina Britvina,**

ORCID: <https://orcid.org/0000-0002-0462-4991>

E-mail: [esolovieva@vgasu.vrn.ru](mailto:esolovieva@vgasu.vrn.ru)

*Received 24.06.2021. Approved after reviewing 11.11.2021. Accepted 12.12.2021.*



